QCD anatomy of photon isolation

Inaugural dissertation
at the Faculty of Science,
University of Bern

presented by

Samuel Favrod

from Château d'Œx (Vaud)

Supervisor of the doctoral thesis:

Prof. Dr. Thomas Becher

Institute for Theoretical Physics
Albert Einstein Center for Fundamental Physics
University of Bern

QCD anatomy of photon isolation

Inaugural dissertation
at the Faculty of Science,
University of Bern

presented by

Samuel Favrod

from Château-d'Œx (Vaud)

Supervisor of the doctoral thesis:

Prof. Dr. Thomas Becher

Institute for Theoretical Physics
Albert Einstein Center for Fundamental Physics
University of Bern

Accepted by the Faculty of Science.

Bern, 9 January 2023

The Dean

Prof. Dr. Marco Herwegh

Contents

Abstract

Energetic photons are a short-distance probe to search for new physics and test the standard model at colliders. In order to differentiate photons from different origins at hadron colliders, it is necessary to impose isolation requirements. These requirements restrict the hadronic radiation inside a cone around the photon. In this thesis, we present a factorization theorem for the QCD effects associated with photon isolation. We show that for small cone radius R, photon isolation effects can be captured by a fragmentation function describing the decay of a parton into a photon accompanied by hadronic radiation. We compute this fragmentation function for different isolation criteria. For small isolation energy, the cone fragmentation function factorizes further into jet and soft functions. Using renormalization-group methods, we resum the leading logarithms of R and the non-global logarithms of the ratio ϵ_γ of the isolation energy and the photon energy, so that we control all logarithmically enhanced terms in the cross section. Finally, in the limit of small R and small ϵ_γ, we provide a simple formula to convert NNLO cross-section results from smooth-cone isolation to fixed-cone isolation.

Chapter 1

Introduction

This thesis sheds light on photon production processes at colliders by performing a careful analysis of enhanced QCD corrections induced by the isolation requirements imposed experimentally. It consists of five chapters and three appendices. Chapters 1, 2, 3 and 4 are introductions. Chapter 2 discusses fundamentals of interest for the rest of this thesis, in particular photon detection and parton distribution functions. Chapter 3 is devoted to photon production at colliders, perturbative photon emission, fragmentation and neutral hadrons decaying into photons are discussed. Chapter 4 is about the most common photon isolation criteria. Chapter 5 presents the main results of this thesis. We calculated the resummation of large logarithms of narrow isolation cones with small isolation energy. This part has been submitted for publication in JHEP. The appendices complement this work and provide technical details on Mellin moments, techniques to solve the DGLAP equation and some useful mathematical relations. The last of the appendices provides a detailed guide on how to use MadGraph and MCFM in order to reproduce results presented in this thesis.

The production of prompt photons can be used to test the standard model and QCD. Experimentally, photons are interesting as they are easier to detect precisely than jets. First, photons will deposit energy only in the electromagnetic (EM) calorimeter, whereas jets will deposit energy in both the EM calorimeters and the hadron calorimeters. Secondly, photons will only deposit energy in a small angular region, which is not the case for jets. Additionally, jet fragmentation and hadronization implies that the measurements of energy of the particle creating a jet is not directly possible. Photons do not have this problem [1].

The study of photon production is important to achieve precise predictions for collider physics. For example, photon production at hadron colliders can be used to improve our knowledge of the gluon parton distribution function (PDF) in the proton due to the leading order QCD Compton scattering $qg \to q\gamma$. The constraint on the gluon PDF from photon production is useful to increase the precision of gluon induced processes at colliders. In particular, it improves the precision of gluon fusion for single Higgs production, which is the dominant channel at the LHC [2]. However, studying the non-perturbative fragmentation of the quark to the photon $\mathcal{D}_{q\to\gamma}$ is necessary in order to reduce uncertainties in the determination of the gluon PDF [3, 4].

The decay of the Higgs boson into two photons is an additional reason to study photon production, since it was one of the discovery channels, despite the small branching ratio of only 0.2% [5]. In 2015, an excess of diphotons at the LHC for an energy of approximatively 750 GeV resulted in a large amount of publications to explain the phenomena of a hypothetical resonance [6]. Instead of the discovery of a new particle, it turned out to be a statistical fluctuation [7]. The production of γ+2 jets was used in [8] in order to

estimate the production of Z+2 jets (where the Z decays then into two neutrinos), which is a background to certain beyond the standard model processes.

Photons can be produced through various processes and predicting each of them allows one to subtract the background from the process of interest. For example, the estimation of the background from π^0 and η mesons can be used to subtract this background in order to get a better determination of the non-perturbative fragmentation functions $\mathcal{D}_{i\to\gamma}$ which are not well known.

It is instructive to study photon isolation, as it is used to distinguish between photons from different origins. In particular, it helps to suppress photons originating from hadron decays. Experimentally isolation criteria with small isolation energy E^T_{iso} compared to the photon energy E^T_γ (so $\epsilon_\gamma = E^T_{\text{iso}}/E^T_\gamma \ll 1$) are used, e.g. at ATLAS [9] where photons were required to have $E^T_\gamma \geq 125$ GeV

$$E^T_{\text{iso}} = 4.2\cdot 10^{-3} E^T_\gamma + 4.8\,\text{GeV} \quad \Rightarrow \quad \frac{E^T_{\text{iso}}}{E^T_\gamma} \leq 0.0426 \quad \text{if } E^T_\gamma \geq 125\,\text{GeV}\,. \tag{1.1}$$

For $E^T_\gamma \geq 150$ GeV as in [10], the ratio is smaller with $E^T_{\text{iso}}/E^T_\gamma \leq 0.0362$. The cone openings R considered are typically $R = 0.2$ or 0.4.

A problem arising in theoretical computations with photon isolation is the presence of large logarithms which are spoiling the perturbative expansion. For instance in [11], when computing the cross section for isolated photons at NLO, it turned out that for small isolation cones, the cross section becomes larger than the non-isolated one. Being able to resum the logarithms of R allows us to make reliable predictions that could be used for future measurements with smaller isolation cones. Performing measurements with narrower cones would increase the available statistics as less events are discarded. Considering tight isolation (i.e. small ratio $\epsilon_\gamma = E^T_{\text{iso}}/E^T$) also suppresses the non-perturbative fragmentation which is a source of uncertainty. Therefore, the isolation of interest is a narrow cone with a small isolation energy.

In the case of a narrow cone $R \ll 1$, the leading logarithm resummation of the large logarithms of the radius was performed in [12]. However, the isolation energy considered E^T_{iso} was not small compared to E^T_γ. The case of a large cone with small isolation energy was studied in [13], where the leading logarithms of ϵ_γ were resummed using a parton shower.

In Chapter 5, a factorization theorem for isolated photon production with narrow cone $R \ll 1$ is presented

$$\frac{\mathrm{d}\sigma(E_0,R)}{\mathrm{d}E_\gamma} = \frac{\mathrm{d}\sigma^{\text{dir}}_{\gamma+X}}{\mathrm{d}E_\gamma} + \sum_{i=q,\bar{q},g}\int dz \frac{\mathrm{d}\sigma_{i+X}}{\mathrm{d}E_i}\mathcal{F}_{i\to\gamma}(z,E_\gamma,E_0,R) + \mathcal{O}(R)\,, \tag{1.2}$$

where $\mathcal{F}_{i\to\gamma}$ is the cone fragmentation function. It encodes the collinear fragmentation of a parton i with energy E_i to a photon with energy $E_\gamma = zE_i$. The hadronic energy in the cone is constrained to be less than E_0. $\sigma^{\text{dir}}_{\gamma+X}$ is the perturbative cross-section for producing a photon without isolation. The logarithms of the radius R are resummed by solving the DGLAP evolution of the cone fragmentation function numerically.
Finally, for a narrow cone with a small isolation energy, a second factorization occurs and $\mathcal{F}_{i\to\gamma}$ can be written as a convolution of jet functions $\mathcal{J}$ and coft (collinear and soft) functions $\mathcal{U}$. The narrow cone with small isolation energy has two types of logarithms, $\ln R$

and $\ln \epsilon_\gamma$, that both need to be resummed. The leading logarithms of ϵ_γ are resummed with the help of a parton shower code, called NGL_Resum [14]. Both resummations can be combined and they lead to a decrease of the cross-section.

Thanks to the work done in this thesis it is now possible to reliably predict photon production with tight isolation at NLO. In the future, these predictions should be generalized to NNLO and would complement recent works to compute the photon production at NNLO with both Frixione and fixed-energy cones with wide cones and small isolation energy [15, 16].

Chapter 2

Particle physics at hadron colliders

2.1 A word on experimental physics

In order to test theories and gain a better understanding of the universe, scientists perform a large variety of experiments. Some of these experiments are not too complex to explain and to build, an example of which is the pitch drop experiment. It is a slow experiment and if one wants to perform it, patience is needed. A schema of the experimental setup can be seen in the Figure 2.1. A very viscous liquid is put in a funnel. The substance may be for example asphalt. Under the funnel a beaker is put to receive potential drops. It is necessary to wait for a drop of the substance to fall. The time for a drop to fall is measured. The glass bell protects the experiment from outside influences. However, it does not protect it from temperature variations. With such experiments, it is possible to see that a certain substance is liquid even if it looks like a solid. Such an experiment was started for example in 1927 in the university of Queensland in Australia and so far only 9 drops fell until today (2022). The next drop will probably fall at the end of the decade or a bit later depending on the temperature in the laboratory [17].

Unlike the pitch drop experiment, some experiments are exorbitant, extremely complex and also very fast. For example the Large Hadron Collider (LHC) at CERN (Conseil Européen pour la Recherche Nucléaire) which lays approximately 100 m deep under the canton of Geneva and the Pays de Gex costed a few billions Swiss francs and has a circumference of 27 km [18]. In this section, we will quickly discuss particle colliders and detectors. When running the LHC performs a collision every 25 ns which is sensibly faster than the waiting time between two drops of the experiment discussed previously.

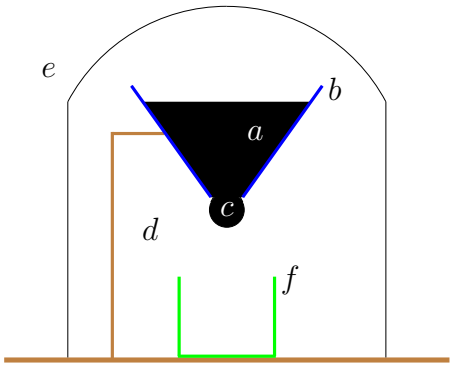

a The viscuous liquid
b The funnel
c Drop slowly forming
d Arm holding the funnel
e Glass bell
f Beaker

Figure 2.1: Schematic representation of a pitch drop experiment.

2.1.1 Particle colliders

In order to study the properties of matter, physicists perform collisions of particles. We can either collide a beam of particles with a fixed target, or we can collide two beams of particles. A famous example of a fixed-target experiment is the Rutherford experiment. In this work we will not discuss fixed-target experiments but only colliders. There are different types of colliders, they are linear or circular, and can collide different types of particles. For example at the LHC protons or ions. Before the LHC at LEP (Large Electron Positron collider) collided electron-positron, at the Tevatron proton-antiproton and at HERA (Hadron Electron Ring Accelerator) electron-proton. Colliding different types of particles allows physicists to study various processes.

The idea is to accelerate two beams of particles, make them interact by smashing into each other and then detecting what comes out of the collision. It may seem simple, but it is complex, costly and requires the work of a substantial amount of people with diverse knowledge. However, it allowed physicists to discover a profusion of particles and gain a better understanding of the universe.

The main collider of interest in this work is the LHC at CERN. We will not discuss how a stable beam of protons is produced and collided at LHC, but will only briefly review the information that is relevant for the rest of this thesis. At the LHC beams of protons with a kinetic energy of a few TeV are collided. The protons are traveling in collimated beams in the opposite direction in the ring and are made to interact at predetermined points. At the end of the Run I (between 2009 and 2013) the protons had an energy up to 4 TeV. During Run II (from 2015 to 2018), the protons had 6.5 TeV. In April 2022, run III started with protons having 6.8 TeV. A beam is composed of bunches of approximately 10^{11} protons and these cross at the interaction points every 25 ns. At every crossing of the two beams, approximately 20 to 30 collisions happen [19, 20] (at Tevatron it was only 5 [21]). During Run II at CMS, it was observed that certain bunch crossings had up to 50 collisions happening. This number of collisions happening at every bunch crossing depends on the intensity of the beam. The LHC is also used to collide ions, however this will not be discussed in this work.

2.1.2 Particle detectors

In order to detect a particle, it is necessary to make this particle interact with a detector. One particle detector known to the general public is the Geiger counter, used to detect ionizing radiation. Different types of detectors are used for different particles. Typically, a particle collider has several detectors; LHC has ALICE, ATLAS, CMS and LHCb. The Tevatron had CDF and DO. The research on particle detectors is an interesting and broad topic and the introduction given here is extremely simplified and short. We want here to briefly explain the general structure of a particle detector used at a particle collider, typically ATLAS, CMS or CDF (see for example the following references [22, 23, 24] respectively), without getting into the technical details of these exquisite machines. The following explanation does not take into account the complexity of detectors but only their overall structure. For example, the tracker of the ATLAS detector is made of 3 parts, however this information is irrelevant for this work.

Figure 2.2 represents a simple schematic representation of a particle detector. It has similarities with the ATLAS or the CMS detector but is extremely simplified. The detector has an onion structure and is made of different layers around the interaction point. The closest detector to the interaction point is the tracker. It is used to get the trajectories of charged particles. As the inside of the detector is in a magnetic field, we also get the

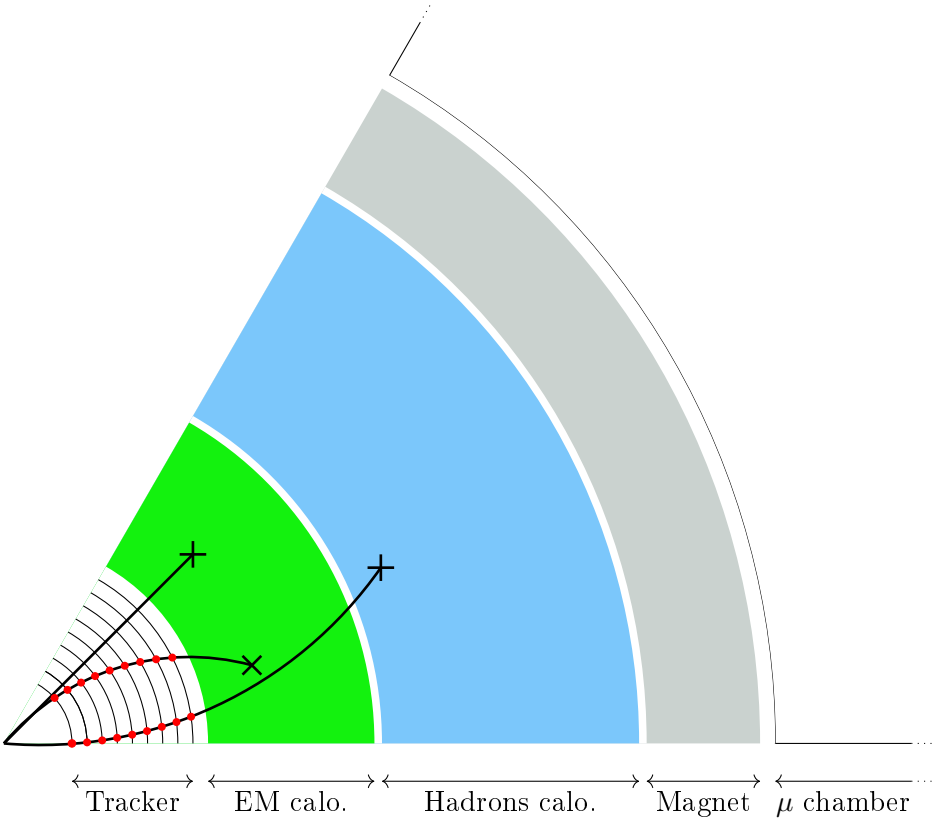

Figure 2.2: Simplified schematic representation of a particle detector and of the trajectory of 3 particles. The scales of the detector are not respected.

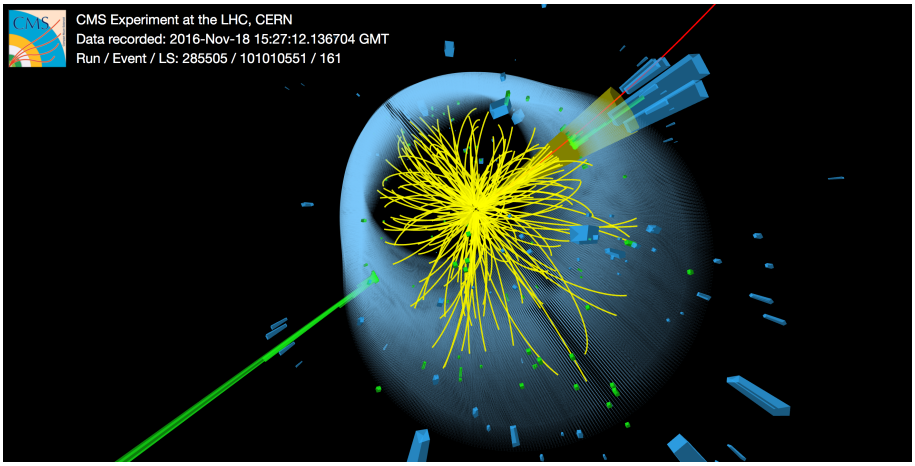

Figure 2.3: Event display at CMS, the green tower on the left is a photon candidate, top right a b jet with in blue the deposits in the hadronic calorimeter, the red line is a muon. Image source: `cds.cern.ch/record/2235235`, Copyright CERN.

charge of a particle and its momentum/mass ratio. The second layer is the electromagnetic calorimeter. This calorimeter stops electrons and photons and measures their energy. Then the hadron calorimeter stops the hadrons and measures their energy. Muons and neutrinos are the only stable particles that pass the calorimeters. The muons are detected in the last layer, which is the muon calorimeter as they interact less with matter than for example electrons. Neutrinos are not detected.

In the figure, 3 trajectories are drawn. The straight one is not bent by the magnetic field, therefore the particle is neutral, it does not leave a track and it is stopped in the electromagnetic calorimeter and is therefore a photon. The second trajectory is bent, the particle can be tracked using the tracker and it is stopped by the electromagnetic calorimeter, it is an electron. The last trajectory is a positively charged particle. It is a hadron as it is stopped in the hadronic calorimeter, it could be a positive pion π^+ or a proton for example. We can only directly detect particles that have a lifetime long enough and enough energy to reach the detectors.

The parts of the detectors that interest us the most in this work are the electromagnetic and hadronic calorimeters, as these two parts are used to detect jets and photons. One limitation of a calorimeter is its resolution. The fact that the hadronic calorimeter has a finite resolution makes certain types of isolation requirements on the photons not usable in practice (see chapter 4). EM calorimeters have better energy resolution than the hadronic ones which is one more reason to study photons [25]. It is also necessary to know some characteristics of a detector, as we need to know which phase space region every part covers. Then it is possible to know for each type of particle what kinematics can be detected. It is necessary to do so to be able to compare theoretical prediction to experimental measurements. For example the ATLAS electromagnetic calorimeter can detect photons with pseudo rapidity $|\eta_\gamma| < 2.37$ except a gap region between 1.37 and 1.56.

Figure 2.3 shows an event display at CMS for proton proton collisions during Run II of the LHC. This event is probably the production of an isolated photon and a b jet. On the bottom left an energetic particle in green is detected in the electromagnetic calorimeter and is probably a photon. The innermost part is the tracker and there are a lot of tracks during this collision. It is isolated as there is only little energy in the same direction in the hadronic calorimeter (in blue). On the top right we can see a bunch of particles all going

approximately in the same direction and energy is deposited in both the hadronic and electromagnetic calorimeters, this is a jet. Finally, a muon (the red line) is detected. The jet may contain a bottom quark. Many more event displays can be found on the CERN website for a wide range of processes.

2.2 Strong coupling and parton distribution functions

In this section a quick summary on the running of the strong and electromagnetic couplings, the hadronic cross-section and the parton distribution functions is given. The vast majority of this section is textbook material and can be found in the following references [26, 25, 27, 21].

2.2.1 Running of α_s and α

The running of α_s is governed by the renormalization equation [28]

$$\mu \frac{\partial \alpha_s}{\partial \mu} = \beta(\alpha_s) = -2\alpha_s \left(\frac{\alpha_s}{4\pi} \beta_0 + \left(\frac{\alpha_s}{4\pi} \right)^2 \beta_1 + \mathcal{O}\left(\alpha_s^3\right) \right), \tag{2.1}$$

where $\beta(\alpha_s)$ is the so-called beta function and it is known up to β_3. The first two β_i are

$$\begin{aligned} \beta_0 &= 11 - \frac{2}{3} n_f \\ \beta_1 &= 102 - \frac{38}{3} n_f, \end{aligned} \tag{2.2}$$

where n_f is the number of quark flavors. For $n_f = 5$, the values are $\beta_0 = 23/3$ and $\beta_1 = 116/3$. Solving the evolution equation of α_S at the lowest-order (only including the β_0 term) is straightforward

$$\alpha_s(\mu^2) = \frac{\alpha_s(\mu_0^2)}{1 + \beta_0 \frac{\alpha_s(\mu_0^2)}{4\pi} \ln\left(\frac{\mu^2}{\mu_0^2}\right)} = \frac{1}{\frac{\beta_0}{4\pi} \ln\left(\frac{\mu^2}{\Lambda^2}\right)}. \tag{2.3}$$

The previous equation allows us to compute the strength of the coupling at a certain scale μ if we already know it at the scale μ_0, if not stated otherwise in this thesis, we will use the value $\alpha_s(M_Z) = 0.119$. The coupling α_s decreases if μ increases as long as β_0 is positive. In the case of $\alpha_s(\mu_0 = M_Z = 91.187) = 0.119$ and 5 quarks, $\Lambda \sim 300\,\text{MeV}$. If the number of quark flavors would be $n_f \geq 17$, the coupling would decrease when μ increases. This is not what has been observed experimentally. In the case of QED, the coupling α also has a similar equation:

$$\mu^2 \frac{\partial \alpha}{\partial \mu^2} = 4\pi\beta(\alpha) = \frac{\alpha^2}{4\pi} \beta_0^{\text{QED}} + \mathcal{O}\left(\alpha^3\right), \tag{2.4}$$

with

$$\beta_0^{\text{QED}} = \frac{4}{3} \sum_f e_f^2. \tag{2.5}$$

The sum $\sum_f e_f^2$ runs over all the fermions and for $f = e, \mu, \tau, d, u, s, c, t$, it is $\frac{38}{9}$. The main difference between QED and QCD is that the QED β_0 is positive. This implies that when μ becomes larger, the coupling $\alpha(\mu)$ increases. Both renormalization equations for α_s and α are valid only at high enough energy (so larger than a few GeV), such that we do not have non-perturbative effects.

Finally one may ask, if QED would change the renormalization equation of α_s. At lowest order in QED we would introduce an extra term on the right-hand side of (2.1) coming from QED correction in the quark loop [29]

$$\frac{\alpha\alpha_s^2}{8\pi^2}\left(\sum_q e_q^2\right), \tag{2.6}$$

with the sum over the quarks, gives a factor 11/9. This term is a lot smaller than the β_1 term.

2.2.2 Hadronic cross-section

When leptons are collided, for example an electron and a positron (as it was done at LEP), it is possible to compute cross-sections using perturbation theory. For example the cross-section at leading-order in QED for $e^+e^- \to \gamma^* \to \mu^+\mu^-$ is

$$\sigma = \frac{4\pi\alpha^2}{3s}, \tag{2.7}$$

where s is the center of mass energy squared, $\sqrt{s} = 2E_{\text{beam}} = Q$. All the energy of the electron and of the positron is used to create the virtual photon γ^*. In the rest frame of the photon we have:

$$p_{e^+} = \left(\frac{Q}{2}, 0, 0, \frac{Q}{2}\right) \quad p_{e^-} = \left(\frac{Q}{2}, 0, 0, -\frac{Q}{2}\right) \quad p_{\gamma^*} = (Q, 0, 0, 0)\,. \tag{2.8}$$

Then the virtual photon carries all the energy of the colliding leptons.

If composite particles are collided like for example protons, things are more complex. The two protons will interact through their constituents. We need to know which part of the protons will interact and with how much of the proton energy. We assume that the protons have the 4-momentum $\left(\frac{Q}{2}, 0, 0, \pm\frac{Q}{2}\right)$. Then a the parton (gluon,quark or anti-quark) from the first proton and b the parton from the second proton, where a and b are the interacting partons, their momentum is

$$p_a = \left(x_a\frac{Q}{2}, 0, 0, x_a\frac{Q}{2}\right) \quad p_b = \left(x_b\frac{Q}{2}, 0, 0, -x_b\frac{Q}{2}\right), \tag{2.9}$$

where the x_i are the fractions of energy carried by both partons. Note that $x_i < 1$. If the two partons are a quark and antiquark, they may annihilate into a virtual photon similar to the e^+e^- case. However the momentum of the photon resulting from the annihilation will be

$$p_a + p_b = p_{\gamma^*} = \left(\frac{x_a + x_b}{2}Q, 0, 0, \frac{x_a - x_b}{2}Q\right). \tag{2.10}$$

We have that $p_{\gamma^*}^2 = x_a x_b Q^2 < Q^2$. This has a crucial implication. If we want to study the creation of a pair of particles from a virtual photon with a certain mass M both in the case of e^+e^- or pp colliders, the necessary center of mass energy s will be a lot larger for the proton collider than for the electron positron one. A question we need to answer is how much energy every constituent of the proton carries and with which probability. To answer it, it is necessary to introduce the parton distribution functions (PDF) $f_{i/p}(z, \mu)$ with z the fraction of longitudinal momentum carried by the parton i out of its proton and μ the factorization scale also often denoted by μ_F. If not stated otherwise, the PDFs are

the ones of a proton in this work, thus the notation $f_i(z, \mu)$ will be used. Sometimes, the PDF f_i is even simply written i.

The factorization formula for the cross-section of two protons scattering to produce X, is

$$\sigma\left(pp \to X\right) = \sum_{a,b=q,\bar{q},g} \int_0^1 \mathrm{d}x_a \int_0^1 \mathrm{d}x_b f_a(x_a, \mu) f_b(x_b, \mu) \sigma_{ab\to X}\left(\mu, \mu_R\right), \tag{2.11}$$

where μ_R is the renormalization scale. The quantity $\sigma_{ab\to X}$ is the partonic cross-section and is computed using perturbation theory. For example X could be a quark and an antiquark $q\bar{q}$. Then we will need to compute following partonic cross-section $\sigma_{q'\bar{q}'\to q\bar{q}}$ and $\sigma_{gg\to q\bar{q}}$. These LO partonic cross-sections can be found in for example [25]. Unlike the example of e^+e^- to $\mu^+\mu^-$, the partonic cross-sections do not depend on s but on $\hat{s} = sx_ax_b$, where s is the center of mass energy of the two protons squared $s = Q^2$. As stated earlier, only a fraction of the energy of the protons is used in the reaction $ab \to X$.

The rest of the colliding protons also interact. This is called "underlying event" (UE) which constitutes a background of the process studied. The underlying event should not be confused with pile-up, which is the background originating from collisions of other protons. Pile-up depends on the accelerator, the more collisions that happen at each bunch crossing the larger the pile-up is. The underlying-event is present even if we only collide 2 protons together (if we manage to have only one collision in a bunch crossing). Both UE and pile-up need to be removed when considering a certain hadronic process.

The particular cases of hadronic cross-section that interest us in this work is $pp \to \gamma + Y$ where Y denotes some extra particles (like a quark or a gluon at LO). However in the case of the photon there is a complication, there is a non-perturbative fragmentation contribution that we can not compute in perturbation theory. This will be discussed in the next chapter. Before discussing photon production at colliders, we first discuss the parton distribution functions in greater detail.

2.2.3 Parton distribution functions

A proton consists of two valence up quarks and one valence down quark. In addition, there are also the sea quarks and gluons. Very naively one may think that each of the valence quarks carry a third of the momentum of the quark. This is not the case as explained below. The up and down quarks PDF have two contributions the valence i_v and the sea i_s quarks

$$d = d_v + d_s \qquad u = u_v + u_s. \tag{2.12}$$

The other quark flavors s, c, b,the anti-quarks and the gluon only have a sea contribution, for example $c = c_s$.

In Figure 2.4, the parton distributions (multiplied by z) of gluon, up, down, anti-up and anti-down are plotted at the energy of 125 GeV. For large z, all of them go to zero. For z going to zero, all the PDFs diverge. At small z, the gluon contribution dominates the quark u and d. At larger z, the PDF of the quarks are larger than the gluon distributions. The up quark is larger than the down quark which is not surprising knowing that a proton is made of two ups and one down. As you can see $\bar{u}$ and $\bar{d}$ are very similar and the other sea quarks that are not shown in the figure are all smaller than the gluon, up and down quarks and look like $\bar{u}$ and $\bar{d}$.

Parton distribution functions have a few interesting properties, for example

$$\sum_{i=q,\bar{q},g} \int_0^1 \mathrm{d}z z f_i(z, \mu) = 1, \tag{2.13}$$

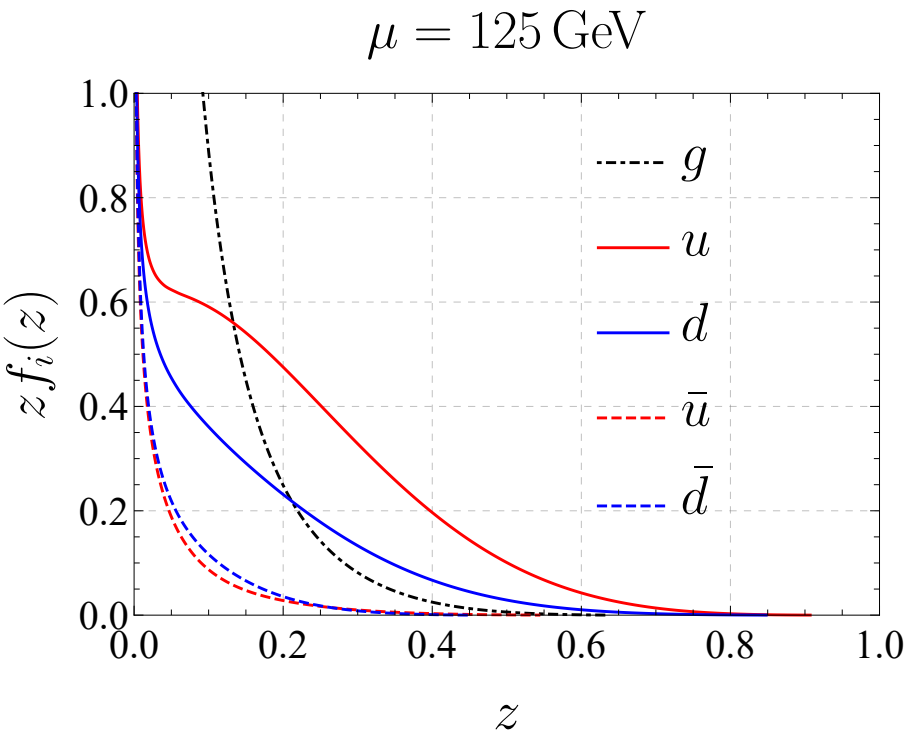

Figure 2.4: Parton distribution functions of the proton from the set `NNPDF23_lo_as_0119_qed` as a function of z, evaluated at 125 GeV. Note that $u = u_v + u_s$ and $d = d_v + d_s$.

which means that the momentum is conserved over all the partons. The amount of momentum carried by the valence quarks up and down depends on the energy considered. The rest of the momentum is taken by the gluon and the sea quark. In Figure 2.4, the PDF set `NNPDF23_lo_as_0119_qed` (which is the leading order version of the one that we use in our work, `NNPDF23_nlo_as_0119_qed`) was used to compute numerically the amount of energy each parton is carrying in the proton for different energy which is done by performing the integral of the above equation for each f_i separately. The result can be seen in Table 2.1. As you can see the higher the energy, the more momentum the gluon and the sea quarks carry and the less the valence quarks carry. For the energies considered, the valence quarks make less than half of the momentum. It is interesting to notice that gluons carry almost half of the energy.

One assumption about PDF is their universality. It means that we can measure the PDF using a certain process and that it is then possible to use the resulting PDF in order to do prediction for a different process. This follows from the factorization of the cross-section.

2.2.4 Evolution equation of the parton distribution functions

Even though the parton distribution functions need to be measured and can not be predicted using perturbative QCD, their evolution in μ is predicted by perturbative QCD. This allows the PDFs to be measured at a certain scale and be used at another scale. The PDFs obey the DGLAP (Dokshitzer–Gribov–Lipatov–Altarelli–Parisi) evolution equation, it is a differential system of $2n_f + 1$ equations, where n_f is the number of quark flavors.

parton at $\mu =$	2 GeV	5 GeV	125 GeV
gluon	0.43	0.45	0.48
up	0.31	0.28	0.21
down	0.16	0.14	0.12
sea quarks	0.10	0.12	0.19

Table 2.1: Approximative fraction of energy carried for the different partons in a proton at different energy μ obtained with the PDF set `NNPDF23_lo_as_0119_qed`. Sea quarks is the sum of s, c, b and the antiquarks $\bar{u}, \bar{d}, \bar{s}, \bar{c}, \bar{b}$, the non-valence parts of the up and down quark were included in the up and down quark fractions see (2.12). The values at 5 GeV add up to 0.99 instead of 1.0, this is in parts due to error of the numerical integration and mostly to the rounding to 2 digits.

The DGLAP equation is

$$\frac{\mathrm{d}}{\mathrm{d}\ln\mu^2}\begin{pmatrix} f_{q_i}(x,\mu) \\ f_g(x,\mu) \end{pmatrix} = \sum_j \int_x^1 \frac{dz}{z} \begin{pmatrix} \mathcal{P}_{q_j\to q_i}(\frac{x}{z},\mu) & \mathcal{P}_{g\to q_i}(\frac{x}{z},\mu) \\ \mathcal{P}_{q_j\to g}(\frac{x}{z},\mu) & \mathcal{P}_{g\to g}(\frac{x}{z},\mu) \end{pmatrix} \begin{pmatrix} f_{q_j}(z,\mu) \\ f_g(z,\mu) \end{pmatrix}, \quad (2.14)$$

where sum runs over quarks and antiquarks. The quantities $\mathcal{P}_{i\to j}$ are the splitting functions, they depend both on z and μ, however the μ dependence arises only via the coupling. We expand $\mathcal{P}_{i\to j}$ in the strong coupling $\alpha_s(\mu)$

$$\mathcal{P}_{i\to j}(z,\mu) = \sum_{n=1}^{\infty} \left(\frac{\alpha_s(\mu)}{2\pi}\right)^n P_{i\to j}^{(n,0)}(z), \quad (2.15)$$

where we used the notation of [30]. In this notation $\mathcal{P}_{i\to j}$ are expanded in power of α and α_s as

$$\mathcal{P}_{i\to j}(z,\mu) = \sum_{n=0}^{\infty}\sum_{m=0}^{\infty} \left(\frac{\alpha_s(\mu)}{2\pi}\right)^n \left(\frac{\alpha(\mu)}{2\pi}\right)^m P_{i\to j}^{(n,m)}(z), \quad (2.16)$$

with obviously the term of order $\alpha^0\alpha_s^0$ vanishing $P_{i\to j}^{(0,0)}(z) = 0$. This notation is useful in the context of photon production.
A more compact formulation of the DGLAP equation is

$$\frac{\mathrm{d}f_i(z,\mu)}{\mathrm{d}\ln\mu^2} = \sum_{j=q,\bar{q},g} \mathcal{P}_{j\to i} \otimes f_j(z,\mu), \quad (2.17)$$

where the convolution $\otimes$ of two functions is defined as

$$(f\otimes g)(z) = \int_0^1 dx \int_0^1 dy\, \delta(z-xy) f(x) g(y) = \int_z^1 \frac{\mathrm{d}y}{y} f(y) g\left(\frac{z}{y}\right). \quad (2.18)$$

Obviously this convolution is commutative $(f\otimes g)(z) = (g\otimes f)(z)$. At the lowest-order the DGLAP equation is solved with the splitting function only expanded up to order $\mathcal{O}(\alpha_s)$

where q is a quark or an antiquark

$$\begin{aligned}
P^{(1,0)}_{q\to q}(z) &= C_F\left(\frac{1+z^2}{1-z}\right)_+,\\
P^{(1,0)}_{q\to g}(z) &= C_F\left(\frac{1+(1-z)^2}{z}\right),\\
P^{(1,0)}_{g\to q}(z) &= T_R\left(z^2+(1-z)^2\right),\\
P^{(1,0)}_{g\to g}(z) &= 2C_A\left(\frac{z}{(1-z)_+}+\frac{1-z}{z}+z(1-z)\right)+\frac{\beta_0}{2}\delta(1-z),
\end{aligned} \tag{2.19}$$

with $\beta_0 = \frac{11N_c-4n_fT_R}{3}$. Other splitting functions are vanishing at this order for example $P^{(1,0)}_{q_i\to q_j}$ vanishes if both quark are not the same and $P^{(1,0)}_{q\to\bar{q}} = 0$. The plus distribution $\frac{1}{(1-z)_+}$ in $P^{(1,0)}_{q\to q}$ and $P^{(1,0)}_{g\to g}$ is defined in Section 1. Solving the DGLAP equation with the splitting functions expanded only at order α_s is not so involved as certain parton distribution functions are not coupled as for example q and $\bar{q}$. More details on how to solve the equation can be found in Appendix B. The splitting functions used for the DGLAP of PDF are avialable up to $P^{(3,0)}_{i\to j}$ [31, 32]. At order α_s^2 the DGLAP equation is more complex as some splitting functions are not vanishing anymore as for example $P^{(2,0)}_{q\to\bar{q}} \neq 0$.

In the chapters 3 and 5, a different DGLAP like equation will be discussed for the non-perturbative photon fragmentation function $\mathcal{D}_{i\to\gamma}$ and for the cone fragmentation function $\mathcal{F}_{i\to\gamma}$. Both functions obey the same equation which shares similarities with the DGLAP equation of the PDF. Some of the splitting functions will have to be expanded at order α and $\alpha\alpha_s$. After studying this QED + QCD DGLAP like equation, one may ask himself what happens to the DGLAP of the PDF if the QED effects are added to the evolution of the PDF. This was studied for example in [33]. In order to do so, it is necessary to also consider PDFs of the photon and of charged leptons in the proton on top of the usual quark and gluon PDFs. For a toy model the authors found that corrections due to the addition of QED can reach 1% for certain values of z. The LO splitting function for pure QED $P^{(0,1)}_{i\to j}$ are [30]

$$\begin{aligned}
P^{(0,1)}_{q\to q}(z) &= e_q^2\left(\frac{1+z^2}{(1-z)_+}+\frac{3}{2}\delta(1-z)\right),\\
P^{(0,1)}_{\gamma\to q}(z) &= N_c e_q^2\left(z^2+(1-z)^2\right),\\
P^{(0,1)}_{q\to\gamma}(z) &= e_q^2\left(\frac{1+(1-z)^2}{z}\right),\\
P^{(0,1)}_{\gamma\to\gamma}(z) &= -\frac{2}{3}\sum_f e_f^2\delta(1-z).
\end{aligned} \tag{2.20}$$

All other splitting function at this order are vanishing, like for example $P^{(0,1)}_{q_i\to q_j} = 0$ if $q_i \neq q_j$ or $P^{(0,1)}_{g\to\gamma} = 0$ and so on. When including $\alpha\alpha_s$ corrections, some functions are not vanishing anymore as for example $P^{(1,1)}_{g\to\gamma}$ that will be used later in Chapters 3 and 5.
Finally a detail we need to address is a small notation problem with the splitting functions, in Chapter 5 we use the following for the splitting $P_{i\to\gamma}$

$$\mathcal{P}_{i\to\gamma} = \frac{\alpha}{\pi}\left(P^{(0)}_{i\to\gamma}+\frac{\alpha_s}{\pi}P^{(1)}_{i\to\gamma}+\mathcal{O}(\alpha_s^2)\right). \tag{2.21}$$

This is slightly different to the one introduced (2.16) which would be

$$\mathcal{P}_{i\to\gamma} = \frac{\alpha}{2\pi}\left(P^{(0,1)}_{i\to\gamma} + \frac{\alpha_s}{2\pi}P^{(1,1)}_{i\to\gamma} + \mathcal{O}(\alpha_s^2)\right). \tag{2.22}$$

The factor $\frac{1}{2}$ factor arises because we will consider $\frac{\mathrm{d}}{\mathrm{d}\ln\mu}$ as $\frac{\mathrm{d}}{\mathrm{d}\ln\mu^2} = \frac{1}{2}\frac{\mathrm{d}}{\mathrm{d}\ln\mu}$. The second factor $\frac{1}{2}$ missing for the splitting proportional to $\alpha\alpha_s$ is absorbed in the definition of $P_{i\to\gamma}$. So we have the following relations

$$P^{(0)}_{i\to\gamma} = P^{(0,1)}_{i\to\gamma} \qquad \text{and} \qquad P^{(1)}_{i\to\gamma} = \frac{1}{2}P^{(1,1)}_{i\to\gamma}. \tag{2.23}$$

Chapter 3

Photon production

Photons at colliders have two origins. The first origin is the decay of hadrons to photons. The second is the emission by a quark or in the decay of a gluon (or other particles). In this work we are mainly interested in the emission from quarks. When a photon is emitted by a quark, it can be emitted perturbatively and it is possible to use perturbative QED and QCD. It can also be emitted non-perturbatively by a quark or during the decay of a gluon by a process called fragmentation. This phenomena can not be fully predicted by perturbative QCD and needs non-perturbative input, the fragmentation functions, which must be measured experimentally. Quarks are going to contribute more than gluons as the emission from a gluon occurs at higher order in α_s.

One distinguishes two types of photons: Prompt photons are photons that are emitted perturbatively. Direct photons are photons that are emitted before hadronization, so photons from the decay of hadrons are not direct photons. Prompt photons are also direct photons. Depending on the measurement, different types of photons are of interest and isolation criteria can be used to discriminate photons from different origins. We will discuss this topic in detail in Chapter 4.

This chapter is organized as follows. First, photons originating from hadron decays will be discussed, then we will discuss prompt photon production at colliders, first the perturbative part with a special emphasis on hadron colliders, then we will discuss the non-perturbative fragmentation function $\mathcal{D}_{i\to\gamma}$, its DGLAP evolution equation and two of the existing determinations of these functions.

3.1 Hadron decays

The lightest hadron that decays to photons is the neutral pion π^0. It decays into 2 photons. Table 3.1 shows non-exhaustive list of decays of hadrons to photons or to lighter hadrons. As discussed in [1, 34, 35, 36], the π^0 is the main background source of photons, the η also contributes, but less. Other hadrons also decay into photons but their contribution is smaller than the one from π^0 and η. Usually photons originating from decays of hadrons are not isolated from hadronic energy as the decaying hadron will often be created together with other hadrons. These decays of hadrons are a background to photons from other sources because direct photon production $pp \to \gamma + X$ has a lot smaller tate than jets production $pp \to$ jets at colliders and the jets contain mesons that decay to photons.

The branching ratio of $\pi^0 \to 2\gamma$ is 0.988 and the one of $\eta \to 2\gamma$ is 0.392 and their respective life times are $\tau_{\pi^0} = 8.45 \cdot 10^{-17}$ s and $\tau_\eta = 7 \cdot 10^{-19}$ s. These particles will decay very shortly after being created and therefore the photons from their decay can be

decay	Branching Ratio [%]
$\pi^0 \to 2\gamma$	98.82
$\eta \to 2\gamma$	39.41
$\eta \to 3\pi^0$	32.68
$\eta \to \pi^+\pi^-\pi^0$	22.92
$\omega \to \pi^0\gamma$	8.28
$K_S^0 \to \pi^0\pi^0$	30.69

Table 3.1: Light hadrons decaying to photons or to hadrons that may themself decay into photons with the branching ratio of each decay. The particles have the following masses: $m_{\pi^0} = 134.98$ MeV, $m_\eta = 547.86$ MeV, $m_\omega = 782.65$ MeV and $m_{K_S^0} = 497.61$ MeV [39].

considered to be emitted where the hadron was created [37]. If we consider a π^0 with a momentum of 50 GeV/c its corresponding Lorentz factor will be approximately $\gamma = 373$ and its speed $v \simeq 0.999996c$ as the neutral pion lifetime is $\tau = 8.45 \cdot 10^{-17}$s we find that the average distance is approximately

$$d = v\gamma\tau \sim 10^{-5} \text{ m} = 10^{-2}\text{mm}\,, \tag{3.1}$$

and thus it will have decayed before reaching the calorimeters. If the π^0 has an energy of 250 GeV, then the γ factor is approximately 1866 and the distance d would be approximately $5 \cdot 10^{-5}$m. Consequently, π^0 will not be detected but its decay products will. A similar computation can be done for the η meson with the same conclusion.

The fact that detectors have a finite resolution plays a role in trying to detect the 2 photons originating from the decay of a neutral pion π^0. Ideally it is possible to detect both photons separately and to reconstruct that they originated from a π^0. At an energy of approximately 50 GeV, the two photons from the decay reach the EM calorimeter with typically a distance of 1 cm [38]. Depending on the speed of the pion and on the resolution of the electromagnetic calorimeter the two photons may be detected as one photon. At CDF for example, it was not possible to separate the two photons from π^0 if its transverse momentum was larger than 15 GeV [1]. On top of that the energy of the two γ's from the decay of a boosted π^0 are not the same and even if the two photons are spatially well separated, the soft one may not be detected [34]. We also need to keep in mind that the hadrons decaying to photons may be created by another event than the one we are considering due to pile-up.

In order to reduce the background due to the π^0 decays various techniques are used. We will later discuss isolation cones in order to suppress this contribution, as typically hadrons like π^0 or η will not be produced without other hadrons [35]. It is also common for experimental physicists to use some Monte-Carlo techniques in order to estimate the background due to these decays as for example in [40] or [37]. In the case of an e^+e^- collider, if the center of mass energy Q^2 and E_γ/Q the fraction of energy that the prompt photon has, are both large, then the background of photons from π^0 and η is small compared to the production of direct photons even without considering any isolation [41]. Photons from hadron decays are problematic when measuring the non-perturbative fragmentation function because isolation suppresses both, this is why all the measurements of $\mathcal{D}_{i\to\gamma}$ were done at lepton collider where the environment is cleaner.

3.2 Prompt photons

In this section, the basics of prompt photon production at colliders are discussed. A more detailed discussion of the perturbative and of the non-perturbative production can be found in the later sections. A prompt photon is a photon that is not resulting from an hadronic decay.

At hadron colliders, photon production with momentum p_γ without any isolation [36] is

$$E_\gamma \frac{\mathrm{d}\sigma^\gamma}{\mathrm{d}^3 p_\gamma} = \sum_{a,b=q,\bar{q},g} \int \mathrm{d}x_a \mathrm{d}x_b f_{a/A}(x_a,\mu^2) f_{b/B}(x_b,\mu^2) \left[E_\gamma \frac{\mathrm{d}\sigma^\gamma_{ab}}{\mathrm{d}^3 p_\gamma}\left(p^\gamma, x_a, x_b, \mu_f^2, \mu_r^2, \mu_a^2\right) + \right.$$
$$\left. \sum_{f=q,\bar{q},g} \int_{z_{min}}^1 \frac{\mathrm{d}z}{z} E_f \frac{\mathrm{d}\sigma^f_{ab}}{\mathrm{d}^3 k_f}(k_f, x_a, x_b, z, \mu_f^2, \mu_r^2, \mu_a^2) \mathcal{D}_{f\to\gamma}(z,\mu_a^2) \right], \tag{3.2}$$

where $d\sigma^\gamma_{ab}$ is the partonic cross-section for creating a photon plus some other particles from the partons a, b from hadron A and B respectively. $\mathrm{d}\sigma^f_{ab}$ is the partonic cross-section to produce a parton f that will fragment to a photon through the fragmentation function $\mathcal{D}_{f\to\gamma}$. The variable z is the fraction of energy taken by the photon from the fragmenting particle f: $E_\gamma = zE_f$. The cross-section $\mathrm{d}\sigma^f_{ab}$ can be computed in perturbative QCD. The phase space integral of all other particles create in $\mathrm{d}\sigma^f_{ab}$ has been performed execpt for particle f. The lower bound of the integral over z is $z_{min} = p^\gamma_{min}/p_f$ with p^γ_{min} is the minimum momentum required for the photon. In Chapter 5, $p^{T,\gamma}_{min} = 125$ GeV is used. The scale μ_a is the fragmentation scale. The cross-section has three artificial scales μ_f, μ_r and μ_a, they are sometimes all set to the same value μ.

In the case of an electron-positron collider, we have to discard the PDFs and the sum over a, b and replace $a = e^-$ and $b = e^+$.

Moreover, the formula (3.2)is consistent with the factorization formula (1.2) with the cone fragmentation function $\mathcal{F}_{i\to\gamma}$. From the fact that

$$\mathrm{d}^3 p_\gamma = \mathrm{d}p_\gamma p_\gamma^2 \mathrm{d}\Omega = \mathrm{d}E_\gamma E_\gamma^2 \mathrm{d}\Omega, \tag{3.3}$$

it follows that

$$E_\gamma \frac{\mathrm{d}\sigma}{\mathrm{d}^3 p_\gamma} = \frac{1}{E_\gamma} \frac{\mathrm{d}\sigma}{\mathrm{d}E_\gamma \mathrm{d}\Omega}. \tag{3.4}$$

Then we get from the fragmentation part (3.2) and using the above formula for both $E_\gamma \frac{\mathrm{d}\sigma^\gamma}{\mathrm{d}^3 p_\gamma}$ and $E_f \frac{\mathrm{d}\sigma}{\mathrm{d}^3 p_f}$

$$\frac{\mathrm{d}\sigma^F}{\mathrm{d}E_\gamma} = \sum_{a,b,f=q,\bar{q},g} \int \mathrm{d}x_a \mathrm{d}x_b f_{a/A}(x_a,\mu^2) f_{b/B}(x_b,\mu^2) \int \mathrm{d}z \frac{\mathrm{d}\sigma^f_{ab}}{\mathrm{d}E_f} \mathcal{D}_{f\to\gamma}, \tag{3.5}$$

where we used the letter F to emphasize that it is the fragmentation part of the cross-section not the whole cross-section. We see that it is similar to the formula (1.2) with the cone fragmentation function $\mathcal{F}_{f\to\gamma}$ instead of $\mathcal{D}_{f\to\gamma}$. Note the sum on a and b and the PDF was here included in σ^f in the case of $\mathcal{F}_{f\to\gamma}$. One issue of the two cross-section formulas is the definition of $\mathcal{D}_{f\to\gamma}$, some references use a different convention which is $d_{f\to\gamma} = z\mathcal{D}_{f\to\gamma}$.

Compared to other inclusive cross-sections, like (2.11), we have in the case of photon production also a fragmentation term. This is due to the fact that in photon production,

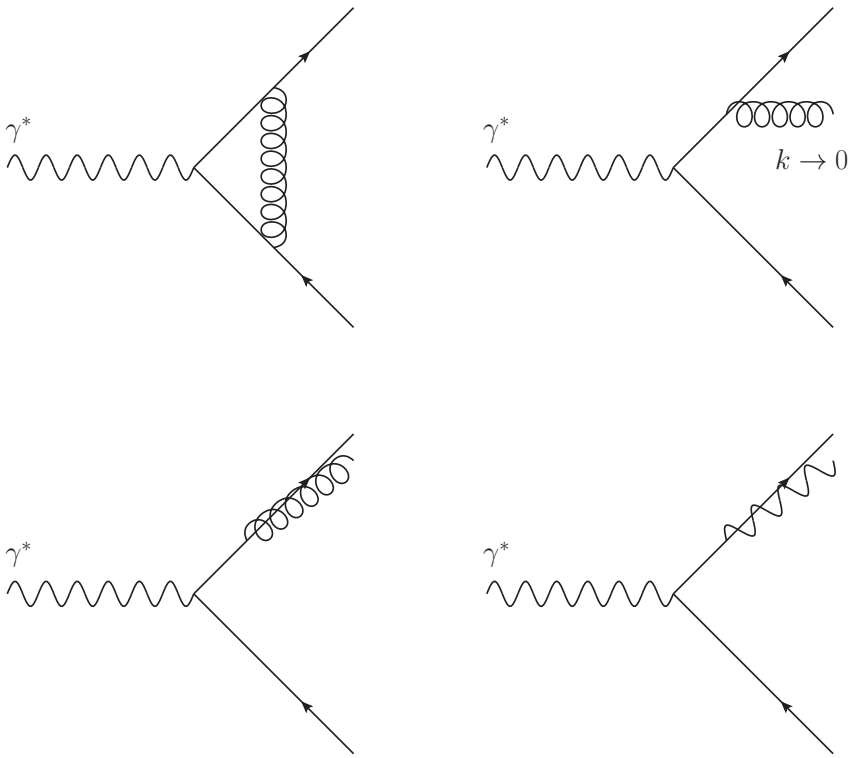

Figure 3.1: Top left, right and bottom left: QCD corrections of $e^+e^- \to \gamma^* \to q\bar{q}$. Top left: loop correction of $\gamma^* \to q\bar{q}$, in DR this diagram creates a $1/\epsilon^2$ singularity. Top right: emission of a soft gluon from $q\bar{q}$, it gives a $1/\epsilon$. Bottom left: emission of a collinear gluon to the quark, this implies a $1/\epsilon$ if the gluon is hard collinear and a singularity $1/\epsilon^2$ if the gluon is both soft and collinear. Bottom right: emission of a collinear photon, if the photon is required to have more than a certain energy, it only contributes a $1/\epsilon$ singularity.

there is a singularity when a photon is emitted collinearly to a quark, which necessitates the fragmentation function and introduces an extra scale μ_a.

In order to understand better why we have this singularity, we can think of a textbook example of the α_s correction to the $q\bar{q}$ production at e^+e^- collider. There are two types of α_s corrections for $e^+e^- \to \gamma^* \to q\bar{q}$. They can be seen in Figure 3.1. First, there is the loop contribution which is singular and has both $1/\epsilon^2$ and $1/\epsilon$ singularities in dimensional regularization (DR). Second, there is the emission of a gluon from one of the quark which has a singularity of $1/\epsilon^2$ from the contribution of the gluon being soft and collinear to the emitting quark and if the gluon is only soft or only collinear $1/\epsilon$ singularities arise. When adding both contributions, all singular terms cancel and finally the $\mathcal{O}(\alpha_s)$ correction to the quark antiquark pair production is finite. Note that the cross-section is inclusive and that it includes contributions of final states that only have the $q\bar{q}$ and no (detected) gluons and of the final state $q\bar{q}g$. An in depth discussion of this problem can be found in [27] and detailed derivations can be found in [42].

If we consider the same corrections in α instead of α_s and there would also be a cancellation of the singularities. However, our process of interest is not the same. We consider the emission of a photon from the $q\bar{q}$ pair and the final state needs one γ. To be able to detect the photon, it needs to have an energy larger than detection threshold of the detector E_{detector} (which was not the case for the gluon earlier). This implies that the photon can not be soft. Moreover, in our case, the photon loop should not be taken

Origin of singularity	Final state γ	Detected γ	D.R.
Soft $E_\gamma \to 0$	✓	✗	ϵ^{-1}
Collinear to e^+ or e^-	✓	✗	ϵ^{-1}
Collinear to q or $\bar{q}$	✓	✓	ϵ^{-1}
Soft and collinear to e^+, e^-, q or $\bar{q}$	✓	✗	ϵ^{-2}
Loops	✗	✗	ϵ^{-1} and ϵ^{-2}

Table 3.2: List of the singularities in the α correction of $e^+e^- \to q\bar{q}$. The only singularity that needs to be taken into account for prompt photon production is the collinear one as it is the only one with a detected photon.

into account as it obviously does not have a real photon in the final state. So of all the singularities that were encountered in the α_s corrections, there is only one type remaining, the collinear singularities (there is no collinear and soft singularity as the γ can not become soft, so no $\frac{1}{\epsilon^2}$ term). Therefore, the only α term that is singular is the case where the photon is collinear to the emitting parton which can be seen in the bottom right of Figure 3.1. As there are no other singular contributions to cancel this $1/\epsilon$-pole, the whole cross-section is singular. Note that initial state radiation from the e^+ or e^- is also possible in this case, the photon can be emitted collinear to one of the lepton, however the photon would be in the beam direction and therefore we would not be able to detect it. The singularity from the emission from the e^+e^- can be regularized by introducing an electron mass or with the PDFs electron. A list that summarizes the singularities of the α correction of $e^+e^- \to q\bar{q}$ can be seen in Table 3.2. This remaining singularity will be absorbed into the fragmentation function $\mathcal{D}_{q\to\gamma}$, which introduces the scale fragmentation scale μ_a into the problem. Both the perturbative and the non-perturbative parts of the cross-section depend on the μ_a scale. The total cross-section should not depend on μ_a. The non-perturbative fragmentation depends on which renormalization scheme is used.

It is interesting in order to understand the cross-section better to see at which order the different parts of the cross-section start and which types of diagrams play a role. Schematically, the cross-section (3.2) can be written as

$$\mathrm{d}\sigma = \mathrm{d}\sigma^\gamma + \mathrm{d}\sigma^f \otimes \mathcal{D}_{f\to\gamma}, \tag{3.6}$$

where the sum over a, b and f were omitted for simplicity. At leading-order, the fragmentation functions $\mathcal{D}_{q\to\gamma}$ and $\mathcal{D}_{g\to\gamma}$ scale after resummation like [36, 43]

$$\begin{aligned} \mathcal{D}_{q\to\gamma} &\sim \frac{\alpha}{\alpha_s}, \\ \mathcal{D}_{g\to\gamma} &\sim \alpha. \end{aligned} \tag{3.7}$$

This scaling is only valid at larger fragmentation scale μ_a and $\mathcal{D}_{q\to\gamma}$ in the above equation are the resummed non-perturbative fragmentation functions. At low scale $\mathcal{D}_{f\to\gamma}$ are non-perturbative objects and like the PDFs, they do not have a α_s scaling, but the evolution kernels can be expanded in α_s, leading to fragmentation functions at different orders in RG-improved perturbation theory. However, in fixed-order computation $\mathcal{D}_{f\to\gamma} \sim 1$ is typically used. The gluon fragmentation starts one order higher in α_s than the quark fragmentation. At leading-order the whole cross-section is of order $\alpha\alpha_s$ for hadron colliders. The different

parts of the cross-section are expanded

$$\begin{aligned} \mathrm{d}\sigma_{ab}^{\gamma} &= \mathrm{d}\sigma_{ab}^{\gamma,\mathrm{LO}} + \mathrm{d}\sigma_{ab}^{\gamma,\mathrm{NLO}} + \mathcal{O}\left(\alpha_s^3\alpha\right) , \\ \mathrm{d}\sigma_{ab}^{f} &= \mathrm{d}\sigma_{ab}^{f,\mathrm{LO}} + \mathrm{d}\sigma_{ab}^{f,\mathrm{NLO}} + \mathcal{O}\left(\alpha_s^4\right) \\ \mathcal{D}_{f\to\gamma} &= \mathcal{D}_{f\to\gamma}^{\mathrm{LO}} + \mathcal{D}_{f\to\gamma}^{\mathrm{NLO}} + \mathcal{O}\left(\alpha_s\alpha\right) , \end{aligned} \tag{3.8}$$

with at leading-order the following

$$\mathrm{d}\sigma^{\gamma,\mathrm{LO}} \sim \alpha\alpha_s \qquad \mathrm{d}\sigma_{ab}^{\gamma,\mathrm{LO}} \sim \alpha\alpha_s \qquad \mathrm{d}\sigma_{ab}^{f,\mathrm{LO}} \sim \alpha_s^2. \tag{3.9}$$

At LO only the quarks fragment so $\mathrm{d}\sigma_{ab}^{f}$ must have at least one quark to be fragmented. At a hadron collider it is typically processes like $qg \to qg$ or $q\bar{q} \to q\bar{q}$. In $qg \to qg$ only the quark fragments at this order. $d\sigma_{ab}^{\gamma}$ at a hadron collider at LO will be discussed in the next section.

At NLO, the cross-section is of order $\mathrm{d}\sigma^{\gamma} \sim \alpha\alpha_s^2$, therefore $d\sigma_{ab}^{\gamma} \sim \alpha\alpha_s^2$. In the fragmenting part the extra power of α_s can appear both in $\mathrm{d}\sigma_{ab}^{f}$ or in the resummed $\mathcal{D}_{f\to\gamma}$ such that the product of both is of order $\alpha\alpha_s^2$. We have for the fragmentation part the following scaling

$$\begin{aligned} \mathrm{LO} &: d\sigma_{ab}^{f,\mathrm{LO}}\mathcal{D}_{f\to\gamma}^{\mathrm{LO}} \sim \alpha\alpha_s, \\ \mathrm{NLO} &: d\sigma_{ab}^{f,\mathrm{NLO}}\mathcal{D}_{f\to\gamma}^{\mathrm{LO}} + \mathrm{d}\sigma_{ab}^{f,\mathrm{LO}}\mathcal{D}_{f\to\gamma}^{\mathrm{NLO}} \sim \alpha\alpha_s^2. \end{aligned} \tag{3.10}$$

$\mathrm{d}\sigma_{ab}^{f,\mathrm{NLO}}$ is of order α_s^3 and has processes of the form $ab \to 3\,\mathrm{partons}$, like for example $qg \to qgg$ and it also has loop correction to the leading-order process. At NLO $\mathcal{D}_{g\to\gamma}^{\mathrm{NLO}}$ is not vanishing and therefore it is also necessary to include in $\mathrm{d}\sigma_{ab}^{f,\mathrm{LO}}$ processes without any quarks in the final state to be fragmented $gg \to gg$ and $q\bar{q} \to gg$. Obviously, processes at LO like $qg \to qg$ can now fragment both partons q and g.

The type of colliders of interest in this thesis are hadron colliders (in particular the LHC), however, before discussing the perturbative emission of γ at hadron colliders in the next section, the case of an e^+e^- collider should be discussed as it was used to measure the non-perturbative fragmentation function at LEP. The process of interest was the production of a jet containing an energetic photon and an extra jet: $e^+e^- \to 1$ jet with an energetic photon in it plus 1 jet. The jet containing an energetic photon has contribution from the quark fragmenting to a photon. At leading-order the process of interest is $e^+e^- \to \gamma^* \to q\bar{q}$ and one of the quarks can emit a photon perturbatively or non-perturbatively.

At order α we have the emission of a photon from the quark or the anti-quark, the emission can be either perturbative or non-perturbative and $\mathcal{D}_{q\to\gamma}$ needs to be evaluated only at order α/α_s. The two diagrams can be seen in Figure 3.2. On top of that there is Bremsstrahlung from the initial state, see Figure 3.3. These photons can be emitted by both leptons and may be emitted in one of the jets. If a photon emitted from the lepton is emitted in the jet, it will then contribute to the cross-section of 1 jet with an energetic photon in it plus 1 jet. These photons can be subtracted and are therefore not a problem. They are mostly emitted along the beam axis [41]. Photons emitted perturbatively from e^+, e^-, q or $\bar{q}$ may also be emitted away from the jets, however such emissions were not of interest for the determination of $\mathcal{D}_{q\to\gamma}$. At NLO, there are more diagrams. It is then necessary to take into account virtual corrections for the order $\mathcal{O}(\alpha)$ diagrams, the emission of a gluon from q or $\bar{q}$ and $\mathcal{D}_{q\to\gamma}$ needs to be evaluated at order $\alpha\alpha_s$. These diagrams can be found in [44].

Prompt photon production at hadron colliders has been computed up to NNLO in QCD with no isolation, fixed-energy cones, Frixione cones and hybrid cones [15, 16]. These results

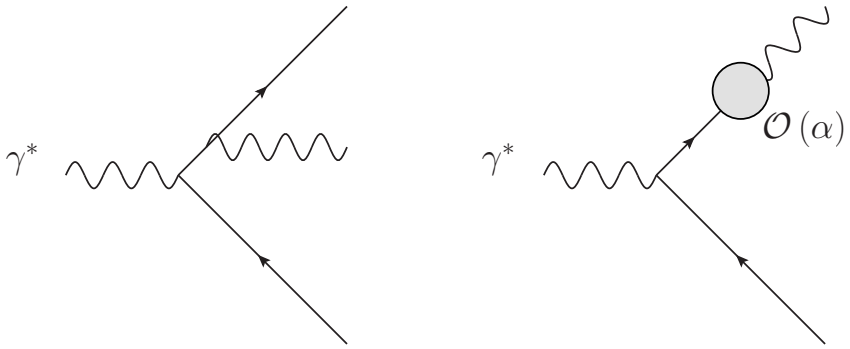

Figure 3.2: Photon production through $e^+e^- \to \gamma^* \to q\bar{q}$. Left, the photon is emitted perturbatively; on the right the photon is emitted through $\mathcal{D}_{q\to\gamma}$, represented by the blob. The photon can also be emitted from the anti-quark. Implicitly the non-perturbative fragmentation is of order $\mathcal{O}\left(\alpha\alpha_s^{-1}\right)$

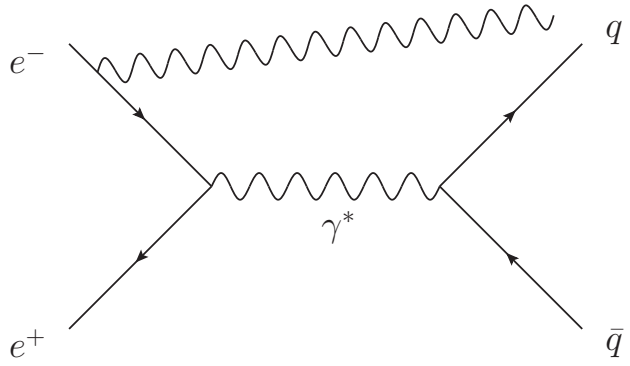

Figure 3.3: Photon production at e^+e^- collider through Bremsstrahlung (initial state radiation). Both the electron and the positron can emit. The photon can be emitted into one of the jets and contribute to the 1 jet with an energetic photon in it + 1 jet production.

have been compared to LHC measurements. One of the issues of the fixed-energy cone and of the non-isolated predictions is their dependence on the fragmentation functions used $\mathcal{D}_{i\to\gamma}$ [45, 16, 15]. For isolated cross-section with fixed-energy and Frixione cones, fixed order computations are only appropriate for $R \sim 1$ and $\epsilon_\gamma \sim 1$, otherwise large logarithms appear and spoil perturbation theory. The generalization for narrow cones and/or small ϵ_γ is not trivial. In Chapter 5, this problem is addressed for NLO cross-sections and the logarithms $\ln R$ and $\ln \epsilon_\gamma$ are resummed.

The dependence of non-isolated and fixed-energy cones on the choice of fragmentation functions can already be seen at NLO. The case of the NLO non-isolated cross-section is discussed at the end of this chapter. The influence of the isolation is studied in Chapter 4.

3.3 Direct photons

A direct photon is a photon which is real and emitted by a quark or a gluon through perturbative emission. One could also call direct photons "perturbative photons". Photons resulting from decays of hadrons or from the non-perturbative fragmentation are not direct. In this section, direct photon production is discussed , in particular at hadron colliders (pp

and $p\bar{p}$). The direct contribution is the first part of (3.2),

$$E_\gamma \frac{\mathrm{d}\sigma^\gamma}{\mathrm{d}^3 p_\gamma} = \sum_{a,b=q,\bar{q},g} \int \mathrm{d}x_a \mathrm{d}x_b f_{a/A}(x_a,\mu^2) f_{b/B}(x_b,\mu^2) \left[E_\gamma \frac{\mathrm{d}\sigma^\gamma_{ab}}{\mathrm{d}^3 p_\gamma}\left(p^\gamma, x_a, x_b, \mu^2, \mu_a^2\right)\right]. \tag{3.11}$$

At leading-order in QCD, there are two types of partonic processes. First there is the annihilation $q\bar{q} \to \gamma g$, secondly the Compton effect $qg \to q\gamma$. The leading-order diagrams are shown in Figure 3.4. Both processes occur at the same order $\mathcal{O}(\alpha\alpha_s)$.

The LO processes can be computed for both the Compton scattering and the annihilation for a virtual or a real photon in the final state. The partonic differential cross-section in term of the Mandelstam variables[1] (with the spin and color indices are summed for the final state and average for the initial one) is [25, 46]

$$\begin{aligned} \frac{\mathrm{d}\sigma^\gamma_{q\bar{q}}}{\mathrm{d}t} &= \frac{\pi\alpha\alpha_s}{s} C_F e_q^2 \left(\frac{t^2+u^2+2s\,(s+t+u)}{tu}\right) && q\bar{q} \to g\gamma^*, \\ \frac{\mathrm{d}\sigma^\gamma_{qg}}{\mathrm{d}t} &= -\frac{\pi\alpha\alpha_s}{s}\frac{e_q^2}{N_c} \left(\frac{s^2+u^2+2t\,(s+t+u)}{su}\right) && qg \to q\gamma^*. \end{aligned} \tag{3.14}$$

If the photon is real we have

$$(s+t+u) = 0, \tag{3.15}$$

since all the particles are massless. All the Mandelstam variables above refer to the partons and the photon, not to the hadrons.

At a pp collider, there are no valence anti-quarks and the PDF of anti-quarks in protons are smaller than the one of the gluon. Therefore, Compton scattering should dominate. At a $p\bar{p}$ collider, there are as many quarks as anti-quarks, so it would make sense that annihilation contributes to a larger fraction of the cross-section that with a pp collider. It would not be surpising than the annihilation process dominates over Compton scattering. As the PDFs depend on what energy and what momentum fraction they are evaluated at, it would be possible to try to estimate for asymptotic values which one dominates using the partonic cross-section. MadGraph can be used to compute the total cross-section for a wide range $p^\gamma_{T,min}$ and to look at the fraction each subprocesses contributes. Note that we consider the cross-section with a minimum photon transverse momentum and not a particular bin of p^γ_T. In the following, we study pp and $p\bar{p}$ collisions at $\sqrt{s} = 13$ TeV and 1.96 TeV. The value 1.96 TeV is chosen as it was the highest center of mass of energy of the Tevatron. The PDFs set `NNPDF23_lo_as_0119_qed` and $\alpha^{-1} = 132.5070$ are used. The precise value of α is irrelevant as both processes are proportional to α. The photon was constrained to have a pseudo-rapidity smaller than $|\eta| < 2.37$ and the jet was not constrained. The fraction that each processes contribute to the whole cross-section $\sigma\left(p^\gamma_{T,min}\right)$ is considered, where the produced photon satisfies $p^\gamma_T > p^\gamma_{T,min}$.

[1] The Mandelstam variable s, t, u are defined for a process $1+2 \to 3+4$ (see for example [26])

$$\begin{aligned} s &= (p_1+p_2)^2, \\ t &= (p_1-p_3)^2, \\ u &= (p_3-p_2)^2. \end{aligned} \tag{3.12}$$

The Mandelstam variables have the property that

$$s+t+u = m_1^2+m_2^2+m_3^2+m_4^2. \tag{3.13}$$

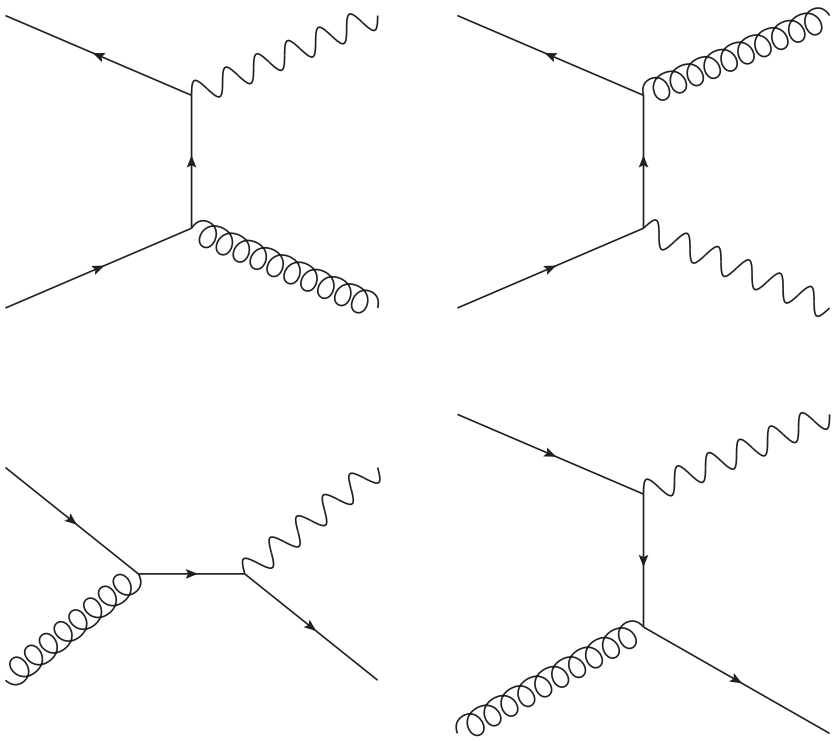

Figure 3.4: Leading order process for $pp \to \gamma$ + jet Top: the two diagrams for quark-antiquark annihilation to a photon and a jet. Bottom: the two diagrams for Compton process $qg \to q\gamma$, the same diagrams with an antiquark instead of a quark also contribute.

The results can be seen in Figures 3.5 and 3.6. Similar plots for lower energies can be found in [47]. In the case of pp collisions, Compton scattering dominates over annihilation for all values of the photon transverse momentum and for both $\sqrt{s}$. The higher $p^{\gamma}_{T,min}$ is, the larger the fraction of the quark annihilation gets. However, it increases slowly and never dominates. In the case of $p\bar{p}$ collisions, at low $p^{\gamma}_{T,min}$, Compton scattering also dominates and contributes more than the annihilation. The main difference here is that the Compton scattering fraction decreases faster than in the pp case and the annihilation fraction increases faster when $p^{\gamma}_{T,min}$ increases. For a $p\bar{p}$ collider at $\sqrt{s} = 13$ TeV, the crossing between the two contributions will happen when $p^{\gamma}_{T,min} \approx 680\,\text{GeV}$, for a total cross-section of 0.24 pb which is tiny. If the collider has a center of mass energy of 1.96 TeV, the crossing happens at $p^{\gamma}_{T,min} \approx 114\text{GeV}$ for a total cross-section of 10.4 pb. Alternatively, it would also be possible to generate events starting a certain p^{γ}_{T} and decide for some binning and to look in every bin how much each sub-process does.

At NLO in QCD, there are many more diagrams and subprocesses, first there are virtual corrections. Then there are new channels like $qg \to \gamma qg$, $gg \to \gamma q\bar{q}$, $q\bar{q} \to \gamma gg$, $q\bar{q} \to \gamma q\bar{q}$ and $qq' \to qq'\gamma$. Two diagrams can be seen in Figure 3.7.

Finally, it is interesting to compare direct photon production with dijet production. Photon production occurs at $\mathcal{O}(\alpha\alpha_s)$ and dijet production at $\mathcal{O}(\alpha_s^2)$. Hence the production of γ+jet will occur less often than the production of 2 jets at hadron collider. The process $pp \to$ jets is a background in the pile-up to $pp \to \gamma + X$. For comparable cuts at the LHC, the LO cross-section for dijets is approximately 10^3 times larger than the one for γ + jet. One reason is that the strong coupling is more than 10 times larger than electromagnetic one. On top of that, dijet productions has more channels than photon production (for example gg can not produce a photon at LO but can create two jets). In [36], the ratio

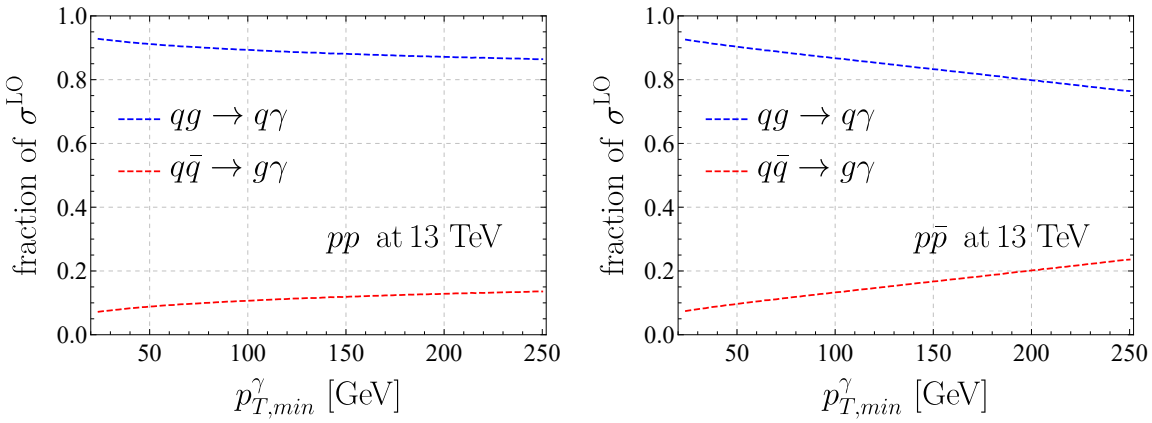

Figure 3.5: Fractions of the LO cross-section of pp or $p\bar{p}$ to γ + jet with a center of mass energy of $\sqrt{s} = 13$ TeV for both Compton and annihilation, results obtained using MadGraph. In the case of the $p\bar{p}$, the annihilation will dominate for $p^{\gamma}_{T,min} > 680$ GeV.

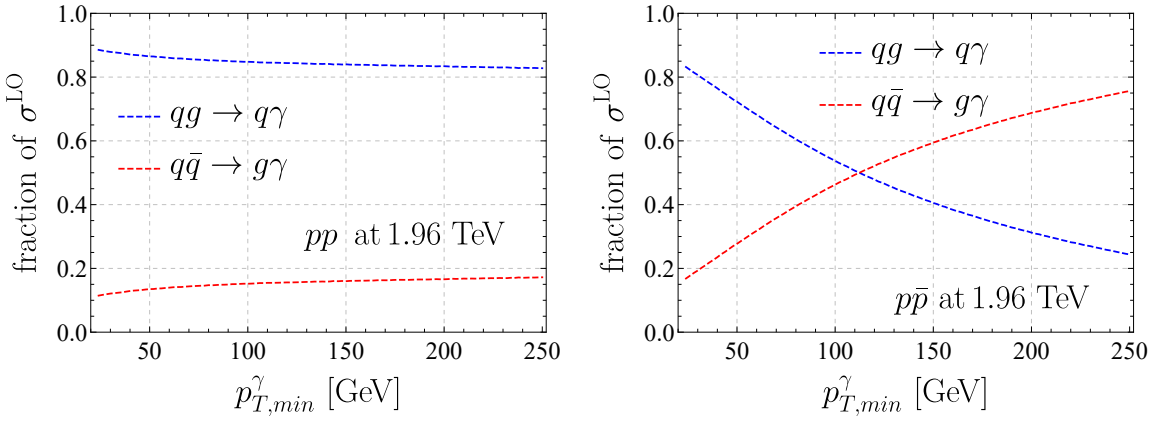

Figure 3.6: Fractions of the LO cross-section of pp or $p\bar{p}$ to γ + jet with a center of mass energy of $\sqrt{s} = 1.96$ TeV for both Compton and annihilation, results obtained using MadGraph.

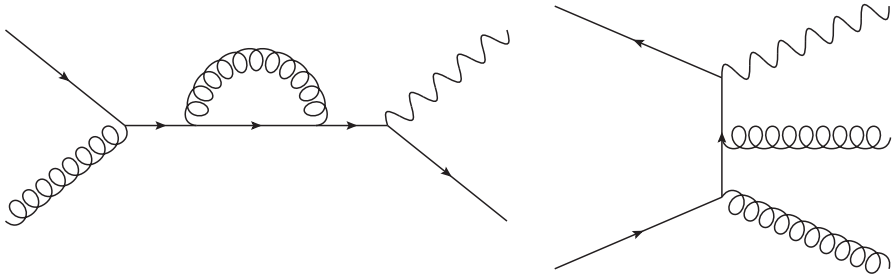

Figure 3.7: Left: one of the virtual diagrams contributing $pp \to \text{jet} + \gamma$ at NLO. Right: one of the real diagrams of $pp \to \gamma + X$ at NLO, here X is two jets or one jet composed of the two gluons.

of γ/jet was found to be of order 10^{-4}. This ratio depends obviously on what kinematics and cuts are considered.
The non-perturbative part contributes in the case of a non-isolated photon or if it is isolated with a fixed-energy cone. At hadron colliders there are the two perturbative contributions (Compton and annihilation) and the non-perturbative one. The fraction of the three processes depends on the parameters. In [4] with the help of the program JETPHOX[2] the fraction of the cross-section at LO of the 3 contributions for a wide range of E_γ^T for both the kinematics of the LHC with $\sqrt{s} = 14$ TeV (and also for the Tevatron) was computed. They considered the cases of a non-isolated photon and a fixed energy cone with $R = 0.4, E_{\text{iso}}^T = 4$ GeV, using the BFGII set and a dynamic scale $\mu_a = \mu_f = \mu_r = E_\gamma^T$. At the LHC, the fragmentation fraction for $E_\gamma^T \sim 125$ GeV is a bit more than 40% of the cross-section in the non-isolated case. Using the fixed energy cone, the fragmentation at this energy is only around 15%. Detailed plots can be found in [4].

3.4 Non-perturbative fragmentation

In this section, the non-perturbative fragmentation function is considered, the second term of (3.2)

$$\sum_{f=q,\bar{q},g} \int_{z_{min}}^{1} \frac{\mathrm{d}z}{z^2} \mathrm{d}\sigma_{ab}^{f}(p^\gamma, x_a, x_b, z, \mu^2, \mu_a^2) \mathcal{D}_{f\to\gamma}(z, \mu_a^2). \tag{3.16}$$

The non-perturbative fragmentation function is denoted by $\mathcal{D}_{i\to\gamma}(z, \mu)$. It depends on the fraction of momentum taken by the photon from the emitting parton z and on the factorization scale μ. Graphically it is often denoted by a circle as shown in Figure 3.8. This diagrammatic representation is a simplification. The emitting parton is not only turning into a photon. A quark can not turn only into a photon due to baryon number conservation. We should actually write $i \to \gamma + Y$ instead of $i \to \gamma$.

The non-perturbative fragmentation functions satisfy a DGLAP-like equation

$$\frac{d}{d\ln\mu} \mathcal{D}_{i\to\gamma}(z, \mu) = \mathcal{P}_{i\to\gamma}(z, \mu) + \sum_{j=q,\bar{q},g} \mathcal{P}_{i\to j} \otimes \mathcal{D}_{j\to\gamma}(z, \mu)\,. \tag{3.17}$$

The same equation is fulfilled by the cone fragmentation functions $\mathcal{F}_{i\to\gamma}$ of (1.2). The Altarelli–Parisi splitting functions $\mathcal{P}_{i\to j/\gamma}$ can be expanded in α and α_s. In order to get

[2]Running JETPHOX is not easy as the program is relatively old and not maintained anymore. It can compute the NLO cross-section of photon production with fixed-energy cone and Frixione cone.

Figure 3.8: Diagramatic representation of the splitting function $\mathcal{D}_{i\to\gamma}$ of a quark and of a gluon to a photon.

the LL evolution equations, it is necessary to expand up to the following

$$\begin{aligned}\mathcal{P}_{i\to\gamma}(z) &= \frac{\alpha}{2\pi}P^{(0,1)}_{i\to\gamma}(z) + \mathcal{O}\left(\alpha\alpha_s\right),\\ \mathcal{P}_{i\to j}(z) &= \frac{\alpha_s}{2\pi}P^{(1,0)}_{i\to j}(z) + \mathcal{O}\left(\alpha_s^2\right).\end{aligned} \tag{3.18}$$

With the coefficient of (2.19) (2.20). Then the DGLAP equations become (as shown in [41]), with the same convolution $\otimes$ as for the DGLAP of PDFs (2.18)

$$\begin{aligned}\frac{d}{d\ln\mu^2}\mathcal{D}_{q\to\gamma}(z,\mu) &= \frac{\alpha e_q^2}{2\pi}P^{(0,1)}_{q\to\gamma}(z) + \frac{\alpha_s}{2\pi} + \left(P^{(1,0)}_{q\to q}\otimes\mathcal{D}_{q\to\gamma} + P^{(1,0)}_{q\to g}\otimes\mathcal{D}_{g\to\gamma}\right),\\ \frac{d}{d\ln\mu^2}\mathcal{D}_{g\to\gamma}(z,\mu) &= \frac{\alpha_s}{2\pi}\left(\sum_{p=q,\bar{q}}P^{(1,0)}_{g\to p}\otimes\mathcal{D}_{p\to\gamma} + P^{(1,0)}_{g\to g}\otimes\mathcal{D}_{g\to\gamma}\right).\end{aligned} \tag{3.19}$$

In order to obtain the next-to-leading log (NLL) equations, it is necessary to expand all the splitting functions one order higher in α_s, so at order $\mathcal{O}\left(\alpha\alpha_s\right)$ for the inhomogeneous terms and $\mathcal{O}\left(\alpha_s^2\right)$ for the homogeneous ones, it is also necessary to consider the running of α_s at two loops. Note that the gluon will have an inhomogeneous term, and as in the case of DGLAP of the PDFs, there are splitting functions coupling different types of quark fragmentation functions. Naively, the α_s expansion of (2.18) does not seem to be correct. The reason of this expansion, is that $\mathcal{D}_{i\to\gamma}$ is actually proportional to $\frac{\alpha}{\alpha_s}$ this can be seen while solving the equation in Mellin space. The cone fragmentation function $\mathcal{F}_{i\to\gamma}$ has exactly the same evolution equation, however the initial conditions are different. The necessary expansion of the splitting functions for the NLL equations are available and can be found in the literature.

At the lowest-order which is α (α_s^0), it is straightforward to solve the DGLAP equations, as they simplify to

$$\frac{\partial\mathcal{D}_{q\to\gamma}(z,\mu)}{\partial\ln\mu^2} = \frac{\alpha}{2\pi}P^{(0,1)}_{q\to\gamma}(z), \qquad \frac{\partial\mathcal{D}_{g\to\gamma}(z,\mu)}{\partial\ln\mu^2} = 0, \tag{3.20}$$

assuming we know $\mathcal{D}_{i\to\gamma}(z,\mu_0)$ at a certain scale μ_0, it follows that

$$\mathcal{D}_{q\to\gamma}(z,\mu) = \frac{\alpha e_q^2}{2\pi}P^{(0,1)}_{q\to\gamma}(z)\ln\frac{\mu^2}{\mu_0^2} + \mathcal{D}_{i\to\gamma}(z,\mu_0) \qquad \mathcal{D}_{g\to\gamma}(z,\mu) = \text{constant}. \tag{3.21}$$

This equation is used for the LO GdRG set. Notice the fact that $\mathcal{D}_{q\to\gamma}$ scales like $\ln\mu^2$ when μ^2 is large. If μ is large compared to μ_0 and $\mathcal{D}_{i\to\gamma}(z,\mu_0)$ is not so large, it is not necessary to care about $\mathcal{D}_{i\to\gamma}(z,\mu_0)$. However, we first need to know if $\mathcal{D}_{i\to\gamma}(z,\mu_0)$ is small and can be neglected compared to the other term. Therefore, it is necessary to measure it.

The fragmentation functions were measured in the 90s. There are a few sets, the GRV (Gluck, Reya, Vogt) [48], the BFG(Bourhis, Fontannaz, Guillet) [49] and finally GdRG

(Gehrmann–De Ridder, Glover) [44, 50] . The GdRG is also called the ALEPH set. Both the BFG and the GdRG are implemented in MCFM. Both GdRG and BFG sets are computed using the $\overline{\text{MS}}$ scheme. The GRV functions were computed using the DIS_γ scheme; there is no available code for the GRV set. The BFG and GdRG sets will be discussed more in depth later in this chapter.

The non-perturbative fragmentation function needs to be measured experimentally. One of the problems to measure it is the background of photons from decay of neutral hadrons. If one wants to use some isolation criteria to suppress this background (as for example a fixed-energy cone), it is then important to keep in mind that the non-perturbative fragmentation contribution is also suppressed by the isolation cuts. In order to measure it it is therefore easier to use a lepton collider as less hadrons are produced and there would be less background. For example LEP was suitable and used to measure it [51]. The measurement at LEP was performed by studying jets containing a photon that carries more than 70 percent of the jet energy. This choice is due to the background of photons from neutral hadrons of jets.

At LHC or Tevatron we have to isolate photons using some isolation cuts because of the decays of hadrons. This background is important at the energy both colliders operate. The problem with adding some isolation criteria is that it will suppress not only the photon of hadronic decays but also part of the photon coming from the fragmentation process. This is problematic for measuring the fragmentation function. The authors of [52] suggested using the RHIC collider at $\sqrt{s} = 200$ GeV and for $p_T^\gamma \leq 16$ GeV in order to get more constraints for small z values that were not accessible in the LEP measurement (so outside of the range $z > 0.7$). In [34], it was also argued that by considering $pp \to (\text{jet}\,\gamma) + X$ at RHIC or at the LHC, where the photon is in a jet (which would be a similar type of measurement as at LEP), it would be possible to gain better knowledge on the fragmentation function. In order to do so it is necessary to subtract the background of photons for hadronic decays. The authors also presented some numerical results. The experimental data was not done yet.

As shown in (3.7), the non-perturbative fragmentation function scales like $\frac{\alpha}{\alpha_s}$. A heuristic argument for this scaling is the following. At large μ, the non-perturbative fragmentation functions satisfy [25]

$$\mathcal{D}_{i\to\gamma}(z,\mu) \sim \ln \mu^2. \tag{3.22}$$

This will be tested later in the case of both the GdRG and BFG sets, see Figures 3.16 and 3.12. On the other hand, the strong coupling scales like $\frac{1}{\ln \mu^2}$ at large μ (2.3), hence $\mathcal{D}_{i\to\gamma} \sim \frac{\alpha}{\alpha_s}$. A more rigorous argument can be done by looking at the leading-log evolution of function $\mathcal{D}_{q\to\gamma}$ that is not coupled to the gluons for simplicity, this will be obvious by looking at (5.97), with $\mathcal{D}$ instead of $\mathcal{F}$, we see that in Mellin space the leading order term of $\mathcal{D}_{q\to\gamma}$ is proportional to $\frac{\alpha}{\alpha_s}$.

3.4.1 Differences between PDFs and fragmentation function DGLAP equations

At first glance the only difference between both DGLAP equations is the inhomogeneous term, however it is not the case. At leading-order in α_s the mixed term of the homogeneous part is not the same. If we consider PDF with only one quark $f_{i/p}(\mu, z)$ the DGLAP equation is

$$\frac{\mathrm{d}}{\mathrm{d}\ln\mu^2}\begin{pmatrix} f_{g/p} \\ f_{q/p} \end{pmatrix} = \begin{pmatrix} \mathcal{P}_{g\to g} & \mathcal{P}_{q\to g} \\ \mathcal{P}_{g\to q} & \mathcal{P}_{q\to q} \end{pmatrix} \otimes \begin{pmatrix} f_{g/p} \\ f_{q/p} \end{pmatrix}. \tag{3.23}$$

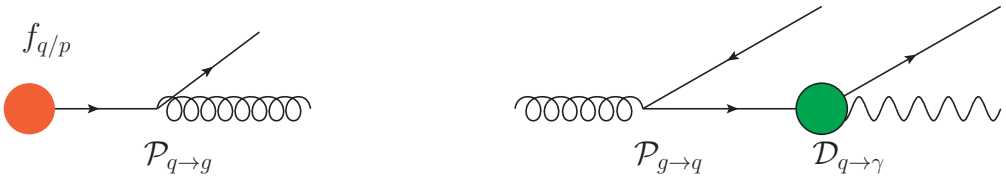

Figure 3.9: Difference of the leading order homogeneous part of the two DGLAP equations. Left: parton distribution function, the circle represents a proton. Right: non-perturbative fragmentation function.

In the case of the non-perturbative fragmentation functions $\mathcal{D}_{i\to\gamma}$ (and also of the cone fragmentation functions of Chapter 5), the DGLAP equation is

$$\frac{\mathrm{d}}{\mathrm{d}\ln\mu^2}\begin{pmatrix}\mathcal{D}_{g\to\gamma}\\ \mathcal{D}_{q\to\gamma}\end{pmatrix} = \begin{pmatrix}\mathcal{P}_{g\to\gamma}\\ \mathcal{P}_{q\to\gamma}\end{pmatrix} + \begin{pmatrix}\mathcal{P}_{g\to g} & \mathcal{P}_{g\to q}\\ \mathcal{P}_{q\to g} & \mathcal{P}_{q\to q}\end{pmatrix} \otimes \begin{pmatrix}\mathcal{D}_{g\to\gamma}\\ \mathcal{D}_{q\to\gamma}\end{pmatrix}. \tag{3.24}$$

The diagonal splitting functions of the homogeneous part are exchanged. The reason for this exchange is obvious when considering diagrams. In Figure 3.9, two processes are represented; on the left there is a diagrammatic representation of a quark originating from a proton splitting to a gluon which will contribute to the pdf of the gluon in the quark $f_{g/p}$. On the right, a diagrammatic representation of a gluon splitting into a quark that later fragment to a photon contributing to the non perturbative fragmentation of the quark $\mathcal{D}_{q\to\gamma}$.

Interestingly, another example of that kind of DGLAP equation is the evolution equation of parton f into a hadron h: $\mathcal{D}_{f\to h}(z,\mu)$ which looks similar to the one of the photon non-perturbative fragmentation [25]

$$\frac{\mathrm{d}}{\mathrm{d}\ln\mu^2}\begin{pmatrix}\mathcal{D}_{g\to h}\\ \mathcal{D}_{q\to h}\end{pmatrix} = \begin{pmatrix}\mathcal{P}_{g\to g} & \mathcal{P}_{g\to q}\\ \mathcal{P}_{q\to g} & \mathcal{P}_{q\to q}\end{pmatrix} \otimes \begin{pmatrix}\mathcal{D}_{g\to h}\\ \mathcal{D}_{q\to h}\end{pmatrix}. \tag{3.25}$$

At leading-order in α_s the DGLAP equation of PDF and of the hadron fragmentation have the same splitting functions $P^{(1,0)}_{i\to j}(z)$, except that the diagonal terms are exchanged. At leading order the splitting functions $P^{(1,0)}_{i\to j}(z)$ in the convolution are the same for these three DGLAP equations. At next-to-leading order this is not the case, there are spacelike and timelike splitting functions and it is necessary to use the right one. The two fragmentation functions $\mathcal{D}_{i\to\gamma}$ and $\mathcal{D}_{f\to h}$ still have the same matrix for the homogeneous term.

An example to illustrate the difference between time-like and space-like splitting functions is shown in Figure 3.10. The splitting of a quark to a photon is considered. At order α, both splitting functions are similar. With the notation of [30], the splitting function of a quark to a photon in pure QED is

$$P^{S,(0,1)}_{q\to\gamma}(z) = P^{T,(0,1)}_{q\to\gamma}(z) = P^{(0,1)}_{q\to\gamma}(z) = e_q^2 P(z) = e_q^2\frac{1+(1-z)^2}{z}. \tag{3.26}$$

At higher order, we need to consider the QCD correction $P^{(1,1)}_{q\to\gamma}(z)$, in this case the spacelike and the timelike splitting are not the same. Let us first consider a quark produced in a process $\mathcal{N}$ and splitting into a photon and a quark. Both of the two particles are outgoing. The situation can be seen on the right of Figure 3.10 and the corresponding timelike

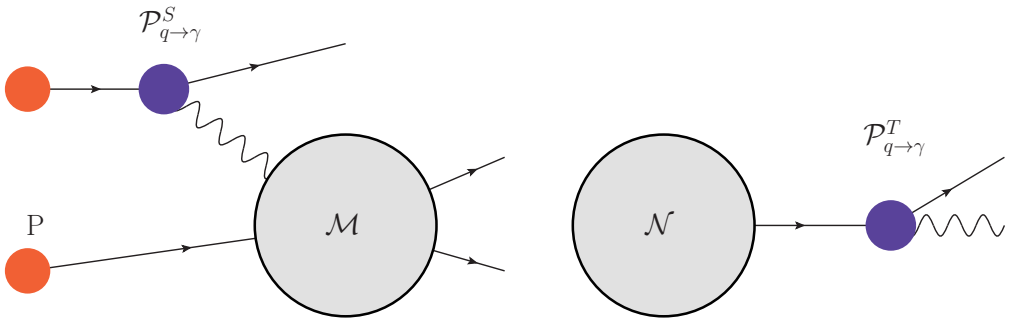

Figure 3.10: Distinction between spacelike and timelike splitting functions with the example of a quark splitting to a photon. Left: spacelike splitting of a quark (originating from a proton in red) to a photon, the photon will interact through amplitude $\mathcal{M}$. Right: timelike splitting of a quark (originating from the amplitude $\mathcal{N}$) into an outgoing photon. Notice that the kinematics of both situations are different. For the spacelike case the quark is outgoing and the photon is not, for the timelike case both the quark and the photon are outgoing. At order α, the two are similar.

splitting function is given in [53]

$$P^{T,(1,1)}_{q\to\gamma}(z) = P^{T,(1,1)}_{\bar{q}\to\gamma}(z) = C_F e_q^2 \left(-\frac{1}{2} + \frac{9}{2}z + \left(\frac{z}{2} - 8\right)\ln z + 2z\ln(1-z) + \left(1-\frac{z}{2}\right)\ln^2 z \right.$$
$$\left. + \left[\ln^2(1-z) + 4\ln z \ln(1-z) + 8\mathrm{Li}_2(1-z) - \frac{4\pi^2}{3}\right] P(z) \right). \tag{3.27}$$

In the second case we have an incoming quark (from a proton) that will emit a photon, this photon will interact in a process $\mathcal{M}$ as depicted in the left of Figure 3.10. The emitting quark is outgoing. The spacelike fragmentation need to be used [30]

$$P^{S(1,1)}_{q\to\gamma}(z) = P^{S(1,1)}_{\bar{q}\to\gamma}(z) = C_F e_q^2 \left(\left(-\ln^2(1-z) - 3\ln(1-z)\right) P(z) - \frac{7z}{2} \right.$$
$$\left. - \left(1-\frac{z}{2}\right)\ln^2(z) + \left(\frac{7z}{2} + 2\right)\ln(z) - 2z\ln(1-z) - \frac{5}{2} \right). \tag{3.28}$$

Obviously, the two splitting functions $P^{(1,1)}_{q\to\gamma}$ are different. A similar distinction is needed for $P^{(1,1)}_{g\to\gamma}$. Differences also arise for the homogeneous part of both DGLAP equations for example $P^{(2,0)}_{q\to q}(z)$. The parton distribution functions need the spacelike splitting function for their DGLAP equation. The photon non-perturbative fragmentation functions $\mathcal{D}_{i\to\gamma}$ (and also the quark to hadron fragmentations $\mathcal{D}_{f\to h}$) have timelike splitting functions. The pure QCD $P^{(3,0)}_{i\to j}(z)$ are known and can be found in [54, 31, 32] for the spacelike and [55, 56] for the timelike case. When solving the LL DGLAP equation of $\mathcal{D}_{i\to\gamma}$ the distinction is irrelevant as only $P^{(1,0)}_{i\to j}(z)$ and $P^{(0,1)}_{i\to\gamma}(z)$ are necessary. The distinction is then important at NLL and beyond.

3.4.2 The GdRG (Gehrmann-de Ridder, Glover) fragmentation functions

The GdRG set has a few simplifications compared to the two other sets. These simplifications make the set easier to implement than the BFG sets. First of all, it does not include

gluons

$$\mathcal{D}_{g\to\gamma}^{\mathrm{GdRG}}(z,\mu)=0. \tag{3.29}$$

The argument of setting it to zero is that in the BFG sets (which are older) the fragmentation of gluons to photons is small compared to the one of the quarks so we can as an approximation not include gluons. This simplification also greatly affects the DGLAP equations, as then each quark is not coupled to anything else. It would be natural to take the initial condition at μ_0 (which is small) of the form

$$\mathcal{D}_{q\to\gamma}(z,\mu_0)=\frac{\alpha e_q^2}{2\pi}f(z),\qquad \mathcal{D}_{g\to\gamma}(z,\mu_0)=0, \tag{3.30}$$

where $f(z)$ is a function of z which is fitted on some data and then to evolve it up using the evolution equation to a higher scale μ and then having the gluon fragmentation to not vanish anymore. This makes little sense as when μ increases α_s decreases and then the gluon coupling to the photon decreases. As you can see in the initial condition, the fragmentation function only depends on the charge of the quarks, but it neglects the mass of the quarks in the initial condition, as the evolution is not mixing quarks, it remains the case at all energies. This is not the case for the two BFG sets.

As the evolution equation is simple at LO, solving the equations is easy as the gluon fragmentation is absent

$$\frac{\partial\mathcal{D}_{q\to\gamma}(z,\mu)}{\partial\ln\mu^2}=\frac{\alpha e_q^2}{2\pi}P_{q\to\gamma}^{(0,1)}+\frac{\alpha e_q^2}{2\pi}\frac{\alpha_s}{2\pi}P_{q\to\gamma}^{(1,1)}+\frac{\alpha_s}{2\pi}P_{q\to q}^{(1,0)}\otimes\mathcal{D}_{q\to\gamma}(z,\mu). \tag{3.31}$$

The convention of $P_{q\to\gamma}^{(1,1)}$ used in this equation is the one from [30] and it is not the exactly same than the one used in Chapter 5 (factor two in the α_s expansion). The splitting function $P_{q\to\gamma}^{(1,1)}$ can be found in [53] (it is not the same as the space-like function given in [30]). The authors choose to include $P_{q\to\gamma}^{(1,1)}$ but not $P_{q\to q}^{(2,0)}$, as it would be necessary in order to be consistent while counting the power of α_s. It is possible that the inclusion of $P_{q\to q}^{(2,0)}$ has a smaller effect than $P_{q\to\gamma}^{(1,1)}$. A perturbative solution of the equation given by the authors of the set is

$$\begin{aligned}\mathcal{D}_{q\to\gamma}(z,\mu)=\mathcal{D}_{q\to\gamma}^{\mathrm{NP}}(z,\mu_0)+\frac{\alpha e_q^2}{2\pi}\ln\left(\frac{\mu^2}{\mu_0^2}\right)P_{q\to\gamma}^{(0,1)}(z)+\frac{\alpha e_q^2}{2\pi}\frac{\alpha_s}{2\pi}\ln\left(\frac{\mu^2}{\mu_0^2}\right)P_{q\to\gamma}^{(1,1)}(z)\\ +\frac{1}{2}\frac{\alpha e_q^2}{2\pi}\frac{\alpha_s}{2\pi}\ln^2\left(\frac{\mu^2}{\mu_0^2}\right)P_{q\to q}^{(1,0)}\otimes P_{q\to\gamma}^{(0,1)}+\frac{\alpha_s}{2\pi}\ln\left(\frac{\mu^2}{\mu_0^2}\right)P_{q\to q}^{(1,0)}\otimes\mathcal{D}_{q\to\gamma}^{\mathrm{NP}}(z,\mu_0).\end{aligned} \tag{3.32}$$

As you can see this equation does not take into account the running of α_s. Therefore using it with μ and μ_0 too different may be problematic. The fragmentation function is measured at the scale μ_0.

The data used for measuring the fragmentation function are data from LEP. It is fitted only for the range where $z>0.7$ where z is the amount of energy the photon is taking from the emitting quark; the types of jets that are considered contain a photon that carries a large fraction of the energy of the "photon-jet". The fitted fragmentation function at LO has two parameters μ_0 and a

$$\mathcal{D}_{q\to\gamma}^{\mathrm{NP,LO}}(\mu_0,z)=\frac{\alpha e_q^2}{2\pi}\left(-P(z)\ln\left((1-z)^2\right)-a\right). \tag{3.33}$$

The fitted values are $\mu_0=0.14$ GeV and $a=13.6$. At NLO, the fit has three parameters μ_0, the b and the c

$$\mathcal{D}_{q\to\gamma}^{\mathrm{NP,NLO}}(\mu_0,z)=\frac{\alpha e_q^2}{2\pi}\left(-P(z)\ln\left((1-z)^2\right)+b(1-z)-c\right), \tag{3.34}$$

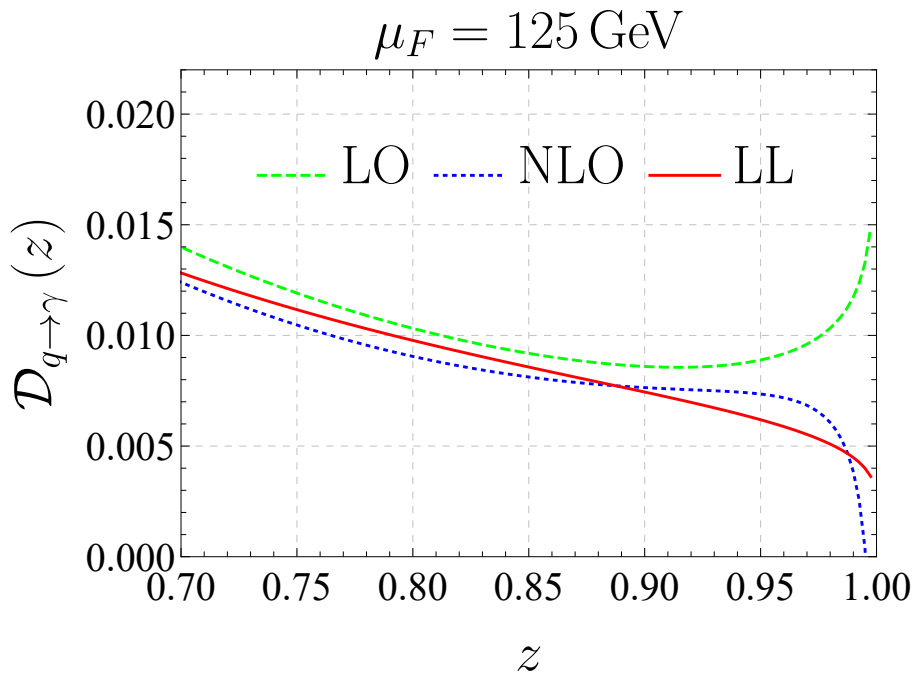

Figure 3.11: Splitting function $\mathcal{D}_{q\to\gamma}$ of the GdRG set at LO, NLO and LL at the scale $\mu = 125$ GeV.

with $\mu_0 = 0.64$ GeV, $b = 20.8$ and $c = 11.07$.
Finally, while turning off the inhomogeneous term $\alpha\alpha_s P^{(1,1)}_{q\to\gamma}$, we solved the DGLAP equation numerically from $\mu_0 = 0.64$ up to $\mu_F = 125$ GeV in order to get the leading-log result. We used the NLO running of $\alpha_s(M_z) = 0.119$ and $\alpha^{-1} = 132.5070$. $e_q = 1$ was chosen for simplicity. The leading-log result is compared to the LO result which is simply

$$\mathcal{D}^{\mathrm{LO}}_{q\to\gamma}(z,\mu) = \mathcal{D}^{\mathrm{NP,LO}}_{q\to\gamma}(z,\mu_0) + \frac{\alpha e_q^2}{2\pi}\ln\left(\frac{\mu^2}{\mu_0^2}\right) P^{(0,1)}_{q\to\gamma}(z), \tag{3.35}$$

and the NLO is (3.32) without $P^{(1,1)}_{q\to\gamma}$. The results of the LL, LO and NLO fragmentation can be seen in Figure 3.11. As you can see the NLO and LL splitting functions are quite similar and the NLO solution is a reasonably good approximation. It is an interesting approximate solution because of its simplicity. The LO fragmentation has a different behavior for $z \to 1$ than the NLO and LL. In Figure 3.12, the dependence of the LL GdRG as a function of $\ln\mu^2$ is shown for an arbitrary value of z, as predicted earlier the LL result is linear.

The leading-order version of the GdRG set is implemented in MCFM, the NLO are not.

3.4.3 BFG (Bourhis, Fontannaz, Guillet) I and II fragmentation functions

The BFG sets [49] have fewer simplifications than the GdRG ones. The BFG sets do not neglect gluons. However, the fragmentation function of gluons is smaller than the one of quarks. Unlike the GdRG set, the quarks of different masses have different fragmentation functions. The underlying idea is to approximate the non-perturbative part of the fragmentation function using a so called vector dominance model (VDM). The photon

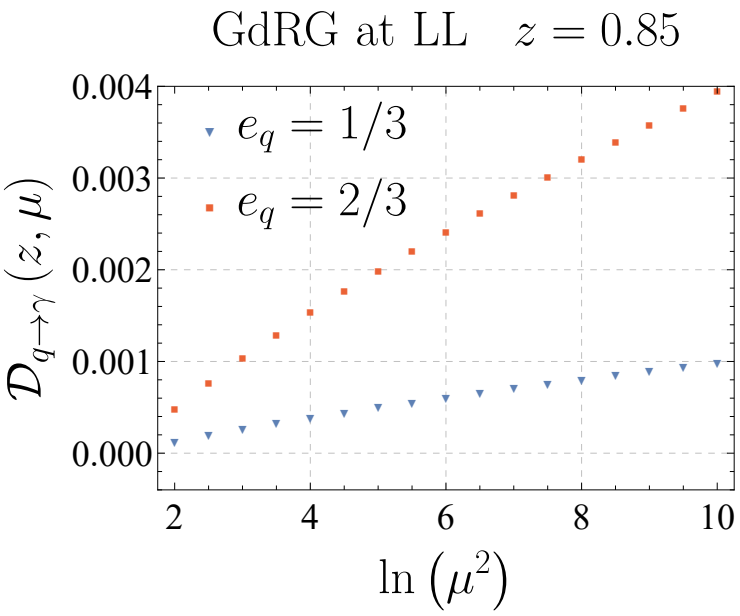

Figure 3.12: Dependence on the fragmentation scale μ of the leading log fragmentation of the GdRG set for both types of quarks for an arbitrary value of z. Both quarks are linear.

fragmentation is approximated by linear combination of parton to meson fragmentation functions. This means that the sets were not fitted on data from photon production but on meson production. More precisely, the experimental data used to perform the fit of the non-perturbative part are not measurements of photons but of the ρ meson. The two sets are interpolated on the same data however different parameters in the interpolations are taken as constant. The two sets when compared to the data of the cross-section $e^-e^+ \to \rho + X$ are giving results in agreement with each other (within uncertainties). The evolution in the BFG sets is done at NLL accuracy.

In all following plots the charges of quarks e_q^2 and the factor $2\sum_f e_i^2$ are both included[3]. There is no publicly available code to call the BFG fragmentation function. However Fortran routines can be found in the code of JETPHOX and MCFM. In both programs, you can find the same data for a grid of 45 points in z space from 0.04627 to 0.99 and in the μ space there are 30 points with $\mu^2 = 2, 2.8, ..., 984800.0$ GeV^2. It is then possible to interpolate for intermediate values. It would also be possible to evolve the fragmentation function by solving the DGLAP equations. Interpolation outside the z range may be problematic and should be avoided. This is particularly a problem for $z > 0.99$. The bottom quark is not included until we reach an energy of 4.5 GeV.

In Figures 3.13 and 3.14, the fragmentation functions of the set I are plotted as a function of z for two different scales. The gluon fragmentation is always smaller than the one of the quarks which was one of the arguments used in the GdRG set not to include gluons. At both low and high energies, the up-type quarks have larger fragmentation than the down-type quarks. At low energy, fragmentation functions of quarks of the same type are more different than at higher energies. The effect of the mass of the quark decreases and at $\mu = 125$ GeV their values get closer for most of the z range. The fragmentation functions decrease when z increases. The fragmentation of the gluons is decreasing drastically for $z \to 1$. Both sets look qualitatively similar. The gluon fragmentation $\mathcal{D}_{g\to\gamma}$ is the one that

[3] In [49], the authors factorized these factors out of the definition of $\mathcal{D}_{i\to\gamma}$.

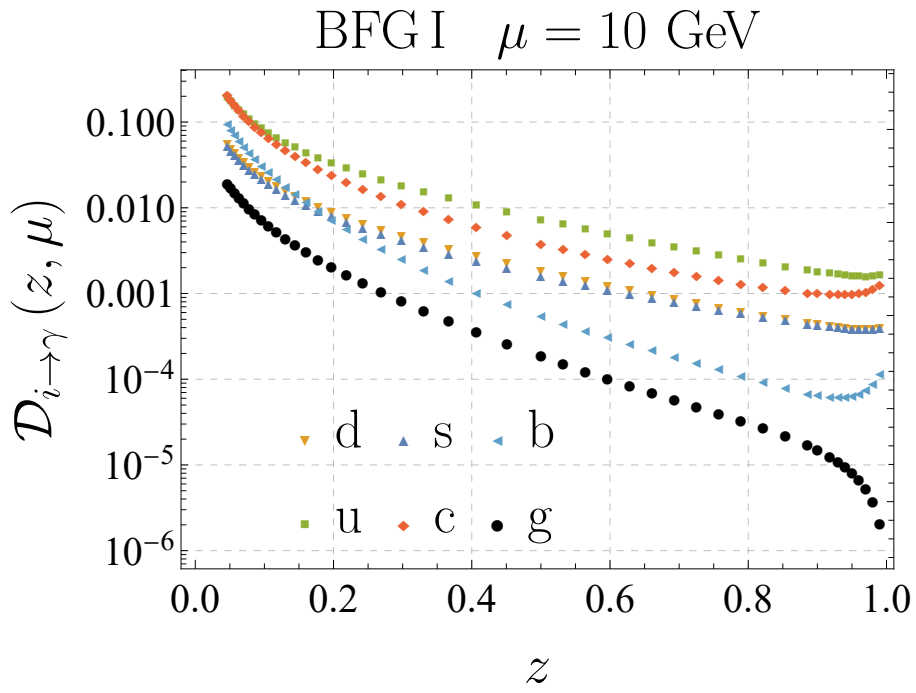

Figure 3.13: Non-perturbative fragmentation functions of the BFG I set at $\mu = 10$ GeV as a function of z.

differs the most between the two sets as you can see in Figure 3.15. The curves do not match at both 10 and 125 GeV. However, the qualitative behavior is similar.
We can also look at the dependency of $\mathcal{D}_{i\to\gamma}$ on $\ln\mu^2$. The results for $z = 0.85$ are shown for a wide range of energy in Figure 3.16. The light quarks are linear in $\ln\mu^2$ on the whole range of energy. The strange and down quarks are very close. The bottom quark fragmentation is also linear but at higher energy, it is obviously zero at scales lower than its mass. The quarks in the BFG II set have a similar dependence, therefore we did not plot them. The gluons of the two sets are different at low energy. The gluon fragmentation in the set I is linear in $\ln\mu^2$ for all the considered range. The gluon of the set II is not linear at low energy scale and will be linear for energies larger than approximately 10 GeV. At high energies, both gluon fragmentation functions agree. One has to keep in mind that these two plots were done for the arbitrary value of $z = 0.85$.

In order to see in a more quantitative way where the two sets differ, the following quantity R_i can be considered

$$R_i(z,\mu) = \left| \frac{\mathcal{D}^I_{i\to\gamma} - \mathcal{D}^{II}_{i\to\gamma}}{\mathcal{D}^I_{i\to\gamma} + \mathcal{D}^{II}_{i\to\gamma}} \right|, \tag{3.36}$$

with $i = g, u, d, ..., b$ and the variable z in the range of the set, so it is not necessary to interpolate outside. μ was chosen to be from $\ln\mu^2 = 1.5$ to $\ln\mu^2 = 11$ which correspond to $\mu = 2.11$ GeV and 244.5 GeV respectively. For the bottom quark it obviously does not make sense to consider $\mu < m_b$ so we took $\ln\mu^2 = 3.009$ [4] as the lower boundary of the range.

Figure 3.17 shows $R_i(z,\mu)$ of the gluon and of the down quark. The strange and bottom quarks have very similar R_i behavior to the down quark. The up and charm are

[4] $\ln\mu^2 = 3.009$ is slightly larger than $\ln m_b^2/\text{GeV}^2$.

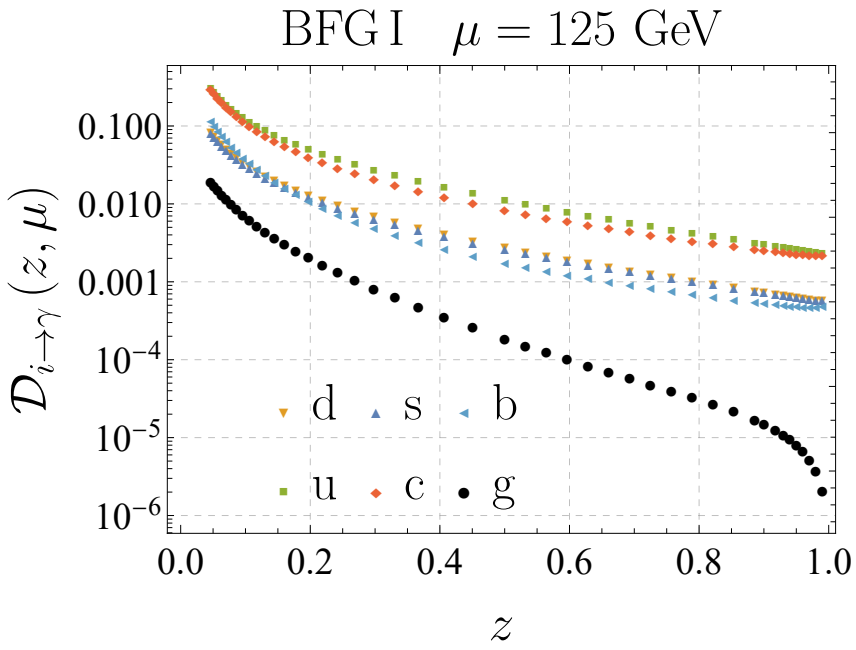

Figure 3.14: Non-perturbative fragmentation functions of the BFG I set at $\mu = 125$ GeV as a function of z.

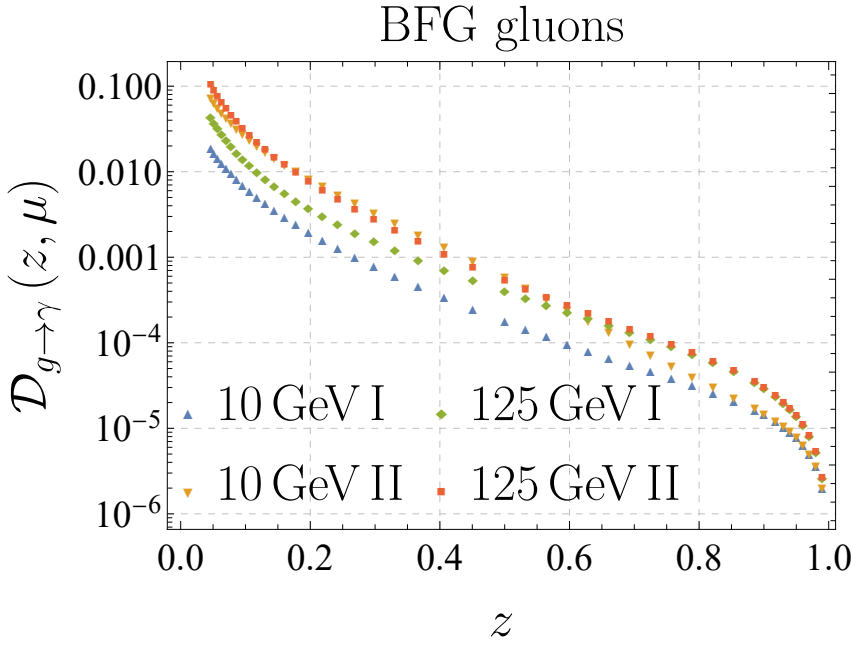

Figure 3.15: Non-perturbative fragmentation functions of the gluons of the two BFG sets at 2 different energy scales as a function of z.

slightly different, there is a region at low $\ln \mu^2$ and small z where R_i can reach 0.1. The only particle where the ratio R_i is large is the gluon. The quarks R_i are smaller. Indeed, the two sets are more similar for the quarks than for the gluon fragmentation.

It is instructive to find the maximum value of R_i for all the quarks and the gluon. You can see the approximate value of R_i with the corresponding parameters in Table 3.3. For the quarks up, down and strange the maximal value is pretty small and the two sets

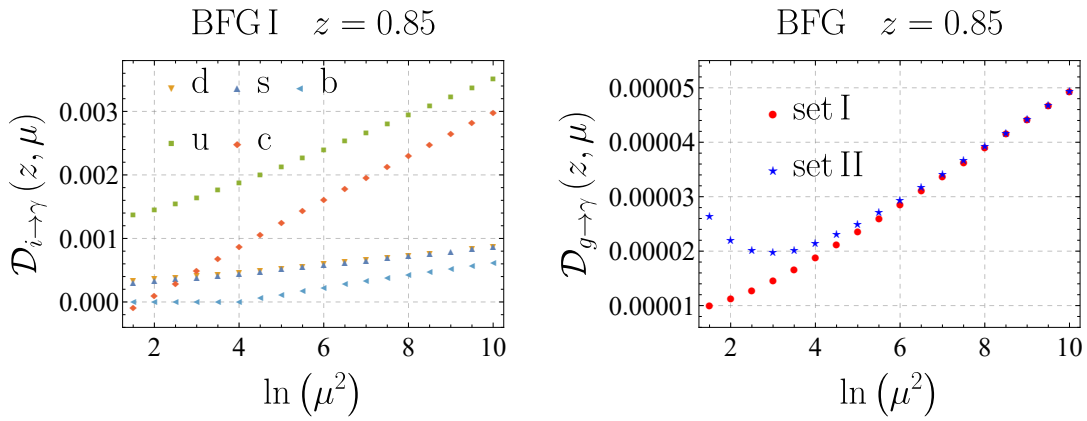

Figure 3.16: Left: Dependence of the fragmentation function of the set I of the quarks on the scale at an arbitrary value of z. Note that $\ln m_b^2/\text{GeV}^2 \sim 3$. Right: Dependence of the gluon fragmentation functions of both sets at an arbitrary value of z.

particle	R_i^{max}	z	μ [GeV]
gluon	0.825	0.51	2.12
up	0.040	0.057	2.12
down	0.133	0.05	48.9
strange	0.144	0.05	40.49
charm	0.829	0.781	2.14

Table 3.3: Maximum value of the ratio $R_i(z,\mu)$ and the approximate parameters at which the maximum occurs.

hence agree with each other. As you can see the gluon and the charm reach a large value. the maximums occur at small z except for the charm and the bottom. The value of the R_b is not shown on purpose. Because the closer the scale μ goes to m_b the larger the maximum R_b is and for those values $\mathcal{D}_{b\to\gamma}$ is anyways tiny. If energies high enough ($\ln\mu^2 > 5$) are considered, R_b is similar to R_d. For the two charm quark, the discrepancy also happens at small energies, however R_c decrease significantly when the scale is larger. So for both charm and bottom, the values of $\mathcal{D}^I_{i\to\gamma}$ at which these maximums occur are extremely small, so this is not relevant. Both sets are quite similar at high energy for all the particles. The differences occur at small energy for the gluon and for the two heavy quarks. The light quarks are quite similar at low energy. Except for the behavior of the two heaviest quark at low energy there is a tendency for R_i to be large at small z value and to be small at larger z. If the fragmentation functions of the BFG sets are used for large z and large fragmentation scale μ, the choice between BFGI or BFGII is irrelevant.

The BFG sets are implemented in the programs MCFM and JETPHOX. They were also used recently in [16] to predict the NNLO photon production at hadron colliders with a fixed-energy cone.

3.4.4 Non-isolated cross-section

Finally, let us look at the prediction of the non-isolated cross-section of the photon production at NLO with MCFM (the NNLO non-isolated cross-section can be found in [16]). Both the non-perturbative fragmentation and the perturbative production will contribute. The cross-section will be dependent on the choice of fragmentation function. The parame-

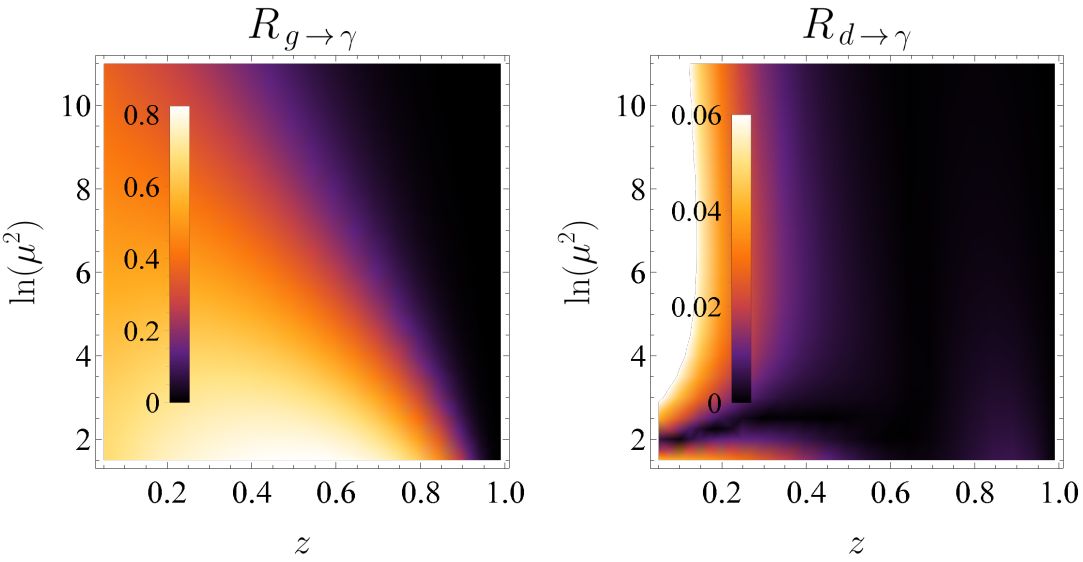

Figure 3.17: Left $R_g(z,\mu)$ and right $R_d(z,\mu)$ for the range $z \in [0.05, 0.99]$ and $\mu \in [2.11, 244.5]$ GeV. Note that the scales R_i of two plots are different.

$\sqrt{s} = 13\,\text{TeV}$	$E_T^\gamma > E_T^{\text{min}} = 125\,\text{GeV}$	$\lvert\eta_\gamma\rvert < 2.37$
NNPDF23_nlo_as_0119_qed_mc	$\alpha_s(M_Z) = 0.119$	$\alpha_{\text{EM}} = 1/132.5070$
$\mu_r = \mu_f = \mu_a$	No isolation	

Table 3.4: Parameters for the cross-section without isolation, both a fixed scale $\mu_i = 125$ GeV and a dynamic scale $\mu_i = p_T^\gamma$ were considered. The jets are unconstrained.

set	$\mu_i = 125$ GeV	$\mu_i = p_T^\gamma$
GdRG	495.51 ± 0.35	473.92 ± 0.34
BFGI	460.14 ± 0.33	437.08 ± 0.33
BFGII	461.51 ± 0.33	437.68 ± 0.32

Table 3.5: Total cross-sections σ^{NLO} [pb] for photon production without any isolation obtained with MCFM for the 3 implemented fragmentation sets. Note that $\mu_i = \mu_r = \mu_f = \mu_a$. The uncertainties are Monte Carlo uncertainties and not scale variation.

ters are given in Table 3.4 and the results for both fixed scale and dynamic scale are given in Table 3.5. The cross-sections are smaller for the dynamic scale than for the fixed-scale as α_s decreases when μ increases. The two parametrizations of the BFG set give similar results which is in agreement with the previous discussion as the fragmentation scale is large. Applying a fixed-energy cone reduces the contribution of the non-perturbative fragmentation in the cross-section and the predictions done by two different sets will be closer. We see that the prediction of the BFG sets and the one of the GdRG are quite different

Chapter 4

Isolation criteria for photons

This chapter provides an introduction on photon isolation. We discuss four types of isolations: the fixed-energy cone, the Frixione cone [57] (also called smooth cone), the hybrid cone and the discretized Frixione cone. The first prescription that had a NNLO result done for single photon production was the Frixione cone, even though it is not realizable experimentally. The hybrid cone used in [15] is a Frixione cone up to a certain radius combined with a fixed-energy cone. The goal was to have a more experimentally realistic isolation than the Frixione cone while avoiding some of the issues of the fixed-energy cone. The recent NNLO calculation for the photon production with a fixed-energy cone [16], made the hybrid cone less relevant. The discretized Frixione (or stairs) was created in order to get an approximation of the Frixone cone that could be used experimentally. It was introduced in [58]. Isolation criteria not based on cones also exist but the focus of this work is on isolation criteria based on cones. The advantages and disadvantages of each type of cone are discussed in the following.

4.1 Goal of isolation

As discussed in Chapter 3, photons have different origins at colliders: the first one being perturbative emission, the second one non-perturbative fragmentation and finally decays of neutral hadrons. In order to enhance photons from a certain origin, it is necessary to define an isolation criterion. For example, one may want to suppress the non perturbative fragmentation function as it induces uncertainties on the cross-section prediction. Moreover, we may not be interested in photons from neutral hadron decays, and therefore we want to suppress them. In Chapter 5, the photons of interest are photons emitted perturbatively and we considered the fixed-energy cone and the Frixione cone.

The choice of the isolation criteria depends on what we want to study. For example one should not use the same isolation criteria in order to determine experimentally the non-perturbative fragmentation function or in order to test perturbative QCD predictions. Photons originating from neutral hadrons can be modeled using techniques that are not photon isolation.

Common to all isolation prescriptions is that the hadronic energy is constrained inside the cone, which is centered around the considered photon. It is important to keep in mind that hadronic energy in the cone may come from a source that is unrelated to the process that produced the photon under consideration. It may originate from pile-up or underlying event. This deposit of hadronic energy in the calorimeter is approximately uniform. Because of this background, the condition for a photon to be isolated is sometimes

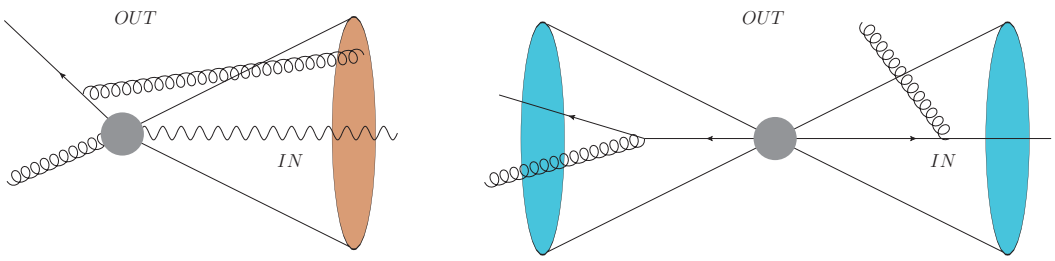

Figure 4.1: Left: photon isolation cone. Here the inside of the cone is the region where there is a restriction on the hadronic energy. Right: cone jets of Sterman and Weinberg. Here the energy is constrained outside of the cones.

loosened and a larger amount of hadronic energy is allowed in the cone [58]. In order to subtract the background, an estimation of the amount of hadronic energy produced by both pile-up and the underlying events has been done for example in [59]. One needs to keep in mind that this is a different problem than trying to exclude photons originating from the decays of hadrons like π^0 or η.

Cone isolation criteria share similarities with jet algorithms. Similar to jet algorithms, a good isolation criteria must be IR safe. The definition of jets by Stermann and Weinberg [60], shares similarities with the fixed-energy cone. The jet definition in [60] is the following: the energy outside two cones of half-angle δ is less than a fraction ϵ of the total energy. The cross section for the process $e^+e^- \to 2\,\text{jets}$ at NLO has logarithms of the parameters δ and ϵ

$$\sigma = \sigma_0 \left[1 - C_F \frac{\alpha_s}{\pi} \left(3 \ln \delta + 4 \ln \delta \ln (2\epsilon) + \frac{\pi^2}{3} - \frac{5}{2}\right)\right]. \tag{4.1}$$

In the case of a narrow cone $\delta \ll 1$, or a small isolation energy $\epsilon \ll 1$, the logarithms become large and may spoil the suppression by α_s. To improve the convergence of the perturbative expansion we count these large logarithms as order $\frac{1}{\alpha_s}$ and sum them to all orders. We call this procedure resummation.

A similar situation occurs in the case of a fixed energy cone with the difference that the energy is constrained inside the cone around the photon instead of outside. Also for photon isolation, large logarithms of the cone opening angle δ and of the fraction of allowed energy ϵ appear. The resummation of these logarithms in the case of photon isolation is performed in Chapter 5. A pictorial representation of a photon isolation cone and of the Stermann-Weinberg dijet can be seen in Figure 4.1.

4.2 Computations with different isolation cones

The cross-section of $pp \to \gamma + X$ was computed at (N)NLO in QCD for various types of isolation prescriptions [11, 12, 61, 62, 15, 16, 58]. At NLO, the publicly available codes MadGraph, MCFM[1] and JETPHOX are able to compute the cross-section for a non-isolated photon, a fixed-energy cone, a Frixione cone, an hybrid cone and the discretized Frixione cone. Theses codes do not perform any resummation, their prediction with extreme parameters may thus be unphysical. At NNLO the cross-section was computed for non-isolated photon and for the Frixione cone, fixed-energy cone and hybrid cone [61, 62, 15, 16].

[1] Details on how to run MadGraph and MCFM for photon production are given in Appendix C.

$\sqrt{s} = 13\,\text{TeV}$	$E_T^\gamma > E_T^{\text{min}} = 125\,\text{GeV}$	$\lvert\eta_\gamma\rvert < 2.37$
NNPDF23_nlo_as_0119_qed_mc	$\alpha_s(M_Z) = 0.119$	$\alpha_{\text{EM}} = 1/132.5070$
$(\mu_a =)\,\mu_r = \mu_f = 125\,\text{GeV}$	γ isolation	No jet cuts

Table 4.1: Parameters for the NLO cross-section of the fixed-energy, Frixione and hybrid cones in Figures 4.2 to 4.4, 4.6 to 4.8 and 4.10 and in Tables 4.2 and 4.3. The partons are unconstrained. The fragmentation scale μ_a is used for the fixed-cone only and a fragmentation function set has to be specified.

Narrow fixed-energy cone at NLO with a resummation of large $\ln R$ was computed in [12]. Without resummation in [11], the authors encounter unphysical cross-sections for small radii. The case of narrow Frixione cones is studied in Chapter 5.

4.3 Kinematics

First of all, it is necessary to discuss kinematics in order to determine if a particle is inside or outside a cone. The cone is centered around the photon. In the case of multiple photons (like in diphoton production), one considers a cone for each of them. At an e^+e^- collider, particles are inside the cone of a photon, if the angle between the ith particle and the photon, $\theta_{i\gamma}$

$$\theta_{i\gamma} < \alpha, \tag{4.2}$$

is smaller than the half opening angle[2] α of the cone. For hadron colliders we define the distance

$$R_{i\gamma} = \sqrt{(\eta_i - \eta_\gamma)^2 + (\phi_i - \phi_\gamma)^2}\,, \qquad \eta_i = \frac{1}{2}\log\left(\frac{|\vec{p}| + p_z}{|\vec{p}| - p_z}\right)\,, \tag{4.3}$$

with η_i the pseudo rapidity of the ith particle. The ith particle is inside the cone if

$$R_{i\gamma} < R, \tag{4.4}$$

where R is the radius of the cone.

For the cones that are discussed later on, the hadronic energy in the cone is bounded from above. For hadron colliders the transverse energy is constrained instead of the energy. There is no constraint outside of the cone.

We need to introduce some SCET notations, for a complete introduction to soft-collinear effective theory see [63]. Two light-cone vectors are introduced

$$n^\mu = (1, 0, 0, 1)\,, \qquad \bar{n}^\mu = (1, 0, 0, -1)\,, \tag{4.5}$$

where n^μ is a reference vector along the direction of the fragmenting parton. We can write the momentum p as

$$p^\mu = \bar{n}\cdot p\frac{n^\mu}{2} + n\cdot p\frac{\bar{n}^\mu}{2} + p_\perp^\mu \tag{4.6}$$

Collinear particles have the following scaling

$$(n\cdot p, \bar{n}\cdot p, p_\perp) \sim E_\gamma(R^2, 1, R)\,, \tag{4.7}$$

[2]Sometimes in the literature α is the opening angle of the cone and sometimes it is the half opening angle.

and the larger momenta is $p_- = \bar{n} \cdot p$.

For lepton colliders and for a small cone, the constraint $\theta_{i\gamma} < \alpha$, if both the parton i and the photon are approximately collinear. The condition of the ith particle being in the cone can be written as

$$p \cdot q = E_p E_q \left(1 - \cos(\theta_{i\gamma})\right) \simeq \frac{p_- q_-}{2} \frac{\left(1 - \cos(\theta_{i\gamma})\right)}{2} = \frac{p_- q_-}{2} \sin^2\left(\frac{\theta_{i\gamma}}{2}\right), \tag{4.8}$$

$$\Rightarrow \frac{2p \cdot q}{p_- q_-} = \sin^2\left(\frac{\theta_{i\gamma}}{2}\right), \tag{4.9}$$

where p and q are the momenta of the photon and of the quark respectively. The above relation is valid in the limit of a narrow cone. Analogously, the condition for the quark to be outside of the cone is

$$\theta_{i\gamma} > \alpha. \tag{4.10}$$

This translates into

$$\sin^2\left(\frac{\theta_{q\gamma}}{2}\right) - \sin^2\left(\frac{\alpha}{2}\right) = \frac{2p \cdot q}{p_- q_-} - \sin^2\left(\frac{\alpha}{2}\right) > 0. \tag{4.11}$$

$$\Rightarrow \frac{2p \cdot q}{p_- q_-} > \sin^2\left(\frac{\alpha}{2}\right) \simeq \tan^2\left(\frac{\alpha}{2}\right) = \delta^2. \tag{4.12}$$

In the case of hadron colliders, we get an extra factor. First, we parameterize the normalized momenta of the quark and of the photon ($p = p^0 n_p$)

$$\begin{aligned} n_q &= (1, \cos\phi_i \sin\theta_i, \sin\phi_i \sin\theta_i, \cos\theta_i)\ , \\ n_p &= (1, \cos\phi_\gamma \sin\theta_\gamma, \sin\phi_\gamma \sin\theta_\gamma \cos\theta_\gamma)\ , \end{aligned} \tag{4.13}$$

where θ_γ is the polar angle to the beam direction and ϕ_γ is the photon azimuthal angle. If we assume that the parton and the photon are nearly collinear to each other we can write

$$\begin{aligned} \eta_i &= \eta_\gamma + \lambda \Delta\eta\,, \\ \phi_i &= \phi_\gamma + \lambda \Delta\phi\,, \end{aligned} \tag{4.14}$$

with $\lambda \ll 1$. We perform the scalar product of both momenta and expand it for small λ

$$n_p \cdot n_q = \frac{1}{2}\left(\Delta\phi^2 + \Delta\eta^2\right) \frac{1}{\cosh {\eta_i}^2} \lambda^2 + \mathcal{O}\left(\lambda^3\right) = R_{i\gamma}^2 \frac{1}{2} \frac{1}{\cosh {\eta_i}^2} + \mathcal{O}\left(\lambda^3\right), \tag{4.15}$$

with $\Delta\phi = \phi_i - \phi_\gamma$ and $\Delta\eta = \eta_i - \eta_\gamma$. On the other hand we have

$$n_p \cdot n_q = (1 - \cos\theta_{i\gamma}) = 2\sin^2\left(\frac{\theta_{i\gamma}}{2}\right) \simeq \frac{\theta_{i\gamma}^2}{2}. \tag{4.16}$$

Therefore $R_{i\gamma} < R$ implies

$$\theta_{i\gamma} < \frac{R}{\cosh\eta_i}, \tag{4.17}$$

The same relation can be found in [64].

At the partonic level, photon isolation starts to have an effect only at NLO. For example in the process $qg \to q\gamma$, the outgoing quark is outside the cone, because the quark and the photon are back to back in the center of mass frame. However at NLO one parton may be inside of the cone.

As a side remark, let us point out that the isolation implemented at the parton level is not the same as at the hadronic level. Imagine a quark close to the side of the isolation cone. At the parton level it is outside the cone. After hadronization, part of its energy may actually be in the cone. The opposite may also happen, if a quark is inside of the cone (but not in the middle), after hadronization part of its energy may be outside of the cone.

4.4 Fixed energy cone

Fixed energy cones are the simplest type of isolation criteria. The total hadronic energy in a cone of radius R around the photon E_{had} is constrained by an upper bound E_{iso}. This value may depend on the energy of the photon,

$$E_{\text{had}} < E_{\text{iso}} = \epsilon_\gamma E_\gamma + E_{\text{threshold}} \qquad \text{for } r \leq R \tag{4.18}$$

with typically $E_{\text{iso}} \ll E_\gamma$. In the literature, one of the two parameters ϵ_γ and $E_{\text{threshold}}$ is sometimes set to 0. It is possible to implement fixed-energy cones experimentally. The choice of the radius R is limited by the resolution of the calorimeters. The main downside is that photons originating from non-perturbative fragmentation are still present in the fixed-energy cone. However this contribution is partially suppressed compared to a non-isolated photon [65], in particular it is still present for large z, the fraction of the energy taken by the photon from the fragmenting parton i, $E_\gamma = zE_i$. For $E_{\text{threshold}} = 0$, the fragmentation contribution is not suppressed for $z > (1+\epsilon_\gamma)^{-1}$. This comes from the fact that after the fragmentation into a γ the left-over hadronic energy is

$$E_{\text{had}} = \frac{1-z}{z} E_\gamma < E_{\text{iso}} = \epsilon_\gamma E_\gamma. \tag{4.19}$$

The smaller the isolation energy is, the smaller is the contribution from $\mathcal{D}_{i\to\gamma}$. The partial suppression of the non-perturbative fragmentation implies that the fixed-energy cone is not suitable to measure these functions [51]. While performing a fixed order computation, the uncertainty on the non-perturbative fragmentation contributes to the uncertainties of the prediction, at NLO and at NNLO in [16, 45]. Fixed-energy cones suppress photons originating from decays of neutral hadrons [35].

In order to be physical, it is necessary for the cross section to satisfy the following condition [66]

$$\begin{aligned} \sigma(R, E_{\text{iso}})\big|_{R=\text{constant}} &\searrow \text{ if } E_{\text{iso}} \searrow, \\ \sigma(R, E_{\text{iso}})\big|_{E_{\text{iso}}=\text{constant}} &\nearrow \text{ if } R \searrow . \end{aligned} \tag{4.20}$$

When the radius R is kept constant, the cross-section has to decrease for decreasing E_{iso}. When E_{iso} is kept constant, the cross-section has to increase for decreasing radius R. The stricter the isolation is, the smaller the cross-section is. And of course, the cross section without isolation is larger than the one with isolation. If the radius R is small for a fixed order computation, large $\ln R$ appear and need to be resummed. In [11], the differential cross-section with a cone of $R = 0.1$ and $\epsilon_\gamma = \frac{2}{15}$ was larger than the non-isolated cross-section. This is unphysical. This issue was addressed in [12] and the leading logarithms of the radii were resummed, however the case of a narrow cone with a small ϵ_γ was not addressed.

In Figures 4.2 to 4.4, the dependence of the NLO cross-section on its parameters R and ϵ_γ are shown for the three sets implemented in MCFM. The non-isolated cross-section is also shown (red line). For both the ϵ_γ and the R dependencies, BFGI and BFGII are very similar, in contrast the behavior of the GdRG fragmentation is qualitatively different at small ϵ_γ.

The R dependence of the three sets is well behaved for the considered values of ϵ_γ, the isolated cross-sections are always smaller than the isolated cross-section. The second relation of (4.20) is also respected. Moreover, the cross-section increases linearly in $\ln 1/R$. The slope is larger for smaller ϵ_γ. This is not surprising, as when a cone gets smaller the portion of phase space constrained gets smaller, the increase of the cross-section coming from decreasing the size of the cone is larger if ϵ_γ was small as the isolation was stricter.

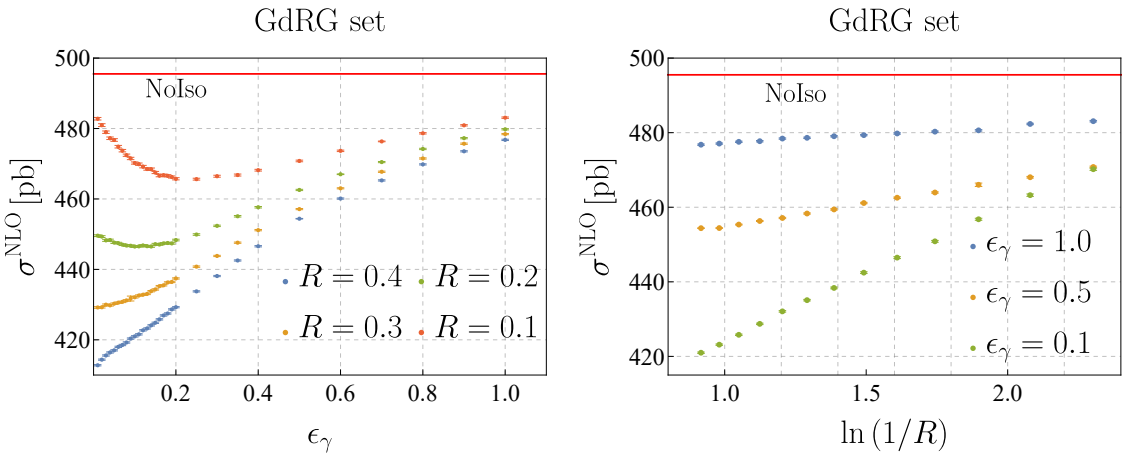

Figure 4.2: Fixed-energy cone NLO cross-section for the GdRG obtained with MCFM. Left: ϵ_γ dependence. Right: R dependence

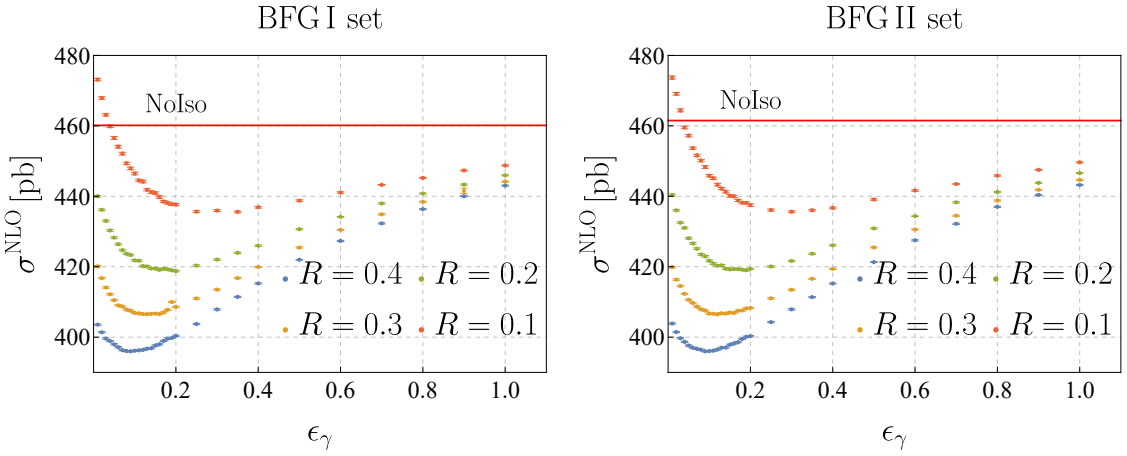

Figure 4.3: Fixed-energy cone NLO cross-section as a function of ϵ_γ for the BFG sets obtained with MCFM.

The dependence on ϵ_γ is more interesting. In the case of the GdRG set, we see that for $R = 0.3, 0.4$, the cross-section decreases with decreasing ϵ_γ. For $R = 0.2, 0.1$, when ϵ_γ is small, it is not the case and (4.20) is violated. For the BFG sets, the cross-section first decreases with ϵ_γ decreasing and when ϵ_γ is small the tendency is reversed. The approximate value of ϵ_γ when the behavior changes depends on the value of the radius R. The smaller R is the earlier it happens. In the case of $R = 0.1$ the isolated cross-section for $\epsilon_\gamma = 0.03, 0.02, 0.01$ is larger than the non-isolated cross-section, as seen in Figure 4.3.

Finally, some values of the cross-section for $R = 0.2, 0.4$ are shown in Tables 4.2 and 4.3, in order to see the dependence on the choice of fragmentation function. In particular the ratio between the GdRG and the BFGI sets is shown. For large ϵ_γ, we see that the isolation is only slightly decreasing the dependence on the choice of set. For $\epsilon_\gamma = 0.05$, the ratio between the cross-sections of GdRG and BFGI are smaller, the reduction of the dependence on the choice of fragmentation function is slightly larger for a smaller radius R. These results need to be considered with caution as the first equation of (4.20) is not satisfied. In Chapter 5, we will perform the resummation of the log of R and ϵ_γ.

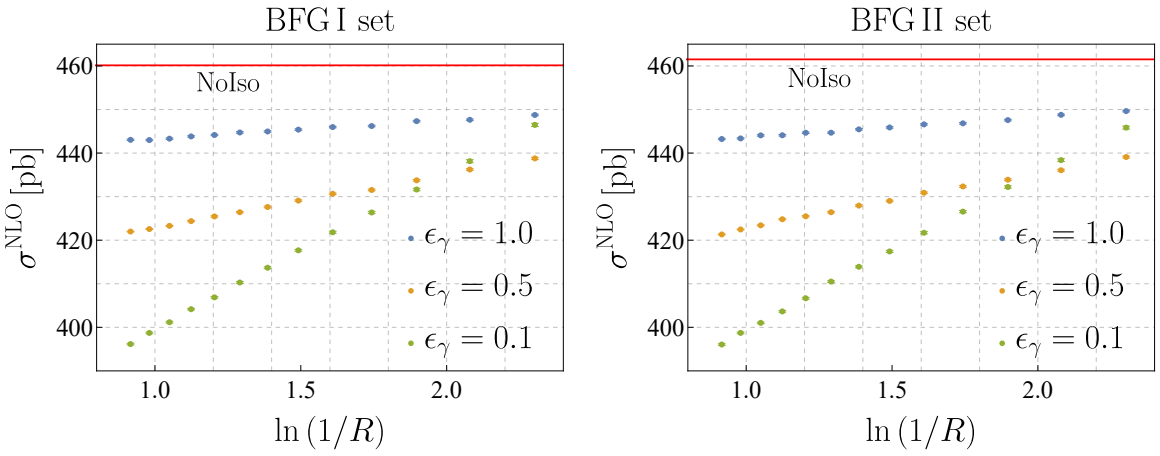

Figure 4.4: Fixed-energy cone NLO cross-section as a function of R for the BFG sets obtained with MCFM.

ϵ_γ	σ^{GdRG}	σ^{BFGI}	σ^{BFGII}	GdRG/BFGI
no Iso	495.51 ± 0.35	460.14 ± 0.33	461.51 ± 0.33	1.077
1.0	476.77 ± 0.18	443.04 ± 0.16	443.23 ± 0.16	1.076
0.5	454.39 ± 0.08	421.99 ± 0.16	421.32 ± 0.87	1.077
0.2	429.26 ± 0.17	400.36 ± 0.09	400.28 ± 0.18	1.072
0.05	417.02 ± 0.18	397.96 ± 0.19	397.63 ± 0.19	1.048

Table 4.2: Total cross-sections σ^{NLO} [pb] for photon production with a fix-energy cone with $R = 0.4$ obtained with MCFM for the three implemented fragmentation sets with parameters of Table 4.1. Uncertainties are from numerical integration of MCFM.

ϵ_γ	σ^{GdRG}	σ^{BFGI}	σ^{BFGII}	GdRG/BFGI
no Iso	495.51 ± 0.35	460.14 ± 0.33	461.51 ± 0.33	1.077
1.0	479.78 ± 0.18	445.97 ± 0.17	446.585 ± 0.17	1.076
0.5	462.56 ± 0.18	430.65 ± 0.18	430.89 ± 0.18	1.074
0.2	448.33 ± 0.23	418.77 ± 0.21	419.34 ± 0.21	1.071
0.05	447.61 ± 0.25	428.26 ± 0.27	428.09 ± 0.26	1.045

Table 4.3: Total cross-sections σ^{NLO} [pb] for photon production with a fix-energy cone with $R = 0.2$ obtained with MCFM for the three implemented fragmentation sets with parameters of Table 4.1.

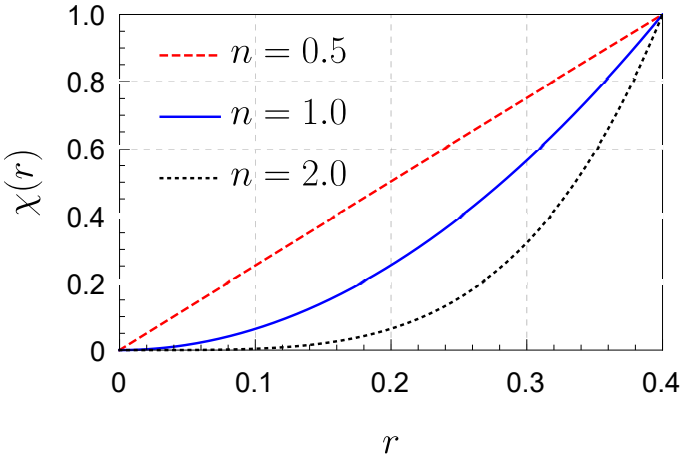

Figure 4.5: Frixione isolation with $R = 0.4$, $\epsilon_\gamma = 1.0$ for three different values of n.

4.5 Frixione cone and smooth cone

In [57], Frixione introduced a new type of photon isolation, which is called smooth cone or Frixione cone isolation. The idea is to constrain the hadronic energy $E_{\text{had}}(r)$ inside all the possible cones of different radii $r \leq R$, by a function $f(r)$

$$E_{\text{had}}(r) \leq E_{\text{iso}}(r) = f(r) \qquad r \leq R\,. \tag{4.21}$$

A photon is said to be isolated if the relation holds for every r. In other words, the isolation energy $E_{\text{iso}}(r)$ is now a function of the distance from the photon in the cone of radius R. In the case of fixed energy cones the function was independent of r. In order to suppress the collinear effects, the isolation energy needs to vanish when $r \to 0$. The typical parameterization is

$$E_{\text{had}}(r) \leq E_{\text{iso}}(r) = E_\gamma \epsilon_\gamma \left(\frac{1-\cos r}{1-\cos R}\right)^n = E_\gamma \chi(r;\epsilon_\gamma, n, R) \qquad r \leq R\,,\ \ n \in \mathbb{R}^+\,. \tag{4.22}$$

Equation (4.22) tells us that, the closer the hadrons are to the photon, the less of their energy is allowed. In the collinear limit $r \to 0$, $E_{\text{iso}} = 0$ and no hadronic energy is allowed. Figure 4.5 shows three different profiles of χ. The parameter n must be positive, otherwise the isolation energy would diverge for small r.

This isolation suppresses both contributions of the photons from hadronic decays and the ones from non-perturbative fragmentation, as long as the pair of parameters (n, ϵ_γ) is suitable. For example it has been shown in [58], that $(n, \epsilon_\gamma) = (0.2, 1)$ is not a suitable choice to suppress the fragmentation function. The fact that particle detectors have a finite resolution makes it impossible to measure $E_{\text{iso}}(r)$ and thus also the use of the Frixione isolation cone. However, a discretized version of the Frixione cone exists and is discussed in Section 4.7. A summary of the differences between fixed cone and Frixione cone isolation can be found in Table 4.4.

Figures 4.6, 4.7 and 4.8 show the NLO cross-section for various isolation parameters, obtained with MCFM. It would be possible to get the same data with the help of MadGraph. A few tendencies can be seen. First, the cross-section increases with increasing ϵ_γ while it decreases with decreasing n and R. The dependence of σ^{NLO} on ϵ_γ looks logarithmic. As discussed in Chapter 5, this is not the case. The cross-section depends linearly on $1/n$ and on $\ln(1/R)$. It is important to note that these plots show only the perturbative

	Fixed Energy	Frixione
γ from hadronic decays suppressed	✓	✓
non-perturbative $\mathcal{D}_{i\to\gamma}$ suppressed	✗	✓
NNLO computations available	✓	✓
Experimentally realizable	✓	✗
$E_{\text{had}} < E_{\text{iso}} =$	$\epsilon_\gamma E_\gamma + E_{\text{threshold}}$	$\epsilon_\gamma E_\gamma \left(\frac{1-\cos r}{1-\cos R}\right)$

Table 4.4: Summary of the two main types of isolation cones used in this work.

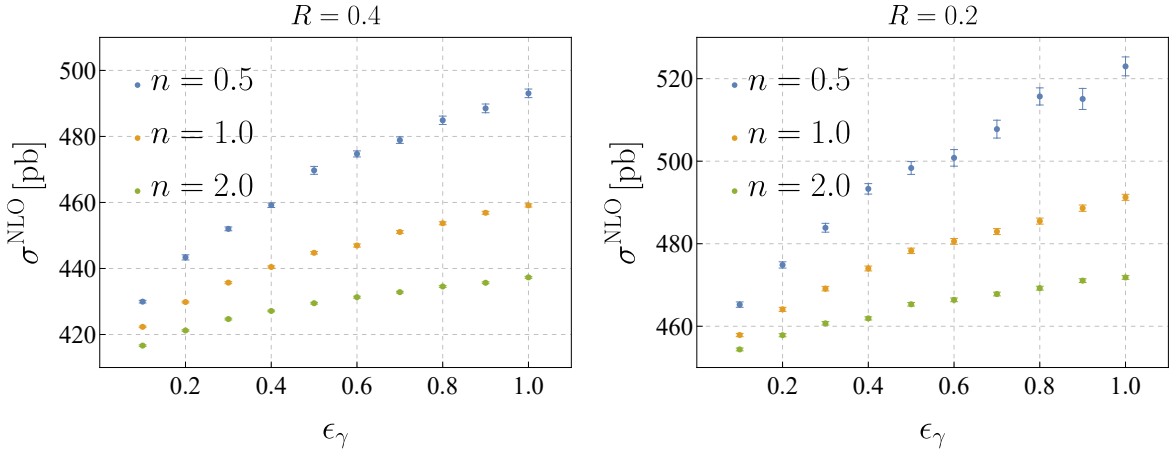

Figure 4.6: ϵ_γ dependence of the NLO cross-section obtained from MCFM for Frixione isolation with different n and R values.

part of the cross-section. The non-perturbative emission is suppressed, and MCFM does not include it while computing the cross-section. A study of how the Frixione parameters influence the non-perturbative part of the cross section has been carried out in [58], with the help of the program JETPHOX. The authors found that, for suitable parameters of the Frixione cone, the non-perturbative fragmentation functions are suppressed. In particular, the choice $n = 0.2$ is problematic and did not suppress the non-perturbative contribution, whereas choices of $n \geq 0.5$ suppressed it.

Similarly to the fixed-energy cone, there are some requirements on the dependence of the cross-section on its parameters [66]

$$\begin{aligned} &\sigma(R,n,\epsilon_\gamma)\big|_{(R,n)=\text{constant}} \searrow \text{ if } \epsilon_\gamma \searrow, \\ &\sigma(R,n,\epsilon_\gamma)\big|_{(n,\epsilon_\gamma)=\text{constant}} \nearrow \text{ if } R \searrow, \\ &\sigma(R,n,\epsilon_\gamma)\big|_{(R,\epsilon_\gamma)=\text{constant}} \searrow \text{ if } n \nearrow . \end{aligned} \tag{4.23}$$

Additionally, comparing a Frixione cone to a fixed-energy cone with $E_{\text{threshold}} = 0$ of the same radius R and ϵ_γ, we find

$$\sigma_{\text{Frixione}}(R,n,\epsilon_\gamma) < \sigma_{\text{Fixed-energy}}(R,\epsilon_\gamma) \quad \forall n\,. \tag{4.24}$$

This relation is due to the fact that the Frixione cone is more restrictive than the fixed-energy cone (if R and ϵ_γ are the same). In order to test (4.24), it could be advantageous to include the suppressed fragmentation contribution also in the case of the Frixione cone cross-section. Unfortunatly MadGraph and MCFM are not designed for such an implementation. Some NLO differential cross sections with the non-perturbative contribution

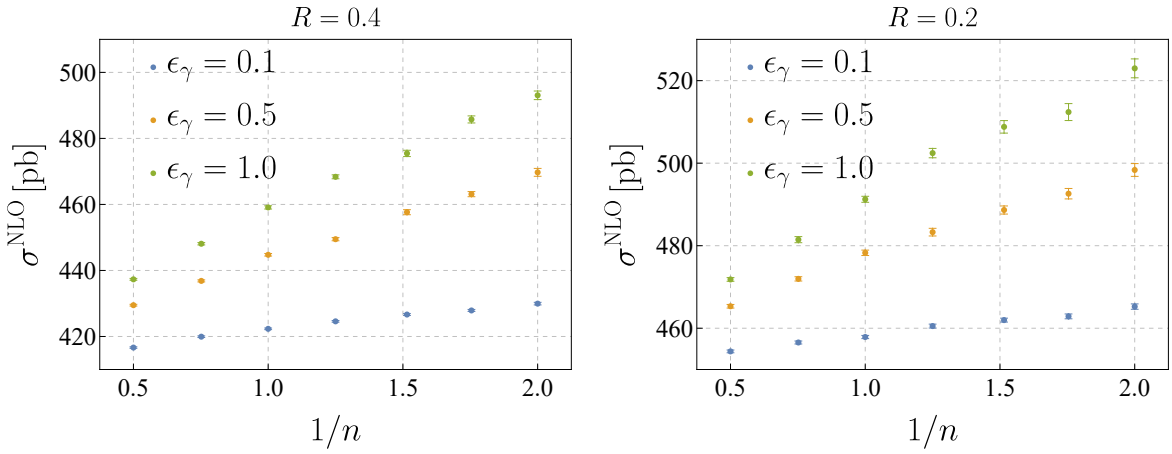

Figure 4.7: n dependence of the NLO cross-section obtained from MCFM for Frixione isolation with different ϵ_γ and R values.

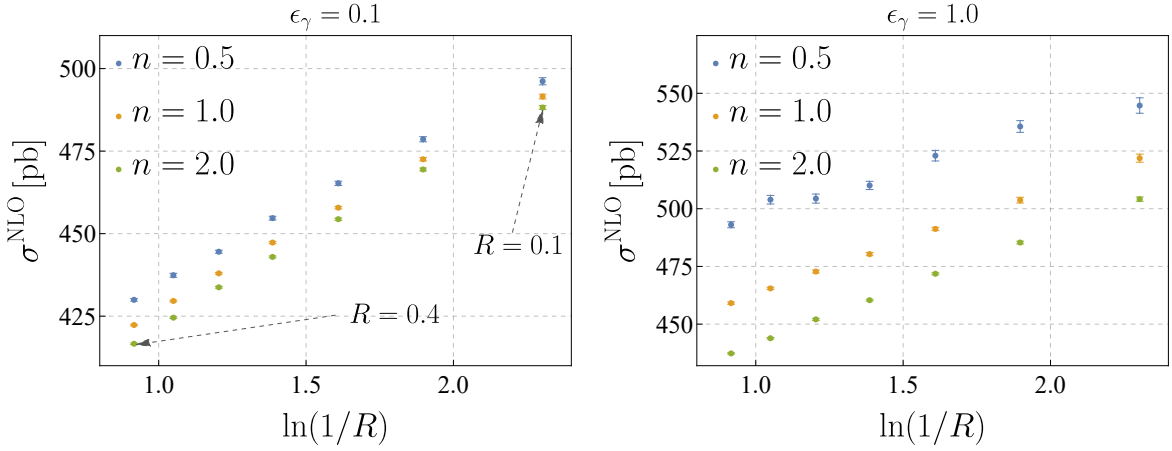

Figure 4.8: R dependence of the NLO cross-section obtained from MCFM for Frixione isolation with different n and ϵ_γ values.

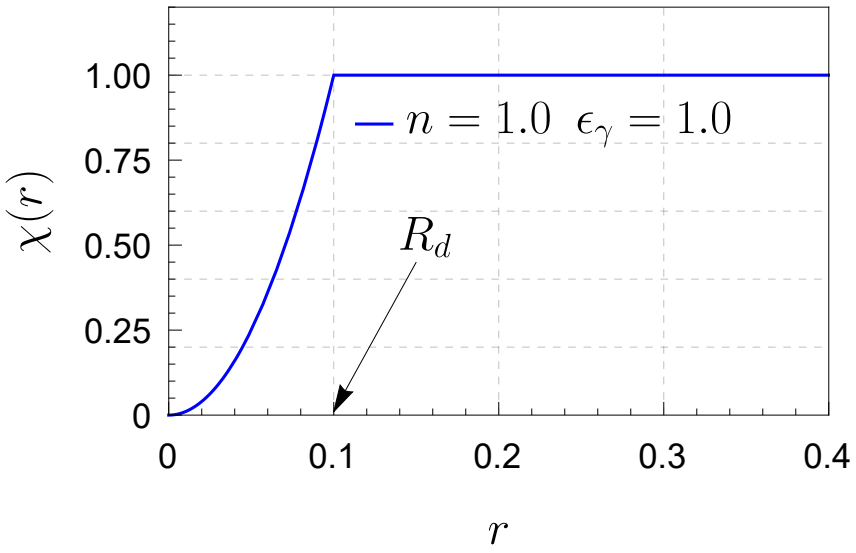

Figure 4.9: Hybrid cone isolation χ for an outside radius of $R = 0.4$ and the inside one of $R_d = 0.1$.

were computed in [58], with the help of JETPHOX. The relation (4.24) was found to be violated in the case of diphoton production for $n = 0.1$ for certain kinematic parameters in [66]. However it was still satisfied e.g. for $n = 0.5$ or $n = 1.0$. In addition, the dependance of the cross-section on the parameter n is larger at small n. Therefore in Chapter 5, we always use $n \geq 0.5$.

4.6 Hybrid cone

The idea of the hybrid cone is to combine a Frixione cone and a fixed energy cone together. NNLO predictions were computed in [15] and a detailed explanation of the hybrid cone can be found in [67]. The goal was to have predictions closer to the experimental isolations and to avoid the non-perturbative fragmentation functions. An hybrid cone has the following isolation energy

$$E_{iso}(r) = E_\gamma \chi(r; \epsilon_\gamma, n, R, R_d) = E_\gamma \epsilon_\gamma \begin{cases} \left(\dfrac{1-\cos r}{1-\cos R_d}\right)^n & 0 \leq r < R_d \\ 1 & R_d < r < R \end{cases} . \tag{4.25}$$

where R_d is the radius of the inner cone. The isolation for r between 0 to R_d is a Frixione cone and from R_d to R a fixed-energy cone. An example of isolation is shown in Figure 4.9. Because the inside cone is a Frixione cone and $E_{iso}(r = 0) \to 0$, the non-perturbative fragmentation is suppressed. The photons originating from decays of neutral hadrons are also suppressed. The first disadvantage of the hybrid cone is that a new parameter is introduced R_d and the cross-section will depend on it [15]. Like the Frixione cone, it is not possible to implement it experimentally. If the inner radius R_d is taken too small, large logarithms also appear and need to be resummed.

In Figure 4.10, the NLO cross-section as a function of the inner radius R_d is shown with the parameters of Table 4.1. The smaller the inner radius R_d is, the larger the cross-section becomes. The logarithms of the inner radius should be resummed. Interestingly, the effect of large logs is smaller when ϵ_γ is small. Unlike the Frixione cone the dependence on

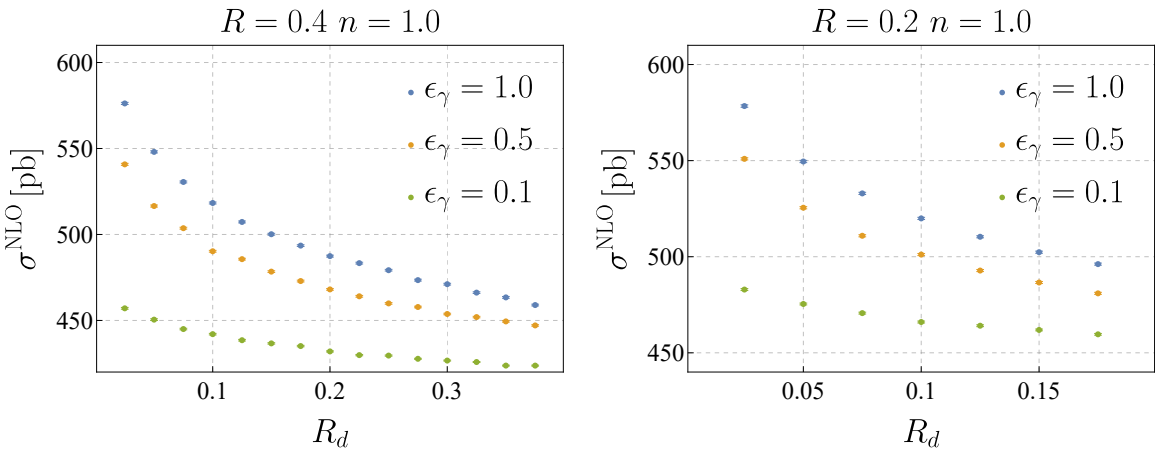

Figure 4.10: NLO cross-section for the hybrid cone as a function of R_d, the data were computed with MCFM 10.2.1. The numerical uncertainties are smaller than the dots. The largest cross-section is obtained for $(R_d = 0.025, R = 0.2, \epsilon_\gamma = 1.0, n = 1.0)$ with $578.4 \pm 0.6\,\mathrm{pb}$.

$E_{\mathrm{iso}}(r) = E_\gamma \chi(r)$	$\gamma\gamma$ in [69]	γ in [58]
$R_i =$	0.1,0.2,0.3,0.4	0.1,0.16,0.22,0.28,0.34,0.4
$\chi(r) \quad r \in [R_{i-1}, R_i]$	$\epsilon_\gamma \left(\frac{1-\cos\left(\frac{1}{2}(R_{i-1}+R_i)\right)}{1-\cos R} \right)^n$	$\epsilon_\gamma \left(\frac{1-\cos R_i}{1-\cos R} \right)^n$

Table 4.5: Summary of the stairs isolations formula of [58] and [69], note that $R_0 = 0.0$.

R_d is only approximately logarithmic. For relatively large R_d the cross-section has values comparable to ones from the Frixione cone isolation.

4.7 Stairs approximation of Frixione cone isolation

Experimentally it is not possible to use the Frixione cone isolation due to the finiteness of the resolution of the detector. However it is possible to implement a discretized version and this was done in the study of the production of isolated photon [58] and diphoton [68, 69]. The idea is the hadronic energy inside the cone of radius R is constrained as

$$E_{\mathrm{had}}(r) \leq E_{\mathrm{iso}}(r) = E_\gamma \chi(r) \qquad r \leq R, \tag{4.26}$$

where $\chi(r)$ is a step function built in order to approximate the Frixione cone; it is made out of a few nested fixed energy cones with different isolation energies. In the innermost cone, the isolation energy is small so that it suppresses the non-perturbative fragmentation function. Different parameterizations of the stairs isolation exist and two examples can be seen in Figure 4.11 with their associated formulas for the radii and the function χ are summarized in Table 4.5. The choice of the intervals of order 0.1 is due to the resolution of the calorimeters.

In the case of only one isolated photon, the comparison between the Frixione cone and its discretized version was done in [58] with six concentric cones. A modified version of the program JETPHOX[3] to compute the cross section with both the direct and the non-perturbative contribution at NLO was used. One of their results is shown in Figure 4.12:

[3] It is probably possible to modify MCFM to implement the discretized isolation.

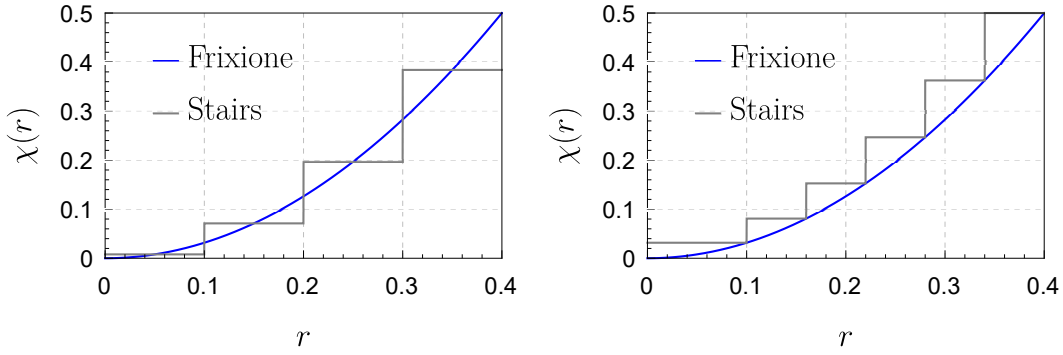

Figure 4.11: The stair isolation compared to Frixione with $R = 0.4$, $\epsilon_\gamma = 0.5$ and $n = 1.0$. Left: Isolation of [69] for diphoton production The Frixione χ cuts every stair in the middle. Right: Isolation of [58] for single photon production, the Frixione χ cuts every step at its right end. The formulas of both isolation can be seen in Table 4.5.

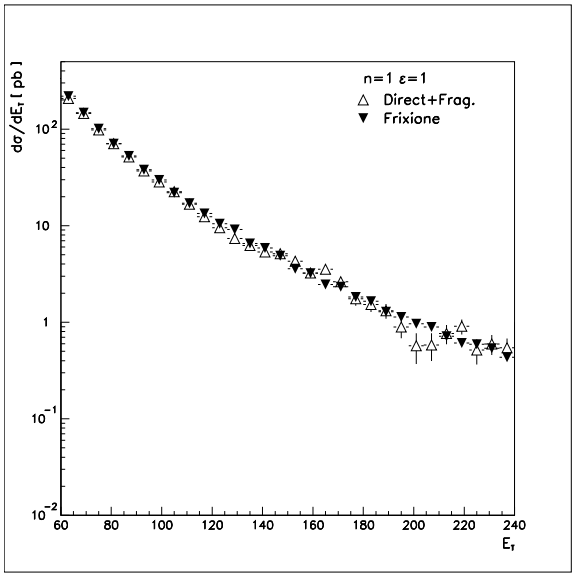

Figure 4.12: Fixed-order NLO differential cross-section with respect to the photon transverse energy E_T^γ done with JETPHOX. The cone parameters are $R = 0.4, n = 1, \epsilon_\gamma = 1.0$. The solid triangles are the Frixione isolation and the open ones with the stairs approximation. Both isolation include the contribution of the non-perturbative fragmentation. Figure taken from [58]. The fragmentation functions set (probably BFG I or II) was not specified.

the agreement between the two cones is good, except at high E_T^γ, probably due to lower statistics in the Monte Carlo.

In [69], diphoton was studied with both a Frixione cone with parameters $n = 1, R = 0.4, \epsilon_\gamma = 0.5$ and the stairs of the left of Figure 4.11. Beyond using the isolation energy approximate Frixione $\epsilon_\gamma^i E_\gamma$, they also introduce a minimum energy $E_i^{\min}$ for each step. The isolation energy at one step was taken to be the maximum of these two values. The list of $E_i^{\min}$ can be seen in Table 4.6. They compared the cross-section obtained with the help of the Frixone cone and of this staircase isolation and they observed a good agreement of the two isolation at high energy. For the smaller values of the transverse mass of the diphoton,

$r < R_i$	ϵ_γ^i	E_i^{minmum}
0.1	0.01	5 GeV
0.2	0.07	10 GeV
0.3	0.20	23 GeV
0.4	0.38	40 GeV

Table 4.6: Value of ϵ_γ^i and E_i^{minimum} for the four nested cones used in [69].

the difference was of the order of magnitude of a few percent.

At high energy the stairs result approximates well the Frixione cone. However, this isolation introduces extra parameters in the isolation and in this case the innermost cone is small, so that it is likely that large logarithms appear.

4.8 Isolation used experimentally

Experimentally fixed-energy cones with some extra cuts are used. For example at ATLAS [9], they required $E_\gamma^T > 125\,\text{GeV}$ with the isolation

- Region $\Delta\eta \times \Delta\phi = 0.125 \times 0.175$ around the photon with $E_{\text{iso}}^T = 0$
- Fixed energy cone of $R = 0.4$ with $E_{\text{iso}}^T = 4.2 \cdot 10^{-3} E_\gamma^T + 4.8\,\text{GeV}$.

The pseudo rapidity of the photon is

$$|\eta^\gamma| \in [0.0, 1.37] \quad \text{and} \quad |\eta^\gamma| \in [1.56, 2.37] \tag{4.27}$$

A cut in η^γ between 1.37 and 1.56 is due to the geometry of the detector.
One example of the isolation used at CDF was [70]:

- Fixed energy cone of $R = 0.4$ with $E_{\text{iso}}^T = 2\,\text{GeV}$.

In addition the photon was required to have $E_\gamma^T > 30\,\text{GeV}$ and $|\eta^\gamma| < 1.0$

Chapter 5

QCD anatomy of photon isolation

This chapter is a copy of a preprint version of [71] published in Journal of High Energy Physics (JHEP01(2023)005).

Abstract

To separate the energetic photons produced in hard scattering processes from those from other sources, measurements impose isolation requirements which restrict the hadronic radiation inside a cone around the photon. In this paper, we perform a detailed factorization analysis of the QCD effects associated with photon isolation. We show that for small cone radius R, photon isolation effects can be captured by a fragmentation function describing the decay of a parton into a photon accompanied by hadronic radiation. We compute this fragmentation function for different isolation criteria and solve the associated renormalization group equations to resum logarithms of R. For small isolation energy, the cone fragmentation function factorizes further, into collinear functions describing energetic quarks and gluons near the cone boundary and functions encoding their soft radiation emitted into the cone. Based on this factorization we also resum the non-global logarithms of the ratio of the photon energy and the isolation energy, so that we control all logarithmically enhanced terms in the cross section. In this limit, we provide a simple formula to convert NNLO cross section results from smooth-cone isolation to fixed-cone isolation.

5.1 Introduction

An important category of physics probes at high-energy colliders are processes with electroweak bosons in the final state. Among these, photons present special challenges: since they are massless, they are abundant and are produced not only during the hard interaction, but can also arise as secondary emissions during jet fragmentation, hadronization and hadron decay. The fragmentation process involves non-perturbative physics encoded in photon fragmentation functions, originating from partons becoming collinear to the photon.

To reduce the contribution from secondary emissions, experiments impose isolation requirements. To isolate a hard photon they put a cone of angular size R around it and restrict the hadronic energy inside the cone to be lower than a certain cutoff E_0. How this cutoff is imposed depends on the isolation criterion. The simplest way is to impose a constraint on the total hadronic energy $E_{\rm tot}(R)$ inside the cone. At an e^+e^- collider one requires

$$\text{fixed-cone isolation:} \quad E_{\rm tot}^{\rm cone}(R) < E_0 = \epsilon_\gamma E_\gamma \tag{5.1}$$

and the quantity R corresponds to the opening half-angle of the cone, i.e. a particle is inside the cone if $\theta < R$, where θ is the angle between the particle and the photon. At hadron colliders, one instead imposes the constraint on the total transverse energy E_T inside the cone and defines $E_0 = \epsilon_\gamma E_T^\gamma$.[1] In the following, we will use the term energy to refer to either the conventional or the transverse energy, depending on the collider under consideration. At a hadron collider a particle is inside the cone if $r < R$ with $r = \sqrt{(\Delta\eta)^2 + (\Delta\phi)^2}$. Here, $\Delta\eta$ and $\Delta\phi$ are the pseudorapidity and azimuthal angle differences between the photon and the particle. Fixed-cone isolation is used in all experimental measurements by ATLAS [72, 9, 10] and CMS [73, 74, 75], but with this isolation criterion the cross section computations need to include the non-perturbative photon fragmentation functions to be collinear finite. The photon fragmentation functions are poorly known and the presence of final-state collinear divergences complicates the perturbative calculations.

Frixione [57] has introduced an alternative isolation criterion designed to eliminate radiation collinear to the photon. Rather than restricting the radiation inside a fixed cone of radius R, it imposes

$$\text{smooth-cone isolation:} \quad E_{\text{tot}}^{\text{cone}}(r) < E_0(r) = \epsilon_\gamma E_\gamma \left(\frac{1-\cos r}{1-\cos R}\right)^n \tag{5.2}$$

for all $r < R$ where the parameter n must be chosen to be $n \geq \frac{1}{2}$. As is obvious from this definition, the isolation becomes stricter as particles get more collinear to the photon and together with collinear radiation, the smooth-cone isolation also eliminates the non-perturbative fragmentation function. Having infrared finite cross sections without the need to subtract collinear final state singularities is a significant technical simplification and in the past all next-to-next-to-leading order (NNLO) computations of photon production were carried out imposing smooth-cone isolation. Such computations are by now available not only for inclusive-photon [61, 15], photon-plus-jet [62, 15] di-photon [76, 77, 66, 78, 79, 80] and even tri-photon production [81, 82]. However, the finite granularity of the detectors makes it impossible to directly implement the criterion (5.2) experimentally. While a discretized version was studied for the LHC [58] and, following earlier work on democratic clustering [51], new isolation criteria based on jet substructure [83] were proposed, all LHC measurements currently impose fixed-cone isolation.

To compare to the experimental results, the above theoretical papers choose parameters n and ϵ_γ of the smooth-cone isolation to mimic the fixed-cone isolation applied in the measurement. In the literature, a variety of parameter choices is found, typically motivated by next-to-leading order (NLO) computations, which are available both with fixed cone and smooth-cone isolation [11]. Given that the two isolation criteria are qualitatively different, the situation is unsatisfactory, especially since the experimental measurements now reach few per-cent accuracy. The paper [78] has shown that photon isolation is a substantial source of uncertainty in precision calculations and has advocated the use of a hybrid isolation scheme, in which a small smooth cone is placed into the center of a fixed cone, to mitigate this problem [84, 78]. Very recently the antenna subtraction method [85, 86, 87] has been extended to final state singularities [88] and by now the first NNLO fixed-cone result is available [16], eliminating the mismatch between the prediction and the experimental measurements.

By construction, the isolation requirement introduces low scales into the cross section, which leads to logarithmically enhanced higher-order terms which can spoil perturbative

[1] The transverse energy of a particle is defined as $E_T = E \sin\theta_b$, where θ_b is its angle with respect to the beam axis.

predictions. The paper [11] has computed the photon cross section at NLO and has shown that for small radius the prediction for the isolated cross section becomes larger than the inclusive cross section, clearly indicating a breakdown of fixed-order perturbation theory. The leading $\ln(R)$ terms were then resummed in [12] curing this pathology. The resummation can be obtained by evolving the fragmentation contribution from the hard scale $\mu_h \sim E_\gamma$ to the scale $\mu_j \sim R\,E_\gamma$ associated with the invariant mass of the radiation in and around the cone. In our paper we perform a detailed factorization analysis of the QCD effects arising due to photon isolation in the framework of Soft-Collinear Effective Theory (SCET) [89, 90, 91]. In addition to the logarithms of the isolation-cone radius R, we will also resum logarithms of $\epsilon_\gamma = E_0/E_\gamma$. These involve the scale $\mu_0 \sim R\,E_0$, which is typically quite low for experimentally imposed isolation criteria.

The factorization of the photon cross section involves two steps. First, we show that for small isolation cone size R, the isolation effects can be captured by an isolation fragmentation function, i.e. a fragmentation function which describes the fragmentation of a parton into a photon plus the accompanying collinear radiation constrained by the isolation criterion. The fragmentation function factorization makes it easy to study the effect of different isolation criteria and the dependence on isolation parameters. It also makes it possible to convert results obtained in one isolation scheme to another, since the cross section difference is driven by the difference in the associated fragmentation functions. Generalized fragmentation functions similar to the one we introduce have been used in a variety of other contexts starting with [92], who considered hadron fragmentation inside a jet. The fragmentation function approach can be used to resum logarithms of the isolation-cone radius R by solving evolution equations to evolve from the hard scale $\mu_h \sim E_\gamma$ down to the typical scale of the fragmentation function $\mu_j \sim E_\gamma R$. The same technique has been used earlier for inclusive jet production, where one can consider fragmentation into a jet to resum logarithms of R, as was done in SCET in [93, 64, 94], following analogous computations in QCD factorization [95, 96]. The resummation of $\ln(R)$ terms has also been studied for exclusive jet production [97, 98, 99] and inclusive jet production near threshold [100, 101], where the R dependence is captured by jet functions instead of fragmentation functions.

In addition to the collinear scale $\mu_j \sim E_\gamma R$, the fragmentation function involves the scale $\mu_0 \sim E_0 R$ associated with radiation inside the isolation cone. We will show that in the limit of small E_0, the cone fragmentation function itself factorizes. This second factorization step then allows us to also resum the logarithms of ϵ_γ, as shown in [13]. The isolation cone is obviously a non-global observable [102] and we use the RG approach of [98, 99] implemented in the code NGLresum [14] to resum them. In this way we control all large logarithms associated with photon isolation.

Our paper is organized as follows. We first present factorization a theorem for photon production with a small isolation cone in Section 5.2. The leading-order fragmentation functions which encode the isolation are computed in Section 5.3. Using these, we can study the differences among isolation criteria and their parameter dependence. We can also resum contributions enhanced by logarithms of the cone radius R by solving the Dokshitzer-Gribov-Lipatov-Altarelli-Parisi (DGLAP) evolution equation for the fragmentation functions as explained in Section 5.4. We then discuss the factorization of the fragmentation function in the limit of small isolation energy in Section 5.5. The leading jet function arising in this factorization theorem is computed in Section 5.6, together with the function describing the soft radiation into the cone. These results are then used to derive a formula to convert smooth-cone cross section results to fixed-cone isolation in the limit of small ϵ_γ. In Section 5.7 we then perform the resummation of logarithms of ϵ_γ. We

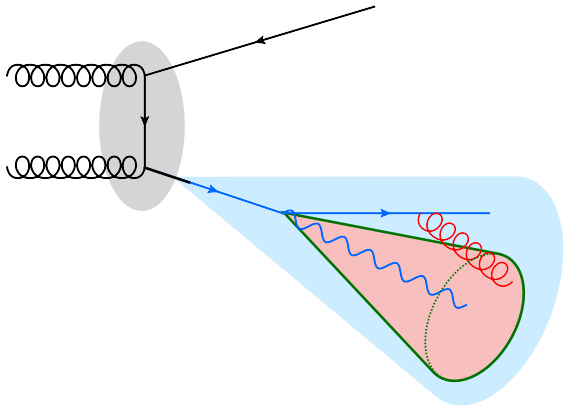

Figure 5.1: Pictorial representation of the factorization theorems (5.3) and (5.49). The gray blob represents the hard function, which describes the production of an energetic parton, which then fragments into a photon plus additional radiation (blue region), as encoded by the cone fragmentation function $\mathcal{F}_{i\to\gamma}$ in (5.3). For small isolation energy, this function factorizes further. The energetic partons (blue lines) produced in the fragmentation are part of the jet function $\boldsymbol{\mathcal{J}}_{i\to\gamma+l}$ and must lie outside the isolation cone. These partons can then radiate soft partons (red) into the isolation cone (green). This radiation is encoded in the functions $\boldsymbol{\mathcal{U}}_l$, which depend on the directions and color charges of the energetic partons.

summarize our results and conclude in Section 5.8.

5.2 Factorization for isolated photon production at small cone radius R

For small isolation cone radius R a factorization theorem for isolated photon production was presented in [13]. It reads

$$\frac{\mathrm{d}\sigma(E_0,R)}{\mathrm{d}E_\gamma} = \frac{\mathrm{d}\sigma^{\mathrm{dir}}_{\gamma+X}}{\mathrm{d}E_\gamma} + \sum_{i=q,\bar{q},g}\int dz \frac{\mathrm{d}\sigma_{i+X}}{\mathrm{d}E_i}\mathcal{F}_{i\to\gamma}(z,E_\gamma,E_0,R) + \mathcal{O}(R)\,, \tag{5.3}$$

where the isolation-cone fragmentation function $\mathcal{F}_{i\to\gamma}$ describes the fragmentation of the hard parton with energy E_i into a photon with energy $E_\gamma = zE_i$ plus accompanying hadronic radiation which is restricted to have energy smaller than E_0 inside the cone, see Figure 5.1. The precise definition of this function is given below. The quantity $\sigma^{\mathrm{dir}}_{\gamma+X}$ is the perturbative cross section for producing a photon without imposing any isolation. The direct part is not collinear safe by itself, but its divergences cancel against the fragmentation part of the cross section. A more compact (and slightly more general) way of writing formula (5.3) is

$$\frac{\mathrm{d}\sigma(\epsilon_\gamma,R)}{\mathrm{d}E_\gamma} = \sum_{i=\gamma,q,\bar{q},g}\int dz \frac{\mathrm{d}\sigma_{i+X}}{\mathrm{d}E_i}\mathcal{F}_{i\to\gamma}(z,E_\gamma,E_0,R)\,. \tag{5.4}$$

Note that in this second form the sum over partons includes the photon. Throughout our paper, we work at leading order in the electromagnetic coupling α and neglect its running

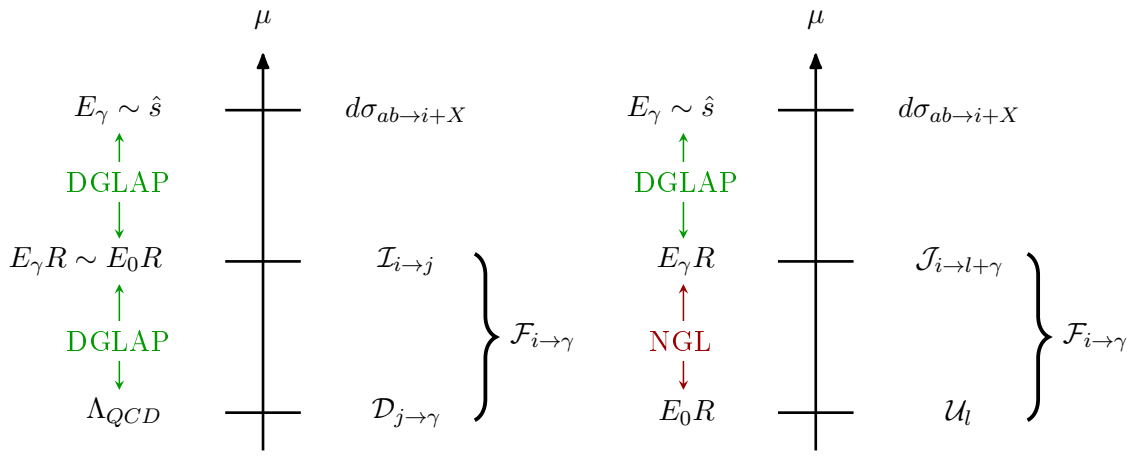

Figure 5.2: The scales arising in the factorization theorems (5.3) and (5.49), together with the type of RG evolution needed to resum the associated logarithms. On the left we show the factorization when R is small and the isolation energy E_0 is parametrically of the same size as the photon energy E_γ. On the right we show the factorization for $R \ll 1$ and $\epsilon_\gamma = E_0/E_\gamma \ll 1$. In this limit non-perturbative fragmentation effects are suppressed by ϵ_γ.

so that we have

$$\mathcal{F}_{\gamma\to\gamma} = \delta(1-z)\,, \tag{5.5}$$

which leads back to the original form (5.3) of the equation.

The fact that the photon cross section involves a fragmentation function which describes the conversion of a parton into a photon plus collinear partons is well known [41, 103, 46], see [104] for a recent review. What is different in our case is the definition and role of the fragmentation function. The standard fragmentation functions encode non-perturbative effects in photon production, while our function includes all physics associated with photon-isolation and therefore also has a perturbative component. The function $\mathcal{F}_{i\to\gamma}$ in (5.4) describes the fragmentation of the energetic parton i into a photon in the presence of the isolation cone, up to corrections suppressed by powers of R. Since we expand in small R, the isolation cone radius is set to zero when the partonic cross section $d\sigma_{i+X}$ is computed, which leads to infrared (IR) divergences which match the UV divergences of the fragmentation function.

In SCET, the fragmentation function is obtained as a matrix element of collinear fields, whose light-cone momentum components scale as

$$(n\cdot p, \bar{n}\cdot p, p_\perp) \sim E_\gamma(R^2, 1, R)\,, \tag{5.6}$$

where n^μ is a reference vector along the direction of the fragmenting parton. The $\perp$-directions are perpendicular to the fragmenting parton, not the beam. In this section, we do not consider the hierarchy between E_γ and E_0, i.e. we treat $E_\gamma \sim E_0$, corresponding to the situation shown on the left-hand side of Figure 5.2. The limit of small E_0 will be considered later in Section 5.5 and will lead to an additional factorization of the fragmentation functions.

The definition of the fragmentation functions for quarks and gluons reads

$$\begin{aligned}
&\frac{\bar{n}\!\!\!/_{\alpha\beta}}{2}\delta^{ab}\mathcal{F}_{q\to\gamma}(z,E_\gamma,E_0,R,\mu)\\
&\qquad=\sum\!\!\!\!\!\!\int_{\gamma+X}\langle 0|\chi^a_{q\alpha}(0)|\gamma{+}X\rangle\langle\gamma{+}X|\,\bar{\chi}^b_{q\beta}(0)\,|0\rangle\,\theta(2E_0-\bar{n}\cdot p_X^{\text{in}})\,\delta\!\left(z-\frac{\bar{n}\cdot p_\gamma}{Q}\right)\\
&\qquad\qquad(2\pi)^{d-1}\delta(Q-\bar{n}\cdot(p_\gamma+p_X))\;\delta^{(d-2)}(p_\gamma^\perp+p_X^\perp)\,,\qquad(5.7)\\
&-g^\perp_{\alpha\beta}\,g_s^2\delta^{ab}\mathcal{F}_{g\to\gamma}(z,E_\gamma,E_0,R,\mu)\\
&\qquad=\sum\!\!\!\!\!\!\int_{\gamma+X}\langle 0|\mathcal{A}^{\perp a}_\alpha(0)|\gamma{+}X\rangle\langle\gamma{+}X|\,\mathcal{A}^{\perp b}_\beta(0)\,|0\rangle\,\theta(2E_0-\bar{n}\cdot p_X^{\text{in}})\,\delta\!\left(z-\frac{\bar{n}\cdot p_\gamma}{Q}\right)\\
&\qquad\qquad(2\pi)^{d-1}Q\,\delta(Q-\bar{n}\cdot(p_\gamma+p_X))\;\delta^{(d-2)}(p_\gamma^\perp+p_X^\perp)\,,\qquad(5.8)
\end{aligned}$$

where we sum over states X containing collinear QCD partons and integrate over the phase space of the partons in X and the photon. The fields $\chi_q = W_c^\dagger\psi_{c,q}$ and $\mathcal{A}_\alpha^{\perp a}t^a = W_c^\dagger iD_{c,\alpha}^\perp W_c$ are the collinear quark and gluon fields in SCET times their associated collinear Wilson lines W_c. The indices a,b and α,β are associated with color and spin, respectively. The coupling g_s is the bare strong coupling constant. The Wilson lines W_c make the fields χ_q and $\mathcal{A}_\mu^\perp$ invariant under collinear gauge transformations and are a product of a QED and a QCD Wilson line. The total momentum of the partons inside the cone of radius R is denoted by p_X^{in} and its large component, not the energy, is bounded by the isolation criterion. Up to power corrections in R the large component $\bar{n}\cdot p$ is equal to twice the energy. The large light-cone component of the momentum of the incoming parton is Q and is given in terms of photon energy as $Q = 2E_\gamma/z$. We have written the constraint for fixed-cone isolation (5.1), but it can easily be adapted for smooth-cone case (5.2).

In general, the fragmentation functions (5.7) and (5.8) also contain a non-perturbative component from partons whose momentum scales as

$$(n\cdot p,\bar{n}\cdot p,p_\perp)\sim E_\gamma(\lambda^2,1,\lambda)\,,\qquad(5.9)$$

with $\lambda\sim\Lambda_{\text{QCD}}/E_\gamma$. These energetic partons are highly collinear to the photon. They are therefore always inside the isolation cone and their energy is constrained. After integrating out the perturbative modes (5.6), one ends up with a low-energy effective theory containing only the modes (5.9) and the fragmentation function becomes of convolution of perturbative coefficients $\mathcal{I}_{i\to j}$ times non-perturbative fragmentation functions $\mathcal{D}_{j\to\gamma}$. The associated two-step fragmentation process is depicted in Figure 5.3. For fixed-cone isolation, the associated factorization formula reads

$$\begin{aligned}
\mathcal{F}_{i\to\gamma}(z,E_\gamma,E_0,R,\mu)=\sum_{j=\gamma,q,\bar{q},g}\int_z^1\frac{dz_h}{z_h}\int dE_{\text{in}}\,\theta\!\left(E_0-E_{\text{in}}-\frac{1-z_h}{z_h}E_\gamma\right)\\
\mathcal{I}_{i\to j}(z/z_h,E_\gamma,E_{\text{in}},R,\mu)\,\mathcal{D}_{j\to\gamma}(z_h,\mu)\,.\qquad(5.10)
\end{aligned}$$

The θ-function is due to photon isolation and constrains the energy inside the cone, which gets contributions from perturbative partons in $\mathcal{I}_{i\to j}$ as well as the non-perturbative partons in $\mathcal{D}_{j\to\gamma}$, which carry the hadronic energy

$$E_h=(1-z_h)E_j=(1-z_h)\cdot z_p\cdot E_i=\frac{1-z_h}{z_h}E_\gamma\,,\qquad(5.11)$$

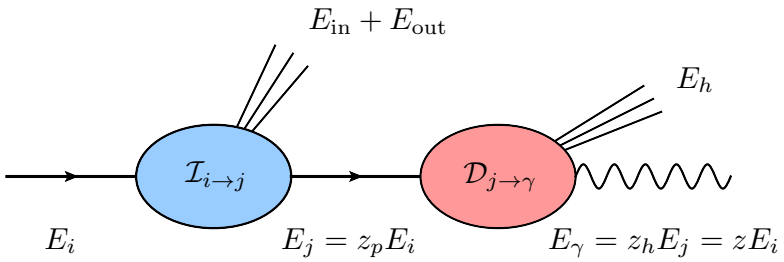

Figure 5.3: Kinematics of the factorization (5.10) of the cone fragmentation function $\mathcal{F}_{i\to\gamma}$ into a perturbative and non-perturbative part. The radiated partons in the perturbative part $\mathcal{I}_{i\to j}$ can be inside or outside the isolation cone, while the non-perturbative radiation in $\mathcal{D}_{j\to\gamma}$ is always inside. The perturbative momentum fraction is $z_p = z/z_h$.

where we used that $z_p = z/z_h$, see Figure 5.3. While the non-perturbative partons are always inside the cone, the perturbative ones scaling as (5.6) can be inside or outside. The constraint only acts on the inside part $E_{\rm in}$ of their energy. The constraint on the energy inside the cone implies that $z_h > 1/(1+\epsilon_\gamma)$. In the limit $\epsilon_\gamma \to 0$, the z_h integration in (5.10) no longer has any support. In this situation, the only contribution arises from $j = \gamma$

$$\mathcal{D}_{\gamma\to\gamma}(z_h, \mu) = \delta(1 - z_h)\,, \tag{5.12}$$

rendering the fragmentation purely perturbative up to power corrections in ϵ_γ. The limit of small isolation energy will be considered in detail below.

The scaling (5.9) and the structure of (5.10) make it clear why there is no non-perturbative contribution for smooth-cone isolation (5.2). Since the non-perturbative partons (5.9) are very close to the center of the isolation cone, they are not allowed to carry any energy since $E_0(r) \to 0$ for $r \to 0$. This enforces $z_h \to 1$ and the integral over z_h has no support and the only contribution arises again from $\mathcal{D}_{\gamma\to\gamma}$ in (5.12). The smooth-cone fragmentation function is purely perturbative up to corrections suppressed by $\Lambda_{\rm QCD}/E_\gamma$.

The factorization formula (5.3) is only valid up to corrections suppressed by the cone radius R, but has the advantage that it captures all dependence on photon isolation. As such it is well suited to analyze the dependence of cross sections on isolation parameters and can also be used to convert a result from one isolation criterion to another. We may, for example, convert a result computed using Frixione isolation to a result in fixed-cone isolation by evaluating the difference of the relevant fragmentation functions. A second advantage of the factorization (5.3) is that it separates the hard scale $E_\gamma \sim \sqrt{\hat{s}}$ from the collinear scale $E_\gamma R$ associated with the fragmentation. This enables us to use renormalization-group (RG) evolution to resum logarithms of R, the ratio of the two scales, as discussed in detail in the next sections.

5.3 Isolation fragmentation functions

We will now analyze the factorization discussed in Section 5.2 in more detail. Let us start by evaluating the isolation fragmentation functions at $\mathcal{O}(\alpha_s)$. At this order, the only nontrivial fragmentation process is $q \to \gamma(k) + q(p)$ and the matrix element in (5.7) is the

usual splitting function in $d = 4 - 2\epsilon$ dimensions

$$\langle 0|\chi_\beta^b(0)|\gamma+q\rangle\langle\gamma+q|\bar\chi_\alpha^a(0)|0\rangle = \delta^{ab}\left(\frac{\not{\bar n}}{2}\right)_{\alpha\beta}\frac{e^2Q_q^2\left((d-2)(\bar n\cdot k)^2+4\,\bar n\cdot k\,\bar n\cdot p+4(\bar n\cdot p)^2\right)}{2p\cdot k\;\bar n\cdot k}\,,$$
$$= \delta^{ab}\left(\frac{\not{\bar n}}{2}\right)_{\alpha\beta}\frac{e^2Q_q^2\,Q}{k\cdot p}\left[\frac{1+(1-z)^2}{z}-\epsilon\,z\right], \tag{5.13}$$

where we have denoted the photon momentum by k and the quark momentum by p and the charge Q_q is $+2/3$ for up-type and $-1/3$ for down-type quarks. In the second line the large light-cone components were written as $k\cdot\bar n = z\,Q$ and $p\cdot\bar n = (1-z)\,Q$. The expression in square brackets is the spin averaged splitting kernel in d dimensions. To obtain the fragmentation function, we need to integrate the matrix element (5.13) over the phase space of the photon and quark in the presence of the kinematic constraints in (5.7). Expanding away components which are power suppressed according to (5.6) , the cone constraint is formulated in terms of the angular quantity

$$\delta_{\gamma q}^2 = \frac{2p\cdot k}{\bar n\cdot p\,\bar n\cdot k}\,, \tag{5.14}$$

which scales as $\mathcal{O}(R^2)$. Up to higher order terms, we can approximate

$$\delta_{\gamma q} \approx \tan\left(\frac{\theta_{\gamma q}}{2}\right) \approx \frac{\theta_{\gamma q}}{2}\,. \tag{5.15}$$

For the fragmentation process $q\to\gamma(k)+q(p)$, the isolation cone constraint in (5.7) takes the explicit form

$$\theta(2E_0-\bar n\cdot p_X^{\rm in}) = \theta(\delta^2-\delta_{\gamma q}^2)\,\theta(2E_0-\bar n\cdot p)+\theta(\delta_{\gamma q}^2-\delta^2)\,. \tag{5.16}$$

The first term on the right-hand side imposes an energy constraint if the quark is inside the cone. The relation of δ to the cone size R depends on the collider. In the limit of small R we have

$$\begin{aligned} e^+e^-\text{ collider:}&\quad \delta = R\,,\\ \text{proton collider:}&\quad \delta = R\sin\theta_\gamma = R/\cosh(\eta_\gamma)\,. \end{aligned} \tag{5.17}$$

The hadron-collider result follows from analyzing $r<R$ with $r^2=(\Delta\eta)^2+(\Delta\phi)^2$ near the limit where the quark is collinear to the photon. To present results independent of the collider, we will express them in terms of the quantities δ and Q. For the product of the two at a hadron collider, we have

$$Q\delta = \frac{2E_\gamma^T}{z\sin\theta_\gamma}R\sin\theta_\gamma = \frac{2E_\gamma^T}{z}R\,, \tag{5.18}$$

while we get $Q\delta = 2E_\gamma R/z$ at a lepton collider.

Due to (5.16) the leading-order fragmentation function can naturally be split into two terms, depending on whether the quark in the final state is inside or outside the isolation cone

$$\mathcal{F}_{q\to\gamma}(z,E_\gamma,E_0,R,\mu) = \mathcal{F}_{q\to\gamma}^{\rm in}(z,E_\gamma,E_0,R,\mu)+\mathcal{F}_{q\to\gamma}^{\rm out}(z,R\,E_\gamma,\mu)\,, \tag{5.19}$$

where the outside part is independent of the isolation. The bare result for the outside part reads

$$\mathcal{F}_{q\to\gamma}^{\rm out}(z,R\,E_\gamma) = \frac{\alpha_{\rm EM}\,Q_q^2}{2\pi}\left\{P(z)\left[\frac{1}{\epsilon}-\ln\left(\frac{\delta^2Q^2}{\mu^2}(1-z)^2z^2\right)\right]-z\right\}, \tag{5.20}$$

$\sqrt{s} = 13\,\text{TeV}$	$E_T^\gamma > E_T^{\text{min}} = 125\,\text{GeV}$	$\lvert\eta_\gamma\rvert < 2.37$
NNPDF23_nlo_as_0119_qed_mc PDFs [105]	$\alpha_s(M_Z) = 0.119$	$\alpha_{\text{EM}} = 1/132.507$

Table 5.1: Kinematics and input parameters used for the cross section computations in this paper. For our fixed-order computations in Section 5.3 we use the default scales $\mu_a = \mu_f = \mu_r = 125\,\text{GeV}$, where μ_r and μ_f are the renormalization and factorization scales, respectively, and μ_a is the scale associated with the non-perturbative fragmentation function. For the resummed results, we use $\mu_h = \mu_f = \mu_r = E_T^\gamma$, $\mu_j = R\,E_T^\gamma$ and $\mu_0 = R\,E_0$ as the default.

with the $d = 4$ splitting kernel

$$P(z) = \frac{1 + (1-z)^2}{z} \tag{5.21}$$

and after expressing the bare electromagnetic coupling α_0 through the $\overline{\text{MS}}$ result via $\alpha_0 = Z_\alpha \alpha_{\text{EM}} (\mu^2\, e^{\gamma_E}/(4\pi))^\epsilon$, where γ_E is the Euler-Mascheroni constant. The renormalized result is then obtained by subtracting the divergence in (5.20). The inside part for smooth-cone isolation (5.2) is given by

$$\mathcal{F}^{\text{in}}_{q\to\gamma}(z, E_\gamma, E_0, R, \mu) = \frac{\alpha_{\text{EM}} Q_q^2}{2\pi} P(z) \frac{1}{n} \ln\left(\frac{z\,\epsilon_\gamma}{1-z}\right) \theta\left(z - \frac{1}{1+\epsilon_\gamma}\right), \tag{5.22}$$

where n is the exponent parameter of the smooth-cone isolation condition (5.2). The function $\mathcal{F}^{\text{in}}_{q\to\gamma}$ is finite and independent of of the cone radius, while the outside part has logarithmic R dependence tied to its divergence. As it should be, the total fragmentation function has a divergence proportional to the splitting kernel. Due to the constraint on the inside energy, the inside fragmentation function has only support for large enough z and vanishes in the limit $\epsilon_\gamma \to 0$. Expanding around this limit, we find

$$\mathcal{F}^{\text{in}}_{q\to\gamma}(z, E_\gamma, E_0, R, \mu) = \frac{\alpha_{\text{EM}} Q_q^2}{2\pi} \frac{1}{n}\, \epsilon_\gamma\, \delta(1-z) + \mathcal{O}(\epsilon_\gamma^2)\,. \tag{5.23}$$

The ϵ_γ suppression is expected since the collinear quark becomes soft and soft quarks are power suppressed.

Let us now consider the inside fragmentation for fixed-cone isolation (5.1). This case is more complicated because the isolation fragmentation also involves non-perturbative fragmentation, see (5.10). At zeroth order in α_s, there are two contributions. We can either have a trivial perturbative part

$$\mathcal{I}_{i\to j}(z, R, E_\gamma, E_{\text{in}}, \mu) = \delta_{ij}\, \delta(1-z) + O(\alpha_s) \tag{5.24}$$

together with a non-perturbative fragmentation contribution, or we have photon production from a quark or anti-quark in the perturbative part $\mathcal{I}_{i\to\gamma}$ followed by the trivial photon-to-photon fragmentation $\mathcal{D}_{\gamma\to\gamma} = \delta(1-z)$. Up to corrections of order α_s, we can thus write the inside part for fixed-cone isolation as

$$\mathcal{F}^{\text{in}}_{i\to\gamma}(z, R, E_\gamma,\, E_0, \mu) \quad = \quad \left[\mathcal{D}_{i\to\gamma}(z,\mu) + \sum_{k=q,\bar{q}} \delta_{ik}\, \mathcal{I}^{\text{in}}_{k\to\gamma}(z, R, E_\gamma, \mu)\right] \theta\left(z - \frac{1}{1+\epsilon_\gamma}\right) \tag{5.25}$$

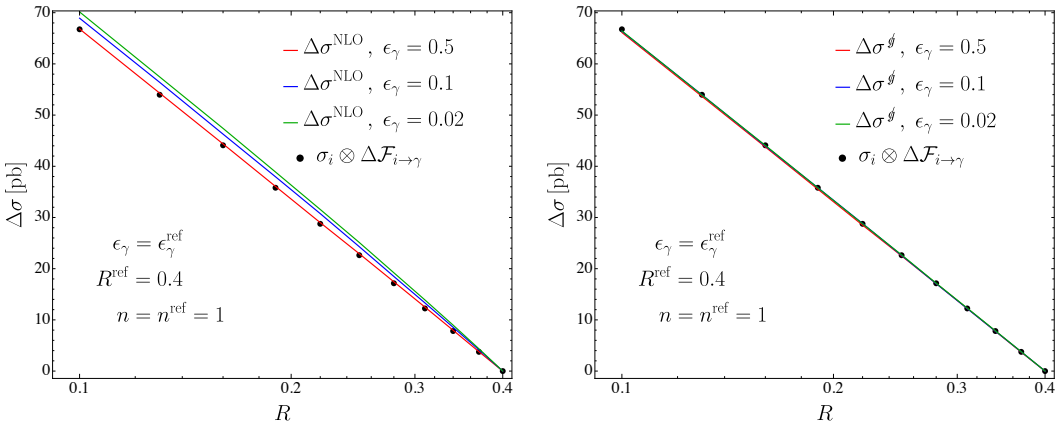

Figure 5.4: Dependence of $\Delta\sigma$ on the cone radius R for smooth-cone isolation (5.2). The lines labeled $\Delta\sigma^{\rm NLO}$ are the difference of the full NLO cross sections. For the lines labeled $\Delta\sigma^{\not g}$ in the right plot gluons inside the isolation cones were vetoed. The dots represent $\Delta\sigma = \sigma_i \otimes \Delta\mathcal{F}_{i\to\gamma}$ computed with the fragmentation function according to (5.28), which is independent of ϵ_γ for $\epsilon_\gamma = \epsilon_\gamma^{\rm ref}$.

and for the perturbative part, we find

$$\mathcal{I}^{\rm in}_{q\to\gamma}(z, R, E_\gamma, \mu) = \frac{\alpha_{\rm EM}\, Q_q^2}{2\pi}\left\{P(z)\left[-\frac{1}{\epsilon} + \ln\left(\frac{\delta^2 Q^2}{\mu^2}(1-z)^2 z^2\right)\right] + z\right\}. \tag{5.26}$$

Note that this is the opposite of $\mathcal{F}^{\rm out}_{q\to\gamma}$ in (5.20). In the absence of the isolation energy constraint in (5.25), the two contributions would exactly cancel since the perturbative part of the fragmentation function becomes scaleless. This is sensible: without the energy constraint, the isolation becomes trivial and the entire fragmentation reduces to the non-perturbative fragmentation function $\mathcal{D}_{i\to\gamma}$. We also note that the anomalous dimension of the fragmentation function is the same for smooth-cone and fixed-cone isolation. Since the same anomalous dimension also drives the evolution of the hard part given by the partonic amplitudes $d\sigma_{i+X}$ in (5.3) it cannot depend on the isolation requirement.

The fragmentation function factorization is valid up to power corrections in R and with the functions at hand, it is interesting to check numerically whether (5.3) describes the isolation effects in the NLO photon production cross section at the experimentally used value $R = 0.4$. To this end, we consider proton proton collisions at $\sqrt{s} = 13\,\text{TeV}$ and compute the cross section for isolated photons with $E_T^\gamma > E_T^{\rm min} = 125\,\text{GeV}$. For our numerical studies of photon isolation effects, we will use the kinematic setup and input parameters listed in Table 5.1 throughout the paper. Our formalism can also be used to study differential distributions, but the focus of our paper is on the effects of photon isolation and these are not strongly dependent on the photon kinematics.

To study the dependence on isolation parameters, we consider smooth-cone isolation (5.2) and compute the difference to a reference cross section

$$\Delta\sigma = \sigma\left(\epsilon_\gamma, n, R\right) - \sigma(\epsilon_\gamma^{\rm ref}, n^{\rm ref}, R^{\rm ref})\,. \tag{5.27}$$

In the difference $\Delta\sigma$ the direct photon part in (5.3) drops out so that it is given by a convolution of the partonic cross section with the fragmentation function. At this order, the fragmenting parton is either a quark or anti-quark so that we have

$$\Delta\sigma = \sum_{i=q,\bar q}\int_{E_T^{\rm min}}^\infty dE_i \int_{z_{\rm min}}^1 dz \frac{d\sigma_{i+X}}{dE_i}\Delta\mathcal{F}_{i\to\gamma}\,, \tag{5.28}$$

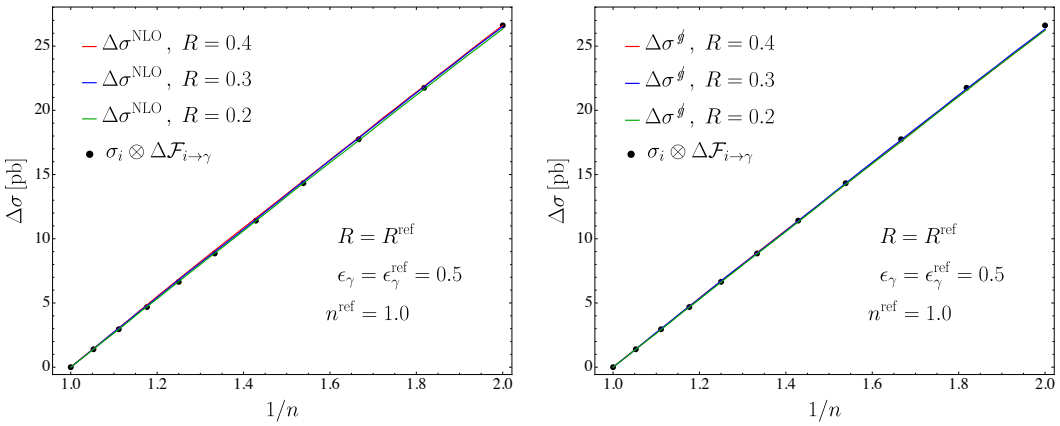

Figure 5.5: Dependence of $\Delta\sigma$ on the value of the parameter n of the smooth-cone isolation (5.2). The lines labeled $\Delta\sigma^{\mathrm{NLO}}$ are the difference of the full NLO cross sections. For the lines labeled $\Delta\sigma^{\not g}$ in the right plot gluons inside the isolation cones were vetoed. The dots represent $\Delta\sigma = \sigma_i \otimes \Delta\mathcal{F}_{i\to\gamma}$ computed with the fragmentation function according to (5.28) and is independent of R for $R = R^{\mathrm{ref}}$.

where

$$\Delta\mathcal{F}_{i\to\gamma} = \mathcal{F}_{i\to\gamma}\left(z, R, \epsilon_\gamma, n\right) - \mathcal{F}_{i\to\gamma}\left(z, R^{\mathrm{ref}}, \epsilon_\gamma^{\mathrm{ref}}, n^{\mathrm{ref}}\right) \tag{5.29}$$

and $z_{\mathrm{min}} = E_T^{\mathrm{min}}/E_i$.

To be able to convert the values for $\Delta\sigma$ into results for the full cross section, we computed some reference cross section values with MCFM [106] for the kinematics listed in Table 5.1. The LO cross section is of course independent of the isolation requirement and corresponds to

$$\sigma^{\mathrm{LO}} = 229^{-20}_{+22}\,\mathrm{pb}\,, \tag{5.30}$$

where the upper and lower values correspond to the change in cross section after increasing and lowering $\mu_f = \mu_r$ from the default value by a factor 2, respectively. The NLO cross section values depend on isolation and we obtain

$$\begin{aligned} \sigma^{\mathrm{NLO}}\Big|_{\text{no isolation}} &= 495^{-51}_{+68}\,\mathrm{pb}\,, \\ \sigma^{\mathrm{NLO}}\Big|_{\text{fixed cone},R=0.4,\epsilon_\gamma=0.02} &= 413^{-35}_{+46}\,\mathrm{pb}\,, \end{aligned} \tag{5.31}$$

The cross section predictions in (5.31) depend on the non-perturbative fragmentation functions $\mathcal{D}_{i\to\gamma}$ and we used the GdRG [53, 50] set as implemented in MCFM. The code offers a second choice, the BFGS sets [49], which would lead to a value of the cross section without isolation which is about 35 pb lower. With fixed-cone isolation, the BFGS cross section would be 11 pb lower than the value in (5.31). These fragmentation function sets were determined about 25 years ago based on LEP data [40, 107] and models of the non-perturbative physics. For smooth-cone isolation, we obtain the reference values

$$\begin{aligned} \sigma^{\mathrm{NLO}}\Big|_{R=0.4,\,n=1,\,\epsilon_\gamma=1.0} &= 459^{-43}_{+56}\,\mathrm{pb}\,, \\ \sigma^{\mathrm{NLO}}\Big|_{R=0.4,\,n=1,\,\epsilon_\gamma=0.5} &= 445^{-40}_{+53}\,\mathrm{pb}\,, \\ \sigma^{\mathrm{NLO}}\Big|_{R=0.4,\,n=1,\,\epsilon_\gamma=0.02} &= 414^{-35}_{+46}\,\mathrm{pb}\,. \end{aligned} \tag{5.32}$$

As a consistency check, we have computed cross sections with several available NLO codes and for convenience we provide precise reference values in Appendix 5.D. We have also extracted the direct cross section in (5.3) by computing the cross section at different R values, subtracting the fragmentation contribution and extrapolating to $R \to 0$. For the default scales in Table 5.1, we find $\sigma_{\rm dir}^{\rm NLO} \approx 308\,{\rm pb}$, with some uncertainty due to the extrapolation since we cannot run the fixed order codes at too small R due to numerical instabilities.

From our results for the fragmentation function in (5.22) and (5.20), we can immediately read off the parameter dependence for a number of special cases, for example

$$\begin{aligned} \Delta\sigma &\propto \ln\left(\frac{R^{\rm ref}}{R}\right) && \text{for} && n = n^{\rm ref} \text{ and } \epsilon_\gamma = \epsilon_\gamma^{\rm ref}\,, \\ \Delta\sigma &\propto \left(\frac{1}{n} - \frac{1}{n^{\rm ref}}\right) && \text{for} && R = R^{\rm ref} \text{ and } \epsilon_\gamma = \epsilon_\gamma^{\rm ref}\,. \end{aligned} \tag{5.33}$$

In addition to the n and R dependence, we can also analyze the ϵ_γ dependence, but this case is more complicated because the difference of fragmentation functions has nontrivial dependence on the parameter ϵ_γ even for $R = R^{\rm ref}$ and $n = n^{\rm ref}$:

$$\Delta\mathcal{F}_{i\to\gamma} = \frac{\alpha_{\rm EM} Q_i^2}{2\pi} P(z) \frac{1}{n} \left[\theta\!\left(z - \frac{1}{1+\epsilon_\gamma}\right) \ln\left(\frac{1-z}{z\,\epsilon_\gamma}\right) - \theta\!\left(z - \frac{1}{1+\epsilon_\gamma^{\rm ref}}\right) \ln\left(\frac{1-z}{z\,\epsilon_\gamma^{\rm ref}}\right)\right]. \tag{5.34}$$

Of course, as is the case for the factorization formula (5.28), these results only hold up to terms which are power suppressed by the cone radius R and it is interesting to check how big the power corrections are numerically by comparing to fixed-order results for $\Delta\sigma$. To this end, we plot the cross section as a function the isolation parameters R, n and ϵ_γ in Figures 5.4, 5.5 and 5.6. The dots in these figures correspond to fragmentation function results obtained using (5.28), while the lines are the NLO fixed-order result for $\Delta\sigma$ computed using MadGraph5_aMC@NLO [108]. The fixed-order photon production cross section only becomes sensitive to isolation at NLO and the cross section difference is insensitive to virtual corrections. We can thus extract the difference directly from a LO computation of the process $pp \to \gamma jj$, where one of the "jets" is recoiling against the photon, while the second one is inside the isolation cone. The details of this fixed-order computation are described in Appendix 5.C.

The differences between the full fixed-order results (lines in the plots) and the fragmentation result (dots) are due to power suppressed contributions such as initial state radiation into the cone. Figures 5.5 and 5.6 show that even for $R = 0.4$, the power corrections are numerically quite small and the factorization theorem (5.3) accurately describes the photon isolation effects. In Figure 5.4 the difference is zero by construction at the reference point $R = R^{\rm ref} = 0.4$. Since the power corrections vanish for $R \to 0$, the difference in this region arises from power corrections to the reference cross section with $R^{\rm ref} = 0.4$. Since the fragmentation contribution can only have (anti-)quarks inside the cone at this order, contributions with gluons inside the cone are suppressed by R. In the right-hand plots in Figures 5.4, 5.5 and 5.6, we have removed the contributions of gluons inside the cone. The close agreement of the fragmentation result with the full fixed-order result shows that gluon radiation into the cone is the main source of power corrections. Indeed, since the power corrections are so small, once gluons are excluded from the isolation cone, the three lines in each plot overlap almost completely.

In Figures 5.4, 5.5 and 5.6 we considered the parameter dependence of cross sections with smooth-cone isolation. It is now interesting to compare to the case of fixed-cone

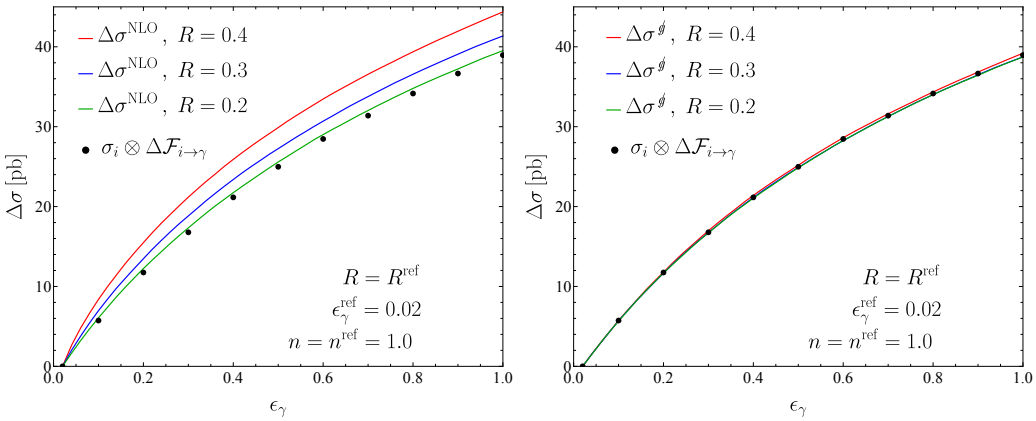

Figure 5.6: Dependence of the cross section on ϵ_γ for smooth-cone isolation (5.2). The lines labeled $\Delta\sigma^{\mathrm{NLO}}$ show the difference of the full NLO cross sections. The dots represent $\Delta\sigma = \sigma_i \otimes \Delta\mathcal{F}_{i\to\gamma}$ computed with the fragmentation function according to (5.28) and are independent of R for $R = R^{\mathrm{ref}}$. For the lines labeled $\Delta\sigma^{\not g}$ in the right plot gluons inside the isolation cones were vetoed.

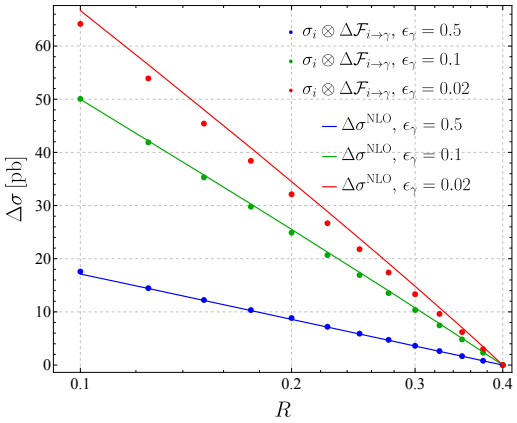

Figure 5.7: Radius dependence for fixed-cone isolation for different ϵ_γ with $R^{\mathrm{ref}} = 0.4$. The lines show the full NLO cross sections, the dots correspond the the result obtained using the cone fragmentation functions. In contrast to the smooth-cone result shown in Figure 5.4, the result depends on ϵ_γ.

isolation. Since the outside part is obviously the same, different behavior is related to the inside part $\mathcal{F}^{\mathrm{in}}_{q\to\gamma}$ given in (5.22) and (5.25), respectively. In addition to the contribution from the non-perturbative fragmentation, a key difference between the two functions is that for fixed-cone isolation, the inside part of the function depends on the cone radius. Setting $\epsilon_\gamma = \epsilon_\gamma^{\mathrm{ref}}$ and computing the difference between the cross section at a given R to a reference value R^{ref}, the non-perturbative part drops out and we obtain

$$\Delta\mathcal{F}_{i\to\gamma} = \frac{Q_i^2\alpha_{\mathrm{EM}}}{\pi} P(z) \ln\left(\frac{R^{\mathrm{ref}}}{R}\right) \theta\left(\frac{1}{1+\epsilon_\gamma} - z\right) . \tag{5.35}$$

We see that due to the presence of the θ-function the coefficient of the logarithm of R now depends on ϵ_γ, in contrast to smooth-cone result shown in Figure 5.4. The smaller the value of ϵ_γ, the bigger the range over which the z-integral has support, resulting in a larger coefficient of the $\ln(R)$ term. This is indeed what we observe in Figure 5.7. In

σ [pb]	fixed cone	$n=1$	$n=2$
$\epsilon_\gamma = 0.02$	414.56 ± 0.34	413.31 ± 0.36	410.41 ± 0.37
$\epsilon_\gamma = 0.1$	420.58 ± 0.38	422.05 ± 0.40	416.57 ± 0.39
$\epsilon_\gamma = 0.2$	429.35 ± 0.32	429.10 ± 0.41	421.71 ± 0.40

Table 5.2: Cross-section at $R = 0.4$ for different photon isolation criteria computed using MCFM [106]. The cross section values correspond to the kinematics and input specified in Table 5.1 with $\mu_f = \mu_r = 125\,\text{GeV}$. For this scale choice, the direct part of the cross section is $\sigma^{\text{dir}} \approx 308\,\text{pb}$.

the limit $\epsilon_\gamma \to 0$, the θ-function becomes trivial and we recover the smooth-cone result for the R dependence of the cross section. This observation is surprising at first sight, but the underlying physics is easy to understand. For small ϵ_γ, the R dependence is driven by energetic partons outside the cone that are close to its boundary. These are independent of the isolation criterion so that the $\ln(R)$ dependence becomes universal. More generally, since the inside part $\mathcal{F}^{\text{in}}_{i\to\gamma}$ involves a soft quark, its contribution is power suppressed for $\epsilon_\gamma \to 0$ and $R \to 0$. In this limit, a dependence on the isolation criterion first arises in the NNLO cross section and will be computed below. To illustrate that the different isolation criteria lead to the similar NLO cross section for $\epsilon_\gamma \to 0$, we have tabulated cross sections values for different isolation criteria in Table 5.2. We observe that the cross section differences indeed decrease for small ϵ_γ. Interestingly, the $n = 1$ cross section is fairly close to the fixed-cone cross section over a fairly wide range of ϵ_γ values.

Having illustrated the parameter dependence of the isolation cross section in different examples and demonstrated that power suppressed effects in R are small, we now turn to the all-order resummation of $\ln(R)$ terms.

5.4 Resummation of $\ln(R)$ terms

Working with the form (5.4) of the factorization theorem, the renormalized fragmentation functions fulfills the usual DGLAP evolution equation

$$\begin{aligned}\frac{d}{d\ln\mu}\mathcal{F}_{i\to\gamma}(z,\mu) &= \sum_{j=\gamma,q,\bar{q},g} \mathcal{P}_{i\to j}\otimes\mathcal{F}_{j\to\gamma} \\ &\equiv \sum_{j=\gamma,q,\bar{q},g}\int_z^1 \frac{dz'}{z'}\mathcal{P}_{i\to j}\Big(\frac{z}{z'}\Big)\mathcal{F}_{j\to\gamma}(z',\mu)\,, \end{aligned} \tag{5.36}$$

where we suppress the dependence on the fragmentation function on the additional arguments E_γ, E_0, R and further parameters such as n. As is conventional, we use here the symbol $\otimes$ to denote the Mellin convolution

$$(f\otimes g)(z) = \int_0^1 dx\int_0^1 dy\,\delta(z-xy)f(x)f(y) = \int_z^1\frac{dz'}{z'}f\Big(\frac{z}{z'}\Big)g(z')\,. \tag{5.37}$$

Separating out the trivial $\mathcal{F}_{\gamma\to\gamma}$ contribution as in (5.5), we can write the DGLAP evolution equation purely in terms of QCD partons

$$\frac{d}{d\ln\mu}\mathcal{F}_{i\to\gamma}(z,\mu) = \mathcal{P}_{i\to\gamma}(z) + \sum_{j=q,\bar{q},g}\mathcal{P}_{i\to j}\otimes\mathcal{F}_{j\to\gamma}\,, \tag{5.38}$$

with $i = q, \bar{q}, g$. In this form, the equation involves an inhomogeneous term. To resum the logarithms of R we will solve (5.38) numerically and evolve the functions $\mathcal{F}_{i\to\gamma}$ from their characteristic scale $\mu_c \sim RE_\gamma$ to the hard scale $\mu_h \sim E_\gamma$. The initial condition $\mathcal{F}_{q\to\gamma}(z, E_\gamma, E_0, R, \mu)$ for $\mu = \mu_c$ was computed in the previous section both for fixed-cone and smooth-cone isolation.

An important simplification for the case of smooth-cone isolation is that the fragmentation function is purely perturbative. The same is true in the limit of small E_0 considered in the next section, since the non-perturbative part involves a soft quark inside the fragmentation cone, which is power suppressed in the limit $E_0 \to 0$. In the absence of non-perturbative effects, and since we do not include the top quark and set the masses of the other quarks to zero, our fragmentation functions have a flavor symmetry: all down-type quarks and anti-quarks have the same fragmentation function, and similarly all up-type quarks and anti-quarks. Instead of evolving the individual flavors, we thus only need the combinations

$$\begin{aligned} \Sigma &= \sum_{i=1}^{n_f} (\mathcal{F}_{q_i\to\gamma} + \mathcal{F}_{\bar{q}_i\to\gamma}) \,, \\ \Delta &= \mathcal{F}_{d\to\gamma} - \mathcal{F}_{u\to\gamma} \,, \\ G &= \mathcal{F}_{g\to\gamma} \,, \end{aligned} \tag{5.39}$$

where d and u denote the down- and up-type quarks respectively. The function Δ is decoupled from the gluon fragmentation function, and satisfies the simple evolution equation

$$\frac{d}{d\ln\mu}\Delta = (\mathcal{P}_{d\to\gamma}(z) - \mathcal{P}_{u\to\gamma}(z)) + \mathcal{P}_{q\to q} \otimes \Delta \,. \tag{5.40}$$

The other two functions Σ and g fulfill the coupled equations

$$\frac{d}{d\ln\mu}\begin{pmatrix}\Sigma\\ G\end{pmatrix} = \begin{pmatrix}\sum_{i=1}^{n_f}(\mathcal{P}_{q_i\to\gamma} + \mathcal{P}_{\bar{q}_i\to\gamma})\\ \mathcal{P}_{g\to\gamma}\end{pmatrix} + \begin{pmatrix}\mathcal{P}_{q\to q} & 2n_f\mathcal{P}_{q\to g}\\ \mathcal{P}_{g\to q} & \mathcal{P}_{g\to g}\end{pmatrix} \otimes \begin{pmatrix}\Sigma\\ G\end{pmatrix} . \tag{5.41}$$

The parton-to-parton splitting kernels relevant for the homogenous part take the form

$$\mathcal{P}_{i\to j}(z) = \frac{\alpha_s}{\pi} P^{(1)}_{i\to j} + \mathcal{O}(\alpha_s^2) \,, \tag{5.42}$$

and the parton-to-photon splitting kernels which constitute the inhomogeneous part of the equation are expanded as

$$\mathcal{P}_{i\to\gamma} = \frac{\alpha}{\pi}\left(P^{(0)}_{i\to\gamma} + \frac{\alpha_s}{\pi} P^{(1)}_{i\to\gamma} + \mathcal{O}(\alpha_s^2)\right) . \tag{5.43}$$

We solve this equation at leading order in RG-improved QCD perturbation theory and therefore need to include the order α_s corrections to the evolution kernels, including the ones to $\mathcal{P}_{i\to\gamma}$. These can be found in [30] and are listed in Appendix 5.A. In traditional terminology, this amounts to next-to-leading logarithmic (NLL) accuracy.

There are two commonly used techniques to solve evolution equations such as (5.38). One possibility is to solve the equations directly in momentum space by interpolating the fragmentation functions over a grid of z values. In this approach computes the μ-dependence step by step and interpolates the result in z at each step. Alternatively, one can solve the equations in Mellin moment space

$$f(N) = \int_0^1 dz z^{N-1} f(z) \,, \tag{5.44}$$

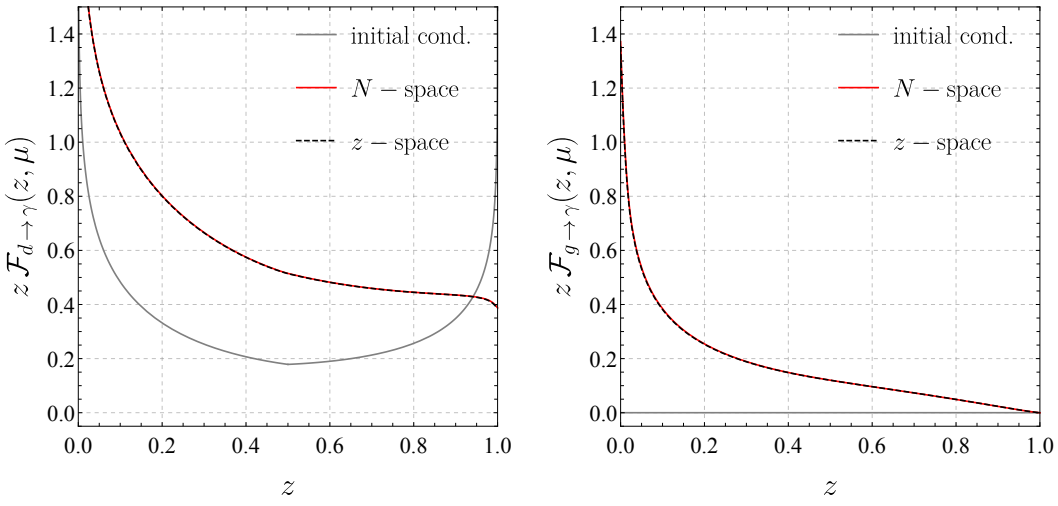

Figure 5.8: Effect of RG-evolution on the cone fragmentation functions $\mathcal{F}_{i\to\gamma}$. The gray lines shows the initial condition given by the LO fixed-order result at $\mu = 10\,\text{GeV}$ and correspond to smooth-cone isolation with $R = 0.4$ with $\epsilon_\gamma = 1$ and $n = 1$. The derivative of the initial condition is discontinuous at $z = (1+\epsilon_\gamma)^{-1} = 0.5$ due to the contribution (5.22). The gluon fragmentation function vanishes at this order. The other lines are the results after evolution to $\mu = 200\,\text{GeV}$ by solving the RG equations either in moment space (red lines) or in momentum space (dashed lines).

which converts Mellin convolutions (5.37) into products

$$(f \otimes g)(N) = f(N) \cdot g(N)\,. \tag{5.45}$$

In moment space (5.38) turns into a set of coupled differential equations for the moments. One can view the flavor indices as matrix indices so that the solution boils down to the solution of a matrix equation. The the inhomogeneous equation (5.38) takes the form

$$\frac{d}{d\ln\mu}\mathcal{F}_{i\to\gamma}(N,\mu) = \mathcal{P}_{i\to\gamma}(N) + \sum_{j=q,\bar{q},g} \mathcal{P}_{i\to j}(N)\mathcal{F}_{j\to\gamma}(N,\mu)\,. \tag{5.46}$$

Introducing the flavor combinations in (5.39), we get a differential equation for Δ and a matrix differential equation for Σ and G, see (5.41). After diagonalizing this two-by-two matrix, one can solve the equations analytically and obtain the exact μ-dependence of the moments. The evaluation then reduces to computing the inverse Mellin transformation numerically. The moment-space solution is detailed in Appendix 5.B. The discussion in this appendix shows that for full NLL accuracy, one will need to include the two-loop correction to the parton-to-parton splitting kernels in (5.42) since $\mathcal{F}_{i\to\gamma}$ formally counts as $\mathcal{O}(1/\alpha_s)$. If the jet scale is not much lower than the hard scale, these corrections will be small and we omit them for simplicity.

Both methods to solve the evolution equations are commonly used. The solution in moment space is, for example, the basis of the PEGASUS code [109], while the APFEL code solves the RGs in z-space [110, 111]. As a cross check, we have implemented both approaches. In Figure 5.8, we compare results for some benchmark values of the scales and find that they are compatible with each other. The moment space method becomes delicate for $z \to 1$ because the Mellin inversion integral suffers from slow numerical convergence. To improve the convergence, we use the same integration contour as the PEGASUS code.

The momentum space method, on the other hand, requires a careful choice of the z grid and interpolation and larger numerical resources to calculate the μ-dependence since it needs to proceed in small steps, but yields similarly precise results for all z-values. In our event-based resummation framework, we prefer to work with the moment-space approach, since a single numerical integral immediately yields the result for any desired μ value. Of course, one could interpolate the results for the fragmentation functions as is done for PDFs, but one would need different grids for different initial conditions, i.e. different isolation parameter choices.

To compute the cross section resummed at NLL, we first evaluate the NLO photon-production cross section with MadGraph5_aMC@NLO [108]. Then we evaluate

$$\frac{d\sigma^{\text{NLO+NLL}}}{dE_\gamma} = \frac{d\sigma^{\text{NLO}}_{\gamma+X}}{dE_\gamma} + \sum_{i=q,\bar{q},g} \int dz \frac{d\sigma_{i+X}}{dE_i} \Delta\mathcal{F}_{i\to\gamma}\,, \tag{5.47}$$

where

$$\Delta\mathcal{F}_{i\to\gamma} = \mathcal{F}_{i\to\gamma}(z, E_\gamma, E_0, R, \mu_j) - \mathcal{F}_{i\to\gamma}(z, E_\gamma, E_0, R, \mu_h)\,. \tag{5.48}$$

Here $\mu_h \sim E_\gamma$ is the scale at which the fixed-order computation was performed. The second term in $\Delta\mathcal{F}_{i\to\gamma}$ in (5.47) subtracts the fixed-order result of the fragmentation contribution and adds the RG-improved result obtained from solving the evolution equation (5.38) to evolve from the hard scale μ_h at which σ_{i+X} is computed to the collinear scale $\mu_j \sim E_\gamma R$. The RG evolution resums the logarithms of R and the subtraction is necessary to avoid a double counting of the fragmentation contribution which is contained in the NLO result.

To compute the fragmentation contribution in (5.47), we use MadGraph5_aMC@NLO as an event generator to produce the leading-order cross section $d\sigma_{i+X}/dE_i$ for different QCD partons i. We then perform the integral over z in (5.3) by randomly choosing a value of z for each event and evaluating the fragmentation function for this value. Since the scales depend on the photon energy $E_\gamma = zE_i$, we have a different μ-values for each event and the moment-space technique to solve DGLAP is very efficient since we control the μ dependence analytically and only need a numerical integration to obtain the fragmentation function at the desired z value. To have a fast way of computing the fragmentation function we have written a small C++ code.

The effect of the resummation of the logarithms of the radius R is shown in Figure 5.9. To show the dependence on R, we again compute the difference to a reference cross section at $R = 0.4$. Before discussing the resummed result, let us compare the full NLO prediction (solid black line) of MadGraph5_aMC@NLO to the result obtained using the fragmentation formalism without resummation (dashed line). They must agree up to small power corrections and we observe that the difference is indeed quite small. Since we subtract the reference cross section, the difference is zero by construction at the reference point $R = 0.4$. The small deviation at small R is due to the difference of the reference cross sections as in Figures 5.4 and 5.7. The red curve shows the difference of the resummed result to the reference cross section without resummation. As expected, resummation lowers the cross section since it dampens the logarithmic growth of the NLO result. We also show the difference between the inclusive photon cross section and the reference cross section obtained from (5.32) as an orange, dash-dotted line in the figure. To be physical, the isolated cross section has to be smaller than the inclusive cross section. The fact that the isolated NLO cross section overshoots the inclusive result for $R < 0.2$ shows that the fixed-order expansion breaks down for small R, as was observed earlier in [11]. Resummation cures this problem. Of course, this unitarity bound has to be taken with a grain of salt, since

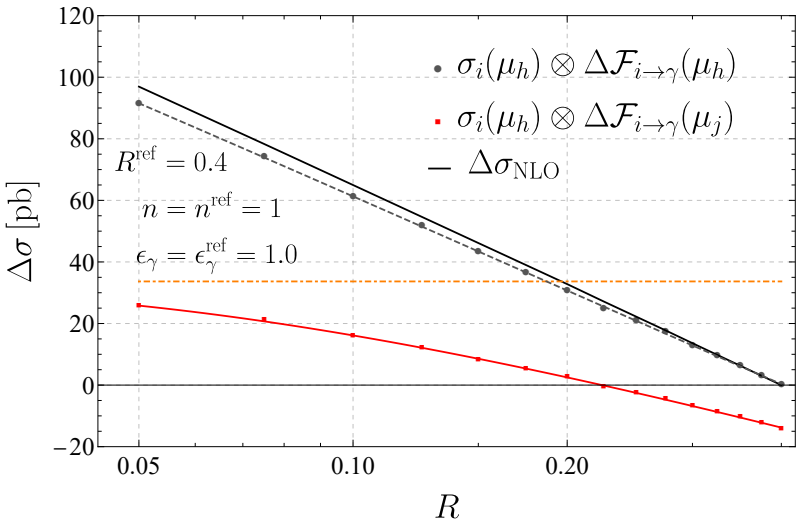

Figure 5.9: Effect of $\ln(R)$ resummation, plotted as the difference to the fixed-order cross section at $R_{\rm ref} = 0.4$. Shown are the resummed result (red) and its fixed-order expansion (dashed) obtained by setting $\mu_j = \mu_h$. We also show the full fixed-order result (black) evaluated with $\mu_r = \mu_f = \mu_h$, which also includes terms which are power suppressed in R. Above the orange dot-dashed line, the cross section with isolation becomes larger than the inclusive cross section, which is unphysical.

the inclusive cross section depends on the non-perturbative fragmentation functions, which are poorly known.

5.5 Factorization for small isolation energy E_0

If the isolation energy E_0 is much smaller than the photon energy E_γ, a scale hierarchy arises in the fragmentation function $\mathcal{F}_{i\to\gamma}$. In the limit of small $\epsilon_\gamma = E_0/E_\gamma$, energetic partons can no longer enter the isolation cone, however, energetic partons outside the cone can radiate back into the cone. This structure is at the heart of a second factorization, which is depicted in Figure 5.1,

$$\mathcal{F}_{i\to\gamma}(z, R\,E_\gamma, R\,E_0, \mu) = \sum_{l=1}^{\infty} \langle \boldsymbol{\mathcal{J}}_{i\to\gamma+l}(\{\underline{n}\}, R\,E_\gamma, z, \mu) \otimes \boldsymbol{\mathcal{U}}_l\,(\{\underline{n}\},\, R\,E_0, \mu)\rangle\,, \tag{5.49}$$

and is valid in the limit of small ϵ_γ. The fragmentation function factorizes into jet functions $\boldsymbol{\mathcal{J}}_{i\to\gamma+l}$ describing the energetic partons accompanying the photon and functions $\boldsymbol{\mathcal{U}}_l$ describing the low-energy radiation into the cone. This radiation is sensitive to the directions $\{\underline{n}\} = \{n_1, \ldots, n_l\}$ and color charges of the l energetic partons. The symbol $\otimes$ denotes the integral over the directions of the hard partons and the photon. The same symbol was used in Section 5.4 to denote the Mellin convolution; the context makes it clear what the symbol indicates. The notation $\langle \ldots \rangle$ indicates the color sum, which can be taken after computing the emissions. In addition to directions of the l energetic partons, the functions also depend on the vectors n and $\bar{n}$ introduced in defining $\mathcal{F}_{i\to\gamma}$ and on the direction of the photon n_γ. More precisely, the functions will depend on scalar products of the different vectors, as we will detail below.

The fragmentation of parton i into a photon of momentum k is encapsulated by the jet functions

$$\overline{\boldsymbol{\mathcal{J}}}_{i\to\gamma+l}(\{\underline{n}\}, R\,E_\gamma, z, \mu) = \sum_{\text{spins}} \prod_{j=1}^{l} \int \frac{dE_j\, E_j^{d-3}}{(2\pi)^{d-2}} \int \frac{dE_k\, E_k^{d-3}}{(2\pi)^{d-2}}\, \Theta_{\text{cone}}\big(\{\underline{p}\}\big)$$
$$|\mathcal{M}_l(p_i;\{k,\underline{p}\})\rangle\langle\mathcal{M}_l(p_i;\{k,\underline{p}\})|\, 2\,(2\pi)^{d-1}\,\delta(\bar{n}\cdot p_i - \bar{n}\cdot k - \bar{n}\cdot p_{X_c})\,\delta^{(d-2)}(k^\perp + p_{X_c}^\perp)\,, \tag{5.50}$$

where the constraint $\Theta_{\text{cone}}\big(\{\underline{p}\}\big)$ enforces that the energetic partons must lie outside the isolation cone. The amplitudes in this formula are the splitting functions for the incoming parton with momentum p_i along the direction n to fragment into the photon and additional l energetic partons $\{\underline{p}\} = \{p_1, \dots, p_l\}$,

$$|\mathcal{M}_l(p_i;\{\underline{p}\})\rangle = \langle k, \underline{p}|\, \Phi_c^{\alpha a}(0)\,|0\rangle\,, \tag{5.51}$$

where $p_i = k + p_{X_c} = k + \sum_{j=1}^{l} p_j$ and $\Phi_c^{\alpha a}$ is a collinear field with the quantum numbers of the incoming parton, i.e. $\Phi_c^{\alpha a} = \chi_c^{\alpha a}$ for an incoming quark and $\Phi_c^{\alpha a} = \mathcal{A}_c^{\perp,\alpha a}$ for an incoming gluon, with spin and color indices α and a. The definition of the jet function includes a sum over spins of the outgoing partons, which for the quark-case produces the structure

$$\overline{\boldsymbol{\mathcal{J}}}_{q\to\gamma+l}(\{\underline{n}\}, R\,E_\gamma, z, \mu) = \left(\frac{\bar{n}\!\!\!/}{2}\right)_{\alpha\beta} \delta^{ab}\, \boldsymbol{\mathcal{J}}_{q\to\gamma+l}(\{\underline{n}\}, R\,E_\gamma, z, \mu)\,, \tag{5.52}$$

with a scalar jet function $\boldsymbol{\mathcal{J}}_{i\to\gamma+l}$, and where α and β are the Dirac indices of the collinear fields in the amplitude and the conjugate amplitude. For an incoming gluon, we instead get

$$\bar{n}\cdot p_i\; \overline{\boldsymbol{\mathcal{J}}}_{g\to\gamma+l}(\{\underline{n}\}, R\,E_\gamma, z, \mu) = -g_{\alpha\beta}^\perp\, g_s^2 \delta^{ab}\, \boldsymbol{\mathcal{J}}_{g\to\gamma+l}(\{\underline{n}\}, R\,E_\gamma, z, \mu)\,. \tag{5.53}$$

The extra factor of $\bar{n}\cdot p_i$ on the left hand side arises because the gluon field has mass dimension 1, while the quark field has dimension $\frac{3}{2}$. While we integrate over the full phase space of the photon with momentum k, the directions of the energetic partons are fixed. Note that the collinear fields in the jet functions scale as (5.6). The integrals in (5.50) are integrals over the large light-cone components $E_j \equiv \bar{n}\cdot p_j/2$.

The energetic partons in the jet functions source soft radiation which can enter the isolation cone. The momenta of this radiation scale as

$$(n\cdot p_t, \bar{n}\cdot p_t, p_t^\perp) \sim E_0(R^2, 1, R)\,. \tag{5.54}$$

It has small energy $E \sim \epsilon_\gamma E_\gamma$ and is collinear to the photon. Since it is both collinear and soft it was called *coft* in [98] and denoted with a subscript t. The coft radiation can be obtained by taking matrix elements of Wilson line operators along the directions $n_1, \dots, n_l$ of the outgoing collinear partons and an additional one along the direction $\bar{n}$, which captures the radiation of all other partons not collinear to the photon. A detailed derivation of the Wilson line structure can be found in [99]. The operator definition for the coft functions reads

$$\boldsymbol{\mathcal{U}}_l(\{\underline{n}\}, E_0 R)$$
$$= \sum\!\!\!\!\!\!\int_{X_t} \langle 0|\, \boldsymbol{U}_0^\dagger(\bar{n})\, \boldsymbol{U}_1^\dagger(n_1) \dots \boldsymbol{U}_l^\dagger(n_l)\,|X_t\rangle\langle X_t|\, \boldsymbol{U}_0(\bar{n}) \dots \boldsymbol{U}_l(n_l)\,|0\rangle\, \theta(2E_0 - \bar{n}\cdot p_{X_t}^{\text{cone}})\,. \tag{5.55}$$

In the limit under consideration, the energy measurement translates into a measurement of the large component of the radiation. Note that the coft radiation can be inside or outside the cone, but only the energy of the partons inside the cone is bounded by E_0.

In the following, we will resum the leading logarithms associated with the scale ratios shown on the right-hand side of Figure 5.2. The resummation of logarithms of the cone radius R, the ratio of the collinear scale RE_γ to hard scale E_γ is carried out as before by numerically solving the DGLAP evolution equation. However, for small $\epsilon_\gamma = E_0/E_\gamma$, a second evolution step is required to evolve from the collinear scale $\mu_j \sim RE_\gamma$ to the low-energy scale $\mu_0 \sim RE_0$ to resum the logarithms of ϵ_γ. These are non-global logarithms and we resum them using a parton-shower algorithm [13, 14] analogous the one originally proposed by Dasgupta and Salam [102].

5.6 Computation of the jet and coft function

As a starting point of the second evolution, we need to compute the jet functions at a scale $\mu = \mu_j \sim RE_\gamma$. There are no large logarithms for this scale choice and all higher-multiplicity jet functions are suppressed by powers of α_s. We thus only need the case $l = 1$, corresponding to the fragmentation process $q \to \gamma + q$.

The jet functions depends on the light-cone reference vector n_μ along the direction of the parton that fragments into the jet, as well as a conjugate reference vector $\bar{n}^\mu$ with $n \cdot \bar{n} = 2$. In addition, the jet functions will depend on the light-cone reference vectors of the collinear partons produced in the fragmentation. For the lowest-order fragmentation process $q \to \gamma + q$ we need a reference vector n_q for the final-state quark and a vector n_γ for the photon. The scalar jet functions $\mathcal{J}_{q\to l+\gamma}$ defined in (5.52) will depend on scalar products of these reference vectors and to compute them, we introduce angular variables that are suited to the limit under consideration. A set of variables which scales as $\mathcal{O}(1)$ is [99]

$$\Theta_i = \frac{1}{\delta}\sqrt{\frac{n\cdot n_i}{\bar{n}\cdot n_i}}\,, \tag{5.56}$$

$$\Phi_{ij} = \frac{2}{\delta^2}\frac{n_i\cdot n_j}{\bar{n}\cdot n_i\,\bar{n}\cdot n_j}\,. \tag{5.57}$$

The first set of variables measures the angle with respect to the axis n, the second one the angle between i and j. In four dimensions, we have

$$\Theta_i = \frac{1}{\delta}\tan\left(\frac{\theta_i}{2}\right)\,, \tag{5.58}$$

$$\Phi_{ij} = \Theta_i^2 + \Theta_i^2 - 2\Theta_i\Theta_j\cos(\Delta\phi_{ij})\,. \tag{5.59}$$

For the leading order fragmentation process $q \to \gamma + q$ these variables are not independent. Momentum conservation enforces $\Delta\phi_{q\gamma} = \pi$ and we therefore have $\Phi_{q\gamma} = (\Theta_q + \Theta_\gamma)^2$. Transverse momentum conservation also relates the ratio of the two angles to the momentum fraction z of the photon

$$\frac{\Theta_\gamma}{\Theta_q} = \frac{z}{1-z} + \mathcal{O}(\delta^2). \tag{5.60}$$

This implies that there is only single independent angular variable and for convenience we choose it as

$$\widetilde{\Theta} = \frac{1}{\sqrt{\Phi_{q\gamma}}} = \delta\cot\frac{\theta_{q\gamma}}{2} + \mathcal{O}(\delta^2)\,. \tag{5.61}$$

Up to power corrections, we have $\widetilde{\Theta} \in [0,1]$. The limit $\widetilde{\Theta} = 1$ corresponds to the quark touching the cone, while $\widetilde{\Theta} = 0$ corresponds to the configuration where the photon and the quark are back to back. To rewrite the angular convolution integral in this variable, we insert

$$1 = \int_0^1 d\widetilde{\Theta}\, \frac{2}{\widetilde{\Theta}^3}\, \delta\left(\widetilde{\Theta}^{-2} - \frac{2}{\delta^2} \frac{n_q \cdot n_\gamma}{\bar{n}\cdot n_q\, \bar{n}\cdot n_\gamma}\right), \tag{5.62}$$

into the original angular convolution, perform the angular integrals and write the result in the form

$$\begin{aligned}\boldsymbol{\mathcal{J}}_{q\to\gamma+q}(\{n_q,n_\gamma\}, R\,E_\gamma, z, \mu) \otimes \boldsymbol{\mathcal{U}}_q\left(\{n_q,n_\gamma\},\, R\,E_0, \mu\right) \\ = \int_0^1 d\widetilde{\Theta}\, \boldsymbol{\mathcal{J}}_{q\to\gamma+q}\Big(\widetilde{\Theta}, R\,E_\gamma, z, \mu\Big)\, \boldsymbol{\mathcal{U}}_q\left(\widetilde{\Theta},\, R\,E_0, \mu\right).\end{aligned} \tag{5.63}$$

To compute the jet function for the process $q \to \gamma(k) + q(p)$, we split the momenta into their light-cone components and write

$$p^\mu = n\cdot p \frac{\bar{n}^\mu}{2} + \bar{n}\cdot p \frac{n^\mu}{2} + p_\perp^\mu \tag{5.64}$$

and analogously for the photon momentum k. We note that

$$\frac{2p\cdot k}{\bar{n}\cdot p\, \bar{n}\cdot k} = \frac{2n_q\cdot n_\gamma}{\bar{n}\cdot n_q\, \bar{n}\cdot n_\gamma} = \frac{\delta^2}{\widetilde{\Theta}^2}. \tag{5.65}$$

According to the definition (5.50), the jet function only involves the energy integrals instead of full phase-space integrations, but in (5.63) we carry out the angular integrals after inserting the δ-function (5.62). Doing so, we recover full phase-space integrals for k and p together with the δ-function constraint (5.62) which keeps the angle between the quark and the photon fixed. This gives

$$\begin{aligned}\mathcal{J}_{q\to\gamma+q}\Big(\widetilde{\Theta}, R\,E_\gamma, z, \mu\Big)\, \delta^{ab} \left(\frac{\not{n}}{2}\right)_{\alpha\beta} = \int [dp][dk] \langle 0|\chi_\beta^b(0)|\gamma{+}q\rangle\langle\gamma{+}q|\chi_\alpha^a(0)|0\rangle \\ (2\pi)^{d-1}\delta^{(d-2)}(\vec{p}_\perp + \vec{k}_\perp)\delta(\bar{n}(p+k) - \tilde{Q})\delta\Big(z - \frac{\bar{n}k}{\tilde{Q}}\Big)\, \frac{2}{\widetilde{\Theta}^3}\delta\left(\frac{2p\cdot k}{\delta^2 \bar{n}\cdot p\, \bar{n}\cdot k} - \frac{1}{\widetilde{\Theta}^2}\right)\end{aligned} \tag{5.66}$$

where $\tilde{Q} = 2E_\gamma/z$ is the large light-cone component of the quark before fragmentation. The matrix element is the same we encountered in the computation of the fragmentation function and was given in (5.13). The only difference to the earlier computation of the fragmentation function is the angular constraint. For the fragmentation function, the quark could be either inside or outside the cone according to (5.16) and we integrated over its direction. The particles inside the jet function, on the other hand, are energetic and cannot be inside the isolation cone. Furthermore we need the result differential in the direction $\widetilde{\Theta}$ of the quark, because the soft radiation depends on it. After inserting (5.13) into (5.66), we can immediately carry out the integrations which leads to the result

$$\begin{aligned}\mathcal{J}_{q\to\gamma+q}\Big(\widetilde{\Theta}, R\,E_\gamma, z, \mu\Big) &= \frac{\mu^2 e^{\gamma_E}}{\Gamma(1-\epsilon)} \frac{Q_i^2\alpha_{\rm EM}}{\pi} \frac{2-2z+(1-\epsilon)z^2}{z} \frac{\left(\frac{\delta^2 Q^2 (z-1)^2 z^2}{\widetilde{\Theta}^2}\right)^{-\epsilon}}{\widetilde{\Theta}} \\ &= \frac{Q_i^2\alpha_{\rm EM}}{2\pi}\left[P(z)\left(\frac{\delta(\widetilde{\Theta})}{\epsilon} - \delta(\widetilde{\Theta})\ln\left(\frac{\delta^2 Q^2}{\mu^2}(z-1)^2 z^2\right) + 2\left[\frac{1}{\widetilde{\Theta}}\right]_+\right) - z\delta(\widetilde{\Theta})\right].\end{aligned} \tag{5.67}$$

The splitting kernel $P(z)$ was given in (5.21). The renormalized jet function is obtained by dropping the divergent term in the second line.

With the jet function at hand, we can now obtain $\mathcal{F}_{i\to\gamma}$ at leading order from (5.49) by convoluting with the trivial lowest-order coft function $\mathcal{U}_q = \mathbf{1}$:

$$\int_0^1 d\widetilde{\Theta}\, \mathcal{J}_{q\to\gamma+q}\Big(\widetilde{\Theta}, R\,E_\gamma, z, \mu\Big) = \frac{Q_i^2\alpha_{\rm EM}}{2\pi}\left[P(z)\left(\frac{1}{\epsilon} - \ln\left(\frac{\delta^2 Q^2}{\mu^2}(z-1)^2 z^2\right)\right) - z\right]. \tag{5.68}$$

This result indeed agrees with $\mathcal{F}^{\rm out}_{q\to\gamma}(z, R\,E_\gamma)$ given in (5.20). In the limit of small ϵ_γ the inside part is power suppressed, since soft quarks are power suppressed compared to soft gluons.

To resum the leading non-global logarithms, it is sufficient to use the trivial LO coft function since the function evaluated at $\mu = \mu_0$ is free of large logarithms. It is nevertheless useful to calculate the NLO function $\boldsymbol{\mathcal{U}}_q^{(1)}$, relevant for the process $q \to \gamma + q$ so that we have an analytic result for the one-loop logarithm and and an idea of the size of the non-logarithmic $\mathcal{O}(\alpha_s)$ corrections. The perturbative expansion of the coft functions takes the form

$$\boldsymbol{\mathcal{U}}_l(\{\underline{n}\},\, R\,E_0, \mu) = \mathbf{1} + \frac{\alpha_s}{4\pi}\boldsymbol{\mathcal{U}}_l^{(1)}(\{\underline{n}\},\, R\,E_0, \mu) + \mathcal{O}\left(\alpha_s^2\right) \tag{5.69}$$

and the NLO correction to the coft function for $q \to \gamma + q$ is obtained by computing the emission of a coft gluon into the isolation cone

$$\frac{\alpha_s}{4\pi}\boldsymbol{\mathcal{U}}_q^{(1)}\left(\widetilde{\Theta},\, R\,E_0, \mu\right) = 2g_s^2 C_F \mathbf{1}\int [dk] \frac{\bar{n}\cdot n_q}{\bar{n}\cdot k\, n_q\cdot k}\theta\left(\delta^2 - \frac{2n_\gamma\cdot k}{\bar{n}\cdot n_\gamma \bar{n}\cdot k}\right)\theta(Q_0 - \bar{n}\cdot k)\,. \tag{5.70}$$

The first θ-function forces the emission to lie inside the cone, the second one restricts the energy, or more precisely the large component of the coft momentum. The expression (5.70) is relevant for fixed-cone isolation. For smooth-cone isolation in the limit of small δ one replaces

$$\theta(Q_0 - \bar{n}\cdot k) \to \theta\left(Q_0\left(\frac{2n_\gamma\cdot k}{\delta^2 \bar{n}\cdot n_\gamma \bar{n}\cdot k}\right)^n - \bar{n}\cdot k\right) \tag{5.71}$$

and identifies $Q_0 = 2\epsilon_\gamma E_\gamma$. Note that the one recovers the fixed-cone isolation for $n = 0$. If the coft gluon is outside the cone its energy is unrestricted leading to a scaleless integral. The squared amplitude is from the emissions from the Wilson line along the direction n_q of the outgoing quark and the Wilson line along the $\bar{n}$ direction which represents the emission from the remaining hard partons in the event. Performing the integrations for smooth-cone isolation, expressing the bare coupling g_s through the $\overline{\rm MS}$ coupling, and defining $\boldsymbol{\mathcal{U}}_q^{(1)} = \mathcal{U}_q^{(1)}\mathbf{1}$, we obtain

$$\mathcal{U}_q^{(1)} = \frac{2C_F}{\epsilon}\ln\left(1-\widetilde{\Theta}^2\right) - 2C_F\left[\ln\left(1-\widetilde{\Theta}^2\right)2\ln\left(\frac{Q_0\delta}{\mu}\right) + \ln^2\left(1-\widetilde{\Theta}^2\right) + (1+2n)\mathrm{Li}_2\left(\widetilde{\Theta}^2\right)\right]. \tag{5.72}$$

The renormalized one-loop function is obtained by dropping the divergent part of this result. For $\mu \sim Q\delta$, the result contains a large logarithm $\ln(Q_0/Q) = \ln(\epsilon_\gamma)$. The rest of the terms enter at NLL.

Given the simple form of the coft function (5.72), we can analytically evaluate the convolution with the leading jet function in (5.67). Note that $\mathcal{U}_q^{(1)}$ vanishes for $\widetilde{\Theta} = 0$. For this reason, only the plus-distribution part in (5.67) contributes. Evaluating the angular

integral, we obtain

$$\left\langle \mathcal{J}_{q\to\gamma+q} \otimes \mathcal{U}_q^{(1)} \right\rangle = \frac{Q_q^2 \alpha_{\rm EM}}{\pi} C_F P(z) \left[-\frac{\pi^2}{6\epsilon} + \frac{\pi^2}{3} \ln \frac{Q_0 \delta}{\mu} - (2n+3)\,\zeta_3 \right] . \tag{5.73}$$

This convolution of the jet and coft function corresponds exactly to the situation depicted in Figure 5.1.

The result (5.73) has a very important application. Consider two cross sections computed at small ϵ_γ but with the same cone radius R. The difference (5.28) is proportional to the difference of fragmentation functions. Since the fragmentation contribution as a whole is suppressed by $\mathcal{O}(\alpha_s)$, we only need the fragmentation function difference to $\mathcal{O}(\alpha_s)$ to evaluate $\Delta\sigma$. In the limit of small ϵ_γ the fragmentation functions factorize into jet and coft functions and only the coft functions are sensitive to the isolation requirements. Since the jet functions are independent of the isolation criterion, the only contribution to the difference of cross sections

$$\Delta\sigma = \sigma_{\rm fixedcone}(R, \epsilon_\gamma) - \sigma_{\rm smoothcone}(R, \epsilon_\gamma^{\rm ref}, n)\,, \tag{5.74}$$

arises from (5.73) and takes the extremely simple form

$$\Delta\sigma = \sum_{i=q,\bar{q}} \int_{E_T^{\rm min}}^{\infty} dE_i \int_{z_{\rm min}}^{1} dz \frac{d\sigma_{i+X}}{dE_i} \frac{Q_q^2 \alpha_{\rm EM}}{\pi} \frac{C_F \alpha_s}{4\pi} P(z) \left[\frac{\pi^2}{3} \ln \frac{\epsilon_\gamma}{\epsilon_\gamma^{\rm ref}} + 2n\,\zeta_3 \right] . \tag{5.75}$$

This formula holds at NNLO up to corrections suppressed by powers of R or ϵ_γ. As we have shown in the earlier sections, even at $R = 0.4$, power suppressed effects are numerically small and experimental measurements use small values of ϵ_γ. For reference, Figure 5.7 shows the size of the power suppressed effects at NLO. For $\epsilon_\gamma = 0.02$, the R dependence at NLO is indeed very close to the one for smooth-cone isolation. We also provided NLO cross section values in Table 5.2 to indicate the size of the remaining differences. Of course, to make optimal use of the formula (5.75), one would only use it to convert the NNLO corrections and separately compute the NLO fixed-cone results so that the power suppressed corrections to the formula are also suppressed by α_s^2. Numerically, the value of $\Delta\sigma$ obtained from (5.75) is quite small. Computing it for our standard setup detailed in Table 5.1 for $n = 1$ and $\epsilon_\gamma = \epsilon_\gamma^{\rm ref}$, we obtain

$$\Delta\sigma = -1.3\,\text{pb}\,. \tag{5.76}$$

5.7 Resummation of $\ln(\epsilon_\gamma)$ terms

To resum the leading logarithms of ϵ_γ we solve the RG equations and run the jet function from the jet scale $\mu_j \sim QR$ down to the scale $\mu_0 \sim Q_0 R = Q\epsilon_\gamma R$, where we combine it with the coft functions. To perform the resummation we will use the parton-shower code NGL_RESUM [14]. This code was developed to numerically perform the RG evolution and the angular integrals over the directions of the additional partons that are emitted during the evolution. It is not possible to apply the code directly to our problem, since we work in the limit $R \to 0$, where the size of the isolation region goes to zero and the MC integration over the angles would become highly inefficient, as additional emissions would be enhanced by logarithms of δ. To use the code, we use the fact that the coft function is not depending on δ and Q_0 individually, but only on the product. This is explicit in

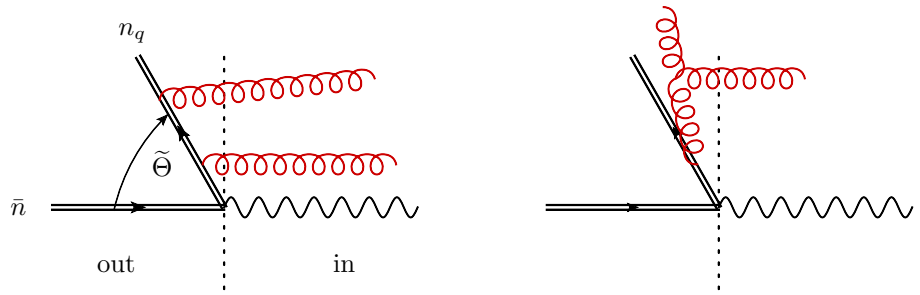

Figure 5.10: Kinematics and example diagrams arising in the the parton shower computation of $\boldsymbol{\mathcal{U}}_q^{\mathrm{LL}}(\widetilde{\Theta}, t)$. We use the rescaling invariance (5.77) and Lorentz invariance of the shower to evaluate the function in a frame where $\bar{n}$ and n_γ are back-to-back and the isolation cone covers the entire right hemisphere. The left diagram shows an example of a two-loop global contribution, the right one a non-global one.

the one-loop result (5.72), but can be proven formally by noting that the coft function is invariant under the rescaling

$$\delta \to \frac{\delta}{\lambda}\,, \quad Q_0 \to \lambda\, Q_0\,, \quad \bar{n} \to \lambda\, \bar{n}\,, \quad n_\gamma \to \frac{n_\gamma}{\lambda}\,, \quad n_i \to \frac{n_i}{\lambda}\,. \tag{5.77}$$

To see this, note that the Wilson lines in (5.55) are invariant under rescalings of the light-cone vectors and the rescaling also leaves the constraints on the energy and the angular variables (5.56) and (5.57) invariant. Setting $\lambda = \delta$, the invariance implies that we can run the shower for $\delta = 1$, where the opening angle is $\pi/2$ after rescaling the energy to $Q_0\delta$. The shower computes the leading-logarithmic (LL) evolution

$$\mathcal{U}_q^{\mathrm{LL}}\left(\widetilde{\Theta},\, R\, E_0, \mu_0\right) = \sum_{m=2}^{\infty} \left\langle \boldsymbol{U}_{2m}(\{\bar{n}, n_q, \underline{n}\}, \mu_j, \mu_0) \,\hat{\otimes}\, \mathbf{1} \right\rangle, \tag{5.78}$$

where the evolution matrix

$$\boldsymbol{U}(\{\bar{n}, n_q, \underline{n}\}, \mu_j, \mu_0) = \mathbf{P} \exp\left[\int_{\mu_0}^{\mu_j} \frac{d\mu}{\mu} \boldsymbol{\Gamma}^H(\{\underline{n}\}, \mu)\right], \tag{5.79}$$

produces additional partons along the directions $\{\underline{n}\}$ and the symbol $\hat{\otimes}$ indicates the integral over their directions. For LL resummation the exponent of the evolution matrix reduces to

$$\int_{\mu_0}^{\mu_j} \frac{d\mu}{\mu}\, \boldsymbol{\Gamma}^H = \int_{\alpha_s(\mu_0)}^{\alpha_s(\mu_j)} \frac{d\alpha}{\beta(\alpha)}\, \frac{\alpha}{4\pi}\, \boldsymbol{\Gamma}^{(1)} = \frac{1}{2\beta_0} \ln \frac{\alpha_s(\mu_0)}{\alpha_s(\mu_j)}\, \boldsymbol{\Gamma}^{(1)} \equiv t\, \boldsymbol{\Gamma}^{(1)}\,. \tag{5.80}$$

The "evolution time" t measures the separation of the scales μ_j and μ_0. The relevant one-loop anomalous dimension $\boldsymbol{\Gamma}^{(1)}$ can be found in [99] (by now also the two-loop result is known [112]) and the solution of the evolution equation is detailed in [13, 14]. The shower starts with a quark along the direction $\bar{n}$ which fragments into a photon and a quark along the n_q direction with angular separation $\widetilde{\Theta}_q$. We use that the shower is Lorentz invariant to choose a frame where

$$n_\gamma^\mu = (1, 0, 0, 1)\,, \qquad \bar{n}^\mu = (1, 0, 0, -1)\,, \qquad n_q^\mu = (1, \sin\theta_{\gamma q}, 0, \cos\theta_{\gamma q})\,, \tag{5.81}$$

so that $\widetilde{\Theta} = \cot(\theta_{\gamma q}/2)$ for our choice $\delta = 1$. The shower then generates successive emissions outside the isolation cone (or hemisphere for $\delta = 1$) , until one emission is inside the cone

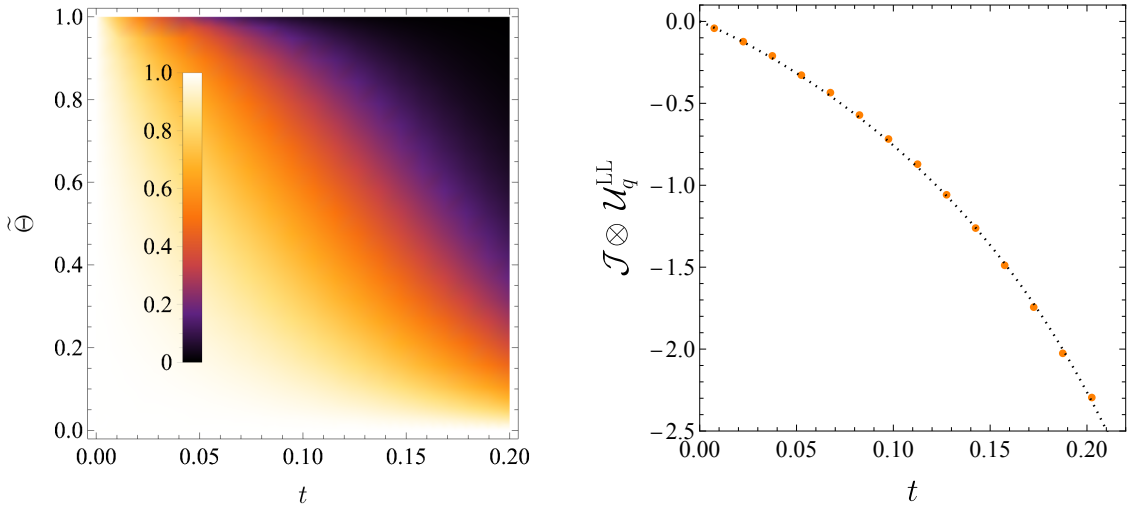

Figure 5.11: The left plot shows the coft function $\mathcal{U}_q^{\mathrm{LL}}(\widetilde{\Theta}, t)$. The right plot shows the convolution of the jet and coft function, more precisely the convolution with the plus distribution shown in (5.83). The orange dots correspond to the results of the parton shower; the dotted line is the fourth-order polynomial in t fitted to these results.

after which it terminates. The resulting function $\mathcal{U}_q^{\mathrm{LL}}(\widetilde{\Theta}, t)$ is plotted on the left hand side of Figure 5.11. One thing that is obvious in the one-loop result (5.72) and in the plot is that the function is trivial for $\widetilde{\Theta} = 0$, where $\mathcal{U}_q^{\mathrm{LL}}(\widetilde{\Theta}, t) = 1$ independently of t. For $\widetilde{\Theta} = 0$, the outgoing quark lies along the direction $\bar{n}$ of the fragmenting quark. In this configuration, the radiation of the two exactly cancels. One can view the fragmenting quark in the initial state as an anti-quark in the final state to make the cancellation manifest. The most radiation arises for $\widetilde{\Theta} = 1$, which corresponds to a configuration where the quark is at the edge of the isolation cone.

One can interpolate the function $\mathcal{U}_q^{\mathrm{LL}}(\widetilde{\Theta}, t)$ and then evaluate the angular convolution with the jet function (5.63), but it is more efficient to also Monte-Carlo integrate over $\widetilde{\Theta}$ and directly compute the convolution (5.63) inside the parton shower code. To do so, we we first use $\mathcal{U}_q^{\mathrm{LL}}(0, t) = 1$ to compute the δ-function terms and obtain

$$\begin{aligned}
&\int_0^1 d\widetilde{\Theta} \left\langle \mathcal{J}_{q\to\gamma+q}\Big(\widetilde{\Theta}, R\,E_\gamma, z, \mu_j\Big)\, \mathcal{U}_q^{\mathrm{LL}}(\widetilde{\Theta}, t)\right\rangle \\
&= \frac{Q_i^2 \alpha_{\mathrm{EM}}}{2\pi}\Big[- P(z) \ln\left(\frac{\delta^2 Q^2}{\mu_j^2}(z-1)^2 z^2\right) - z + 2P(z) \int_0^1 d\widetilde{\Theta} \left[\frac{1}{\widetilde{\Theta}}\right]_+ \mathcal{U}_q^{\mathrm{LL}}(\widetilde{\Theta}, t)\Big]\,. \qquad (5.82)
\end{aligned}$$

The variable $t \equiv t(\mu_j, \mu_0)$ encodes the dependence on the low scale. Since $\mathcal{U}_q^{\mathrm{LL}}(0, t) = 1$, we can drop the plus-prescription and evaluate

$$\int_0^1 \frac{d\widetilde{\Theta}}{\widetilde{\Theta}}\, \mathcal{U}_q^{\mathrm{LL}}(\widetilde{\Theta}, t) \approx -\frac{\pi^2}{2} t - 31.5 t^2 + 105.\, t^3 - 535.\, t^4\,. \qquad (5.83)$$

where the result on the right-hand side was obtained by fitting a fourth order polynomial to the numerical parton shower results, obtained by sampling the $\widetilde{\Theta}$ integral with 25×10^5 values and running 500 showers at each value. The results of the parton shower are compared to the fit results in the right panel of Figure 5.11 and agree quite well up to values of t relevant for phenomenological applications. Up to running effects, the different

powers of t correspond to the successive terms in the expansion in α_s since

$$t = \frac{\alpha_s}{4\pi} \ln \frac{\mu_j}{\mu_0} + \mathcal{O}(\alpha_s^2). \tag{5.84}$$

The leading term in the expansion in t can be obtained analytically by integrating the logarithmic term in our result (5.72). In addition to performing the resummation, our parton shower also computes this term and the numerical value agrees with the analytic result to an accuracy better than a permille. The term linear in t is captured by NNLO fixed-order computations of photon production. NNLO is necessary since σ_{i+X}, the cross section to produce the fragmenting parton, is α_s suppressed. Our parton shower also computes the coefficient of the t^2 term, with an accuracy of order of a few per cent. The remaining two terms were determined by fitting to the shower results. Taking the exponential of the one-loop contribution yields the "global" logarithms. Adopting this terminology, the two-loop term is split into

$$-31.5 = -43.7\,(\text{“non-global”}) + 12.2\,(\text{“global”}) \tag{5.85}$$

where we approximated $\pi^4/8 \approx 12.2$. The non-global part is thus significantly larger than the global part and the same remains true at higher orders. Diagrams for the two contributions are shown in Figure 5.10. The global contribution arises from emissions from the quark before or after the fragmentation as indicated on the left diagram in Figure 5.10. The non-global terms arise from sequential emissions off gluons emitted outside the isolation cone, see the right diagram. In the shower, we include a collinear cutoff $\eta_{\text{cut}} = 6$ (see [13, 14]) as well as a technical cutoff $\widetilde{\Theta} > \kappa_{\text{cut}} \approx 10^{-3}$ in the angular integral. We have checked that for $t < 0.2$ our results are insensitive to these cutoffs. The fact that we are able to fit the shower results with a polynomial in t implies that the fixed-order expansion of the logarithmic terms is well-behaved in the region we perform our computation.

Let us now look at the effect of the resummation on the cross section. For illustration, we will again consider proton proton collisions at $\sqrt{s} = 13\,\text{TeV}$ and compute the cross section for isolated photons with $E_T^\gamma > E_T^{\text{min}} = 125\,\text{GeV}$ and $|\eta_\gamma| < 2.37$ following ATLAS [113]. The result shown in Figure 5.12 includes both the resummation of $\ln(R)$ and $\ln(\epsilon_\gamma)$ terms. The resummation is achieved by first evolving from the hard scale $\mu_h \sim E_\gamma$ to the jet scale $\mu_j \sim R\,E_\gamma$ by solving the DGLAP equation as discussed in Section (5.4) and then evolving to the coft scale $\mu_0 \sim \epsilon_\gamma\,R\,E_\gamma$ using the parton shower framework. We can distinguish the effect of the two resummations by choosing different scales. Setting $\mu_j = \mu_h$ switches off the $\ln(R)$ resummation, while the choice $\mu_j = \mu_0$ eliminates the higher-order $\ln(\epsilon_\gamma)$ terms. The effect of these choices is shown in Figure 5.12. Since we work at fixed $R = 0.2$, the $\ln(R)$ resummation amounts to an overall reduction of the cross section. The $\ln(\epsilon_\gamma)$ become important for $\epsilon_\gamma \lesssim 0.1$. The plot shows fixed-order results for smooth-cone isolation with $n = 1$, but our leading-logarithmic (LL) resummation of NGLs is insensitive to the isolation prescription since it only depends on the isolation via the associated scale μ_0. The isolation requirement changes the one-loop term (5.72), but this is a NLL effect.

ATLAS imposes $E_0 = \epsilon\,E_\gamma^T + E_{\text{th}}^T$ with $E_{\text{th}}^T = 4.8\,\text{GeV}$ and $\epsilon = 0.0042$, which which corresponds to a value $\epsilon_\gamma = E_0/E_\gamma^T \approx 0.04$ for $E_\gamma^T = 125\,\text{GeV}$. The threshold term E_{th}^T is added by ATLAS to avoid that E_0 reaches non-perturbative values, but our analysis makes it clear that the lowest scale in the problem is $R\,E_0$ which is close to $1\,\text{GeV}$ for $R = 0.2$ and $E_\gamma^T = 125\,\text{GeV}$. This corresponds to a value $t \approx 0.066$. (The value of t very slowly increases for larger E_γ^T and reaches $t \approx 0.07$ for $E_\gamma^T = 1\,\text{TeV}$.) Figure 5.12 shows that for $R = 0.2$ the resummation lowers the cross section by about 39 pb, about half of which is due to $\ln(R)$ resummation, while the other half is due to $\ln(\epsilon_\gamma)$ terms. For $R = 0.4$, the

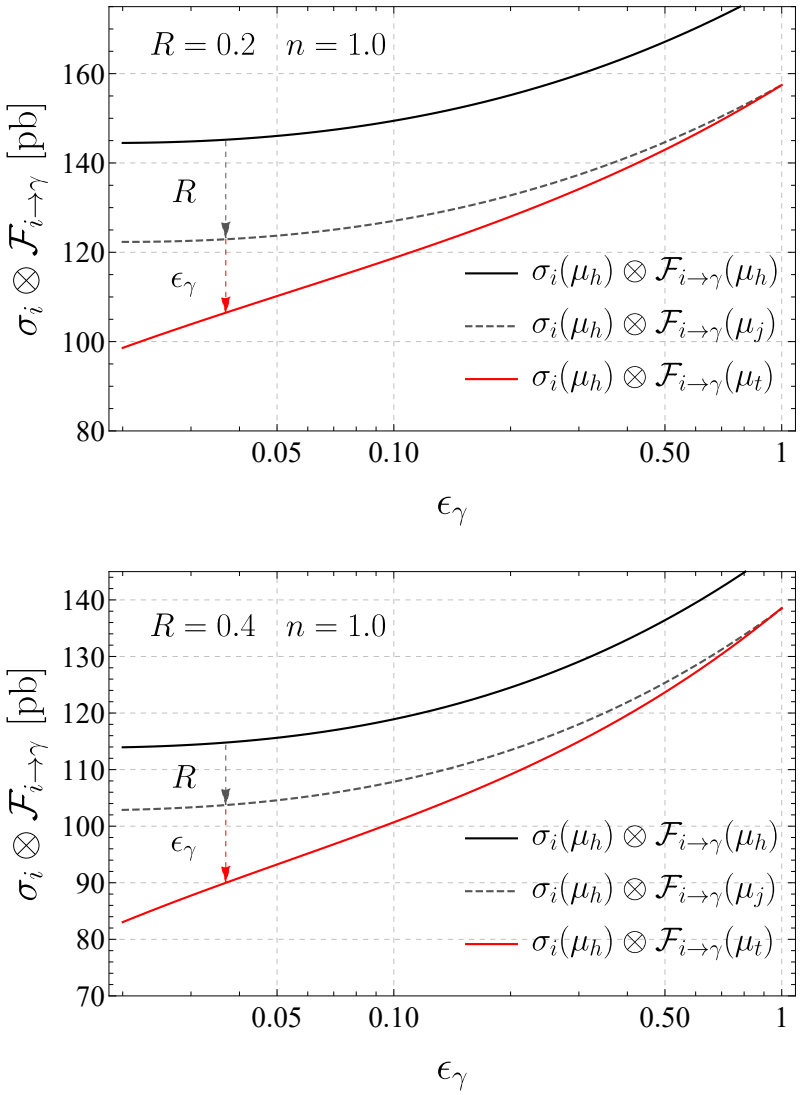

Figure 5.12: Effect of the resummation of $\ln(R)$ and $\ln(\epsilon_\gamma)$ terms for $R = 0.2$ (upper plot) and $R = 0.4$ (lower plot). The solid black curve shows the result without resummation, the dashed curve includes the resummation of $\ln(R)$ terms. The red curve resums both types of logarithms. Only the fragmentation contribution is shown, to obtain the full cross section the direct photon production contribution with $\sigma^{\rm dir} \approx 290\,{\rm pb}$ has to be added. (The direct cross section is somewhat lower than the one given in Section 5.3 because we use dynamic scales rather than fixed ones, see Table 5.1.)

$\ln(R)$ resummation effects are about half as large, while the size $\ln(\epsilon_\gamma)$ remains about the same.

5.8 Summary and conclusion

In this paper, we have studied in detail the structure of QCD effects associated with isolation requirements imposed in experimental measurements of photon production at high-energy colliders. We have have shown that for small cone radius R, the isolation effects can be described by cone fragmentation functions $\mathcal{F}_{i\to\gamma}$ describing the transition of an energetic quark or gluon into a photon plus accompanying QCD radiation. For small

isolation energy $E_0 = \epsilon_\gamma E_\gamma$, these fragmentation function factorize further into jet functions $\boldsymbol{\mathcal{J}}_{i\to\gamma+l}$ describing the l energetic partons outside the isolation cone boundary, and Wilson line matrix elements $\boldsymbol{\mathcal{U}}_l$ encoding the soft radiation emitted from these partons into the cone. Our factorization theorem separates the different scales present in the cross section: the hard scale $\mu_h \sim E_\gamma$, the jet scale $\mu_j \sim RE_\gamma$ and the isolation energy scale $\mu_0 \sim RE_0$. Using RG methods, we have resummed the leading logarithms of R and the non-global logarithms of ϵ_γ. The renormalization group also lets us evaluate each contribution at its natural scale.

To avoid low scales in the relevant perturbative computations current experimental measurements impose $E_0 \gtrsim 5\,\text{GeV}$, but our analysis demonstrates that for low jet radii one still reaches the dangerously low scale $\mu_0 \sim RE_0$. Values around $R = 0.2$ are commonly used in diphoton measurements, for example in [73, 114]. The presence of the low scale μ_0 is problematic for precision computations of photon production and higher-order problems might not immediately be visible since the isolation is a NLO effect which only affects a certain region of phase space. Even if the perturbative expansion fails for the isolation effects this might not yet be visible at NNLO, since there are other higher-order effects which are of the same size. Indeed, the NNLO cross sections are higher than the NLO results while the resummation effects we computed reduce the cross section.

Another simple but important result of our analysis is that the effect of non-perturbative fragmentation is suppressed by ϵ_γ. For small isolation energy this effect can thus be neglected, which is good news since the non-perturbative fragmentation functions are quite poorly known.

Our formalism cannot only be used to perform resummation, but also to convert results from one isolation prescription to another. Indeed, in our paper we have often discussed the difference between cross sections since it is directly proportional to the cone fragmentation functions. An interesting application of our fragmentation framework is to convert NNLO results computed with smooth-cone isolation to results in the fixed-cone scheme. We have presented a simple formula, which achieves this conversion in the limit of small ϵ_γ, which should be sufficient for most applications. Interestingly, the cross section difference is proportional to $n\,\zeta_3$, where n is the parameter of smooth-cone isolation. One could extend this result to arbitrary ϵ_γ by computing $\mathcal{F}_{i\to\gamma}$ at NLO.

Our computations were carried out in RG-improved perturbation theory at NLO. Since the fragmentation contribution only arises at $\mathcal{O}(\alpha_s)$, this corresponds to NLL resummation of the $\ln(R)$ terms and LL resummation of the $\ln(\epsilon_\gamma)$ contributions. To match the accuracy of fixed-order NNLO computations, we should extend the resummation to subleading logarithms of R and ϵ_γ. For the $\ln(R)$ resummation, the α_s^2 corrections to $P_{q\to\gamma}(z)$ and $P_{g\to\gamma}(z)$ are as of yet unknown and would need to be computed. For the resummation of $\ln(\epsilon_\gamma)$ the most important ingredient, namely the two-loop evolution, is available [115, 116, 112]. Only the one-loop boundary conditions, in particular the jet function with an additional parton, will need to be determined and implemented. We look forward to doing so in the future.

Acknowledgments

The authors thank Daniel de Florian, Thomas Gehrmann, Alexander Huss, Tobias Neumann and Ze Long Liu for interesting discussions and comments. We are grateful to Alexander Huss for providing benchmark cross section numbers for NNLOJET and to John Campbell and Tobias Neumann for help with MCFM. TB would like to thank the Pauli Center at ETHZ and the CERN theory department for hospitality during the com-

pletion of this work. This research is supported by the Swiss National Science Foundation (SNF) under grant 200020_182038.

5.A Splitting functions

The expansion coefficients of the splitting functions were defined in (5.42) and (5.43). The well-known leading-order QCD splitting functions are

$$\begin{aligned}
P^{(1)}_{q\to q}(z) &= P^{(1)}_{\bar{q}\to\bar{q}}(z) = C_F\left(\left(1+z^2\right)\left[\frac{1}{1-z}\right]_+ + \frac{3}{2}\delta(1-z)\right),\\
P^{(1)}_{g\to g}(z) &= C_A\left(z\left[\frac{1}{1-z}\right]_+ + \frac{1-z}{z} + z(1-z)\right) + \frac{\beta_0}{2}\delta(1-z),\\
P^{(1)}_{g\to q}(z) &= P^{(1)}_{g\to\bar{q}}(z) = T_F\left(z^2+(1-z)^2\right),\\
P^{(1)}_{q\to g}(z) &= P^{(1)}_{\bar{q}\to g}(z) = C_F\,P(z) = C_F\frac{1+(1-z)^2}{z},
\end{aligned} \tag{5.86}$$

with $\beta_0 = \frac{11}{3}N_c - \frac{4}{3}n_f T_F$. The coefficients of the parton-to-photon splitting kernels can be found in [53] and are given by

$$\begin{aligned}
P^{(0)}_{g\to\gamma}(z) &= 0\,,\\
P^{(0)}_{q\to\gamma}(z) &= P^{(0)}_{\bar{q}\to\gamma}(z) = Q_q^2\,P(z)\,,\\
P^{(1)}_{q\to\gamma}(z) &= P^{(1)}_{\bar{q}\to\gamma}(z) = \frac{C_F Q_q^2}{2}\left(-\frac{1}{2}+\frac{9}{2}z+\left(\frac{z}{2}-8\right)\ln z + 2z\ln(1-z) + \left(1-\frac{z}{2}\right)\ln^2 z\right.\\
&\quad\left.+\left[\ln^2(1-z)+4\ln z\ln(1-z)+8\,\mathrm{Li}_2(1-z)-\frac{4\pi^2}{3}\right]P(z)\right)\\
P^{(1)}_{g\to\gamma}(z) &= \frac{T_F\sum_{q=1}^{n_f}Q_q^2}{2}\left(-2+6z-\frac{82}{9}z^2+\frac{46}{9z}+\left(5+7z+\frac{8}{3}z^2+\frac{8}{3z}\right)\ln z+(1+z)\ln^2 z\right).
\end{aligned} \tag{5.87}$$

The factor $\sum_{q=1}^{n_f} Q_q^2$ is due to a quark loop and is 11/9 for $n_f = 5$ quark flavors. We note that the kernels $P^{(1)}_{q\to\gamma}(z)$ and $P^{(1)}_{g\to\gamma}(z)$ differ from the ones relevant for the space-like case, which are given in [30]. Note that compared to the expressions in [53, 30] we have an additional factor $\frac{1}{2}$ in $P^{(1)}_{q\to\gamma}$ and $P^{(1)}_{g\to\gamma}$ due different conventions: these references expand in $\frac{\alpha_s}{2\pi}$ instead of $\frac{\alpha_s}{\pi}$ and writes the evolution equations in the variable μ^2 instead of μ.

5.B Solution of the RG equations of the fragmentation functions

In order to solve (5.46), we perform a transformation of the fragmentation function such that the differential equations are decoupled from each other, i.e. one performs a basis change

$$\hat{\mathcal{F}}_{i\to\gamma}(N,\mu) = U_{ij}(N)\mathcal{F}_{j\to\gamma}(N,\mu) \tag{5.88}$$

and chooses the matrix $U_{ij}(N)$ in such a way that the splitting kernel becomes diagonal

$$U_{ij}(N)\mathcal{P}_{j\to k}(N,\mu)U^{-1}_{kl}(N) = \hat{\mathcal{P}}_{i\to i}(N,\mu)\delta_{il}\,. \tag{5.89}$$

This diagonalization step is only necessary for Σ and G in (5.41) since Δ is already decoupled from the other two quantities. The diagonalized evolution equation (5.46) takes the form

$$\frac{d}{d\ln\mu}\hat{\mathcal{F}}_{i\to\gamma}(N,\mu) = \hat{\mathcal{P}}_{i\to\gamma}(N,\mu) + \hat{\mathcal{P}}_{i\to i}(N,\mu)\hat{\mathcal{F}}_{i\to\gamma}(N,\mu)\,. \tag{5.90}$$

The solution of this differential equation is

$$\begin{aligned}\hat{\mathcal{F}}_{i\to\gamma}(N,\mu) = \exp\left[\int_{\mu_0}^{\mu} d\ln\mu'\,\hat{\mathcal{P}}_{i\to i}(N,\mu')\right] \\ \left\{\hat{\mathcal{F}}_{i\to\gamma}(N,\mu_0) + \int_{\mu_0}^{\mu} d\ln\mu''\exp\left[-\int_{\mu_0}^{\mu''} d\ln\mu'\,\hat{\mathcal{P}}_{i\to i}(N,\mu')\right]\hat{\mathcal{P}}_{i\to\gamma}(N,\mu'')\right\}\,.\end{aligned} \tag{5.91}$$

Because $\hat{\mathcal{P}}_{i\to i}(N,\mu)$ only depends on μ via the strong coupling,

$$\hat{\mathcal{P}}_{i\to i}(N,\mu) = \frac{\alpha_s(\mu)}{\pi}\hat{P}^{(1)}_{i\to i}(N) + \left(\frac{\alpha_s(\mu)}{\pi}\right)^2\hat{P}^{(2)}_{i\to i}(N) + \dots\,, \tag{5.92}$$

we can rewrite the exponential as

$$\begin{aligned}\mathcal{K}(\alpha_s(\mu_0),&\alpha_s(\mu)) = \exp\left[\int_{\mu_0}^{\mu} d\ln\mu'\hat{\mathcal{P}}_{i\to i}(N,\mu')\right] = \exp\left[\int_{\alpha_s(\mu_0)}^{\alpha_s(\mu)}\frac{d\alpha}{\beta(\alpha)}\hat{\mathcal{P}}_{i\to i}(N,\mu')\right] \\ &= \left(\frac{\alpha_s(\mu_0)}{\alpha_s(\mu)}\right)^{\frac{2\hat{P}^{(1)}_{i\to i}(N)}{\beta_0}}\left[1 + \frac{\alpha_s(\mu)-\alpha_s(\mu_0)}{4\pi}\frac{2}{\beta_0}\left(\frac{\beta_1}{\beta_0}\hat{P}^{(1)}_{i\to i}(N) - 4\hat{P}^{(2)}_{i\to i}(N)\right)\right]\end{aligned} \tag{5.93}$$

in which we have expanded

$$\beta(\alpha) = -2\alpha_s\left(\beta_0\frac{\alpha_s}{4\pi} + \beta_1\left(\frac{\alpha_s}{4\pi}\right)^2 + \dots\right) \tag{5.94}$$

and dropped higher-order terms. The solution can thus be rewritten as

$$\hat{\mathcal{F}}_{i\to\gamma}(N,\mu) = \mathcal{K}(\alpha_s(\mu_0),\alpha_s(\mu))\left[\hat{\mathcal{F}}_{i\to\gamma}(N,\mu_0) + \int_{\alpha_s(\mu_0)}^{\alpha_s(\mu)}\frac{d\alpha}{\beta(\alpha)}\mathcal{K}(\alpha,\alpha_s(\mu_0))\hat{\mathcal{P}}_{i\to\gamma}(\alpha)\right]\,, \tag{5.95}$$

where we suppressed the argument N of the splitting function on the right-hand side of the equation. Expanding also the inhomogeneous $\hat{\mathcal{P}}_{i\to\gamma}(N,\mu)$ as

$$\hat{\mathcal{P}}_{i\to\gamma}(N,\mu) = \frac{\alpha_{\text{EM}}}{\pi}\left(\hat{P}^{(0)}_{i\to\gamma}(N) + \frac{\alpha_s}{\pi}\hat{P}^{(1)}_{i\to\gamma}(N)\right)\,, \tag{5.96}$$

the final form of the solution reads

$$\begin{aligned}\hat{\mathcal{F}}_{i\to\gamma}(N,\mu) = &\frac{2\,\alpha_{\text{EM}}\,\hat{P}^{(0)}_{i\to\gamma}}{\alpha_s(\mu)(\beta_0 - 2\hat{P}^{(1)}_{i\to i})}\left(1 - \frac{\alpha_s(\mu)}{\alpha_s(\mu_0)}\mathcal{K}(\alpha_s(\mu_0),\alpha_s(\mu))\right) \\ &- \frac{\alpha_{\text{EM}}}{\pi}\left(\frac{\hat{P}^{(1)}_{i\to\gamma}}{\hat{P}^{(1)}_{i\to i}} - \frac{\beta_1}{4\beta_0}\frac{\hat{P}^{(0)}_{i\to\gamma}}{\hat{P}^{(1)}_{i\to i}} - \frac{\beta_1\hat{P}^{(0)}_{i\to\gamma}}{2\beta_0\left(\beta_0 - 2\hat{P}^{(1)}_{i\to i}\right)}\right)(1 - \mathcal{K}(\alpha_s(\mu_0),\alpha_s(\mu))) \\ &+ \mathcal{K}(\alpha_s(\mu_0),\alpha_s(\mu))\hat{\mathcal{F}}_{i\to\gamma}(N,\mu_0)\,,\end{aligned} \tag{5.97}$$

The first term in this solution corresponds to LL resummation and is proportional $1/\alpha_s$, the remaining two terms are the NLL corrections. In these two terms one can omit the $\mathcal{O}(\alpha_s)$ corrections to $\mathcal{K}$ in (5.93). In our numerical evaluation, we do not include β_1 terms and the corrections from $\hat{P}^{(2)}_{i\to i}(N)$ in the first line of (5.97) for simplicity, even though they would formally be needed for NLL accuracy and are available [48]. We verified that the β_1 terms are numerically very small.

After solving for $\hat{\mathcal{F}}_{i\to\gamma}(N,\mu)$ we first undo the decoupling change of variables (5.88) and go back to the original functions $\mathcal{F}_{j\to\gamma}(z,\mu)$. We then use the same Mellin inversion contour as in [117] to transform the $\hat{\mathcal{F}}_{i\to\gamma}(N,\mu)$ back to z space:

$$\mathcal{F}_{j\to\gamma}(z,\mu) = \frac{1}{\pi}\int_0^\infty \mathrm{d}r\,\mathrm{Im}\left[e^{i\phi}z^{-c-re^{i\phi}}\hat{\mathcal{F}}_{j\to\gamma}\left(N=c+re^{i\phi},\mu\right)\right], \tag{5.98}$$

where ϕ and c are parameters chosen as $\phi=\frac{3\pi}{4}$ and $c=1.8$ in our numerical evolution code.

5.C Computation of $\Delta\sigma$

To study the dependence on the parameters (ϵ_γ, n, R) of the smooth-cone isolation (5.2) we compute the difference to a reference cross section,

$$\Delta\sigma = \sigma\left(\epsilon_\gamma, n, R\right) - \sigma(\epsilon_\gamma^{\mathrm{ref}}, n^{\mathrm{ref}}, R^{\mathrm{ref}})\,.$$

In order for the difference to be be positive we require that the reference isolation $\left(\epsilon_\gamma^{\mathrm{ref}}, n^{\mathrm{ref}}, R^{\mathrm{ref}}\right)$ is the more restrictive one and we impose

$$\epsilon_\gamma \geq \epsilon_\gamma^{\mathrm{ref}} \quad , \quad n \leq n^{\mathrm{ref}} \quad , \quad R \leq R^{\mathrm{ref}}\,. \tag{5.99}$$

In this appendix, we provide details on the fixed-order determination of $\Delta\sigma$ and the computation of the difference based on cone fragmentation functions using (5.28).

5.C.1 Event-based fixed-order computation

Rather than computing the difference of NLO photon production cross sections, it is much more efficient to directly extract the cross section difference from the process $pp\to\gamma\,j\,j$ at LO by imposing suitable cuts on the partons. Working in this way, we can compute the difference from event files generated with MadGraph5_aMC@NLO [108] instead of needing individual NLO runs for all parameter values.

In order to get a contribution to $\Delta\sigma$ we need that at least one of the partons in the $pp\to\gamma\,j\,j$ event to be inside the larger cone with radius R^{ref}. The second parton will be outside the cone, since it is recoiling against the energetic photon. For an event to contribute to $\Delta\sigma$ it should respect the constraint imposed by isolation (ϵ_γ, n, R) but fail the one with the reference values $\left(\epsilon_\gamma^{\mathrm{ref}}, n^{\mathrm{ref}}, R^{\mathrm{ref}}\right)$. To formulate the resulting constraints on the transverse momenta p_i^T of the two final-state QCD partons $i\in\{1,2\}$ in the event explicitly, we distinguish three angular regions indicated in Figure C.2:

(I) $r_i > R^{\mathrm{ref}}$: at most one parton, no constraint on p_i^T,

(II) $R < r_i < R^{\mathrm{ref}}$: $\epsilon_\gamma^{\mathrm{ref}}\left(\frac{1-\cos r_i}{1-\cos R^{\mathrm{ref}}}\right)^{n^{\mathrm{ref}}} \leq \frac{p_i^T}{p_\gamma^T}$,

(III) $r_i < R$: $\epsilon_\gamma^{\mathrm{ref}}\left(\frac{1-\cos r_i}{1-\cos R^{\mathrm{ref}}}\right)^{n^{\mathrm{ref}}} \leq \frac{p_i^T}{p_\gamma^T} \leq \epsilon_\gamma\left(\frac{1-\cos r_i}{1-\cos R}\right)^{n}$,

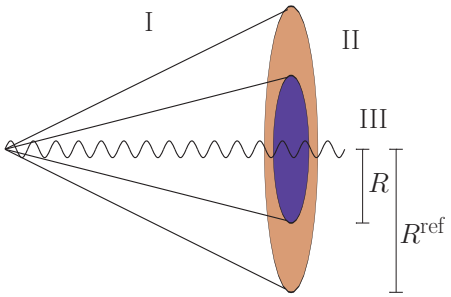

Figure 5.13: Isolation cones of radius R and R^{ref} and associated angular regions. The difference $\Delta\sigma$ is obtained from partonic configurations which fulfill the isolation criterion for cone radius R, but fail it for R^{ref}.

where r_i is the angular distance of the parton to the photon. The implementation of these non-standard cuts in MadGraph5_aMC@NLO is achieved by modifying the file `cuts.f`.

5.C.2 Fragmentation contribution

The fixed-order results are then compared with (5.28) based on the factorization theorem (5.3). According to (5.28) the leading contribution to the difference of cross sections is given by the partonic cross section $d\sigma_{i+X}/dE_i$ convoluted with the difference of fragmentation functions

$$\Delta\mathcal{F}_{i\to\gamma} = \mathcal{F}_{i\to\gamma}\left(z, R, \epsilon_\gamma, n\right) - \mathcal{F}_{i\to\gamma}\left(z, R^{\mathrm{ref}}, \epsilon_\gamma^{\mathrm{ref}}, n^{\mathrm{ref}}\right) . \tag{5.100}$$

We obtain the partonic cross section by using MadGraph5_aMC@NLO to generate event files for the process $pp \to j\,j$ at leading order. These have two QCD partons in the final state, each one of which can then fragment into a photon.

In the main text, we computed and plotted $\Delta\sigma$ for three different cases and we now list the relevant $\Delta\mathcal{F}_{i\to\gamma}$. To study the n-dependence of $\Delta\sigma$, we set $R = R^{\mathrm{ref}}$ and $\epsilon_\gamma = \epsilon_\gamma^{\mathrm{ref}}$ which yields

$$\Delta\mathcal{F}_{i\to\gamma} = \frac{\alpha_{\mathrm{EM}} Q_i^2}{2\pi} P(z)\,\theta\!\left(z - \frac{1}{1+\epsilon_\gamma}\right) \ln\left(\frac{1-z}{z\epsilon_\gamma}\right)\left(\frac{1}{n} - \frac{1}{n^{\mathrm{ref}}}\right) . \tag{5.101}$$

To study the R dependence, we set $\epsilon_\gamma = \epsilon_\gamma^{\mathrm{ref}}$ and $n = n^{\mathrm{ref}}$ which leads to

$$\Delta\mathcal{F}_{i\to\gamma} = \frac{\alpha_{\mathrm{EM}} Q_i^2}{\pi} P(z) \ln\left(\frac{R^{\mathrm{ref}}}{R}\right) . \tag{5.102}$$

The most complicated case is the ϵ_γ-dependence for which the relevant $\Delta\mathcal{F}_{i\to\gamma}$ for $R = R^{\mathrm{ref}}$ and $n = n^{\mathrm{ref}}$ was given in the main text in (5.34).

5.D Reference cross section values

In the main text we used MadGraph5_aMC@NLO [108] and MCFM [106] for our computations. The authors of [16] have compared their NNLOjet fixed-energy cone results at NLO to the JetPhoX code [11] and have provided reference cross section numbers for fixed-cone isolation in their paper. We have verified that MCFM reproduces the reference cross section in [16] within numerical uncertainties. The authors of [16] were kind enough to also provide us with reference cross section numbers for smooth-cone isolation

with $R = 0.4$, $n = 1.0$ and $\epsilon_\gamma = 0.0042$ and we have verified that all the above codes produce compatible results within numerical uncertainties. These reference cross sections were computed for $\alpha_{\rm EM} = 1/137$ and NNPDF31_nnlo_as_0118_mc PDFs, after imposing $E_\gamma^T \geq 125\,\text{GeV}$, $|\eta_\gamma| \leq 2.37$ and setting $\mu_F = \mu_R = p_\gamma^T$. For the leading order cross section and the NLO correction, they obtain

$$\sigma^{\rm LO} = (192.524 \pm 0.015)\,\text{pb}\,, \qquad \Delta\sigma^{\rm NLO} = (163.44 \pm 0.11)\,\text{pb}\,. \tag{5.103}$$

After requiring at least one jet with $p_{\rm jet}^T \geq 100\,\text{GeV}$ and $|\eta_{\rm jet}| \leq 2.37$ defined using the k_T algorithm with $R_{\rm jet} = 0.4$, the NLO correction reduces to

$$\Delta\sigma^{\rm NLO} = (121.441 \pm 0.065)\,\text{pb}\,. \tag{5.104}$$

Chapter 6

Outlook

In this thesis, a factorization theorem for narrow isolation cones is presented, where the cone fragmentation function $\mathcal{F}_{i\to\gamma}$ is describing the effect of the isolation for both Frixione and fixed-energy cones. We are able to separate the scales of the problem with our formalism. With the help of renormalization group methods, we are able to resum the logarithm of R and of ϵ_γ at NLL and LL respectively.

In the future, several extensions of this work would be of interest. First of all, our formalism could easily be extended to hybrid cone isolation, resumming the logarithms of the inner radius R_d and ϵ_γ would be instructive. To do so, the relevant fragmentation function needs to be computed. The NLO cross-section in other isolation prescriptions such as the hybrid cone at small R_d would be reduced by resummation and the prediction would become more reliable.

Moreover, performing both resummations at LL for the fixed-energy cone with the GdRG set and the BFG sets would allow us to get realistic and physical cross-sections with small ϵ_γ. Resummation will be physical, resummation would cure the unphysical behavior observed at NLO.

Computing the fragmentation function $\mathcal{F}_{i\to\gamma}$ at order $\alpha\alpha_s$ would be an obvious next step. This includes computing the α_s correction of the quark cone fragmentation function and computing the gluon cone fragmentation function. As a result, performing the $\ln R$ resummations at subleading logarithmic accuracy would be possible. This should not be too complicated, the $\ln R$ resummation at NNLL only requires the implementation of the splitting function $\mathcal{P}_{i\to j}$ at order α_s^2. Concerning the NLL resummation of the $\log\epsilon_\gamma$ terms, the resummation is performed with the help of the two-loop evolution [112, 115, 116]. The implementation is underway. These two subleading resummations and the NLO cone splitting functions would allow us to make interesting comparisons with the NNLO cross-sections of [15, 16]. It would also be good to combine the resummation with NNLO fixed-order result. This will result in NNLO predictions in RG-improved perturbation theory, i.e NNLO predictions without large logarithms of isolation parameters. The formula of (5.75) allows us to convert NNLO cross-sections from a Frixione cone to a fixed-energy cone, putting it to test would be instructive and could be done using NNLOJET.

On the experimental side, it would be interesting to have a measurement of isolated photons at the LHC with different cones sizes and isolation energy. This would allow us to test the predictions of Chapter 5 more extensively. Another important goal must be a more accurate determination of the non-perturbative fragmentation functions, which would reduce the uncertainties in the fixed-energy cone computations.

Appendix A

Mathematical tools

In this Appendix, some mathematical tools needed in this thesis are discussed. In particular, we review the so-called plus distribution, the Mellin transform/moment, its inversion and finally the Mellin moment of the splitting functions. This appendix is aimed at physicists, not mathematicians.

1 The plus distribution

Parts of the content of this section can be found in various books for example [26, 25, 27, 21]. Reference [118] was also used for this section.
The plus distribution arose in two contexts in this work. First it appeared in the computation of the Jet function in [71]. Second for the DGLAP equation, it can be found in the splitting functions (as in (2.19) for QCD and (2.20) for QED). In both contexts the plus distribution appears because of the divergences $x^{-1-\epsilon}$ and $(1-x)^{-1-\epsilon}$ respectively. The plus distribution is defined, for a test function $f(x)$

$$\begin{aligned}\int_0^1 \mathrm{d}x \left(\frac{1}{x}\right)_+ f(x) &= \int_0^1 \mathrm{d}x \frac{f(x)-f(0)}{x},\\ \int_0^1 \mathrm{d}x \left(\frac{1}{1-x}\right)_+ f(x) &= \int_0^1 \mathrm{d}x \frac{f(x)-f(1)}{1-x}.\end{aligned} \tag{A.1}$$

First let us discuss the plus distribution found in the jet function. The plus distribution of the jet function $\mathcal{J}_{q\to\gamma+q}$ of (5.67) will act on the coft function $\mathcal{U}_q$ of (5.72) while doing the integration on the variable $\widetilde{\Theta}$ as for example in (5.73). The plus distribution appeared while expanding in ϵ of dimensional regularization and we have an integral of the form

$$\int_0^1 \mathrm{d}\widetilde{\Theta} \frac{1}{\widetilde{\Theta}^{1+\epsilon}} \mathcal{U}_q\left(\widetilde{\Theta}\right). \tag{A.2}$$

Let us consider the integral (with $\epsilon < 0$) where we use x instead of $\widetilde{\Theta}$

$$\int_0^1 \mathrm{d}x \frac{1}{x^{1+\epsilon}} f(x). \tag{A.3}$$

We have the relation

$$\frac{1}{x^{1+\epsilon}} = -\frac{1}{\epsilon}\delta(x) + \left(\frac{1}{x}\right)_+ - \epsilon\left(\frac{\log x}{x}\right)_+ + \mathcal{O}\left(\epsilon^2\right). \tag{A.4}$$

The proof of which is straightforward

$$\begin{aligned}
&\int_0^1 \mathrm{d}x \frac{1}{x^{1+\epsilon}} f(x) = \int_0^1 \mathrm{d}x \frac{1}{x^{1+\epsilon}} \left(f(x) - f(0) + f(0)\right) = \\
&f(0) \int_0^1 \mathrm{d}x \frac{1}{x^{1+\epsilon}} + \int_0^1 \mathrm{d}x \frac{1}{x} \left(1 - \epsilon \log x + \mathcal{O}\left(\epsilon^2\right)\right) \left(f(x) - f(0)\right) = \\
&-\frac{1}{\epsilon} \int_0^1 \mathrm{d}x \delta(x) f(x) + \int_0^1 \mathrm{d}x \left(\frac{1 - \epsilon \log x}{x}\right)_+ f(x) + \mathcal{O}\left(\epsilon^2\right),
\end{aligned} \tag{A.5}$$

where we used $\int_0^1 \mathrm{d}x \frac{1}{x^{1+\epsilon}} = -\frac{1}{\epsilon}$.

The other context where the plus distribution appears in this work is the splitting function while solving the evolution of the fragmentation function. We have an equivalent relation to (A.6)

$$\frac{1}{(1-x)^{1+\epsilon}} = -\frac{1}{\epsilon}\delta(1-x) + \left(\frac{1}{1-x}\right)_+ - \epsilon \left(\frac{\log 1 - x}{1-x}\right)_+ + \mathcal{O}\left(\epsilon^2\right). \tag{A.6}$$

A subtlety that arises in this problem but also does in the context of the DGLAP equation of the PDF is the boundary of the integral in the convolution. Integral of the following form are found

$$\int_z^1 \mathrm{d}x \left(\frac{1+x^2}{1-x}\right)_+ f(x), \tag{A.7}$$

however the plus distribution is defined for integration from 0 to 1 and not from z to 1. The solution is to add a Heaviside function

$$\begin{aligned}
&\int_z^1 \mathrm{d}x \left(\frac{1+x^2}{1-x}\right)_+ f(x) = \int_0^1 \mathrm{d}x \left(\frac{1+x^2}{1-x}\right)_+ f(x)\theta(x-z) = \\
&\int_0^1 \mathrm{d}x \frac{1+x^2}{1-x} \left(f(x)\theta(x-z) - f(1)\theta(1-z)\right) = \\
&\int_z^1 \mathrm{d}x \frac{1+x^2}{1-x} \left(f(x) - f(1)\right) - f(1) \int_0^z \mathrm{d}x \frac{1+x^2}{1-x} = \\
&\int_z^1 \mathrm{d}x \frac{1+x^2}{1-x} \left(f(x) - f(1)\right) + f(1) \left(\frac{z^2}{2} + z + 2\log(1-z)\right),
\end{aligned} \tag{A.8}$$

and we get an extra term $f(1)\left(\frac{z^2}{2} + z + 2\log(1-z)\right)$. A similar trick can be used for the convolution with the splitting function $P_{g\to g}(x)$. The term of interest is

$$\int_z^1 \mathrm{d}x \frac{x}{(1-x)_+} f(x) = \int_z^1 \mathrm{d}x \frac{1}{1-z} \left[x f(x) - f(1)\right] - f(1)\ln(1-z). \tag{A.9}$$

Another interesting feature of the plus distribution can be seen when looking at the definitions of $P_{q\to q}^{(1,0)}(z)$. Two different ones are used in the literature and they are equivalent

$$P_{q\to q}^{(1,0)}(x) = C_F \left(\frac{1+x^2}{(1-x)_+} + \frac{3}{2}\delta(1-x)\right) \quad \text{or} \quad P_{q\to q}^{(1,0)}(x) = C_F \left(\frac{1+x^2}{(1-x)}\right)_+. \tag{A.10}$$

More generally we have the relation

$$\left(\frac{g(x)}{1-x}\right)_+ = \frac{g(x)}{(1-x)_+} - C\delta(1-x), \tag{A.11}$$

with $C = \int_0^1 \mathrm{d}x \left(\frac{1}{1-x}\right)_+ g(x)$. If the function on the $g(x)$ vanishes at 1, the + on the right-hand side of the above equation may be omitted. The relation can be proven simply

$$\begin{aligned}
&\int_0^1 \mathrm{d}x \left[\left(\frac{g(x)}{1-x}\right)_+ - \frac{g(x)}{(1-x)_+}\right] f(x) = \\
&\int_0^1 \mathrm{d}x \frac{g(x)}{1-x}\left(f(x) - f(1)\right) - \frac{1}{1-x}\left(g(x)f(x) - g(1)f(1)\right) = \\
&f(1)\int_0^1 \mathrm{d}x \frac{1}{1-x}\left(g(1) - g(x)\right) = -f(1)\int_0^1 \mathrm{d}x \frac{1}{(1-x)_+} g(x).
\end{aligned} \tag{A.12}$$

In the case of the quark to quark splitting function $g(x) = 1+x^2$ and therefore the constant is $C = -3/2$, which proves the equivalence of the two formulas for $P_{q\to q}^{(1,0)}$ in (A.10). The plus function can be omitted if not evaluated at the value of the pole

$$\left(\frac{f(x)}{1-x}\right)_+ = \frac{f(x)}{1-x} \quad \text{if } x \neq 1. \tag{A.13}$$

An alternative definition of the plus distribution can be found in [26]:

$$\frac{1}{(1-z)_+} = \lim_{\alpha\to 0}\left[\frac{1}{1-z}\theta\left(1-z-\alpha\right) - \delta\left(1-z\right)\int_0^{1-\alpha} \mathrm{d}y \frac{1}{1-y}\right]. \tag{A.14}$$

2 Mellin transform and Mellin moments

In this thesis, Mellin moments are used in order to solve a DGLAP equation. Mellin transform and moment have various other applications. In this appendix, we will first define the Mellin moment, show the inverse transformation with a simple example and give the Mellin moment of the splitting functions of (2.19) and (2.20). The content of this section can be found in the references [117, 118, 119].
The Mellin transform $\mathcal{MT}$ of a function $f(z)$ is defined as

$$\mathcal{MT}\left[f(z)\right](N) = \int_0^{+\infty} \mathrm{d}z z^{N-1} f(z). \tag{A.15}$$

The Mellin moment $\mathcal{M}$ of a function $f(z)$ is defined as

$$\mathcal{M}\left[f(z)\right](N) = \hat{f}(N) = \int_0^1 \mathrm{d}z z^{N-1} f(z). \tag{A.16}$$

In some references, the Mellin moment is called Mellin transform. The confusion also arises because performing the inversion of both the Mellin moment and the Mellin transform is pretty similar. Here, the Mellin moment is the one of interest and we will not discuss Mellin transform further, as in order to solve the evolution equation of the cone fragmentation function $\mathcal{F}_{i\to\gamma}$ (5.38), Mellin moments were used.

2.1 Properties of Mellin moments

The main property of the Mellin moment that we will need is

$$\mathcal{M}\left((f\otimes g)(z)\right) = \hat{f}(N)\hat{g}(N), \tag{A.17}$$

where $\otimes$ indicated the convolution defined in(2.18)

$$(f\otimes g)(z) = \int_0^1 dx \int_0^1 dy\, \delta(z-xy) f(x) g(y) = \int_z^1 \frac{\mathrm{d}y}{y} f(y)\, g\left(\frac{z}{y}\right). \tag{A.18}$$

The property (A.17) can be proven easily

$$\mathcal{M}(f\otimes g) = \int_0^1 \mathrm{d}z z^{N-1} (f\otimes g)(z) = \int_0^1 \mathrm{d}z \int_0^1 \mathrm{d}x \int_0^1 \mathrm{d}y\, z^{N-1}\delta(z-xy) f(x) g(y) = \int_0^1 \mathrm{d}x x^{N-1} f(x) \int_0^1 \mathrm{d}y y^{N-1} g(y) = \hat{f}(N)\hat{g}(N).$$

It is interesting to note that the Mellin moment is related to the Laplace transform $\mathcal{L}$ through

$$\mathcal{L}\left[f(z)\right](N) = \int_0^{\infty} \mathrm{d}z e^{-Nz} f(z) = \int_0^1 y^{N-1} f(-\ln y) = \mathcal{M}\left[f(-\ln y)\right](N), \tag{A.19}$$

where we used the change of variables $z = -\ln y$.

2.2 Inversion of Mellin moments

The inversion of the Mellin moment $\hat{f}(N)$ is done using the formula

$$f(z) = \frac{1}{2\pi i}\int_{c-i\infty}^{c+i\infty} \mathrm{d}N z^{-N}\hat{f}(N), \tag{A.20}$$

where c is a real number that has to be larger than all the real part of the poles of $\hat{f}(N)$. It means that $\hat{f}(N)$ has no real poles on the right of the integration contour between $c-i\infty$ and $c+i\infty$. This is shown on the left side of Figure A.1.
A useful way of performing this integral, can be found in [117], for a function satisfying $\hat{f}(N)^* = \hat{f}(N^*)$, by performing the change of variables $N \to c + r\exp(i\phi)$ the inversion is

$$f(z) = \frac{1}{\pi}\int_0^\infty \mathrm{d}r \mathrm{Im}\left[e^{i\phi}z^{-c-r\exp(i\phi)}\hat{f}\left(N = c + r\exp(i\phi)\right)\right]. \tag{A.21}$$

For the choice $\phi = \frac{\pi}{2}$, it follows

$$f(z) = \frac{1}{\pi}\int_0^\infty \mathrm{d}r \mathrm{Re}\left[z^{-c-ir}\hat{f}\left(c+ir\right)\right]. \tag{A.22}$$

2.3 Mellin moments: a simple example

We want to perform explicitly the Mellin moment and the inverse of the following function

$$f(z) = \theta\left(z - z_0\right). \tag{A.23}$$

We compute the Mellin moments

$$\hat{f}(N) = \int_0^1 \mathrm{d}z z^{N-1}\theta\left(z-z_0\right) = \frac{1}{N} - \frac{z_0^N}{N}. \tag{A.24}$$

Using the inverse formula, it is necessary to perform the following integral

$$\frac{1}{2\pi i}\int_{c-i\infty}^{c+i\infty} \mathrm{d}N \frac{1}{N}\left(\frac{1}{z^N} - \frac{z_0^N}{z^N}\right). \tag{A.25}$$

The following integral for with $\xi = \frac{1}{z}$ or $\frac{z_0}{z}$

$$\frac{1}{2\pi i}\int_{c-i\infty}^{c+i\infty} \mathrm{d}N \frac{\xi^{-N}}{N} = \begin{cases} 1 \, \xi < 1 \\ \frac{1}{2} \, \xi = 1 \\ 0 \, \xi > 1 \end{cases}. \tag{A.26}$$

is needed. In order to compute this integral for $\xi = 1$, the same change of variables than in (A.22) $N \to c + ri$ can be used

$$\begin{aligned} &\frac{1}{2\pi i}\int_{c-i\infty}^{c+i\infty} \mathrm{d}N \frac{\xi^{-N}}{N} = \frac{1}{2\pi}\int_{-\infty}^{+\infty} \mathrm{d}r \left(\xi^{-c-ir}\frac{1}{c+ir}\right) = \\ &\frac{1}{\pi}\int_0^\infty \mathrm{d}r \mathrm{Re}\left(\xi^{-c-ir}\frac{1}{c+ir}\right) = \frac{1}{\pi}\int_0^\infty \mathrm{d}r \xi^{-c}\frac{c\cos(r\ln\xi) - r\sin(r\ln\xi)}{c^2+r^2}, \end{aligned} \tag{A.27}$$

then with $\xi = 1$, the integral becomes the well-known integral

$$\frac{1}{\pi}\int_0^\infty \mathrm{d}r \frac{c}{c^2+r^2} = \frac{1}{2}. \tag{A.28}$$

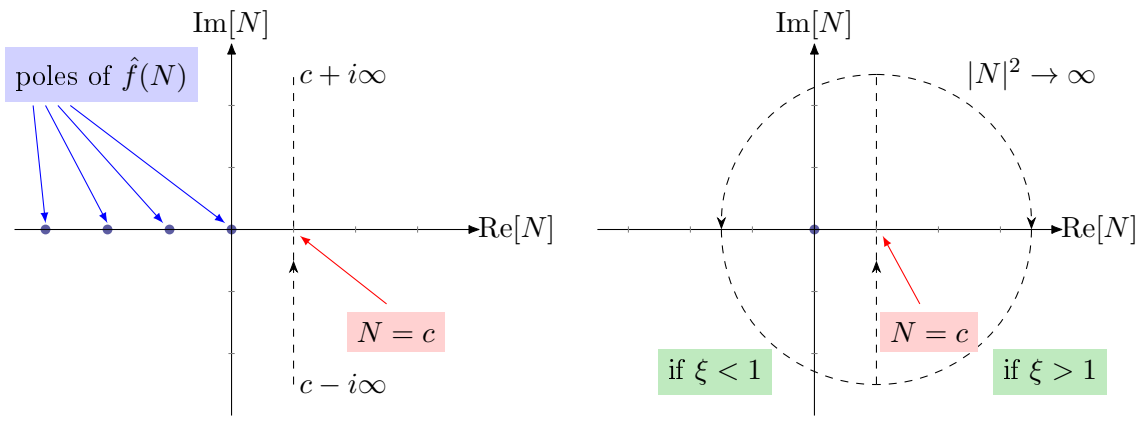

Figure A.1: Left: The line integral used to invert $\hat{f}(N)$ in (A.20). Note that all the real poles are on the left side of the line. Right: Integral contour used for the integral of (A.26), with the pole of $\frac{\xi^{-N}}{N}$ at $N = 0$ and $c = 1$. If $\xi > 1$, the contour is closed on the right, if $\xi < 1$ it is closed on the left.

For $\xi \neq 1$, it is possible to compute the integral with the help of some special functions. However, a simpler way of computing the integral is to use the Cauchy residue formula. The residue of the pole of ξ^{-N}/N at $N = 0$ is 1. The contours are shown in Figure A.1. If $\xi > 1$, we close the contour on the right and the contour does not have any pole and therefore the integral vanishes. If $\xi < 1$, we close the contour to the left, the contour has the pole and therefore the integral is 1.
We can now perform the inverse transformation and it follows that

$$\frac{1}{2\pi i}\int_{c-i\infty}^{c+i\infty} \mathrm{d}N \left(\frac{1}{z^N} - \frac{z_0^N}{z^N}\right) = \theta(1-z) - \theta\left(1 - \frac{z_0}{z}\right) = \theta(z - z_0) = f(z) : \tag{A.29}$$

2.4 Mellin moments of the splitting functions

In order to use the Mellin moment to solve the DGLAP equation, the Mellin moments of the QCD or QED leading order splitting functions need to be computed. This is straightforward if the Mellin moments of the following functions are known

$$\begin{aligned} \mathcal{M}\left(\delta(1-z)\right) &= 1, \\ \mathcal{M}\left(z^\alpha\right) &= \frac{1}{N+\alpha}, \\ \mathcal{M}\left(\frac{z^M}{(1-z)_+}\right) &= -\sum_{i=1}^{M+N-1} \frac{1}{i}. \end{aligned} \tag{A.30}$$

The proof of the two first equations is trivial. In order to show the last one, the geometric sum is used

$$\sum_{i=1}^{K-1} z^{i-1} = \frac{z^{K-1} - 1}{z - 1}, \tag{A.31}$$

as

$$\mathcal{M}\left(\frac{z^M}{(1-z)_+}\right) = \int_0^1 \mathrm{d}z \frac{z^M}{(1-z)_+} z^{N-1} = \int_0^1 \mathrm{d}z \frac{z^{N+M-1} - 1}{z - 1}. \tag{A.32}$$

Mellin moments of various functions can be found in [120] and [118]. The Mellin moment of the LO QCD splitting functions (2.19) are

$$\begin{aligned}
\hat{P}^{(1,0)}_{q\to q}(N) &= C_F\left(\frac{3}{2}-\frac{1}{N}-\frac{1}{(1+N)}-2(\gamma_E+\psi(N))\right),\\
\hat{P}^{(1,0)}_{g\to q}(N) &= \frac{T_R}{N}\frac{1}{2+N}\frac{2+N+N^2}{N+1},\\
\hat{P}^{(1,0)}_{q\to g}(N) &= -C_F\frac{2+N+N^2}{N^2+N},\\
\hat{P}^{(1,0)}_{g\to g}(N) &= 2C_A\left(\frac{2(1+N+N^2)}{(N(1+N)(-2+N+N^2)}-\gamma_E-\psi(N+1)\right)+\frac{\beta_0}{2},
\end{aligned} \tag{A.33}$$

with $\psi(N)$ the digamma function. If N is an integer the following relation holds

$$\gamma_E+\psi(N)=\sum_{k=1}^{N-1}\frac{1}{k}. \tag{A.34}$$

As one can see, the moment of the splitting functions containing a plus distribution $\left(\frac{1}{1-z}\right)_+$ diverge as $N\to\infty$, as predicted by a theorem from [118].
We can easily compute the Mellin moments of the LO QED splitting functions $P^{(0,1)}_{i\to j}$ (see (2.20)). They are quite similar to the QCD ones

$$\begin{aligned}
\hat{P}^{(0,1)}_{q\to q}(N) &= e_q^2\left(\frac{3}{2}-\frac{1}{N}-\frac{1}{(1+N)}-2(\gamma_E+\psi(N))\right),\\
\hat{P}^{(0,1)}_{\gamma\to q}(N) &= \frac{N_c e_q^2}{N}\frac{1}{2+N}\frac{2+N+N^2}{N+1},\\
\hat{P}^{(0,1)}_{q\to \gamma}(N) &= -e_q^2\frac{2+N+N^2}{N^2+N},\\
\hat{P}^{(0,1)}_{\gamma\to \gamma}(N) &= -\frac{2}{3}\sum_f e_f^2.
\end{aligned} \tag{A.35}$$

The last one is the only one that is actually significantly different. It is also possible (but more tedious) to perform the Mellin moment of the non-homogeneous term of (5.87)

$$\begin{aligned}
\hat{P}^{(1,1)}_{q\to \gamma}(N) = C_F e_q^2\Bigg[&(\psi(N)+\gamma_E)\frac{-6+N+17N^2+2N^2+3N^4-N^5}{N^2(N^2-1)^2}\\
&+\frac{N^2\left(35+47N+22N^2+8N^3\right)-4}{4N^3(1+N)^3}\\
&-\left(3\psi^{(1)}(N)+\frac{7\pi^2}{6}+(\psi(N)+\gamma_E)^2\right)\frac{N^2+N+2}{2N-2N^3}\Bigg]\\
\hat{P}^{(1,1)}_{g\to \gamma}(N) = T_F\sum_q e_q^2\frac{8-N\left[4+N\left(54+N(79+2N^2+7N)(7-N+N^2)\right)\right]}{2N^3(1+N)^2(N^2+N-2)^2}.
\end{aligned} \tag{A.36}$$

Appendix B

More details on the DGLAP equations

In this appendix, two changes of variables to simplify the DGLAP equation of PDF are discussed. These two changes of variables are instructive in order to learn how to solve other DGLAP-like equations like for example the one of $\mathcal{F}_{i\to\gamma}$. A simple example of a DGLAP-like equation is considered. This equation is solved both in z space and using the Mellin moments. This example is relevant for both the DGLAP equations of the PDF and photon fragmentation (both $\mathcal{D}_{i\to\gamma}$ and $\mathcal{F}_{i\to\gamma}$). This appendix complements Appendix 5.B and Chapter 2.

1 Change of variable for the DGLAP equation

Recall that the DGLAP equation for PDFs with n_f quark flavors is a $2n_f+1$ equation system. If the splitting functions $\mathcal{P}_{i\to j}$ are expanded to order α_s the DGLAP equation reads

$$\frac{\mathrm{d}f_i(z,\mu)}{\mathrm{d}\ln\mu^2} = \frac{\alpha_s(\mu)}{2\pi}\sum_{j=q,\bar{q},g} P^{(1,0)}_{j\to i}\otimes f_j(z,\mu), \tag{B.1}$$

where some of the $P^{(1,0)}_{j\to i}$ are vanishing. In the case of two quarks flavors u and d, at first order in QCD the splitting function between different quark flavors vanishes: $P_{q_i\to q_j} = \delta_{qiqj}P_{q\to q}$ where q_i and q_j are quarks or anti quarks. In the following we omit the $(1,0)$ superscript for readability. We use the short-hand notation that i is actually f_i the PDF of the parton i. Therefore the DGLAP equation is

$$\frac{d}{d\ln\mu^2}\begin{pmatrix} g\\ u\\ \bar{u}\\ d\\ \bar{d}\end{pmatrix}(z,\mu^2) = \frac{\alpha_s(\mu^2)}{2\pi}\begin{pmatrix} P_{g\to g} & P_{q\to g} & P_{q\to g} & P_{q\to g} & P_{q\to g}\\ P_{g\to q} & P_{q\to q} & 0 & 0 & 0\\ P_{g\to q} & 0 & P_{q\to q} & 0 & 0\\ P_{g\to q} & 0 & 0 & P_{q\to q} & 0\\ P_{g\to q} & 0 & 0 & 0 & P_{q\to q}\end{pmatrix}\otimes\begin{pmatrix} g\\ u\\ \bar{u}\\ d\\ \bar{d}\end{pmatrix}(z,\mu^2)\,. \tag{B.2}$$

To simplify such an equation a change of basis is performed. Typically a change of variables like the following is used in the literature, from the PDF of each parton $\left(g,u,\bar{u},d,\bar{d}\right)$ to

the following combinations

$$\begin{pmatrix} g \\ \Sigma \\ u_v \\ d_v \\ \Delta_c \end{pmatrix} = M \begin{pmatrix} g \\ u \\ \bar{u} \\ d \\ \bar{d} \end{pmatrix} = \begin{pmatrix} g \\ u+\bar{u}+d+\bar{d} \\ u-\bar{u} \\ d-\bar{d} \\ u+\bar{u}-d-\bar{d} \end{pmatrix}, \qquad M = \begin{pmatrix} 1 & 0 & 0 & 0 & 0 \\ 0 & 1 & 1 & 1 & 1 \\ 0 & 1 & -1 & 0 & 0 \\ 0 & 0 & 0 & 1 & -1 \\ 0 & 1 & 1 & -1 & -1 \end{pmatrix}. \tag{B.3}$$

where M is an invertible matrix. This change of variable is the analogue of the 2 quark flavors change of variables (B.6). The DGLAP equation then simplify to

$$\frac{d}{d\ln\mu^2} \begin{pmatrix} g \\ \Sigma \\ u_v \\ d_v \\ \Delta_c \end{pmatrix} (\mu^2, z) = \frac{\alpha_s(\mu^2)}{2\pi} \begin{pmatrix} P_{g\to g} & P_{q\to g} & 0 & 0 & 0 \\ 4P_{g\to q} & P_{q\to q} & 0 & 0 & 0 \\ 0 & 0 & P_{q\to q} & 0 & 0 \\ 0 & 0 & 0 & P_{q\to q} & 0 \\ 0 & 0 & 0 & 0 & P_{q\to q} \end{pmatrix} \otimes \begin{pmatrix} g \\ \Sigma \\ u_v \\ d_v \\ \Delta_c \end{pmatrix} (z). \tag{B.4}$$

Different changes of variables can be used to simplify the resolution of the DGLAP equations. The goal is to have only a few PDFs coupled in the convolution. In the case of n_f quark flavors the matrix is of dimension $(2n_f+1)$. Changes of variable can also be perform to bring it to a 2x2 matrix and a $2n_f - 1$ identity matrices

$$\begin{pmatrix} P_{g\to g} & P_{q\to g} & 0 \\ 2n_f P_{g\to q} & P_{q\to q} & \\ 0 & & \mathcal{I}_{2_f-1} P_{q\to q} \end{pmatrix}, \tag{B.5}$$

or something of a similar form with a maximum of one 2 times 2 matrix where 2 PDFs are coupled. This system of equations is simpler to solve than the original one. The 2 times 2 system and each 1 times 1 system need to be solved either in z space or using the Mellin moment. Let us quickly look at two possible changes of variables that can be used. First in [33] if you do not take into account the QED part of the variable you can find the following change of variables for $n_f = 5$

$$\begin{aligned} &g, \\ &\Sigma = \sum_q (q+\bar{q}), \\ &\Delta_1 = u+\bar{u}-\left(d+\bar{d}\right), \\ &\Delta_2 = u+\bar{u}+d+\bar{d}-2\left(s+\bar{s}\right), \\ &\Delta_3 = u+\bar{u}+d+\bar{d}+s+\bar{s}-3\left(c+\bar{c}\right), \\ &\Delta_4 = u+\bar{u}+d+\bar{d}+s+\bar{s}+c+\bar{c}-4\left(b+\bar{b}\right), \\ &q_v = q-\bar{q} \quad \text{with} \quad q = u,d,s,c,b, \end{aligned} \tag{B.6}$$

which is the change of basis we used earlier for 2 quark flavors in (B.3). Another slightly different basis can be found for example in [110] with $q_1 = u$, $q_2 = d$, $q_3 = ...$

$$\begin{aligned}
&g, \\
&\Sigma = \sum_q \left(q + \bar{q}\right), \\
&q^+_{NS,i} = q_i + \bar{q}_i - (q_1 + \bar{q_1}) \quad i = 2, ..., 5, \\
&q^-_{NS,i} = q_i - \bar{q}_i - (q_1 - \bar{q_1}) \quad i = 2, ..., 5, \\
&q^V_{NS} = \sum_i \left(q_i - \bar{q}_i\right),
\end{aligned} \tag{B.7}$$

with for example $q^+_{NS,2} = d + \bar{d} - (u + \bar{u})$ and so on. The letters NS stand for non-singlet and it means that these variables are then uncoupled from the rest. g and Σ are singlet and are coupled. One can check that both of these changes of variables bring the DGLAP equation to the form of (B.5).

In the case of the cone fragmentation function $\mathcal{F}_{i\to\gamma}$ the change of variable is given in (5.39). The change is in this case even more efficient than in the PDF case because instead of $2n_f - 1$ 1 times1 equations, we only have 1 of those equations due to the symmetry of the initial condition. This symmetry does not exist for the PDF and for example the variable $u_v = u - \bar{u}$ is not vanishing.

2 Two methods to solve a DGLAP-like equation

In this section, we want to briefly discuss a few examples of DGLAP-like equations and how to solve them in both z and Mellin space. The equation of interest in this section is a DGLAP-like equation of the function $F(\mu, z)$ of the following form

$$\frac{\mathrm{d}F(\mu, z)}{\mathrm{d}\ln\mu^2} = \mathcal{P}_{\text{inho}}(z, \mu) + \left(\mathcal{P}_{q\to q} \otimes F\right)(\mu, z), \tag{B.8}$$

with $\mathcal{P}_{\text{inho}}(z, \mu)$ an inhomogeneous splitting function. The equation shares similarities with the 1x1 non-singlet part of the cone fragmentation function $\mathcal{F}_{\Delta\to\gamma}$. In the case of DGLAP of PDFs the inhomogeneous term is absent, whereas for both the photon non-perturbative fragmentation $\mathcal{D}_{i\to\gamma}$ and the cone fragmentation function $\mathcal{F}_{i\to\gamma}$ there is such a term. For the sake of simplicity, we will first omit it.

Recall that the convolution is defined as

$$(f \otimes g)(z) = \int_z^1 \frac{\mathrm{d}y}{y} f(y) g(z/y). \tag{B.9}$$

We will discuss both the leading log (LL) solution and the next-to-leading log (NLL) of (B.8) with $\mathcal{P}_{\text{inho}} = 0$. For the LL equation, the splitting function need to be expanded at order α_s

$$\mathcal{P}_{q\to q}(z, \mu) = \frac{\alpha_s(\mu)}{2\pi} P^{(1,0)}_{q\to q}(z) + \mathcal{O}\left(\alpha_s^2\right), \tag{B.10}$$

and the running of α_s will be taken only at one loop ($\beta_i = 0$, $i > 0$). For the NLL equation, the splitting function needs to be expanded at order α_s^2

$$\mathcal{P}_{q\to q}(z, \mu) = \frac{\alpha_s(\mu)}{2\pi} P^{(1,0)}_{q\to q}(z) + \left(\frac{\alpha_s(\mu)}{2\pi}\right)^2 P^{(2,0)}_{q\to q}(z) + \mathcal{O}\left(\alpha_s^3\right), \tag{B.11}$$

and the running of α_s at two loops. Recall that the quark to quark splitting function $P^{(1,0)}_{q\to q}(z)$ is

$$P^{(1,0)}_{q\to q}(z) = C_F \left(\frac{1+z^2}{1-z}\right)_+ . \tag{B.12}$$

There are two ways of solving the equation which are equivalent. Either directly numerically in z-space i.e. step by step in μ or by using Mellin moments. In the case of the cone fragmentation function $\mathcal{F}_{i\to\gamma}$, both techniques were used. The agreement of both techniques can be seen in Figure 5.8.

If we decide to add an inhomogeneous term $\mathcal{P}_{\text{inho}}$ like it is the case for the cone fragmentation DGLAP equation the equation becomes at LL

$$\frac{\mathrm{d}F(z,\mu)}{\mathrm{d}\ln\mu^2} = \mathcal{P}_{\text{inho}} + \frac{\alpha_s(\mu)}{2\pi} P^{(1,0)}_{q\to q}(z) \otimes F(z,\mu)\,, \qquad F(z,\mu_0) = F_0(z), \tag{B.13}$$

in the case of $\mathcal{F}_{q\to\gamma}$ at leading-order this $\mathcal{P}_{\text{inho}}$ would be the QED splitting of a quark to a photon. In the following the function $\mathcal{P}_{\text{inho}}(z) = \frac{\alpha}{2\pi} P^{(0,1)}_{q\to\gamma}$ would be used as an example. By solving this equation with the correct initial condition we get the LL result of Figure 3.11.

2.1 The z-space solution

We need to use an extra Heaviside function as the plus distribution is defined between 0 and 1 and not between z and 1

$$\begin{aligned} P^{(1,0)}_{q\to q}(z) \otimes F(z,\mu) &= \int_z^1 \frac{\mathrm{d}y}{y} P_{q\to q}(y) F\left(\frac{z}{y},\mu\right) = \int_0^1 \mathrm{d}y\, C_F \left(\frac{1+y^2}{1-y}\right)_+ \frac{\Theta(y-z)}{y} F\left(\frac{z}{y},\mu\right) \\ &= C_F \int_z^1 \mathrm{d}y \frac{1+y^2}{1-y} \left(\frac{F\left(\frac{z}{y},\mu\right)}{y} - F(z,\mu)\right) - F(z,\mu)\, C_F \int_0^z \mathrm{d}y \frac{1+y^2}{1-y}. \end{aligned} \tag{B.14}$$

If the initial condition $F(z,\mu_0)$ diverges for $z\to 0$, we define $G(z,\mu) = zF(z,\mu)$ with no divergence at $z=0$. We obtain the following

$$\begin{aligned} &\mu\frac{dG(\mu,z)}{d\mu} = \frac{z}{\mu}\frac{\alpha_s(\mu)}{\pi} P^{(1,0)}_{q\to q}(z) \otimes F(\mu,z) = \\ &\frac{\alpha_s(\mu)}{\pi} C_F \left(\int_z^1 \mathrm{d}y \frac{1+y^2}{1-y}\left[G\left(\frac{z}{y},\mu\right) - G(z,\mu)\right] - G(z,\mu)\int_0^z \mathrm{d}y \frac{1+y^2}{1-y}\right) = \\ &\frac{\alpha_s(\mu)}{\pi} C_F \left(\int_z^1 \mathrm{d}y \frac{1+y^2}{1-y}\left[G\left(\frac{z}{y},\mu\right) - G(z,\mu)\right] + G(z,\mu)\left[\frac{1}{2}z(2+z) + 2\log(1-z)\right]\right). \end{aligned} \tag{B.15}$$

Note the presence of an extra term $G(z,\mu)\left(\frac{1}{2}z(z+2) + 2\ln(1-z)\right)$, see (A.8) and (A.9).

We can now discretize both the z space and the μ space to solve the equation. The choice of the z grid depends on the problem. A uniform grid is in the case of $\mathcal{F}_{i\to\gamma}$ not the optimal choice, however it can be used if efficiency is not important. Choosing a grid with more points where the function varies is more efficient. In this example, taking a grid with more points close to 0 and 1 will give better results in the case we considered in [71]. For example using a 60 points grid with 20 points in each intervals $[z_{min}, z_a] = [0.01, 0.1]$,

$[z_a, z_b] = [0.1, 0.9]$ and $[z_b, z_{max}] = [0.9, 0.99]$ respectively

$$z_i = \begin{cases} z_{min}^{1/3} + i/20 \left(z_a^{1/3} - z_{min}^{1/3} \right)^3 \\ z_a + i \dfrac{z_b - z_a}{20} \\ z_b^{1/3} + i/20 \left(z_{max}^{1/3} - z_b^{1/3} \right)^3 \end{cases} . \tag{B.16}$$

with $i = 0, 1, ..., 19$ was obviously more efficient than taking the same amount of points uniformly distributed between z_{min} and z_{max}.

In order to discretize the μ space it is more efficient to take a logarithmic discretisation than a linear one. We choose the μ_i

$$(\mu_0, \mu_1, ..., \mu_{N-1}, \mu_N = \mu_f) = (\mu_0, \mu_0 \exp(\Delta L), ..., \mu_0 \exp((N-1)\Delta L), \mu_0 \exp(N \Delta L) = \mu_f) ,$$

with $\Delta L = \log\left(\frac{\mu_f}{\mu_0}\right)/N$. The derivative is approximated using the Euler method

$$\frac{dG(z_k, \mu,)}{d\mu}\Big|_{\mu=\mu_{i+1}} \simeq \frac{G(z_k, \mu_{i+1}) - G(z_k, \mu_i)}{\mu_{i+1} - \mu_i} = \frac{G(z_k, \mu_{i+1}) - G(z_k, \mu_i)}{\mu_i (\exp(\Delta L) - 1)}. \tag{B.17}$$

In this scheme, we find that

$$\begin{aligned} G(z_k, \mu_{i+1}) = G(z_k, \mu_i) + (\exp(\Delta L) - 1) \frac{\alpha_s(\mu_i)}{\pi} C_F \left(\int_{z_k}^1 \mathrm{d}y \frac{1+y^2}{1-y} \left[G\left(\frac{z_k}{y}, \mu\right) - G(z_k, \mu) \right] \right. \\ \left. + G(z_k, \mu) \left[\frac{1}{2} z_k (2 + z_k) + 2 \log(1 - z_k) \right] \right) . \end{aligned} \tag{B.18}$$

Then for every z_k, it is possible to perform the integral over y numerically, which implies that for each μ_i it is necessary to perform a few integrals. The evolution is done step by step in μ. To solve a 2x2 coupled system of equations like the one for Σ and g (see (B.5)) directly in z space, one uses the same method in a 2-dimension vector space.

In the case of a non-homogeneous term $P_{\text{inho}}(z, \mu)$ the equation for G becomes

$$\mu \frac{dG(z, \mu)}{d\mu} = 2z \left(P_{\text{inho}} + \frac{\alpha_s(\mu)}{2\pi} P_{q \to q}^{(1,0)}(z) \otimes F(z, \mu) \right) . \tag{B.19}$$

We simply need to add on the RHS of (B.18) a term

$$2 z_k \left(\exp(\Delta L) - 1 \right) P_{inho} \left(z_k, \mu_i \right) . \tag{B.20}$$

Also in the case of the NLL equation, it is of course possible to also use the technique above.

2.2 Mellin space solution

With the help of the property (A.17) of Mellin moment

$$\mathcal{M} \left((f \otimes g)(z) \right) = \hat{f}(N) \hat{g}(N), \tag{B.21}$$

the LL equation in Mellin space is

$$\frac{\mathrm{d}\hat{F}\left(N, \mu\right)}{\mathrm{d} \ln \mu^2} = \frac{\alpha_s(\mu)}{2\pi} \hat{P}_{q \to q}^{(1,0)}(N) \hat{F}\left(N, \mu\right) , \tag{B.22}$$

which can be written

$$\frac{\mathrm{d}\hat{F}\left(N,\mu\right)}{\mathrm{d}\mu}=\frac{\alpha_s(\mu)}{\mu\pi}\hat{P}_{q\to q}^{(1,0)}(N)\hat{F}\left(N,\mu\right). \tag{B.23}$$

Solving this equation is straightforward

$$\hat{F}\left(\mu,N\right)=\hat{F}\left(N,\mu_0\right)\exp\left(\hat{P}_{q\to q}(N)\int_{\mu_0}^{\mu}\frac{\mathrm{d}\mu'}{\mu'}\frac{\alpha_s\left(\mu'\right)}{\pi}\right)=\hat{F}\left(N,\mu_0\right)\left(\frac{\alpha_s(\mu_0)}{\alpha_s(\mu)}\right)^{\frac{2\hat{P}_{q\to q}^{(1,0)}(N)}{\beta_0}}. \tag{B.24}$$

The last equality comes from the evolution equation of α_s at leading-order (2.2.1)

$$\mu^2\frac{\mathrm{d}\alpha_s\left(\mu\right)}{\mathrm{d}\mu^2}=-\frac{\alpha_s^2\left(\mu\right)}{4\pi}\beta_0\Rightarrow\frac{\mathrm{d}\mu'}{\pi\mu'}=-\mathrm{d}\alpha_s\frac{2}{\alpha_s^2\beta_0}. \tag{B.25}$$

The μ evolution is done in only one step in Mellin space, this tends to make it faster than the z space solution for the equation considered in this work. Then the solution is given by the inverse Mellin moment of $\hat{F}\left(\mu,N\right)$. This inversion is performed numerically with the help of (5.98).

The equation with an inhomogeneous term for example $\mathcal{P}_{\mathrm{inho}}=\frac{\alpha}{2\pi}P_{q\to\gamma}^{(0,1)}$ is

$$\frac{\mathrm{d}\hat{F}\left(N,\mu\right)}{\mathrm{d}\ln\mu}=\frac{\alpha}{\pi}\hat{P}_{q\to\gamma}^{(0,1)}(N)+\frac{\alpha_s(\mu)}{\pi}\hat{P}_{q\to q}^{(1,0)}(N)\hat{F}\left(N,\mu\right). \tag{B.26}$$

This equation is similar to the equation of Δ in the case of the cone fragmentation $\mathcal{F}_{i\to\gamma}$, except that the charge of Δ is not the same than the one of a quark. Therefore there is a prefactor in the initial condition of $\mathcal{F}_{\Delta\to\gamma}$ and in the inhomogeneous part which is due to the charge of the quark need to be replace by the charge of Δ. However, these differences are irrelevant for the present discussion. This equation is solved by

$$\begin{aligned}\hat{F}\left(\mu,N\right)&=\exp\left(\hat{P}_{q\to q}^{(1,0)}(N)\int_{\mu_0}^{\mu}\mathrm{d}\mu'\frac{\alpha_s\left(\mu'\right)}{\mu'\pi}\right)\left[\hat{F}\left(\mu_0,N\right)+\right.\\&\left.\int_{\mu_0}^{\mu}\frac{\mathrm{d}\mu''}{\mu''}\exp\left(-\hat{P}_{q\to q}^{(1,0)}(N)\int_{\mu_0}^{\mu''}\frac{\mathrm{d}\mu'}{\mu'}\frac{\alpha_s\left(\mu'\right)}{\pi}\right)\frac{\alpha}{\pi}\hat{P}_{q\to\gamma}^{(0,1)}(N)\right]\\&=\left(\frac{\alpha_s(\mu_0)}{\alpha_s(\mu)}\right)^{\frac{2\hat{P}_{q\to q}^{(1,0)}(N)}{\beta_0}}\left[\hat{F}\left(\mu_0,N\right)+\frac{\alpha}{\pi}\hat{P}_{q\to\gamma}^{(0,1)}(N)\int_{\mu_0}^{\mu}\frac{\mathrm{d}\mu''}{\mu''}\left(\frac{\alpha_s(\mu_0)}{\alpha_s(\mu'')}\right)^{\frac{-2\hat{P}_{q\to q}^{(1,0)}(N)}{\beta_0}}\right],\end{aligned} \tag{B.27}$$

the first part of the solution is the homogeneous one and there is an extra term due to the inhomogeneous splitting function. This solution is a simplified version of (5.91). The μ'' integral can be computed easily.

Finally, for the NLL, the splitting function is expanded up to α_s^2. In Mellin space the equation is

$$\frac{\mathrm{d}\hat{F}\left(N,\mu\right)}{\mathrm{d}\mu}=\frac{\alpha_s(\mu)}{\mu\pi}\left(\hat{P}_{q\to q}^{(1,0)}(N)+\frac{\alpha_s(\mu)}{2\pi}\hat{P}_{q\to q}^{(2,0)}(N)\right)\hat{F}\left(N,\mu\right), \tag{B.28}$$

where $\alpha_s(\mu)$ is computed at two-loop. Then the solution is given by

$$\hat{F}\left(\mu,N\right)=\hat{F}\left(\mu_0,N\right)\exp\left(\int_{\mu_0}^{\mu}\mathrm{d}\mu'\frac{\alpha_s\left(\mu'\right)}{\mu'\pi}\left[\hat{P}_{q\to q}^{(1,0)}(N)+\frac{\alpha_s\left(\mu'\right)}{2\pi}\hat{P}_{q\to q}^{(2,0)}(N)\right]\right), \tag{B.29}$$

where we used

$$\frac{\mathrm{d}\mu'}{\pi\mu'} = -\mathrm{d}\alpha_s \frac{2}{\alpha_s^2} \frac{1}{\beta_0 + \alpha_s \frac{\beta_1}{4\pi}}. \tag{B.30}$$

After the change of variables for μ' to $\alpha_s(\mu')$, it is possible to write the solution as

$$\hat{F}\left(N,\mu\right) = \hat{F}\left(N,\mu_0\right) \exp\left(\hat{P}_{q\to q}^{(1,0)}(N) I_1 + \hat{P}_{q\to q}^{(2,0)}(N) I_2\right), \tag{B.31}$$

with the two integrals that need to be computed

$$\begin{aligned} I_1 &= 2\int_{\alpha_s(\mu)}^{\alpha_s(\mu_0)} \mathrm{d}\alpha_s \frac{1}{\beta_0 + \alpha_s \frac{\beta_1}{4\pi}} = \frac{2}{\beta_0}\left(\ln\left[\frac{\alpha_s(\mu_0)}{1+\frac{\beta_1}{4\pi\beta_0}\alpha_s(\mu_0)}\right] - \ln\left[\frac{\alpha_s(\mu)}{1+\frac{\beta_1}{4\pi\beta_0}\alpha_s(\mu)}\right]\right), \\ I_2 &= \frac{1}{\pi}\int_{\alpha_s(\mu)}^{\alpha_s(\mu_0)} \mathrm{d}\alpha_s \frac{1}{\beta_0 + \alpha_s \frac{\beta_1}{4\pi}} = \frac{4}{\beta_1} \ln\left(\frac{\beta_0 + \frac{\beta_1}{4\pi}\alpha_s(\mu_0)}{\beta_0 + \frac{\beta_1}{4\pi}\alpha_s(\mu)}\right). \end{aligned} \tag{B.32}$$

The I_1 part of the exponential gives

$$\exp\left(\hat{P}_{q\to q}^{(1,0)}(N) I_1\right) = \left(\frac{\alpha_s(\mu_0)}{\alpha_s(\mu)} \frac{\beta_0 + \frac{\beta_1}{4\pi}\alpha_s(\mu)}{\beta_0 + \frac{\beta_1}{4\pi}\alpha_s(\mu_0)}\right)^{2\hat{P}_{q\to q}^{(1,0)}(N)/\beta_0}. \tag{B.33}$$

This recovers the LL results of (B.24), if we set $\beta_1 = 0$. The second part of the exponential is

$$\exp\left(\hat{P}_{q\to q}^{(2,0)}(N) I_2\right) = \left(\frac{\beta_0 + \frac{\beta_1}{4\pi}\alpha_s(\mu_0)}{\beta_0 + \frac{\beta_1}{4\pi}\alpha_s(\mu)}\right)^{4\hat{P}_{q\to q}^{(2,0)}(N)/\beta_1}. \tag{B.34}$$

If we expand the whole result (B.31) in $\alpha_s\left(\mu_0\right) \sim \alpha_s\left(\mu\right)$, we find (5.95) (except for a factor 2 due to the definition of the splitting functions). We find the solution of (5.97)

$$\hat{F}\left(N,\mu\right) = \hat{F}\left(N,\mu_0\right) \mathcal{K}(\alpha_s(\mu_0), \alpha_s(\mu)), \tag{B.35}$$

with all of the inhomogeneous parts of the equation set to 0. Expending $\mathcal{K}$ for small α_s is straightforward. The main challenge is to numerically perform the inverse Mellin moment transformation efficiently,especially for $z \to 1$. For more details on the Mellin moments see [109].

Appendix C

Use of MadGraph and MCFM

In order to write this thesis and [71], it was necessary to use both MadGraph5_aMC@NLO [108] and MCFM [106, 121]. Both programs were used to compute various cross-sections and to generate "Les Houches event files" [122]. In this appendix, details on how to reproduce the results presented in this work with the help of these programs.

I used the version 2.9.3 of MadGraph and 9.1 of MCFM. In order to get a prediction for the hybrid cone, I also used the version 10.2.1 of MCFM. The authors of MadGraph call their program MadGraph5_aMC@NLO, however for simplicity, I will call it MadGraph or use the abbreviation MG. In the following I will assume the reader has a basic knowledge on how to install and use MadGraph and MCFM. The references [123, 124] are helpful for getting started with MadGraph. MCFM has a manual [121].

Both MadGraph and MCFM are programs using Monte-Carlo methods in order to compute a vast variety of cross-sections. The two programs are written in Fortran. Both of these two programs have advantages and disadvantages. It was useful to be able to use both. For example MadGraph allows us to generate Les Houches event files, while MCFM can not do that. MCFM is able to compute cross-section with fixed energy cones, MadGraph is not. One extra reason to learn how to use both is that other photon codes such as JETPHOX and DIPHOX are old and not maintained anymore.

This appendix is organized as follows. First as an introduction, an example not directly related to my work will be discussed. This example is diphoton production at a proton collider with both MCFM and MadGraph. Doing an example is interesting to learn more about how to use both programs. It is also useful to test that the results of both programs are in agreement. Then the process of interest $pp \to \gamma + X$ will be discussed first with MadGraph, where I will discuss the problem of the precision of NLO fixed-order prediction. In the case of MCFM, I will discuss an issue I encounter: some parameters could not be passed by the user and some internal files have to be modified. The fixed energy cone σ^{NLO} will be compared to the predictions of other programs. Finally the procedure to generate non-isolated photon cross-sections at NLO will be discussed.

Disclaimers: part of my work was modifying some internal files of both programs, I am not a Fortran nor a MadGraph or MCFM expert and the following is addressed to beginners. While using MCFM, I encountered some problems, in particular for certain parameters of fixed-energy cones that were not particularly small or large, MCFM was not able to converge. The reason for this problem remains unknown to me as of today. Some cross-sections were computed with MCFM and checked with values generated with other programs like MadGraph, NNLOJET, JETPHOX or DIPHOX. All the checked results were in agreement. I only ran MCFM and MadGraph, the cross-section from the three other programs are either taken from a reference. The NNLOJET values in Tables C.7

$\sqrt{s} = 14\,\text{TeV}$	$20 \leq m_{\gamma\gamma} \leq 250$ GeV	$\mu_R = \mu_F = a m_{\gamma\gamma}$
$p_{T1}^{\gamma} \geq 25$ GeV	$p_{T2}^{\gamma} \geq 40$ GeV	$\lvert\eta_\gamma\rvert < 2.5$
`MSTW2008lo68cl` [125]	`MSTW2008nlo68cl`	$\alpha = \frac{1}{137}$
$R = 0.4$	$\epsilon_\gamma = 0.5$	$n = 1.0$

Table C.1: Parameters for the diphoton production used in [77, 76], and here with MadGraph and MCFM to reproduce the results of both references. Note that the parameter a for scale variation is taken to be 1,2 and $\frac{1}{2}$ and Frixione cone was used. The values of the strong coupling are for `MSTW2008lo68cl` $\alpha_s(M_Z) = 0.139$ and for `MSTW2008nlo68cl` $\alpha_s(M_Z) = 0.120$.

and C.8 were generously provided by Alexander Huss.

1 Warmup: $pp \to \gamma\gamma$ using MadGraph and MCFM

In order to test if MadGraph and MCFM predictions are compatible and to learn how to use both programs, I will reproduce with MadGraph the results for diphoton production at a pp collider from [77]. These results were obtained with MCFM. These predictions were also compared to results from [76] obtained with the program DIPHOX. [1]

I want to compute the total cross section of $pp \to \gamma\gamma$ both at leading-order and next-to-leading order ($pp \to \gamma\gamma + X$) with the parameters of Table C.1. Even though this problem is not directly linked to the production of a single isolated photon, it is instructive as it is necessary to modify certain MadGraph files. It allows us to see differences in the use of both programs. The first difference between MG and MCFM arises while trying to use 5 massless quark flavors for all the following computations. For MadGraph, we have to tell it to use the bottom quark by importing an extra model in order to include the (massless) bottom quark, the instructions to provide to MadGraph are:

```
import model loop_sm-no_b_mass
generate p p > a a [QCD]
output name_of_output
launch
```

Recall that in MG, photons are designated by the letter `a`. The `[QCD]` is here to say that we want to have next to leading-order in α_s. In MCFM, the bottom quark is included when we call the process 285. However it is not massless by default and it is required to change its mass in the input file.

The parameters used in our computation are in Table C.1. The two photons are isolated using Frixione cones. The listed parton distribution functions used are `MSTW2008lo68cl` for LO and `MSTW2008nlo68cl` for NLO. Note that using the NLO PDFs set for the leading order computation increases the cross-section. Ones uses the PDFs and α_s to generate part of the NLO terms. The harder of the 2 photons was required to have more than 40 GeV of transverse momentum and the softer one more than 25 GeV. Conveniently in MCFM,

[1] The idea of reproducing these results with both MG and MCFM was suggested by Tobias Neumann.

most parameters are implemented in the `.ini` file. To set the scales, we have to do the following in input file:

```
[scales]
# Renormalization scale
renscale = 1
# Factorization scale
facscale = 1
# Controls use of dynamical scale
# when different from 'none', set renscale and facscale to 1
dynamicscale = m(34)
# perform scale variation
doscalevar = .true.
# can be 2 or 6 for 2-point or 6-point scale-variation
maxscalevar = 2
```

While for MadGraph, it is more involved, it is required to change the `/SubProcesses/setscales.f`. This file reads:

```
LOGICAL IS_A_J(NEXTERNAL),IS_A_LP(NEXTERNAL),IS_A_LM(NEXTERNAL)
LOGICAL IS_A_PH(NEXTERNAL)
COMMON /TO_SPECISA/IS_A_J,IS_A_LP,IS_A_LM,IS_A_PH
double precision pgammatot(0:3)
...
...
elseif(dynamical_scale_choice.eq.10) then
ccccccccccccccccccccccccccccccccccccccccccccccccccccccccccccccccccccccccc
cc USER-DEFINED SCALE: ENTER YOUR CODE HERE cc

tmp = 0d0
do j=0,3
pgammatot(j)=0d0
enddo

do i=3, nexternal
if(is_a_ph(i)) then
do j=0,3
pgammatot(j)=pgammatot(j)+pp(j,i)
enddo
endif
enddo
tmp=dsqrt(pgammatot(0)*pgammatot(0)-pgammatot(1)*pgammatot(1)-
pgammatot(2)*pgammatot(2)-pgammatot(3)*pgammatot(3))
ccccccccccccccccccccccccccccccccccccccccccccccccccccccccccccccccccccccccc
endif
scale_global_reference=tmp
```

We first need to make sure that we have access to the function `is_a_ph()`, which allows us to say if a particle is a photon. Then we declare an array of four `double precision` in order to store $p_1^\gamma + p_2^\gamma$, the sum of the four-momentum of the two photons . We then loop over the external particles (so from 3 to `nexternal`, as 1 and 2 are the incoming partons)

and if it is a photon, we add its four-momentum to the total four-momentum `pgammatot`. Finally the transverse mass $m_{\gamma\gamma} = \sqrt{(p_{x\gamma}^2 + p_{y\gamma}^2)}$ is computed and stored in the variable `tmp`. Moreover we need to set `dynamical_scale_choice = 10` in the `runcard.dat`.

Then we have to require that the invariant mass of the diphoton satisfies $20\,\text{GeV} \leq m_{\gamma\gamma} \leq 250\,\text{GeV}$. On top of that we require one of the photons to have at least $p_T = 25$ GeV and the second to have 40 GeV. Both are implemented in the `.ini` file in MCFM

```
[masscuts]
# minimum mass of 3-4 system
m34min = 20.0
# optional, maximum mass of 3-4 system, otherwise sqrts
m34max = 250.0

...

[photon]
# include fragmentation
fragmentation = .false.
# fragmentation set
fragmentation_set = GdRG__LO
# fragmentation scale
fragmentation_scale = 1.0
# minimum photon pT; can also have gammptmax
gammptmin = 40.0
# maximum photon rapidity; can also have gammrapmin
gammrapmax = 2.5
# second photon minimum pT
gammpt2 = 25.0
...
```

In the case of MadGraph a little more effort is required, we have to modify the `/SubProcesses/cuts.f`. For the transverse momentum, I required first both photons to have at least $p_T = 25$ GeV in the `run_card.dat`

```
25.0 = ptgmin ! Min photon transverse momentum
2.5 = etagamma ! Max photon abs(pseudo-rap)
0.4 = R0gamma ! Radius of isolation code
1.0 = xn ! n parameter of eq.(3.4) in hep-ph/9801442
0.5 = epsgamma ! epsilon_gamma parameter of eq.(3.4) in hep-ph/9801442
True = isoEM ! isolate photons from EM energy (photons and leptons)
```

and then in the `/SubProcesses/cuts.f`, it is enforced that one of the two photon has at least 40 GeV

```
double precision maa
double precision pgammatot(0:3)
...
...
C*************************************************************
```

```
C--------------------------------------------------------------------
C PUT HERE YOUR USER-DEFINED CUTS
C--------------------------------------------------------------------
C--------------------------------------------------------------------
C

do j=0,3
pgammatot(j)=pgamma(j,1)+pgamma(j,2)
enddo
maa=dsqrt(pgammatot(0)*pgammatot(0)-pgammatot(1)*pgammatot(1)-
pgammatot(2)*pgammatot(2)-pgammatot(3)*pgammatot(3))
if((maa.lt. 20d0) .or. (maa.gt. 250d0))then
passcuts_user=.false.
return
endif

if(( dsqrt(pgamma(1,1)**2+pgamma(2,1)**2) .lt. 40d0) .and.
( dsqrt(pgamma(1,2)**2+pgamma(2,2)**2) .lt. 40d0 )) then
passcuts_user=.false.
return
endif
```

First, the invariant mass `maa` is declared (MG calls photons `a`) and the total photon momentum `pgammatot`. While doing the cuts, the momentums of the photons are already extracted and stored in `pgamma(i,j)` with `i=0,1,2,3` and `j=1,...,nph`. Here we only have 2 photons `j=1,2`. Then in the part of the file that is planned to add user-defined cuts, I first compute the total photon momentum and the invariant mass of the diphoton system. Then if it is not in the interval 20 to 250, `passcuts_user` is set to `false`. After that I test both transverse momentum $p_i^T = \sqrt{p_{xi}^2 + p_{yi}^2}$ and if both are less than 40 GeV, I also set `passcuts_user` to `false` as at least one of the two γ needs to have more than 40 GeV. Finally in both cases, we need to make sure we use the same electromagnetic coupling α, in the case of MCFM, it is hidden in `src/User/mdata.f`:

```
* Calculational scheme for EW couplings *
************************************************************************
c
c ewscheme=-1 : Old MCFM default
c input values = Gf,alpha(m_Z),m_W,m_Z
c output values = sin^2(theta_W),mtop
c
c ewscheme=0 : Old MadEvent default (= AlpGen with iewopt=2)
c input values = sin^2(theta_W),alpha(m_Z),m_Z
c output values = m_W,Gf.
c ....
c
c
include 'ewinput.f'
data ewscheme / 0 / ! Chooses EW scheme
data Gf_inp / 1.16639e-5_dp / ! G_F
```

σ [fb]	LO	NLO
$\mu_F = \mu_R = m_{\gamma\gamma}/2$	5045 ± 1	26581 ± 23
$\mu_F = \mu_R = m_{\gamma\gamma}$	5712 ± 2	26402 ± 25
$\mu_F = \mu_R = 2m_{\gamma\gamma}$	6319 ± 2	26045 ± 24

Table C.2: Cross-sections of diphoton production obtained using DIPHOX from [76].

σ [fb]	LO	NLO
$\mu_F = \mu_R = m_{\gamma\gamma}/2$	5043 ± 1	26578 ± 13
$\mu_F = \mu_R = m_{\gamma\gamma}$	5710 ± 1	26444 ± 12
$\mu_F = \mu_R = 2m_{\gamma\gamma}$	6315 ± 2	26110 ± 13

Table C.3: Cross-sections of diphoton production obtained using MCFM from [77]. The input file described in this section generates similar values.

```
data aemmz_inp / 7.29927e-3_dp / ! alpha_EM(m_Z)=1/137
data xw_inp / 0.2223_dp / ! sin^2(theta_W)
data wmass_inp / 80.385_dp / ! W mass
data zmass_inp / 91.1876_dp / ! Z mass
**********************************************************************
```

where I only changed the value of `aemmz_inp`. For MadGraph it is simply in the `param_card.dat`

```
BLOCK SMINPUTS #
1 1.370000e+02 # aewm1
```

All other parameters that need to be tuned, are tuned in the `.ini` file for MCFM or in the `run_card.dat` for MadGraph. Note that every time you modify a file in the `src` folder of MCFM, you have to make the program again.

Using MadGraph we obtain similar results for the total cross-section, see Tables C.2 to C.4. The cross-section computed from MadGraph were obtained by averaging $N = 5$ runs in order to achieve better precision. The error was computed using the formula

$$\delta\sigma = \sqrt{\frac{\sum_{i=1}^{N} \delta\sigma_i^2}{N^2}}, \tag{C.1}$$

where $\delta\sigma_i$ is the error of run number i.

σ [fb]	LO	NLO
$\mu_F = \mu_R = m_{\gamma\gamma}/2$	5046 ± 1	26592 ± 5
$\mu_F = \mu_R = m_{\gamma\gamma}$	5716 ± 1	26460 ± 5
$\mu_F = \mu_R = 2m_{\gamma\gamma}$	6322 ± 1	26115 ± 4

Table C.4: Cross-sections of diphoton production obtained using MadGraph

2 MadGraph: single photon production

In this section, the use of MadGraph to compute the production of a photon at NLO is discussed in detail. The issue of the precision of MadGraph for NLO single photon production is also discussed. Finally the details on how to compute $\Delta\sigma$. This complements the appendix 5.C of [71].

2.1 $pp \to \gamma + X$ at NLO

In order to use MadGraph at NLO for the process $pp \to \gamma$ + jet(s), we need:

```
import model loop_sm-no_b_mass
generate p p > a j [QCD]
output name_of_file
launch
```

Note that this will generate both $pp \to \gamma + 2\,\text{partons}$ and the loop corrections of $pp \to \gamma + 1\,\text{parton}$. In the run card we need to change a few things, in the beginning:

```
10000 = nevents ! Number of unweighted events requested
0.003 = req_acc_FO ! Required accuracy (-1=ignored, and use the !
number of points and iter. below)
```

If we want to study the dependence of σ on the parameters (ϵ_γ, n, R) of the Frixione isolation. MadGraph is not extremely precise and we need to make multiple runs in order to see a clear tendency. I ran MadGraph at NLO with the parameters of Table C.5. The exact value of the parameters is not relevant for the following discussion. In order to use for μ_F and μ_R the dynamic scale p_γ^T, it is necessary to modify the `/SubProcesses/setscales.f`, it has similarities with what was required to do for the diphoton production to set $m_{\gamma\gamma}$ as the dynamic scale. The modified file reads

```
LOGICAL IS_A_J(NEXTERNAL),IS_A_LP(NEXTERNAL),IS_A_LM(NEXTERNAL)
LOGICAL IS_A_PH(NEXTERNAL)
COMMON /TO_SPECISA/IS_A_J,IS_A_LP,IS_A_LM,IS_A_PH
...
...
    elseif(dynamical_scale_choice.eq.10) then
    ccccccccccccccccccccccccccccccccccccccccccccccccccccccccccccccccccccc
    cc USER-DEFINED SCALE: ENTER YOUR CODE HERE cc

    tmp = 0d0
    do i=3, nexternal
        if(is_a_ph(i)) then
            tmp=tmp+et(pp(0,i))
        endif
    enddo
ccccccccccccccccccccccccccccccccccccccccccccccccccccccccccccccccccccc
    endif

scale_global_reference=tmp
```

Where I looped over the `nexternal` particles and stored the photon transverse energy in the `tmp` variable. The results of a few runs can be seen in Figure C.1.

σ^{LO} does not depend on the variation of the ϵ_γ parameters. The reason is that at leading order the jet will not be in the cone due to kinematics. At next-to-leading order we see that the cross-section decreases when ϵ_γ decreases. The smaller ϵ_γ, the less energy is allowed in the cone, hence the stricter the constraint is. The following relation should hold (4.23)

$$\sigma(\epsilon_\gamma) \searrow \quad \text{if} \quad \epsilon_\gamma \searrow . \tag{C.2}$$

However the change of the cross-section is small. We see that if we had run the NLO only once, we may think that the cross-section is even independent of the isolation parameter or worse we could see the opposite behavior. For example, the 9th run with $\epsilon_\gamma = 0.9$ ($\sim 434.5\,\mathrm{pb}$) is larger than the 3rd run with $\epsilon_\gamma = 1.0$ ($\sim 433\,\mathrm{pb}$) and the relation of (C.2) would not be satisfied. The accuracy of single runs is not sufficient. The averages over the 10 runs satisfy $\sigma^{\mathrm{NLO}}(\epsilon_\gamma = 1.0) > \sigma^{\mathrm{NLO}}(\epsilon = 0.9)$ and the condition (C.2) is satisfied. Moreover the uncertainty of a single run is large compared to the dependence of the cross-section on ϵ_γ.

In conclusion, it is necessary to run MadGraph multiple times with a higher accuracy, if we want to study the dependence of the cross-section on its parameters. This is time consuming on a personal computer and we had to resort to using the cluster. In order to avoid this problem, it is useful to directly compute cross-section differences. This will be discussed in the following section.

2.2 $\Delta\sigma$ of $pp \to \gamma +$ jet(s) at NLO

Rather than computing the difference of NLO photon production cross sections, it is much more efficient to directly extract the cross section difference from the process $p\,p \to \gamma\,j\,j$ at LO by imposing suitable cuts on the partons. Working in this way, we can compute the difference from event files generated with MadGraph5_aMC@NLO [108] instead of needing individual NLO runs for all parameter values.

The idea is the following: first we compute precisely the cross section for a certain set of reference parameters, for example

$$\epsilon_\gamma^{\mathrm{ref}} = 1.0 \quad n^{\mathrm{ref}} = 1.0 \quad R^{\mathrm{ref}} = 0.4. \tag{C.3}$$

We then modify some internal files of MadGraph to compute $\Delta\sigma$. This is the difference of a cross-section $\sigma\left(\epsilon_\gamma, n, R\right)$ with parameters (ϵ_γ, n, R) to the reference cross-section $\sigma^{\mathrm{ref}} = \sigma\left(\epsilon_\gamma^{\mathrm{ref}}, n^{\mathrm{ref}}, R^{\mathrm{ref}}\right)$.

For an event to contribute to $\Delta\sigma$ it should respect the constraint imposed by isolation (ϵ_γ, n, R) but fail the one with the reference values $\left(\epsilon_\gamma^{\mathrm{ref}}, n^{\mathrm{ref}}, R^{\mathrm{ref}}\right)$. In other words, the (ϵ_γ, n, R) cone is satisfied and the reference $\left(\epsilon_\gamma^{\mathrm{ref}}, n^{\mathrm{ref}}, R^{\mathrm{ref}}\right)$ one should not be. In order to get a contribution to $\Delta\sigma$ we need that at least one of the partons in the $p\,p \to \gamma\,j\,j$ event to be inside the larger cone with radius R^{ref}. The second parton will be outside the cone, since it is recoiling against the energetic photon. In order for $\Delta\sigma$ to be positive and for the procedure to be working, it is imperative that the reference cone $\left(\epsilon_\gamma^{\mathrm{ref}}, n^{\mathrm{ref}}, R^{\mathrm{ref}}\right)$ is more restrictive than the (ϵ_γ, n, R) cone. Recall that in order for this constraint to be respected we need to impose that

$$\epsilon_\gamma \geq \epsilon_\gamma^{\mathrm{ref}} \quad , \quad n \leq n^{\mathrm{ref}} \quad , \quad R \leq R^{\mathrm{ref}} . \tag{C.4}$$

In terms of the transverse momenta p_i^T of the two final-state QCD partons $i \in \{1, 2\}$ in the event explicitly, we distinguish three angular regions. Regions I) is outside both cones

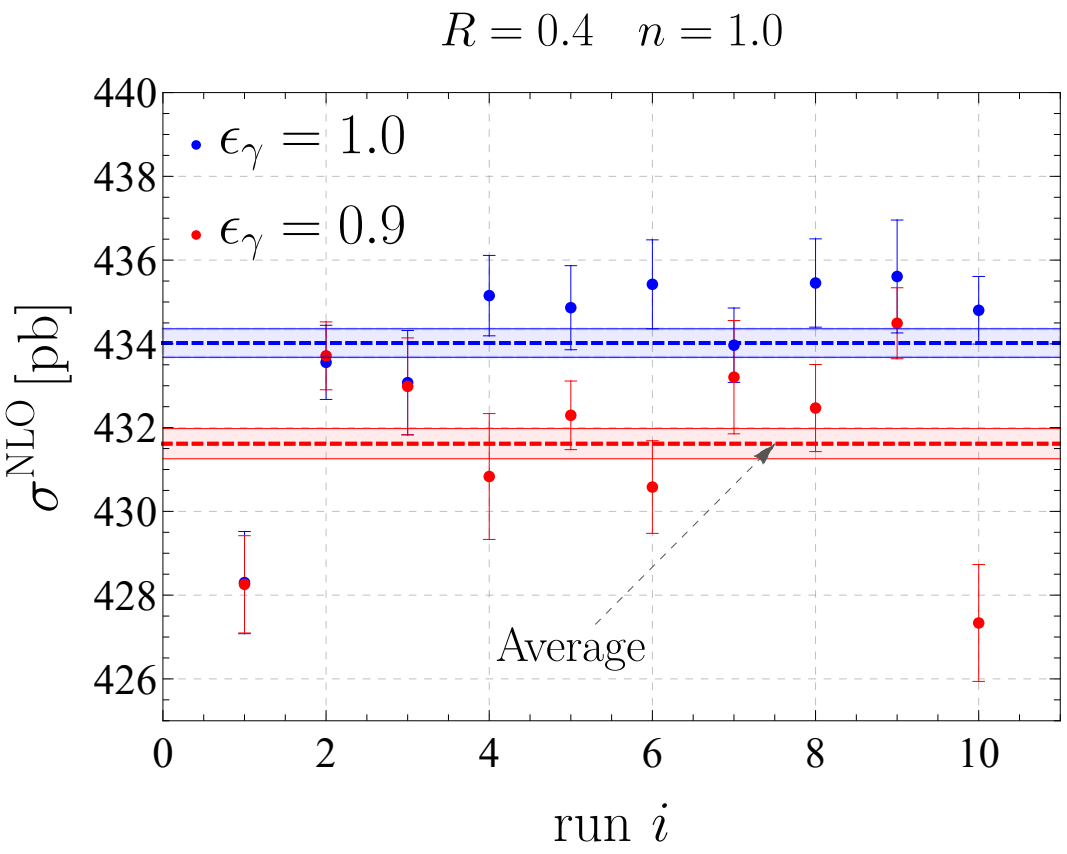

Figure C.1: Results of 20 runs of MadGraph for the NLO cross-section of $pp \to \gamma + X$ with two different values of ϵ_γ and their respective average with averaged errors.

$r_i > R^{\mathrm{ref}}$. II) is inside the reference cone and outside the R cone $R < r_i < R^{\mathrm{ref}}$ and III) is inside both cones $r_i < R \leq R^{\mathrm{ref}}$. If $R = R^{\mathrm{ref}}$, the region II does not exist. These regions can be seen in Figure C.2. In more mathematical terms the constraints are

(I) $r_i > R^{\mathrm{ref}}$: at most one parton, no constraint on p_i^T,

(II) $R < r_i < R^{\mathrm{ref}}$: $\epsilon_\gamma^{\mathrm{ref}} \left(\frac{1-\cos r_i}{1-\cos R^{\mathrm{ref}}}\right)^{n^{\mathrm{ref}}} \leq \frac{p_i^T}{p_\gamma^T}$,

(III) $r_i < R$: $\epsilon_\gamma^{\mathrm{ref}} \left(\frac{1-\cos r_i}{1-\cos R^{\mathrm{ref}}}\right)^{n^{\mathrm{ref}}} \leq \frac{p_i^T}{p_\gamma^T} \leq \epsilon_\gamma \left(\frac{1-\cos r_i}{1-\cos R}\right)^{n}$,

where r_i is the angular distance of the parton to the photon. The implementation of these non-standard cuts in MadGraph5_aMC@NLO is achieved by modifying the file `cuts.f` as explained below.

After telling Madgraph how to compute a cross-section with these requirement, the cross-section for parameters (ϵ_γ, n, R) is computed using

$$\sigma\left(\epsilon_\gamma, n, R\right) = \Delta\sigma\left(\epsilon_\gamma, n, R; \epsilon_\gamma^{\mathrm{ref}}, n^{\mathrm{ref}}, R^{\mathrm{ref}}\right) + \sigma\left(\epsilon_\gamma^{\mathrm{ref}}, n^{\mathrm{ref}}, R^{\mathrm{ref}}\right). \tag{C.5}$$

Doing so is more efficient than computing multiple cross-sections individually. For example, if we are interested in the ϵ_γ dependence of the cross-section and we consider two cones of the same radius $R = R^{\mathrm{ref}}$ with $n = n^{\mathrm{ref}}$ and we vary ϵ_γ. Then certain events of

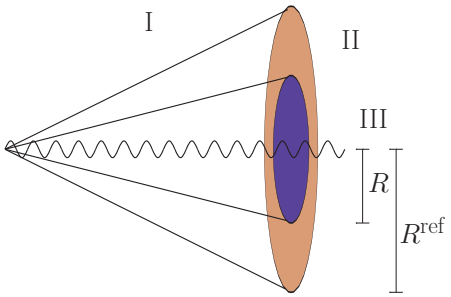

Figure C.2: Isolation cones of radius R and R^{ref} and associated angular regions. The difference $\Delta\sigma$ is obtained from partonic configurations which fulfill the isolation criterion for cone radius R, but fail it for R^{ref}.

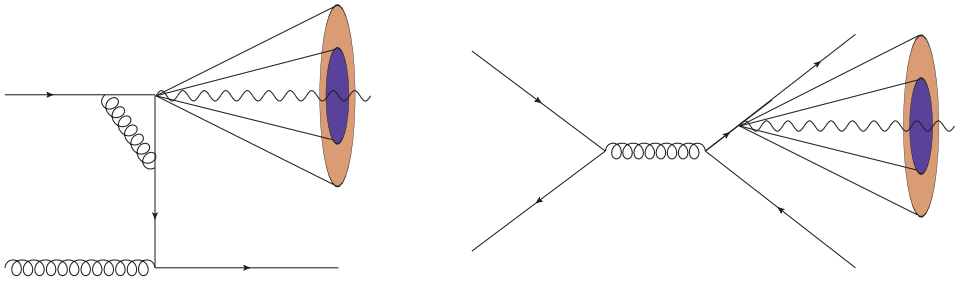

Figure C.3: Example of two processes of $pp \to \gamma + X$ at NLO that are unaffected by both cones, the blue cone has parameters (ϵ_γ, n, R) and the red one $\left(\epsilon_\gamma^{\text{ref}}, n^{\text{ref}}, R^{\text{ref}}\right)$ with $R < R^{\text{ref}}$. The two processes contribute similarly to the cross-sections σ and σ^{ref}. Left: One of the loop correction of the $pp \to \gamma q$, the virtual gluon is unaffected by the cones. The loops are not computed when doing $pp \to jj\gamma$, they are performed when computing σ^{ref}. Right: $q\bar{q} \to \gamma q\bar{q}$ with both quarks being outside the cones.

$pp \to jj\gamma$ will contribute similarly for both cross section $\sigma(\epsilon_\gamma)$ and $\sigma(\epsilon_\gamma^{\text{ref}})$. For instance, if we have two jets outside of the cone, in both cases the jets do not see the cone and contribute similarly to both cross-sections. It is wasteful to ask MadGraph to compute this configuration multiple times. The virtual contributions do not see the isolation cones and would be also computed every time. Note that these virtual corrections of $pp \to j\gamma$ are not computed when we call $p\,p \to jj\gamma$.

In order to compute $\Delta\sigma$ for $pp \to jj\gamma$, we need to modify the `cuts.f` file. There are 6 parameters, I arbitrarily decided that (ϵ_γ, n, R) will be passed in the `run_card.dat` and $\left(\epsilon_\gamma^{\text{ref}}, n^{\text{ref}}, R^{\text{ref}}\right)$ will be directly defined in the `SubProcesses/cuts.f`. This is done in the beginning:

```
logical alliso
real*8 :: R0gammaREF =0.4
real*8 :: xnREF = 1.0
real*8 :: epsgammaREF = 1.0
```

we then need to modify the original isolation

```
do i=1,nQCD
    drlist(i)=sngl(iso_getdrv40(pgamma(0,j),pQCD(0,i)))
enddo
```

```
call sortzv(drlist,isorted,nQCD,ismode,isway,izero)
Etsum(0)=0.d0
nin=0
do i=1,nQCD
    if(dble(drlist(isorted(i))).le.R0gamma)then
        nin=nin+1
        Etsum(nin)=Etsum(nin-1)+pt(pQCD(0,isorted(i)))
    endif
enddo
do i=1,nin
    alliso=alliso .and.
    # Etsum(i).le.chi_gamma_iso(dble(drlist(isorted(i))),
    # R0gamma,xn,epsgamma,ptg)
enddo
```

to the following

```
do i=1,nQCD
    drlist    (i)=sngl(iso_getdrv40(pgamma(0,j),pQCD(0,i)))
enddo
call sortzv(drlist,isorted,nQCD,ismode,isway,izero)
Etsum(0)=0.d0
nin=0
do i=1,nQCD
    if(dble(drlist(isorted(i))).le.dble(R0gammaREF)) then
        nin=nin+1
        Etsum(nin)=Etsum(nin-1)+pt(pQCD(0,isorted(i)))
    endif
enddo
if(nin.eq.0) then
    passcuts_user=.false.
    return
endif
do i=1,nin
    if((dble(drlist(isorted(i))).le.R0gamma)) then
        alliso=alliso .and.
        # Etsum(i).le.chi_gamma_iso(dble(drlist(isorted(i))),
        # R0gamma,xn,epsgamma,ptg).and.
        # Etsum(i).ge.chi_gamma_iso(dble(drlist(isorted(i))),
        # R0gammaREF,xnREF,epsgammaREF,ptg)
    else
        alliso= alliso .and.
        # Etsum(i).ge.chi_gamma_iso(dble(drlist(isorted(i))),
        # R0gammaREF,xnREF,epsgammaREF,ptg)
    endif
enddo
```

It is important to note that `alliso` is initialized to be true.
We have changed the definition of `nin`, the new definition is that `nin` is `true` if the par-

$\sqrt{s} = 13\,\text{TeV}$	$E_T^\gamma > E_T^{\text{min}} = 125\,\text{GeV}$	$\lvert\eta_\gamma\rvert < 2.37$
NNPDF23_nlo_as_0119_qed_mc	$\alpha_s(M_Z) = 0.119$	$\alpha_{\text{EM}} = 1/132.5070$
$\mu_R = \mu_F = 125$ GeV	Frixione cone	no jet cuts

Table C.5: Parameters for the $\Delta\sigma$ computation.

ticle is inside the reference cone R^{ref} and not the R cone as it used to be. If there is no particle in the reference cone, we have actually no chances of failing its isolation so we set `passcuts=.false.`, it would mean that all partons are in region I) . If it is not the case, we then loop over these partons `if (dble(drlist(isorted(i))).le.R0gamma)` which means if the parton is inside both cones, which is region III), we test if it respect the R cone using `Etsum(i).le.chi_gamma_iso(dble(drlist(isorted(i))), R0gamma,xn,epsgamma,ptg)` and fail the R^{ref} cone. If it is the case, we keep `alliso` to be true. If the parton is not in the R cone (therefore in the region II), we only test if it does fail the R^{ref} cone. If yes, `alliso` is kept to be `true`, otherwise it is set to `false`. An event satisfies the cuts if `alliso` is true.

This technique works well in order to compute the NLO cross-section efficiently and to study the dependence of the cross-section on its parameters. It is easy to test it by computing the reference cross-section and a cross-section for (ϵ_γ, n, R) both precisely and finally by running with the modified cuts file. In the Figure C.4 a few values of the cross-section were computed using both the trick using (C.5) and directly using MadGraph. The reference cross-section is taken for the parameters $R = R^{\text{ref}} = 0.4$, $n = n^{\text{ref}} = 1.0$ and $\epsilon_\gamma^{\text{ref}} = 0.1$. The rest of the parameters can be found in Table C.5. As you can see, both predictions are close to each other. Similarly, it is also possible to study the n or R dependence as shown in Figures 5.4 and 5.5. When ϵ_γ gets larger the difference increases, this may be due to the fact that the size of the allowed region of phase space for $\Delta\sigma$ is increasing. In order to get a precise prediction using the $\Delta\sigma$ method, it is crucial to have a precise reference cross-section σ^{ref}.

3 MCFM: single photon production

In this section, the use of MCFM to compute the production of a photon at NLO is discussed in detail. On top of that some details on how to use MCFM to produce cross-section with a fixed energy cone and without any isolation are also discussed.

3.1 General use for $pp \to \gamma + X$

While trying to compare the cross-section generated with MadGraph, NNLOJET and MCFM, we stumbled upon a problem with MCFM 9.1 that needed to be solved before running it[2]. The process for photon production has number 280 (`nproc = 280`). It is imperative to implement the following change. In `/src/Cuts/setscales.f`, you will find the following

```
elseif (nproc == 280) then
    c direct photon production, presence of jet not required
```

[2]The authors of MCFM are aware of this issue and it should be solved in a future release.

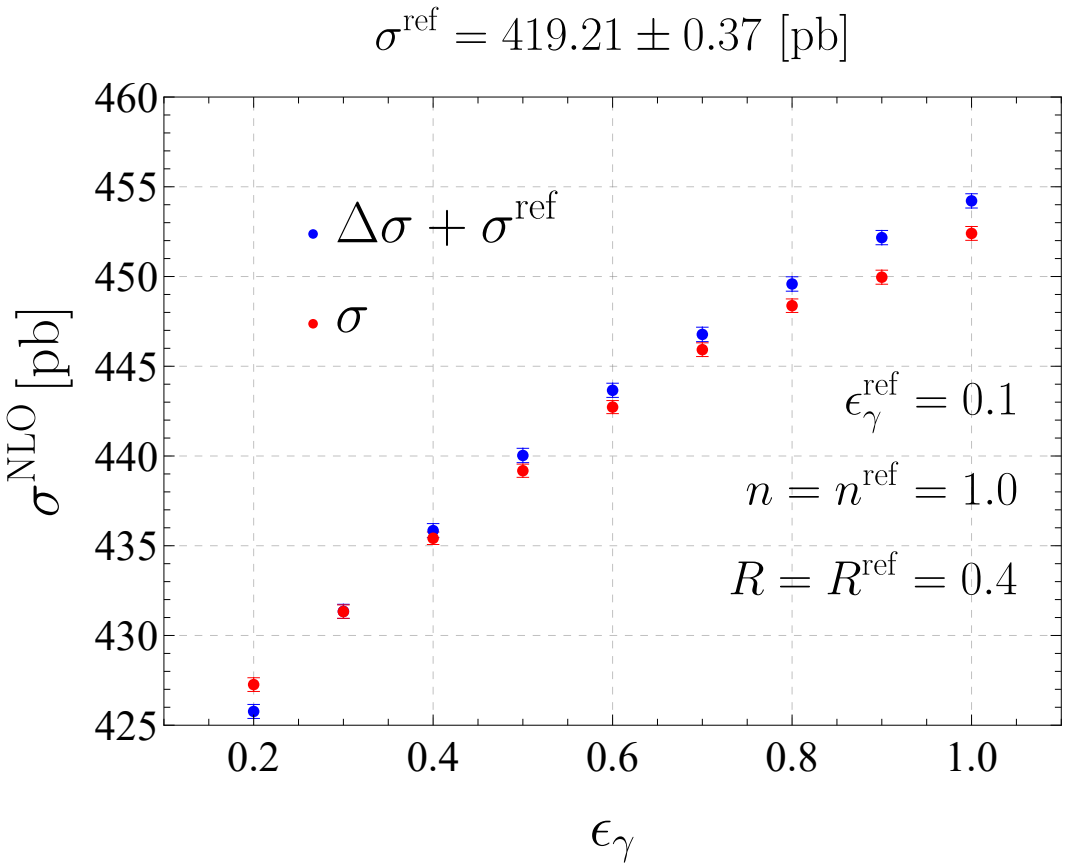

Figure C.4: Next-to-leading order cross-section $\sigma^{\text{NLO}}(\epsilon_\gamma)$ obtained by computing $\Delta\sigma$ trick and the cross-section σ obtained directly using Madgraph for different values of ϵ_γ.

```
    notag=1
```

The variable `notag` needs to be changed to 0 `notag=0`.
In `/src/Procdep/chooser.f` you will find

```
elseif (nproc == 280) then
    ndim=4
    kcase=kdirgam
    plabel(3)='ga'
    plabel(4)='pp'
    plabel(5)='pp'
    lastphot=3
    nqcdjets=1
    n3=0
    inclusive=.true.
```

The `inclusive=.true.` needs to be removed or commented out. This parameter is normally passed in the input file and should not have been hard coded in this file. If `inclusive=.false.`, then we would have only one jet at NLO and this is not the process of interest here. At leading-order this does not change the cross-section.
In order to cross check the prediction of MCFM, the cross-section of $pp \to \gamma + X$ with

$\sqrt{s} = 13\,\text{TeV}$	$E_T^{jet} > 100\,\text{GeV}$	$\lvert\eta_{jet}\rvert < 2.37$
$\mu_R = \mu_F = p_\gamma^T$	$E_T^\gamma > E_T^{\min} = 125\,\text{GeV}$	$\lvert\eta_\gamma\rvert < 2.37$
NNPDF31_nnlo_as_0118_mc	$\alpha_s(M_Z) = 0.118$	$\alpha_{\text{EM}} = 1/137$
$R = 0.4$	$\epsilon_\gamma = 0.0042$	$n = 1.0$

Table C.6: Kinematics and input parameters used for the cross section computations for comparing MCFM, MadGraph and MCFM with Frixione isolation. The constrained on the jets were applied once with the jet k_T jet algorithm and $R_{jet} = 0.4$ we also compute the cross-section without any constraints on the jets ($E_T^{jet} > 0\,\text{GeV}$ and $\lvert\eta_{jet}\rvert < \infty$).

σ [pb]	LO	NLO
MadGraph	192.348 ± 0.060	312.363 ± 0.128
NNLOJET	192.524 ± 0.015	313.965 ± 0.067
MCFM	192.532 ± 0.093	313.833 ± 0.434

Table C.7: Cross-sections computed with MadGraph, NNLOJET and MCFM with a cut on the jets.

Frixione cone is computed with MCFM, MadGraph and NNLOJET.[3] The parameters are listed in the Table C.6. The cross-sections were computed both with cuts on the jets and without. The results can be seen in the Tables C.7 and C.8 (note that as always NLO = LO + dNLO). As you can see the results agree. Note that I ran every MadGraph at NLO 40 times to be precise. The error on the cross-sections from MadGraph could be decreased further by running it a larger number of times.

3.2 Fixed-energy cone

MadGraph can not generate a cross-section or event file using the fixed energy cone since non-perturbative fragmentation functions are not implemented. On the other hand MCFM has three possible choices of fragmentation function; the GdRG LO (see (3.35)) and both BFG sets. To use a fixed-energy cone, it is required to write `fragmentation=.true.` in the input file and to select the set of fragmentation functions by setting `fragmentation_set` to the values `GdRG__LO` , `BFGset_I` or `BFGsetII`. In the manual of MCFM it is recommended

[3] The cross-sections with NNLOJET of Tables C.7 and C.8 were generously provided by Alexander Huss.

σ [pb]	LO	NLO
MadGraph	210.263 ± 0.074	372.307 ± 0.147
NNLOJET	210.843 ± 0.0015	374.283 ± 0.111
MCFM	210.814 ± 0.093	374.556 ± 0.432

Table C.8: Cross-sections computed with MadGraph, NNLOJET and MCFM without any jet cuts.

to use `BFGSet_I` and `BFGSetII` which caused the program to crash. This issue was solved in the latest version of MCFM.

In MCFM, two types of fixed energy cone are implemented depending on the value of the parameter `epsilon_h`

$$\begin{aligned} &\text{if } \texttt{epsilon\_h} < 1 \rightarrow E_{\text{iso}}^T = \texttt{epsilon\_h}\, p_\gamma^T, \\ &\text{if } \texttt{epsilon\_h} \geq 1 \rightarrow E_{\text{iso}}^T = \texttt{epsilon\_h}. \end{aligned} \tag{C.6}$$

The variable `imode` is used to choose the type of fixed cone isolation $E_{\text{iso}}^T = \epsilon_\gamma p_\gamma^T$ or $E_{\text{iso}}^T = E_{\text{threshold}}^T$. The variable is determined in `src/Cuts/iso.f` and depends on the value of `epsilon_h` as explained earlier. In the latest version of MCFM 10.2.1, it is now possible to specify how `epsilon_h` needs to be used directly in the input file. However if we want to use the isolation cone of ATLAS with $E_{\text{iso}}^T = \epsilon_\gamma E_\gamma^T + E_{\text{threshold}}^T$ with $\epsilon_\gamma = 0.0042$ and $E_{\text{threshold}}^T = 4.8$ GeV, we need to modify the internal file of MCFM as explained below. It is unfortunate to have to modify three files as it is not clear which one is used by the program. In `src/Cuts/photo_iso.f` we have to change `z_c` from `z_c = one/opepsilon_h` to

```
opepsilon_h = one+epsilon_h

if (imode == 1) then
!--- isolation using scaling cut
z_c = one/(opepsilon_h+4.8d0/pt(phot_id,p))
```

It is similar in `src/Cuts/photo_iso_phys.f`

```
opeps=one+epsilon_h
if(imode==1) then
!======= this is scaling isolation E_T_max < epsilon_h * pt_gamma
z_c=one/(opeps+4.8d0/pt(phot_id,p))
```

and in `/src/Cuts/photo_iso_z.f`

```
opeps=one+epsilon_h
if(imode==1) then
!======= this is scaling isolation: E_T_max < epsilon_h * pt_gamma
z_c = one/(opeps+4.8d0/pt(phot_id,p))
```

MCFM predictions for fixed-energy cone are compared with the ones of JETPHOX and NNLOJET given in [16], the kinematics and parameters are given in the Table C.9 and the resulting cross-section can be seen in the Table C.10 . The predictions are in agreement.

3.3 Convergence issues with MCFM

One issue we encountered with MCFM 9.1 is that for certain parameters of the cone, the program does not manage to converge. This happens even after trying to run it multiple times. For example while studying the ϵ_γ dependence of the fixed-energy cone, there were some couples of (R, ϵ_γ) values that would not converge. With the parameters of Table 5.1, fixed scale $\mu_i = 125$ GeV $(i = a, f, r)$, the BFGII set and using $R = 0.2$ and taking the value of $\epsilon_\gamma = 0.2, 0.21, 0.22, ..., 0.97, 0.98, 0.99$, the two values of $\epsilon_\gamma = 0.61$ and $\epsilon_\gamma = 0.62$ would

$\sqrt{s} = 13\,\text{TeV}$	$E_T^{jet} > 100\,\text{GeV}$	$\lvert\eta_{jet}\rvert < 2.37$
BFGsetII [49]	$E_T^{\gamma} > E_T^{\min} = 125\,\text{GeV}$	$\lvert\eta_{\gamma}\rvert < 2.37$
NNPDF31_nnlo_as_0118_qed_mc [126]	$\alpha_s(M_Z) = 0.118$	$\alpha_{\text{EM}} = 1/137.036$
$R = 0.4$	$\epsilon_{\gamma} = 0.0042$	$E^T_{\text{threshold}} = 10\,\text{GeV}$

Table C.9: Kinematics and parameters used for the cross-section computations in [16]. The dynamic scale $\mu_f = \mu_r = \mu_a = E_T^{\gamma}$ and k_T-jet algorithm with a radius of 0.4 were used. The cuts are similar to the ones of the Table C.6, except that instead of a Frixione cone, a fixed-energy cone is used and therefore a fragmentation set need to be chosen.

σ [pb]	LO	NLO
MCFM	192.492 ± 0.095	305.011 ± 0.318
NNLOJET	192.487 ± 0.009	304.645 ± 0.059
JETPHOX	192.488 ± 0.003	304.49 ± 0.14

Table C.10: Cross-sections for photon production with fixed energy cones and the kinematics of Table C.9. The values from JETPHOX and NNLOJET are taken from [16].

not converge. The other 78 values of ϵ_{γ} were converging. The value of the cross-sections of neighbors of these two problematic values were reasonable. A partially satisfactory solution of this problem is to run MCFM with slightly different parameters around the problematic one and then to average the values, however this solution does not always work. In this particular case it did not. The following values $\epsilon_{\gamma} = 0.609, 0.611, 0.619, 0.621$ also did not converge. The origin of this problem is unknown to us. Further investigations would be interesting.

3.4 Cross-section without isolation

Unlike MadGraph, MCFM can be used to compute the cross-section without any photon isolation. There are three different equivalent ways to compute the cross-section for photon production without any isolation. We need to set `fragmentation =.true.` in order to have a fixed energy cone. The official way, that you can find in the file `src/Cuts/iso.f` is to take `cone_ang` $< 10^{-4}$ or `epsilon_h` $\leq 10^{-4}$. A more natural way of doing it is to set `epsilon_h` to be the center of mass energy of the collision. It also works and gives the same cross-section. The 3 methods are equivalent. Values of the non-isolated NLO cross-sections can be seen in Table 3.5 with parameters of Table 3.4. These non-isolated cross-sections depend on the choice of the non-perturbative fragmentation function $\mathcal{D}_{i\to\gamma}$.

Bibliography

[1] F. Abe *et al.* [CDF], Phys. Rev. D **48** (1993), 2998-3025 doi:10.1103/PhysRevD.48.2998

[2] J. Baglio and A. Djouadi, JHEP **03** (2011), 055 doi:10.1007/JHEP03(2011)055 [arXiv:1012.0530 [hep-ph]].

[3] W. Vogelsang and A. Vogt, Nucl. Phys. B **453** (1995), 334-354 doi:10.1016/0550-3213(95)00424-Q [arXiv:hep-ph/9505404 [hep-ph]].

[4] D. d'Enterria and J. Rojo, Nucl. Phys. B **860** (2012), 311-338 doi:10.1016/j.nuclphysb.2012.03.003 [arXiv:1202.1762 [hep-ph]].

[5] C. Patrignani *et al.* [Particle Data Group], Chin. Phys. C **40** (2016) no.10, 100001 doi:10.1088/1674-1137/40/10/100001

[6] A. Strumia, [arXiv:1605.09401 [hep-ph]].

[7] [CMS], CMS-PAS-EXO-16-027.

[8] Z. Bern, G. Diana, L. J. Dixon, F. Febres Cordero, S. Hoche, H. Ita, D. A. Kosower, D. Maitre and K. J. Ozeren, Phys. Rev. D **84** (2011), 114002 doi:10.1103/PhysRevD.84.114002 [arXiv:1106.1423 [hep-ph]].

[9] G. Aad *et al.* [ATLAS], JHEP **10** (2019), 203 doi:10.1007/JHEP10(2019)203 [arXiv:1908.02746 [hep-ex]].

[10] G. Aad *et al.* [ATLAS], JHEP **03** (2020), 179 doi:10.1007/JHEP03(2020)179 [arXiv:1912.09866 [hep-ex]].

[11] S. Catani, M. Fontannaz, J. P. Guillet and E. Pilon, JHEP **05** (2002), 028 doi:10.1088/1126-6708/2002/05/028 [arXiv:hep-ph/0204023 [hep-ph]].

[12] S. Catani, M. Fontannaz, J. P. Guillet and E. Pilon, JHEP **09** (2013), 007 doi:10.1007/JHEP09(2013)007 [arXiv:1306.6498 [hep-ph]].

[13] M. Balsiger, T. Becher and D. Y. Shao, JHEP **08** (2018), 104 doi:10.1007/JHEP08(2018)104 [arXiv:1803.07045 [hep-ph]].

[14] M. Balsiger, T. Becher and A. Ferroglia, JHEP **09** (2020), 029 doi:10.1007/JHEP09(2020)029 [arXiv:2006.00014 [hep-ph]].

[15] X. Chen, T. Gehrmann, N. Glover, M. Höfer and A. Huss, JHEP **04** (2020), 166 doi:10.1007/JHEP04(2020)166 [arXiv:1904.01044 [hep-ph]].

[16] X. Chen, T. Gehrmann, E. W. N. Glover, M. Höfer, A. Huss and R. Schürmann, isolation," JHEP **08**, 094 (2022) doi:10.1007/JHEP08(2022)094 [arXiv:2205.01516 [hep-ph]].

[17] Wikipedia contributors Pitch drop experiment — Wikipedia, The Free Encyclopedia. (2022), `https://en.wikipedia.org/w/index.php?title=Pitch_drop_experiment&oldid=1091512547`, [Online; accessed 5-June-2022]

[18] Cern, Facts and figures about the LHC, `https://home.cern/resources/faqs/facts-and-figures-about-lhc`, [Online; accessed 22-September-2022]

[19] Outreach, A. ATLAS Fact Sheet : To raise awareness of the ATLAS detector and collaboration on the LHC. (2010), https://cds.cern.ch/record/1457044

[20] [CMS], CMS-PAS-JME-18-001.

[21] J. Campbell, J. Huston and F. Krauss, Oxford University Press, 2017, ISBN 978-0-19-965274-7

[22] G. Aad *et al.* [ATLAS], JINST **3** (2008), S08003 doi:10.1088/1748-0221/3/08/S08003

[23] S. Chatrchyan *et al.* [CMS], JINST **3** (2008), S08004 doi:10.1088/1748-0221/3/08/S08004

[24] F. Abe *et al.* [CDF], Nucl. Instrum. Meth. A **271** (1988), 387-403 doi:10.1016/0168-9002(88)90298-7

[25] R. K. Ellis, W. J. Stirling and B. R. Webber, Camb. Monogr. Part. Phys. Nucl. Phys. Cosmol. **8** (1996), 1-435 Cambridge University Press, 2011, ISBN 978-0-511-82328-2, 978-0-521-54589-1 doi:10.1017/CBO9780511628788

[26] M. E. Peskin and D. V. Schroeder, Addison-Wesley, 1995, ISBN 978-0-201-50397-5

[27] M. D. Schwartz, Cambridge University Press, 2014, ISBN 978-1-107-03473-0, 978-1-107-03473-0

[28] A. Deur, S. J. Brodsky and G. F. de Teramond, Nucl. Phys. **90** (2016), 1 doi:10.1016/j.ppnp.2016.04.003 [arXiv:1604.08082 [hep-ph]].

[29] A. A. Pivovarov, Phys. Atom. Nucl. **65** (2002), 1319-1340 doi:10.1134/1.1495645 [arXiv:hep-ph/0011135 [hep-ph]].

[30] D. de Florian, G. F. R. Sborlini and G. Rodrigo, Eur. Phys. J. C **76** (2016) no.5, 282 doi:10.1140/epjc/s10052-016-4131-8 [arXiv:1512.00612 [hep-ph]].

[31] S. Moch, J. A. M. Vermaseren and A. Vogt, Nucl. Phys. B **688** (2004), 101-134 doi:10.1016/j.nuclphysb.2004.03.030 [arXiv:hep-ph/0403192 [hep-ph]].

[32] A. Vogt, S. Moch and J. A. M. Vermaseren, Nucl. Phys. B **691** (2004), 129-181 doi:10.1016/j.nuclphysb.2004.04.024 [arXiv:hep-ph/0404111 [hep-ph]].

[33] M. Roth and S. Weinzierl, Phys. Lett. B **590** (2004), 190-198 doi:10.1016/j.physletb.2004.04.009 [arXiv:hep-ph/0403200 [hep-ph]].

[34] T. Kaufmann, A. Mukherjee and W. Vogelsang, Phys. Rev. D **93** (2016) no.11, 114021 doi:10.1103/PhysRevD.93.114021 [arXiv:1604.07175 [hep-ph]].

[35] A. Adare *et al.* [PHENIX], Phys. Rev. D **86** (2012), 072008 doi:10.1103/PhysRevD.86.072008 [arXiv:1205.5533 [hep-ex]].

[36] R. Brock *et al.* [CTEQ], Rev. Mod. Phys. **67** (1995), 157-248 doi:10.1103/RevModPhys.67.157

[37] B. I. Abelev *et al.* [STAR], Phys. Rev. C **81** (2010), 064904 doi:10.1103/PhysRevC.81.064904 [arXiv:0912.3838 [hep-ex]].

[38] C. W. Fabjan and F. Gianotti, Rev. Mod. Phys. **75** (2003), 1243-1286 doi:10.1103/RevModPhys.75.1243

[39] P. A. Zyla *et al.* [Particle Data Group], PTEP **2020** (2020) no.8, 083C01 doi:10.1093/ptep/ptaa104

[40] D. Buskulic *et al.* [ALEPH], Z. Phys. C **69** (1996), 365-378 doi:10.1007/BF02907417

[41] K. Koller, T. F. Walsh and P. M. Zerwas, Z. Phys. C **2** (1979), 197 doi:10.1007/BF01474661

[42] R. D. Field, Front. Phys. **77** (1989), 1-366

[43] M. Gluck, L. E. Gordon, E. Reya and W. Vogelsang, Phys. Rev. Lett. **73** (1994), 388-391 doi:10.1103/PhysRevLett.73.388

[44] A. Gehrmann-De Ridder, T. Gehrmann and E. W. N. Glover, Phys. Lett. B **414** (1997), 354-361 doi:10.1016/S0370-2693(97)01186-6 [arXiv:hep-ph/9705305 [hep-ph]].

[45] R. Schuermann, X. Chen, T. Gehrmann, E. W. N. Glover, M. Höfer and A. Huss, PoS **LL2022** (2022), 034 doi:10.22323/1.416.0034 [arXiv:2208.02669 [hep-ph]].

[46] J. F. Owens, Rev. Mod. Phys. **59** (1987), 465 doi:10.1103/RevModPhys.59.465

[47] T. Horaguchi,Prompt photon production in proton proton collisions at $\sqrt{s} = 200$GeV, PhD thesis at Tokyo Institute of Technology

[48] M. Gluck, E. Reya and A. Vogt, Phys. Rev. D **48** (1993), 116 [erratum: Phys. Rev. D **51** (1995), 1427] doi:10.1103/PhysRevD.51.1427

[49] L. Bourhis, M. Fontannaz and J. P. Guillet, Eur. Phys. J. C **2** (1998), 529-537 doi:10.1007/s100520050158 [arXiv:hep-ph/9704447 [hep-ph]].

[50] A. Gehrmann-De Ridder and E. W. N. Glover, Eur. Phys. J. C **7** (1999), 29-48 doi:10.1007/s100520050382 [arXiv:hep-ph/9806316 [hep-ph]].

[51] E. W. N. Glover and A. G. Morgan, Z. Phys. C **62** (1994), 311-322 doi:10.1007/BF01560245

[52] Z. Belghobsi, M. Fontannaz, J. P. Guillet, G. Heinrich, E. Pilon and M. Werlen, Phys. Rev. D **79** (2009), 114024 doi:10.1103/PhysRevD.79.114024 [arXiv:0903.4834 [hep-ph]].

[53] A. Gehrmann-De Ridder and E. W. N. Glover, Nucl. Phys. B **517** (1998), 269-323 doi:10.1016/S0550-3213(97)00818-3 [arXiv:hep-ph/9707224 [hep-ph]].

[54] S. Moch, J. A. M. Vermaseren and A. Vogt, Nucl. Phys. B **646** (2002), 181-200 doi:10.1016/S0550-3213(02)00870-2 [arXiv:hep-ph/0209100 [hep-ph]].

[55] A. Mitov, S. Moch and A. Vogt, Phys. Lett. B **638** (2006), 61-67 doi:10.1016/j.physletb.2006.05.005 [arXiv:hep-ph/0604053 [hep-ph]].

[56] S. Moch and A. Vogt, Phys. Lett. B **659** (2008), 290-296 doi:10.1016/j.physletb.2007.10.069 [arXiv:0709.3899 [hep-ph]].

[57] S. Frixione, Phys. Lett. B **429** (1998), 369-374 doi:10.1016/S0370-2693(98)00454-7 [arXiv:hep-ph/9801442 [hep-ph]].

[58] T. Binoth *et al.* [SM and NLO Multileg Working Group], [arXiv:1003.1241 [hep-ph]].

[59] M. Cacciari, G. P. Salam and G. Soyez, JHEP **04** (2008), 005 doi:10.1088/1126-6708/2008/04/005 [arXiv:0802.1188 [hep-ph]].

[60] G. F. Sterman and S. Weinberg, Phys. Rev. Lett. **39** (1977), 1436 doi:10.1103/PhysRevLett.39.1436

[61] J. M. Campbell, R. K. Ellis and C. Williams, Phys. Rev. Lett. **118** (2017) no.22, 222001 [erratum: Phys. Rev. Lett. **124** (2020) no.25, 259901] doi:10.1103/PhysRevLett.118.222001 [arXiv:1612.04333 [hep-ph]].

[62] J. M. Campbell, R. K. Ellis and C. Williams, Phys. Rev. D **96** (2017) no.1, 014037 doi:10.1103/PhysRevD.96.014037 [arXiv:1703.10109 [hep-ph]].

[63] T. Becher, A. Broggio and A. Ferroglia, Lect. Notes Phys. **896** (2015), pp.1-206 Springer, 2015, doi:10.1007/978-3-319-14848-9 [arXiv:1410.1892 [hep-ph]].

[64] L. Dai, C. Kim and A. K. Leibovich, Phys. Rev. D **94** (2016) no.11, 114023 doi:10.1103/PhysRevD.94.114023 [arXiv:1606.07411 [hep-ph]].

[65] P. Aurenche, M. Fontannaz, J. P. Guillet, E. Pilon and M. Werlen, Phys. Rev. D **73** (2006), 094007 doi:10.1103/PhysRevD.73.094007 [arXiv:hep-ph/0602133 [hep-ph]].

[66] S. Catani, L. Cieri, D. de Florian, G. Ferrera and M. Grazzini, JHEP **04** (2018), 142 doi:10.1007/JHEP04(2018)142 [arXiv:1802.02095 [hep-ph]].

[67] M. Höfer, Higher order corrections to photon production in hadronic collisions at the LHC, PhD thesis at university of Zürich

[68] J. Alcaraz Maestre *et al.* [SM, NLO MULTILEG Working Group and SM MC Working Group], [arXiv:1203.6803 [hep-ph]].

[69] C. Frye, M. Freytsis, J. Scholtz and M. J. Strassler, JHEP **03** (2016), 171 doi:10.1007/JHEP03(2016)171 [arXiv:1510.08451 [hep-ph]].

[70] T. Aaltonen *et al.* [CDF], Phys. Rev. D **80** (2009), 111106 doi:10.1103/PhysRevD.80.111106 [arXiv:0910.3623 [hep-ex]].

[71] T. Becher, S. Favrod and X. Xu, JHEP **01** (2023), 005 doi:10.1007/JHEP01(2023)005 [arXiv:2208.01554 [hep-ph]].

[72] M. Aaboud *et al.* [ATLAS], Phys. Lett. B **770** (2017), 473-493 doi:10.1016/j.physletb.2017.04.072 [arXiv:1701.06882 [hep-ex]].

[73] S. Chatrchyan *et al.* [CMS], Eur. Phys. J. C **74** (2014) no.11, 3129 doi:10.1140/epjc/s10052-014-3129-3 [arXiv:1405.7225 [hep-ex]].

[74] A. M. Sirunyan *et al.* [CMS], Eur. Phys. J. C **79** (2019) no.1, 20 doi:10.1140/epjc/s10052-018-6482-9 [arXiv:1807.00782 [hep-ex]].

[75] A. M. Sirunyan *et al.* [CMS], Eur. Phys. J. C **79** (2019) no.11, 969 doi:10.1140/epjc/s10052-019-7451-7 [arXiv:1907.08155 [hep-ex]].

[76] S. Catani, L. Cieri, D. de Florian, G. Ferrera and M. Grazzini, Phys. Rev. Lett. **108** (2012), 072001 [erratum: Phys. Rev. Lett. **117** (2016) no.8, 089901] doi:10.1103/PhysRevLett.108.072001 [arXiv:1110.2375 [hep-ph]].

[77] J. M. Campbell, R. K. Ellis, Y. Li and C. Williams, JHEP **07** (2016), 148 doi:10.1007/JHEP07(2016)148 [arXiv:1603.02663 [hep-ph]].

[78] T. Gehrmann, N. Glover, A. Huss and J. Whitehead, JHEP **01** (2021), 108 doi:10.1007/JHEP01(2021)108 [arXiv:2009.11310 [hep-ph]].

[79] H. A. Chawdhry, M. Czakon, A. Mitov and R. Poncelet, JHEP **09** (2021), 093 doi:10.1007/JHEP09(2021)093 [arXiv:2105.06940 [hep-ph]].

[80] S. Badger, T. Gehrmann, M. Marcoli and R. Moodie, Phys. Lett. B **824** (2022), 136802 doi:10.1016/j.physletb.2021.136802 [arXiv:2109.12003 [hep-ph]].

[81] H. A. Chawdhry, M. L. Czakon, A. Mitov and R. Poncelet, JHEP **02** (2020), 057 doi:10.1007/JHEP02(2020)057 [arXiv:1911.00479 [hep-ph]].

[82] S. Kallweit, V. Sotnikov and M. Wiesemann, Phys. Lett. B **812** (2021), 136013 doi:10.1016/j.physletb.2020.136013 [arXiv:2010.04681 [hep-ph]].

[83] E. Hall and J. Thaler, JHEP **09** (2018), 164 doi:10.1007/JHEP09(2018)164 [arXiv:1805.11622 [hep-ph]].

[84] F. Siegert, J. Phys. G **44** (2017) no.4, 044007 doi:10.1088/1361-6471/aa5f29 [arXiv:1611.07226 [hep-ph]].

[85] A. Gehrmann-De Ridder, T. Gehrmann and E. W. N. Glover, JHEP **09** (2005), 056 doi:10.1088/1126-6708/2005/09/056 [arXiv:hep-ph/0505111 [hep-ph]].

[86] A. Daleo, T. Gehrmann and D. Maitre, JHEP **04** (2007), 016 doi:10.1088/1126-6708/2007/04/016 [arXiv:hep-ph/0612257 [hep-ph]].

[87] J. Currie, E. W. N. Glover and S. Wells, JHEP **04** (2013), 066 doi:10.1007/JHEP04(2013)066 [arXiv:1301.4693 [hep-ph]].

[88] T. Gehrmann and R. Schürmann, JHEP **04** (2022), 031 doi:10.1007/JHEP04(2022)031 [arXiv:2201.06982 [hep-ph]].

[89] C. W. Bauer, S. Fleming, D. Pirjol and I. W. Stewart, Phys. Rev. D **63** (2001), 114020 doi:10.1103/PhysRevD.63.114020 [arXiv:hep-ph/0011336 [hep-ph]].

[90] C. W. Bauer, D. Pirjol and I. W. Stewart, Phys. Rev. D **65** (2002), 054022 doi:10.1103/PhysRevD.65.054022 [arXiv:hep-ph/0109045 [hep-ph]].

[91] M. Beneke, A. P. Chapovsky, M. Diehl and T. Feldmann, Nucl. Phys. B **643** (2002), 431-476 doi:10.1016/S0550-3213(02)00687-9 [arXiv:hep-ph/0206152 [hep-ph]].

[92] M. Procura and I. W. Stewart, Phys. Rev. D **81** (2010), 074009 [erratum: Phys. Rev. D **83** (2011), 039902] doi:10.1103/PhysRevD.81.074009 [arXiv:0911.4980 [hep-ph]].

[93] Z. B. Kang, F. Ringer and I. Vitev, JHEP **10** (2016), 125 doi:10.1007/JHEP10(2016)125 [arXiv:1606.06732 [hep-ph]].

[94] P. Cal, F. Ringer and W. J. Waalewijn, JHEP **05** (2019), 143 doi:10.1007/JHEP05(2019)143 [arXiv:1901.06389 [hep-ph]].

[95] M. Dasgupta, F. Dreyer, G. P. Salam and G. Soyez, JHEP **04** (2015), 039 doi:10.1007/JHEP04(2015)039 [arXiv:1411.5182 [hep-ph]].

[96] M. Dasgupta, F. A. Dreyer, G. P. Salam and G. Soyez, JHEP **06** (2016), 057 doi:10.1007/JHEP06(2016)057 [arXiv:1602.01110 [hep-ph]].

[97] Y. T. Chien and I. Vitev, JHEP **12** (2014), 061 doi:10.1007/JHEP12(2014)061 [arXiv:1405.4293 [hep-ph]].

[98] T. Becher, M. Neubert, L. Rothen and D. Y. Shao, Phys. Rev. Lett. **116** (2016) no.19, 192001 doi:10.1103/PhysRevLett.116.192001 [arXiv:1508.06645 [hep-ph]].

[99] T. Becher, M. Neubert, L. Rothen and D. Y. Shao, JHEP **11** (2016), 019 [erratum: JHEP **05** (2017), 154] doi:10.1007/JHEP11(2016)019 [arXiv:1605.02737 [hep-ph]].

[100] X. Liu, S. O. Moch and F. Ringer, Phys. Rev. Lett. **119** (2017) no.21, 212001 doi:10.1103/PhysRevLett.119.212001 [arXiv:1708.04641 [hep-ph]].

[101] X. Liu, S. O. Moch and F. Ringer, Phys. Rev. D **97** (2018) no.5, 056026 doi:10.1103/PhysRevD.97.056026 [arXiv:1801.07284 [hep-ph]].

[102] M. Dasgupta and G. P. Salam, Phys. Lett. B **512** (2001), 323-330 doi:10.1016/S0370-2693(01)00725-0 [arXiv:hep-ph/0104277 [hep-ph]].

[103] E. Laermann, T. F. Walsh, I. Schmitt and P. M. Zerwas, Nucl. Phys. B **207** (1982), 205-232 doi:10.1016/0550-3213(82)90162-6

[104] T. Kaufmann, A. Mukherjee and W. Vogelsang, CERN Proc. **1** (2018), 211 doi:10.23727/CERN-Proceedings-2018-001.211 [arXiv:1708.06683 [hep-ph]].

[105] R. D. Ball, V. Bertone, S. Carrazza, C. S. Deans, L. Del Debbio, S. Forte, A. Guffanti, N. P. Hartland, J. I. Latorre and J. Rojo, *et al.* Nucl. Phys. B **867** (2013), 244-289 doi:10.1016/j.nuclphysb.2012.10.003 [arXiv:1207.1303 [hep-ph]].

[106] J. Campbell and T. Neumann, JHEP **12** (2019), 034 doi:10.1007/JHEP12(2019)034 [arXiv:1909.09117 [hep-ph]].

[107] K. Ackerstaff *et al.* [OPAL], Eur. Phys. J. C **2** (1998), 39-48 doi:10.1007/s100520050122 [arXiv:hep-ex/9708020 [hep-ex]].

[108] J. Alwall, R. Frederix, S. Frixione, V. Hirschi, F. Maltoni, O. Mattelaer, H. S. Shao, T. Stelzer, P. Torrielli and M. Zaro, JHEP **07** (2014), 079 doi:10.1007/JHEP07(2014)079 [arXiv:1405.0301 [hep-ph]].

[109] A. Vogt, Comput. Phys. Commun. **170** (2005), 65-92 doi:10.1016/j.cpc.2005.03.103 [arXiv:hep-ph/0408244 [hep-ph]].

[110] G. P. Salam and J. Rojo, Comput. Phys. Commun. **180** (2009), 120-156 doi:10.1016/j.cpc.2008.08.010 [arXiv:0804.3755 [hep-ph]].

[111] "APFEL: A PDF Evolution Library with QED corrections," Comput. Phys. Commun. **185** (2014), 1647-1668 doi:10.1016/j.cpc.2014.03.007 [arXiv:1310.1394 [hep-ph]].

[112] T. Becher, T. Rauh and X. Xu, JHEP **08**, 134 (2022) doi:10.1007/JHEP08(2022)134 [arXiv:2112.02108 [hep-ph]].

[113] G. Aad *et al.* [ATLAS], JHEP **10** (2019), 203 doi:10.1007/JHEP10(2019)203 [arXiv:1908.02746 [hep-ex]].

[114] G. Aad *et al.* [ATLAS], JHEP **11** (2021), 169 doi:10.1007/JHEP11(2021)169 [arXiv:2107.09330 [hep-ex]].

[115] A. Banfi, F. A. Dreyer and P. F. Monni, JHEP **10** (2021), 006 doi:10.1007/JHEP10(2021)006 [arXiv:2104.06416 [hep-ph]].

[116] A. Banfi, F. A. Dreyer and P. F. Monni, JHEP **03** (2022), 135 doi:10.1007/JHEP03(2022)135 [arXiv:2111.02413 [hep-ph]].

[117] D. Graudenz, M. Hampel, A. Vogt and C. Berger, Z. Phys. C **70** (1996), 77-82 doi:10.1007/s002880050083 [arXiv:hep-ph/9506333 [hep-ph]].

[118] M. Bonvini, [arXiv:1212.0480 [hep-ph]].

[119] G. Alvarez, G. Cvetic, B. A. Kniehl, I. Kondrashuk and I. Parra-Ferrada, doi:10.3204/PUBDB-2016-06335 [arXiv:1611.08787 [hep-ph]].

[120] G. Altarelli, R. K. Ellis and G. Martinelli, Nucl. Phys. B **157** (1979), 461-497 doi:10.1016/0550-3213(79)90116-0

[121] Campbell, J., Ellis, R., Neumann, T. & Williams, C. MCFM-10.2 manual. (2019)

[122] J. Alwall, A. Ballestrero, P. Bartalini, S. Belov, E. Boos, A. Buckley, J. M. Butterworth, L. Dudko, S. Frixione and L. Garren, *et al.* Comput. Phys. Commun. **176** (2007), 300-304 doi:10.1016/j.cpc.2006.11.010 [arXiv:hep-ph/0609017 [hep-ph]].

[123] E. A. Smith. (2016) TWiki at CERN `https://twiki.cern.ch/twiki/pub/Main/KUCMStHqAnalysis/MadGraph_Guide.pdf` [Online; accessed 10-August-2022]

M. Zaro H. Shao B. Hespel A. Martini I. Tsinikos

[124] M. Zaro*et al.* (2016) `https://indico.cern.ch/event/555228/sessions/203428/attachments/1315471/1970459/tutorial-CMSandATLAS-2016.pdf` [Online; accessed 10-August-2022]

[125] A. D. Martin, W. J. Stirling, R. S. Thorne and G. Watt, Eur. Phys. J. C **63** (2009), 189-285 doi:10.1140/epjc/s10052-009-1072-5 [arXiv:0901.0002 [hep-ph]].

[126] R. D. Ball *et al.* [NNPDF], Eur. Phys. J. C **82** (2022) no.5, 428 doi:10.1140/epjc/s10052-022-10328-7 [arXiv:2109.02653 [hep-ph]].

Remerciements

C'est à cause que tout doit finir
que tout est si beau.

Charles Ferdinand Ramuz

Il me sera difficile de remercier toutes les personnes qui m'ont permis d'accomplir cette thèse de doctorat, car elles sont nombreuses à avoir à un moment été d'une aide précieuse durant ces quatre années.

Premièrement, j'aimerais remercier mon superviseur Thomas Becher professeur à l'université de Berne qui m'a encadré durant mon doctorat. Il a été un excellent superviseur, toujours de bonne humeur, toujours disponible même en ayant un emploi du temps chargé, notamment par diverses obligations administratives inhérentes à sa fonction. Il a su faire preuve d'énormément de patience pour répondre à mes nombreuses questions et a toujours été ouvert aux suggestions bonnes ou mauvaises de ses collaborateurs. Il me faut aussi remercier Thomas Gehrmann professeur à l'université de Zurich et Michele Weber professeur à l'université de Berne pour avoir accepter d'être expert externe pour ma thèse et de présider ma défense respectivement.

De plus, cela a été un plaisir de passer quatre ans à l'université de Berne entouré de gens si sympathiques, en particulier Rudi Rahn, Thomas Rauh et Xiaofeng Xu avec qui j'ai eu la chance de partager un bureau. Mes remerciements s'adressent aussi aux autres doctorants de l'institut pour les nombreux bon moments passés ensemble, en particulier: Joachim Monnard, Francesco Saturnino, Laetitia Laub, Manes Hornung, Simona Procacci, Sebastian Burri, Patrick Bühlmann et Martina Cottini. Je voudrais aussi remercier tout particulièrement mes deux collègues de doctorat et amis Marcel Balsiger et Nicolas Schalch pour les nombreuses et intéressantes discussions et suggestions.

Je voudrais aussi remercier Susanne Reffert et Domenico Orlando pour l'intense et intéressante demi-année passée à faire de la recherche avec eux durant mon travail de master.

Finalement, toute ma gratitude va aux personnes qui dans ma vie privée m'ont soutenu, ont fait preuve de patience ou simplement ont été de bonne compagnie. Elles sauront se reconnaître.

Erklärung

gemäss Art. 18 PromR Phil.-nat. 2019

Name/Vorname: Favrod Samuel

Matrikelnummer: 13-824-412

Studiengang: Physik

Bachelor ☐ Master ☐ Dissertation ☑

Titel der Arbeit: QCD anatomy of photon isolation

LeiterIn der Arbeit: Prof. Dr. Thomas Becher

Ich erkläre hiermit, dass ich diese Arbeit selbständig verfasst und keine anderen als die angegebenen Quel-len benutzt habe. Alle Stellen, die wörtlich oder sinn-gemäss aus Quellen entnommen wurden, habe ich als solche gekennzeichnet. Mir ist bekannt, dass andern-falls der Senat gemäss Artikel 36 Absatz 1 Buchstabe r des Gesetzes über die Universität vom 5. September 1996 und Artikel 69 des Universitätssta-tuts vom 7. Juni 2011 zum Entzug des Doktortitels be-rechtigt ist.
Für die Zwecke der Begutachtung und der Überprüfung der Einhaltung der Selbständigkeitserklärung bzw. der Reglemente betreffend Plagiate erteile ich der Univer-sität Bern das Recht, die dazu erforderlichen Perso-nendaten zu bearbeiten und Nutzungshandlungen vor-zunehmen, insbesondere die Doktorarbeit zu vervielfäl-tigen und dauerhaft in einer Datenbank zu speichern sowie diese zur Überprüfung von Arbeiten Dritter zu verwenden oder hierzu zur Verfügung zu stellen.

Ort/Datum

Unterschrift